

JOHANNES GUTENBERG
UNIVERSITÄT MAINZ



SEARCH FOR NEW PHYSICS WITH INTENSE
PION AND ELECTRON BEAMS

Luca Doria

Habilitationsschrift
zur Erlangung der *venia legendi* im Fach
Experimentalphysik

vorgelegt beim Fachbereich Physik, Mathematik
und Informatik der Johannes
Gutenberg-Universität Mainz

September 2018

Deutsche Zusammenfassung

Die Suche nach neuer Physik ist heutzutage ein sehr spannendes Thema. Mit der Entdeckung des Higgs-Bosons im Jahr 2012 am CERN, würden alle vom Standardmodell vorhergesagten Teilchen gefunden. Obwohl das ein historischer Meilenstein ist, stehen weitere Herausforderungen bevor. Das Standardmodell gibt eine genaue Beschreibung der Wechselwirkung der Elementarteilchen, aber viele seiner Eigenschaften bleiben unklar: Beispiele sind das Generationenproblem, die Größe der vorhergesagten CP-Verletzung, die genaue Natur der Neutrinos und die unnatürlich kleine Masse des Higgs-Bosons. Andere Herausforderungen kommen von astrophysikalischen und kosmologischen Beobachtungen, die die Existenz von dunkler Materie und dunkler Energie offenbaren. Diese neuen Phänomene sind im Moment völlig außerhalb des Standardmodells. Es gibt viele Kandidaten für Theorien, die neue Physik jenseits des Standardmodells vorhersagen, aber keine eindeutigen experimentellen Beweise für Abweichungen davon. Während Beschleuniger wie der LHC versuchen die höchstmöglichen Energien zu erreichen, versuchen Präzisionsexperimente Abweichungen von den Vorhersagen, mit ausgewählten Observablen zu messen. Diese Arbeit besteht aus zwei Teilen. Der erste beschreibt das PIENU-Experiment zur genauen Messung des $\pi \rightarrow e\nu$ Verzweigungsverhältnisses. Dieses Observable ist sehr empfindlich auf Beiträge von neuer Physik, und es ist gleichzeitig eine der präzisesten Rechnungen innerhalb des Standardmodells. Der zweite Teil beschäftigt sich mit einem neuen Experiment zur Suche nach dunkler Materie. Dieses Experiment zielt insbesondere darauf ab, neue "Dark Sector" Modelle der leichten dunklen Materie zu testen und es wird auf dem zu entwickelnden Beschleuniger MESA an der Johannes-Gutenberg Universität Mainz basiert sein.

*To my twin sons
Emanuele and Leonardo*

Preface

The Standard Model of particle physics (SM) was devised initially between the 60s and the 70s of the previous century and since then it has been applied to the description of elementary particle interactions with remarkable success. Several decades of intense research aimed to improve collision energies and precision has not revealed any flaws in the model.

The SM made a series of predictions which were verified one after the other. The most striking ones were about the existence of new particles, which have been indeed discovered. From the discovery of the plethora of strongly interacting bound states (60s), the massive vector bosons of the electroweak interaction (1983) [1, 2], and the top quark (1995) [3, 4], the SM unleashed an incredible sequence of successes.

The crowning achievement of the SM was the prediction and final discovery in 2012 at CERN, of the Higgs boson [5, 6]. This was the last undiscovered particle required by the SM and as to the time of writing, it behaves exactly as predicted. Why do we keep pushing the limits of our accelerators and experimental techniques since the SM has been so successful?

The reasons are manifold and connected to new experimental findings from one side and to features of the SM which are not fully satisfactory to the other. The first hint that the SM is not complete is the experimental evidence of a non-zero mass for neutrinos. According to the SM, these elusive particles are massless, and how to take into account a massive version of them is still an open question. Another puzzling feature of the SM is family replication: there are 3 families of particles in the SM, each of which is described by the same mathematical structure. We know that the existence of 3 families leads to CP violation, but at the same time its amount is not sufficient to explain the matter-antimatter asymmetry in

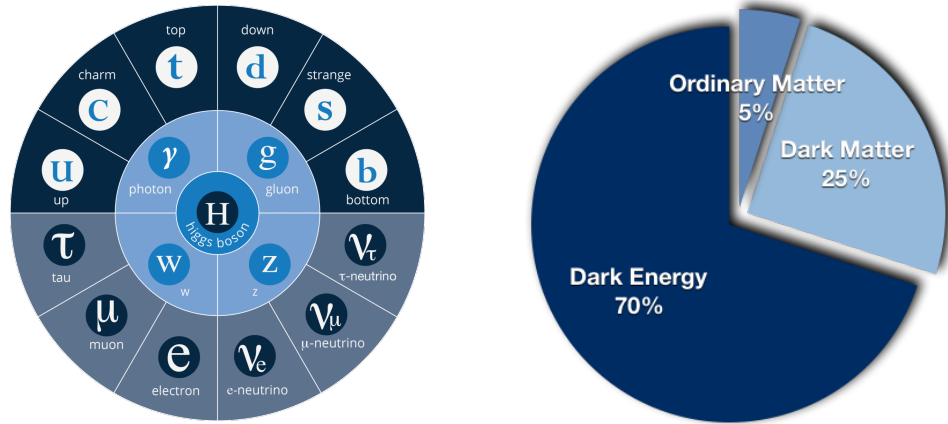


Figure 1: (Left) The particle content of the Standard Model of Particle Physics (figure from the ATLAS collaboration at CERN). (Right) Matter content of the Universe according to the latest measurements supporting the Λ CDM model [7, 8].

the Universe.

Despite the successful discovery of the Higgs boson, its relatively light mass poses additional questions, since radiative corrections tend to push its mass to very high values: delicate cancellations are required for keeping the mass at its measured value [9].

Other big challenges come from astrophysical and cosmological measurements in the form of dark matter and dark energy. The most recent results established the Λ CDM as the standard model of cosmology. This model [10] explains the observations with a cosmological constant term (Λ) and cold dark matter (CDM). The exact physical nature of these two components is still a mystery.

If new particles are responsible for these new phenomena, the SM should be extended to be able to account for them.

Last but not least, the SM does not include gravity. This force is still accurately described by a classical theory: general relativity [11].

All these questions motivate an intense research program to either directly discover new particles or to push the tests of the SM to the limit until deviations from its predictions are observed.

In this work, we describe two different experiments, one completed and one in its design phase, aimed at uncovering physics beyond the SM.

-
1. The **PIENU experiment** is an experiment designed to make a precise measurement of the branching ratio

$$R_\pi = \frac{\pi^+ \rightarrow e^+ \nu_e}{\pi^+ \rightarrow \mu^+ \nu_\mu \rightarrow e^+ \nu_e \bar{\nu}_\mu} .$$

This observable is the most precisely calculated SM observable involving quarks. Comparing its theoretical value with a precise measurement can provide an important test of the SM. In particular, it is possible to test *lepton universality*, an underlying assumption for the SM which implies that every lepton generation couples with the same strength to the electroweak force. The large collected sample of pion decays allows also for searches of new particles, like massive neutrinos.

The experiment was designed, built, and operated from 2008 to 2012 at TRIUMF (Canada's Laboratory for Particle and Nuclear Physics) where intense pion beams are available. The experiment is now complete and the data analysis is in its last phase.

2. At the Institute for Nuclear Physics of the Johannes Gutenberg University in Mainz (Germany) a new high-current electron accelerator is currently in its advanced design phase. The accelerator is a modern superconducting energy recovery linac which will allow new precision experiments in particle, hadron, and nuclear physics. One of the experiments foreseen is a **Beam Dump Experiment** for the search of Dark Matter. This experiment is in its design phase, and simulation studies of the feasibility and sensitivity will be described.

In preparing this thesis, I benefited from the excellent work carried out by many Bachelor, Master, and PhD students. In particular, the following theses were important sources of information:

Kaoru Yamada, *Search for massive neutrinos in the $\pi^+ \rightarrow e^+ \nu_e$ decay*, Ph.D. 2010 (Osaka University, Japan).

Chloe Malbrunot, *Study of the $\pi^+ \rightarrow e^+ \nu_e$ decay*, Ph.D. 2012 (University of British Columbia, Canada).

Dorothea vom Bruch, *Studies for the PIENU Experiment and on the Direct Radiative Capture of Muons in Zirconium*, M.Sc. 2013 (University of British Columbia, Canada).

Kevin Yin, *Improving the Time and Energy Resolution in the PIENU Calorimeter System*, B.Sc. 2015 (University of British Columbia, Canada)

Shintaro Ito, *Measurement of the $\pi^+ \rightarrow e^+ \nu_e$ Branching Ratio*, Ph.D. 2016 (Osaka University, Japan).

Tristan S. Sullivan, *A high-precision measurement of the $\pi^+ \rightarrow e^+ \nu_e$ branching ratio*, Ph.D. 2017 (University of British Columbia, Canada)

Saul Cuen-Rochin, *Precise Measurement of Rare Pion Decays*, 2019 (University of British Columbia, Canada).

The PIENU experiment was conceived, constructed, and operated over almost a decade, delivering important results in the field of precision physics and new physics searches.

The work I carried out recently with the PIENU data on massive neutrinos represents for me the first step towards the physics of dark matter, which is now my main research interest and the subject of the second part of the thesis.

For all incorrect statements and inaccuracies in the present work, I am personally responsible ¹.

Luca Doria

Mainx, September 2018.

¹During the habilitation process and following the submission of the thesis, corrections and updates were included.

Contents

I	Search for New Physics with Pion Beams	1
1	Introduction	3
1.1	Pion Decay Experiments: a Historical Perspective	4
1.2	Previous Experimental Measurements	5
1.3	Towards the new Experiment	6
1.4	The PIENU Experiment	8
1.5	Search for new Physics with Pion Decays	11
1.6	Summary	11
2	Theoretical Aspects	13
2.1	The Standard Model of Particle Physics	13
2.1.1	Electroweak Interactions	13
2.1.2	Strong Interaction	15
2.1.3	Neutrinos	16
2.2	Pions in an Effective Field Theory of QCD	19
2.3	The Pion Decay	22
2.3.1	Helicity Suppression	23
2.3.2	Lepton Universality	25
2.3.3	Pion Decay Modes	26
2.4	Precision Theoretical Calculations of R_π	26
2.4.1	Summary of the SM Calculations	30
2.5	Physics Beyond the Standard Model	30
2.5.1	New Scalar and Pseudoscalar Interactions	31
2.5.2	Supersymmetry	32
2.5.3	Charged Higgs	34

2.5.4	Leptoquarks	34
2.5.5	Partial Compositeness	35
2.5.6	Heavy Neutrinos	35
2.5.7	Majorons	37
2.6	Status of Universality Violation Searches	38
2.7	Summary	41
3	Experimental Setup	43
3.1	The TRIUMF Cyclotron	43
3.2	The M13 Beamline	43
3.3	The PIENU Detector	49
3.3.1	Design Considerations	50
3.3.2	Plastic Scintillators	53
3.3.3	Wire Chambers	54
3.3.4	Silicon Detectors	55
3.3.5	NaI(Tl) Crystal Calorimeter	57
3.3.6	CsI Crystal Calorimeter	58
3.3.7	Tracking	59
3.3.8	Trigger	64
3.3.9	Data Acquisition	66
3.3.10	Final Detector Assembly	72
3.4	Datataking History	73
3.4.1	2009 Run	74
3.4.2	2010 Run	74
3.4.3	2011 Run	74
3.4.4	2012 Run	75
3.5	Summary	75
4	Data Analysis	77
4.1	Blind Analysis Technique	77
4.2	Calibration Procedures	79
4.2.1	Scintillators	79
4.2.2	Silicon Detectors	79
4.2.3	NaI(Tl) Crystal	81
4.2.4	CsI Crystals	81
4.3	Event Selection	82
4.3.1	Pion Identification	82
4.3.2	Positron Identification	84

CONTENTS

4.3.3	Pileup Rejection	85
4.4	Additional Cuts	87
4.5	Acceptance Definition	89
4.6	Energy Spectrum	90
4.7	Time Spectrum Fit	91
4.8	Fitting function	91
4.8.1	Low energy time spectrum	91
4.8.2	High energy time spectrum	92
4.9	Summary	96
5	Corrections	99
5.1	The Low Energy Tail Correction	99
5.1.1	Estimation of the Low Energy Tail with a Positron Beam	100
5.1.2	Positron Beam Data Analysis	101
5.1.3	Muon Correction	102
5.1.4	Simulation of the Photonuclear Reactions	105
5.1.5	Systematic Uncertainties	106
5.1.6	Calculation of the Low Energy Tail	106
5.1.7	Simulation of the Pion Beam	107
5.2	Acceptance Correction	110
5.3	Muon Decay in Flight Correction	112
5.4	t_0 Correction	113
5.5	Summary	113
6	Results	115
6.1	The $\pi^+ \rightarrow e^+ \nu_e$ Branching Ratio	115
6.2	Systematic Checks	121
6.3	Combination of the Datasets	122
6.4	Branching Ratio Results	125
6.5	Search for Heavy Neutrinos in the $\pi^+ \rightarrow e^+ \nu_e$ Decay	126
6.6	Other BSM Searches	130
6.6.1	Search for Heavy Neutrinos in the $\pi^+ \rightarrow \mu^+ \nu_\mu$ Decay	130
6.6.2	Search for Majorons in the $\pi^+ \rightarrow e^+ \nu_e$ Decay	133
6.7	Summary	134

7	Limits on New Physics	137
7.1	Lepton Universality	137
7.2	New Pseudo-Scalar Interactions	138
7.3	R-Parity violating SUSY	138
7.4	Charged Higgs Bosons	139
7.5	Massive Neutrinos	140
7.6	Summary and Outlook	141
II	Search for Dark Matter with Electron Beams	143
8	Introduction	145
8.1	A Brief Historical Account	146
8.2	Summary	150
9	Dark Matter Models	153
9.0.1	WIMPS	154
9.0.2	Other Dark Matter Candidates	158
9.0.3	Light Dark Matter and The Dark Sector	159
9.1	Light Dark Matter and Vector Mediators	162
9.2	Modified Gravity	164
9.3	Summary on Dark Matter Models	165
10	Search for Dark Matter with a Beam-Dump Experiment	167
10.1	Experiments for LDM Detection	169
10.2	Beam-Dump Experiments	169
10.3	Beam-Dump Experiments: Theoretical Background	171
10.4	Expected Experimental Yield	174
11	The darkMESA Experiment	175
11.1	A Beam-Dump Experiment at MESA	175
11.1.1	The MESA Accelerator	175
11.2	Simulation of the darkMESA Experiment	177
11.3	Detector Concept	180
11.4	Experimental Tests for the Calorimeter Material	181
11.5	Simulation Results	184
11.5.1	Simulation Parameters	185

CONTENTS

11.5.2 Interactions in the Detector	186
11.5.3 Exclusion Limits	187
11.6 darkMESA Prototype	190
11.7 Conclusion and Outlook	191
Appendix A PIENU Detector Technical Drawings	195
Appendix B Trigger Diagram of the PIENU Experiment	201
Appendix C Time spectrum for $\pi \rightarrow \mu \rightarrow e$	203
Appendix D Z-vertex determination with Tracking	205
Appendix E Detector Scattering Kinematics	207
E.1 $e\chi$ Scattering	207
E.2 $p\chi$ and $N\chi$ Scattering	208
Appendix F Crystal Tests for darkMESA	211
Bibliography	247
List of Figures	260
List of Tables	262
Glossary	263
Related Publications	271
Acknowledgments	273

Part I

Search for New Physics with Pion Beams

Chapter 1 | Introduction



quark-antiquark states are known as *mesons*.

With a mass of $139.6 \text{ MeV}/c^2$ the charged pion is the lightest meson [12] and it was discovered in cosmic rays in 1947 and later directly produced at particle accelerators. At the beginning, the study of this particle played a special role in proving the correctness of the new emerging theory of weak interactions. The initial puzzle concerning pions was their observed decay mode: $\pi^+ \rightarrow \mu^+ \nu_\mu$ (or $\pi^- \rightarrow \mu^- \bar{\nu}_\mu$). Why pions do not decay preferentially into electrons or positrons, since these particles are 200 times lighter than a muon?

At the time, only the newly developed theory of weak interactions could explain this puzzle. The final discovery of the $\pi^+ \rightarrow e^+ \nu_e$ decay with a branching ratio of $\mathcal{O}(10^{-4})$ helped in establishing the new theory as the correct description of the weak interaction.

After pions were used to establish the SM, nowadays we can use them to challenge it, measuring its properties with great precision and try to detect deviations from predictions. The pion branching ratio (including the radiative counterparts of the decays¹)

$$R_\pi = \frac{\Gamma(\pi^+ \rightarrow e^+ \nu_e + \pi^+ \rightarrow e^+ \nu_e \gamma)}{\Gamma(\pi^+ \rightarrow \mu^+ \nu_\mu + \pi^+ \rightarrow \mu^+ \nu_\mu \gamma)} . \quad (1.1)$$

is the most precisely calculated SM observable involving quarks: $R_\pi^{\text{th}} = 1.2352 \pm 0.0002$ [13]. By contrast, the experimental value $R_\pi^{\text{exp}} = 1.2327 \pm 0.0023$ [14] is an order of magnitude less precise and therefore a new precision experiment is called for. This is the goal of the PIENU experiment at TRIUMF, which was designed with the aim of improving the precision by a factor 5 over previous experiments. Deviations from the SM predic-

¹After the pion decay, the resulting muon decays as $\mu^+ \rightarrow e^+ \nu_e \bar{\nu}_\mu$

tion imply a violation of lepton universality and therefore the presence of new physics beyond the SM.

1.1 Pion Decay Experiments: a Historical Perspective

The pion was discovered in 1947 in cosmic rays by C. Powell and collaborators [15]. A particle with the properties of the pion was already predicted by H. Yukawa in 1935 [16]. Both H. Yukawa and C. Powell were awarded the 1949 and 1950 Nobel Prizes respectively [17].

The muon had been discovered earlier [18] and at first it was believed to be the particle predicted by Yukawa: the carrier of a strong and short range force which can bind nucleons in nuclei. After the initial excitement, the muon appeared to be a sort of heavy electron and therefore not able to interact strongly.

The pion is the lightest meson and it can thus only decay into leptons. From pure phase space considerations, a decay to electrons should be favored but for 20 years after the pion discovery, only the muon decay mode was observed.

In an experiment carried out in 1957 at the E. Fermi Institute [19] no $\pi^+ \rightarrow e^+ \nu_e$ decays were identified and a limit for the branching ratio was set at $R_{1957} < 10^{-6}$ confirming a previous result by S. Lokanathan and J. Steinberger [20].

Such negative results were in contradiction with the otherwise successful V-A theory of weak interactions proposed by E.C.G. Sudarshan and R.E. Marshak [21] which predicted a branching ratio of the order of 10^{-4} . In [22], R.P. Feynman and M. Gell-Mann supported the proposed V-A theory but also commented:

Experimentally no $\pi \rightarrow e + \nu$ have been found, indicating that the ratio is less than 10^{-5} . This is a very serious discrepancy. The authors have no idea on how it can be resolved.

Evidence for parity violation in the weak interactions was at that time available and the most striking verification was provided by the experiment of C. Wu and collaborators in 1956 [23]. The validity of the V-A the-

ory was holding and therefore further attempts to measure the branching ratio were made. The $\pi^+ \rightarrow e^+\nu_e$ decay was finally discovered in 1958 first at CERN [24] and then at Columbia University [25]. With the availability of the first computer² at CERN, at the end of the same year it has been possible to implement a Monte Carlo simulation, estimate the detector inefficiency, and provide finally the value for the branching ratio $R_{1958} = (1.22 \pm 0.3) \cdot 10^{-4}$ [26].

A personal historical account of the discovery of the $\pi^+ \rightarrow e^+\nu_e$ decay is given in [27] by G. Fidecaro, one of the original authors of the CERN first-discovery paper.

1.2 Previous Experimental Measurements

After the discovery, the first precise measurement of the branching ratio was performed by the team of H. L. Anderson (who was also an author of the previous negative results) using a magnetic spectrometer [28]. The measured branching ratio was $R_{1960} = (1.27 \pm 0.07) \times 10^{-4}$. Including 2.5% radiative corrections, it was completely in agreement with the SM and the V-A structure of the weak interaction.

Other following experiments confirmed the agreement with more precision. The experiment of Di Capua *et al.* [29] used a 23 cm diameter, 24 cm long NaI(Tl) detector sensitive also to photons from radiative decays. With more than 10^4 $\pi^+ \rightarrow e^+\nu_e$ events collected, the obtained branching ratio was $R_{1964} = (1.247 \pm 0.028) \times 10^{-4}$ (later revised to $R_{1964,r} = (1.274 \pm 0.024) \times 10^{-4}$ [30] to account for a change in the pion lifetime).

Another experiment with a larger NaI(Tl) crystal was carried out at TRIUMF by Bryman *et al.* [31] measuring $R_{1986} = (1.218 \pm 0.014) \times 10^{-4}$ from a sample of 3×10^4 $\pi^+ \rightarrow e^+\nu_e$ events.

Two subsequent experiments were carried out at PSI [32] and TRIUMF [33] (E248 experiment) few years later. The TRIUMF experiment used again a NaI(Tl) crystal as main calorimeter while the PSI experiment used a 4π BGO calorimeter. Both experiments achieved comparable levels of statistical and systematic uncertainties yielding as combined result $R_{1994_{av}} = (1.231 \pm 0.005) \times 10^{-4}$, in agreement with the SM which

²A vacuum-tube based Ferranti Mercury. Built in the UK, it was used at CERN from 1958 to 1965.

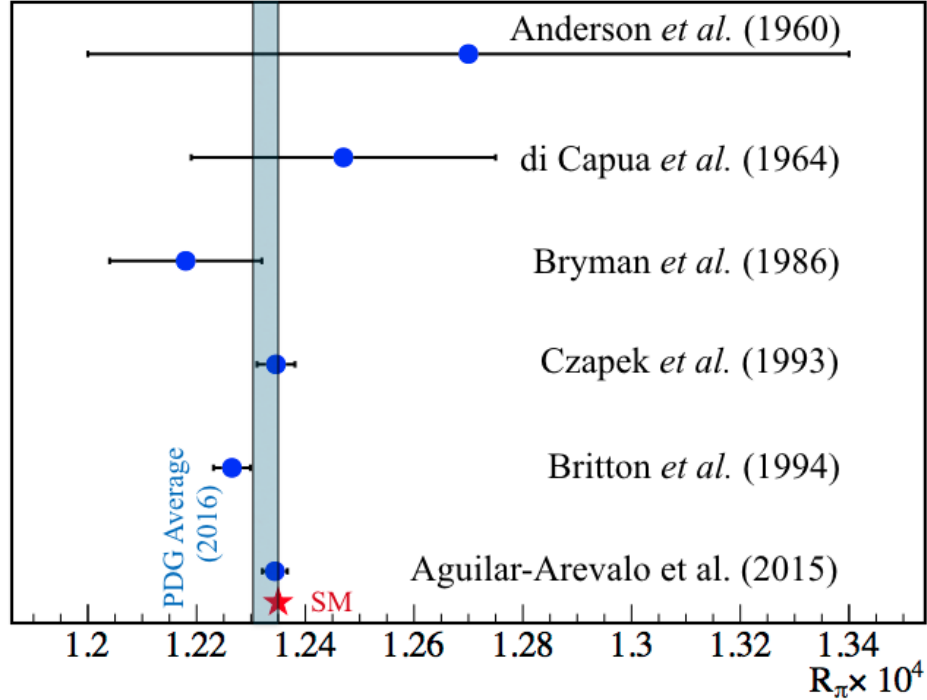


Figure 1.1: History of the $\pi^+ \rightarrow e^+ \nu_e$ branching ratio measurements. The blue band is the average reported in [14] and the red star represents the most recent Standard Model calculation [13].

was predicting $R_\pi^{\text{th}} = (1.2350 \pm 0.0005) \times 10^{-4}$ [34]. The average value reported in 2017 by the Particle Data Group using R_{1986} , the last data from PSI, and from TRIUMF was $R_{\text{PDG16}} = (1.2327 \pm 0.0023) \times 10^{-4}$ [14]. The evolution in time of the experimental results is summarized in Fig. 1.1.

1.3 Towards the new Experiment

The experimental setup of the last TRIUMF experiment E248 is shown in Fig. 1.3 (left) [33]. Pions were stopped in a scintillator target and decay positrons were detected in a cylindrical NaI(Tl) crystal whose axis was oriented at 90° with respect to the beam for avoiding backgrounds. The experiment collected about 10^5 $\pi^+ \rightarrow e^+ \nu_e$ events in one month of datataking. The branching ratio result was $R_{1992} = (1.2265 \pm 0.0034(\text{stat}) \pm$

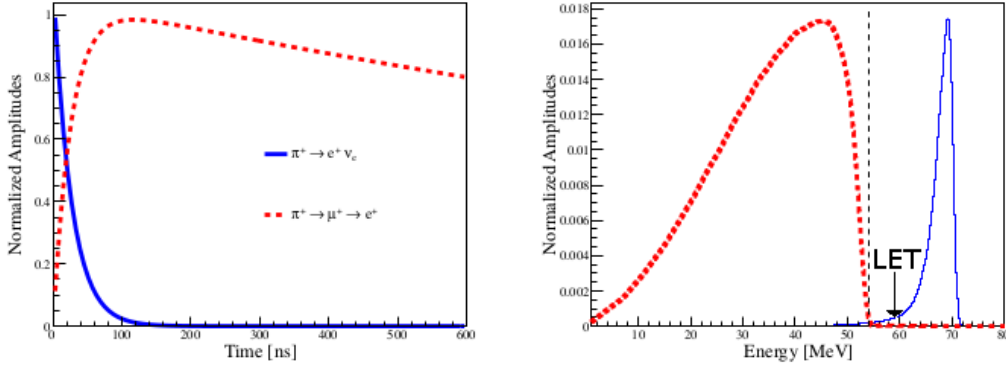


Figure 1.2: Time (**left**) and energy (**right**) distributions for the $\pi^+ \rightarrow e^+ \nu_e$ (blue line) and $\pi^+ \rightarrow \mu^+ \nu_\mu \rightarrow e^+ \nu_e \bar{\nu}_\mu$ (red dashed line) decays normalized to the same number of events.

$0.0044(\text{sys}) \times 10^{-4}$ [35, 33].

For understanding the challenges of such experiments, it is useful to consider the differences in the two pion decay modes. In Fig. 1.2 (right) the energy distribution of the positrons arising from the two decay modes is shown. The two-body decay $\pi^+ \rightarrow e^+ \nu_e$ gives rise to a clear peak at 69.8 MeV, while the three-body muon decay in $\pi^+ \rightarrow \mu^+ \nu_\mu \rightarrow e^+ \nu_e \bar{\nu}_\mu$ produces a broad energy distribution (the so-called Michel spectrum [36]) from 0 to a sharp endpoint (the "Michel edge") at 52.8 MeV. The time distribution of the $\pi^+ \rightarrow e^+ \nu_e$ decay follows an exponential distribution characterized by the pion lifetime. The decay chain $\pi^+ \rightarrow \mu^+ \nu_\mu \rightarrow e^+ \nu_e \bar{\nu}_\mu$ follows a different distribution (see App. C) where both the pion and the muon lifetimes play a role. The peaked energy distribution of the $\pi^+ \rightarrow e^+ \nu_e$ decay shows a distinctive **low energy tail (LET)** to its left. The LET arises because of losses in the calorimeter measuring the positron energy, and from radiative decays $\pi^+ \rightarrow e^+ \nu_e \gamma$.

The LET extends under the overwhelming $\pi^+ \rightarrow \mu^+ \nu_\mu \rightarrow e^+ \nu_e \bar{\nu}_\mu$ distribution and since it is not directly measurable, its knowledge constitutes the main correction to the branching ratio. As such, it represents also the main uncertainty in the E248 experiment and in general in experiments employing a calorimetric method.

In E248, for estimating the LET, the so-call "suppressed spectrum" was

obtained, highly suppressing with stringent cuts³ events identified as $\pi^+ \rightarrow \mu^+ \nu_\mu \rightarrow e^+ \nu_e \bar{\nu}_\mu$ events (see fig. 1.3 right). In the suppressed spectrum, a $\pi^+ \rightarrow \mu^+ \nu_\mu \rightarrow e^+ \nu_e \bar{\nu}_\mu$ component was still clearly visible: these were mostly events where the pion decayed in flight before the target and deposited a smaller amount of energy with respect to stopped pions. The fraction of events below 52 MeV with respect to the total number of $\pi^+ \rightarrow e^+ \nu_e$ events was about 20%. The remaining background and the statistics were limiting factors for a precise estimation of the low energy tail, which is the main correction to the branching ratio and therefore a main contributor to the final error.

The new PIENU experiment at TRIUMF was designed with the lessons learned with E248 in mind, thus carefully thinking at methods for estimating the low energy tail of $\pi^+ \rightarrow e^+ \nu_e$ events. Besides the use of modern technologies and better detectors, the main ideas for the tail estimation were:

- Addition of tracking capabilities for suppressing pion decay-in-flight events.
- Possibility to rotate the detector setup with respect to the beam for carefully investigating the calorimeter response to a positron beam.

In order to increase the statistics, the calorimeter was placed directly in front of the beam. In this way, the target can be placed closer to the calorimeter, increasing the angular acceptance for decay positron tracks. The experimental setup will be described in more details in Chapter 3.

1.4 The PIENU Experiment

The PIENU experiment at TRIUMF was based on the stopped pion technique. Pions were produced by protons striking a beryllium target and guided to the experiment by a secondary beamline. The stopping target was a plastic scintillator where pions decayed into the two modes: $\pi^+ \rightarrow \mu^+ \nu_\mu \rightarrow e^+ \nu_e \bar{\nu}_\mu$ and $\pi^+ \rightarrow e^+ \nu_e$. In the $\pi^+ \rightarrow \mu^+ \nu_\mu \rightarrow e^+ \nu_e \bar{\nu}_\mu$ case, the kinetic energy of the muon is 4.12 MeV and its range is ~ 1 mm.

³The main suppression cut was applied to the energy deposit in the target where the pion stops. The presence of the muon in $\pi^+ \rightarrow \mu^+ \nu_\mu \rightarrow e^+ \nu_e \bar{\nu}_\mu$ raised the energy deposit with respect to $\pi^+ \rightarrow e^+ \nu_e$.

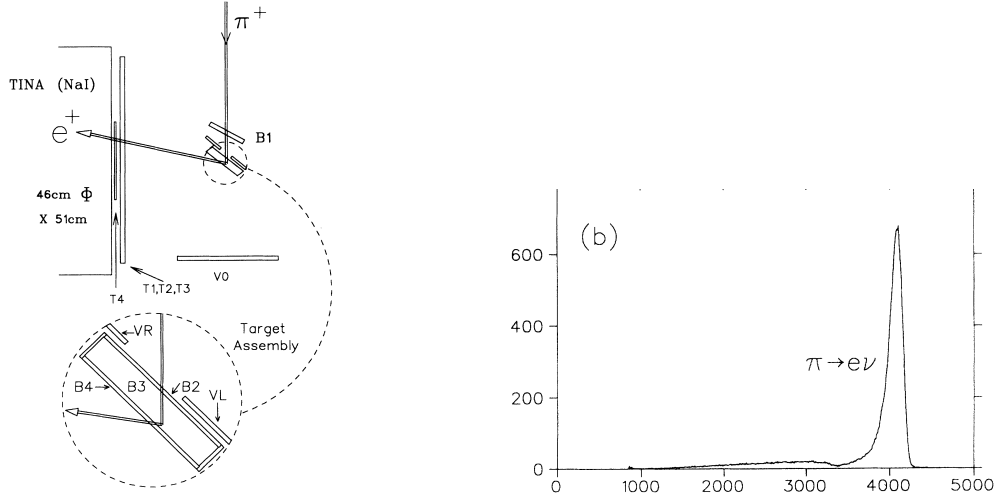


Figure 1.3: **Left:** Experimental setup of the E248 experiment at TRIUMF. **Right:** Positron energy spectrum obtained suppressing $\pi^+ \rightarrow \mu^+ \nu_\mu \rightarrow e^+ \nu_e \bar{\nu}_\mu$ events. Events in the low energy side of the $\pi^+ \rightarrow e^+ \nu_e$ peak come mainly from pions decaying in flight.

Since the target was about 8 cm thick, the muon remained contained into the target, decaying into a positron and two neutrinos (see Fig. 1.4). The decay positrons from the two decays emerge from the target and are measured by the PIENU detectors. This technique allows to measure the two decay modes at the same time with the same apparatus and in this way most of the uncertainties cancel in the branching ratio.

Measuring the branching ratio requires to identify precisely the two decays modes and the various backgrounds.

In principle, counting the number of events above and below the Michel edge can provide an estimate of the branching ratio, but such an estimate would neglect backgrounds, pileup effects, and most importantly the low energy tail of the $\pi^+ \rightarrow e^+ \nu_e$ decay. Knowing the shape of the LET and the energy distributions of all the backgrounds, it would be possible to extract the branching ratio. Since these shapes cannot be known with sufficient accuracy and would require mostly inputs from Monte Carlo simulations, another technique was used instead.

The idea was to consider the decay time distributions (Fig. 1.2 (left)).

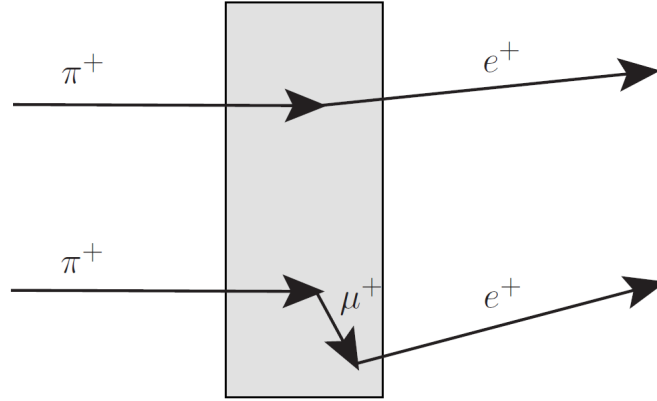


Figure 1.4: Working principle of the stopped pion technique. Pions lose energy through different detectors and stop in an active target. The muon remains confined in the target and only positrons from both decays $\pi^+ \rightarrow e^+ \nu_e$ and $\pi^+ \rightarrow \mu^+ \nu_\mu \rightarrow e^+ \nu_e \bar{\nu}_\mu$ emerge from it.

The $\pi^+ \rightarrow e^+ \nu_e$ decay is dominated by the pion lifetime $\tau_\pi = 26.033 \pm 0.005$ ns [14] and its time distribution is $\sim e^{-t/\tau_\pi}$. The $\pi^+ \rightarrow \mu^+ \nu_\mu \rightarrow e^+ \nu_e \bar{\nu}_\mu$ decay is a chain decay with the pion and the longer muon lifetime $\tau_\mu = 2196.9811(22)$ ns [14] with time distribution $\sim e^{-t/\tau_\pi} - e^{-t/\tau_\mu}$ (see App. C). The shapes of the two signals are therefore known analytically, like also most of the backgrounds (see Chapter 4).

Dividing the energy spectrum into a low energy (LE) and high energy (HE) parts (with the cutoff around the Michel edge), two time spectra can be built: the LE time spectrum containing mainly $\pi^+ \rightarrow \mu^+ \nu_\mu \rightarrow e^+ \nu_e \bar{\nu}_\mu$ events and the HE time spectrum, containing mainly $\pi^+ \rightarrow e^+ \nu_e$ events. Performing a simultaneous fit of signal and background shapes to the two time spectra, the branching ratio can be extracted.

The LET is too small to be extracted from the LE time spectrum fit, and therefore it has to be treated as a correction to the fitted branching ratio. This means that the LET has to be estimated with another method.

The idea is to "look" at the LET directly and removing most of the detectors in front of the positron calorimeter, being able to inject positron beam into it at different angles and energies to completely characterize the response [37]. This set of measurements allowed to estimate the LET

to sufficient accuracy. This technique is explained in Chapter 4.

1.5 Search for new Physics with Pion Decays

The discovery of the $\pi^+ \rightarrow e^+\nu_e$ decay helped in consolidating the SM as the correct theory of the electroweak interactions solving a long-standing puzzle. Pushing the precision at which the decay branching ratio is measured is aiming at challenging the SM and at detecting deviations from its predictions.

This strategy is in general pursued with other rare meson and lepton decays, for example with the analogous kaon decay $K^+ \rightarrow e^+\nu_e$.

A fundamental assumption present in the SM is that the electroweak interactions are universal, *i.e.* that they couple with the same strength to each lepton generation. This assumption goes under the name of *lepton universality*. If this assumption were wrong, the $\pi^+ \rightarrow e^+\nu_e$ branching ratio would be modified.

Violation of lepton universality is induced in various physics beyond the SM models and therefore, measuring with high precision the $\pi^+ \rightarrow e^+\nu_e$ branching ratio represents a way to constrain such models or discover new physics effects. A description of models leading to violation of lepton universality is given in Chapter 2.

1.6 Summary

The $\pi^+ \rightarrow e^+\nu_e$ branching ratio has a long history starting from the early days of cosmic ray physics and the discovery of the pion. This particular decay played an important role in establishing the V-A theory of weak interactions which was predicting a $\mathcal{O}(10^{-4})$ branching ratio if the pion were a pseudoscalar particle. The final observation of this decay was another striking confirmation of the new theory, representing an important milestone in the development of the Standard Model.

After its discovery, the decay became a high-precision observable, sensitive to contributions of new physics beyond the Standard Model together with other meson and lepton decays. Theoretical calculations are one order of magnitude more precise than present experimental results and this gives a strong motivation for a new improved experiment.

Chapter 2 | Theoretical Aspects

Pions are the lightest mesons and as such they play a unique role in Quantum Chromodynamics (QCD), the theory describing the strong interactions [38, 39]. In this chapter, the main features of the SM will be reviewed, together with the properties of pions in the framework of effective field theories [40, 41].

Testing the $\pi^+ \rightarrow e^+ \nu_e$ branching ratio translates into precisely testing lepton universality. Theories beyond the SM (BSM) predicting the violation of lepton universality will be reviewed. A precise test of the universality hypothesis can set stringent limits on BSM theories or uncover new physics.

2.1 The Standard Model of Particle Physics

The SM is a quantum field theory describing the interaction of all the known particles via three forces: electromagnetic, weak, and strong. In particular, the SM is a gauge theory based on the group

$$\underbrace{SU(3)}_{\text{strong}} \times \underbrace{SU(2) \times U(1)}_{\text{electroweak}} . \quad (2.1)$$

The model unifies the electromagnetic and weak force ("electroweak" force) within the $SU(2) \times U(1)$ group introducing the corresponding gauge bosons W_μ^i for SU(2) and B_μ for U(1) and coupling constants g and g' .

2.1.1 Electroweak Interactions

The electroweak theory is a chiral theory, since left or right handed chiral components of the fermion fields transform differently. The left-handed

fermion fields of each family $i = 1, 2, 3$ transform as doublets under $SU(2)$:

$$\Psi_i = \begin{pmatrix} \nu_i \\ l_i^- \end{pmatrix} ; \begin{pmatrix} u_i \\ d_i' \end{pmatrix} , \quad (2.2)$$

and $d_i' = \sum_j V_{ij} d_j$ is the Cabibbo-Kobayashi-Maskawa matrix (CKM, see Fig. 2.1) [42, 43] describing quark mixing:

$$\begin{pmatrix} d' \\ s' \\ b' \end{pmatrix} = \begin{pmatrix} V_{ud} & V_{us} & V_{ub} \\ V_{cd} & V_{cs} & V_{cb} \\ V_{td} & V_{ts} & V_{tb} \end{pmatrix} \begin{pmatrix} d \\ s \\ b \end{pmatrix} . \quad (2.3)$$

The right-handed fermion fields transform as $SU(2)$ singlets.

The SM fermions are massive (with the exception of the massless¹ neutrinos ν_i). The mass is provided by a spontaneous symmetry breaking mechanism driven by the presence of a scalar field: the Higgs field ϕ [44, 45, 46].

Concretely, a complex scalar doublet is introduced

$$\phi = \begin{pmatrix} \phi^+ \\ \phi^0 \end{pmatrix} , \quad (2.4)$$

together with the potential

$$V(\phi) = \mu^2 \phi^\dagger \phi + \frac{\lambda^2}{2} (\phi^\dagger \phi)^2 . \quad (2.5)$$

If μ^2 is negative, the Higgs field has a non-zero vacuum expectation value $v/\sqrt{\lambda} = \mu/\lambda$ with $v \approx 246$ GeV. The Higgs complex doublet has four degrees of freedom and after spontaneous symmetry breaking three of them are "eaten up" by 3 of the 4 $SU(2) \times U(1)$ generators, leading to 3 new massive particles: W^\pm and Z^0 , while leaving the fourth massless. This last massless particle is identified with the photon γ of the electromagnetic interaction. After spontaneous symmetry breaking, the SM electroweak

¹Neutrinos are implemented as massless fermions in the SM, although it is known experimentally that at least two of them must have a mass. How to implement massive neutrinos in the SM is a subject of current research.

lagrangian becomes

$$\begin{aligned}
 \mathcal{L}_{EMweak}^{SM} = & \underbrace{\bar{\psi}_i(i\cancel{\partial} - m_i - \frac{m_i H}{v})\psi_i}_{\text{Dirac Fermion Masses from Higgs coupling}} \\
 & - \underbrace{\frac{g}{2\sqrt{2}}\bar{\Psi}_i\gamma^\mu(1 - \gamma^5)(T^+W_\mu^+ + T^-W_\mu^-)\Psi_i}_{\text{Charged current weak interaction}} \\
 & \underbrace{-eQ_i\bar{\psi}_i\gamma^\mu\psi_i A_\mu}_{\text{Electromagnetic Interaction (QED)}} \\
 & - \underbrace{\frac{g}{2\cos\theta_W}\bar{\psi}_i(g_V^i - g_A^i)\psi_i Z_\mu}_{\text{Neutral current weak interaction}} , \tag{2.6}
 \end{aligned}$$

where repeated family indices i are summed over and $\cancel{\partial} = \gamma^\mu\partial_\mu$. The angle $\theta_W = \tan^{-1}(g'/g)$ is called Weinberg (or weak) angle, $e = g \sin \theta_W$ is the electromagnetic charge, and $A_\mu = B_\mu \cos \theta_W + W_\mu^3 \sin \theta_W$ is the photon field.

The three new massive carriers of the weak force are $W_\mu^\pm = W_\mu^1 \mp iW_\mu^2$ and $Z_\mu = -B_\mu \sin \theta_W + W_\mu^3 \cos \theta_W$. T^\pm are the weak isospin rising and lowering operators. At first order in perturbation theory, the new boson masses are:

$$\begin{aligned}
 M_H &= \lambda v \quad , \\
 M_W &= \frac{1}{2}g v = \frac{ev}{2\sin\theta_W} \quad , \\
 M_Z &= \frac{1}{2}\sqrt{g^2 + g'^2}v = \frac{M_W}{\cos\theta_W} \quad , \\
 M_\gamma &= 0 \quad .
 \end{aligned} \tag{2.7}$$

2.1.2 Strong Interaction

The theory of strong interactions or Quantum Chromodynamics (QCD) represents the $SU(3)$ component in the SM gauge group. The QCD lagrangian is

$$\mathcal{L}_{QCD}^{SM} = \bar{\psi}_{q,a}(i\gamma^\mu\partial_\mu\delta_{ab} - g_s\gamma^\mu t_{ab}^C A_\mu^C - m_q\delta_{ab})\psi_{q,b} - \frac{1}{4}F_{\mu\nu}^A F^{A\mu\nu} \quad , \tag{2.8}$$

where repeated indices are summed over. The index $q = u, d, s, c, b, t$ represents the quark flavour, while $a = 1, 2, 3$ is the color index. The gluon fields are represented by A_μ^C with $C = 1..8$ (SU(3) has 8 generators). The field tensor of the gluon field is given by

$$F_{\mu\nu}^A = \partial_\mu A_\nu^A - \partial_\nu A_\mu^A - g_s f_{ABC} A_\mu^B A_\nu^C \quad , \quad (2.9)$$

where f_{ABC} are the structure constants of SU(3) and g_s is the strong coupling constant. An important feature of QCD is Asymptotic Freedom [38, 39], meaning that the strong coupling becomes smaller with increasing momentum transfer in particle interactions. One of the consequences of the QCD running coupling is that at low energies quarks are confined in uncolored bound states (baryons and mesons).

In the low energy regime the QCD coupling constant cannot be considered small and this implies that a perturbative treatment is not possible. Non-perturbative methods have to be used, like for example Chiral Perturbation Theory [47] or Lattice QCD [48, 49].

2.1.3 Neutrinos

Neutrinos require a separate discussion, given the recent discoveries regarding their oscillation properties which lead to Nobel prize awards in 2015 to T. Kajita and A.B. McDonald [50].

Neutrinos are embedded in the SM as massless particles with a definite helicity state. However, the discovery of neutrino oscillations [51, 52] implies that at least two of them must have a non-zero mass. Massive neutrinos imply that the flavour $\nu_{e,\mu,\tau}$ and mass eigenstates $\nu_{1,2,3}$ are different, like in the case of quarks. These states are related by a unitary mixing matrix: the Pontecorvo-Maki-Nakagawa-Sakata Matrix (PMNS [53, 54], see Fig. 2.1) U :

$$\begin{pmatrix} \nu_e \\ \nu_\mu \\ \nu_\tau \end{pmatrix} = \begin{pmatrix} U_{e1} & U_{e2} & U_{e3} \\ U_{\mu1} & U_{\mu2} & U_{\mu3} \\ U_{\tau1} & U_{\tau2} & U_{\tau3} \end{pmatrix} \begin{pmatrix} \nu_1 \\ \nu_2 \\ \nu_3 \end{pmatrix} \quad . \quad (2.10)$$

Neutrino mixing gives rise to the neutrino oscillation phenomenon, which has been observed experimentally. The probability of the oscillation from

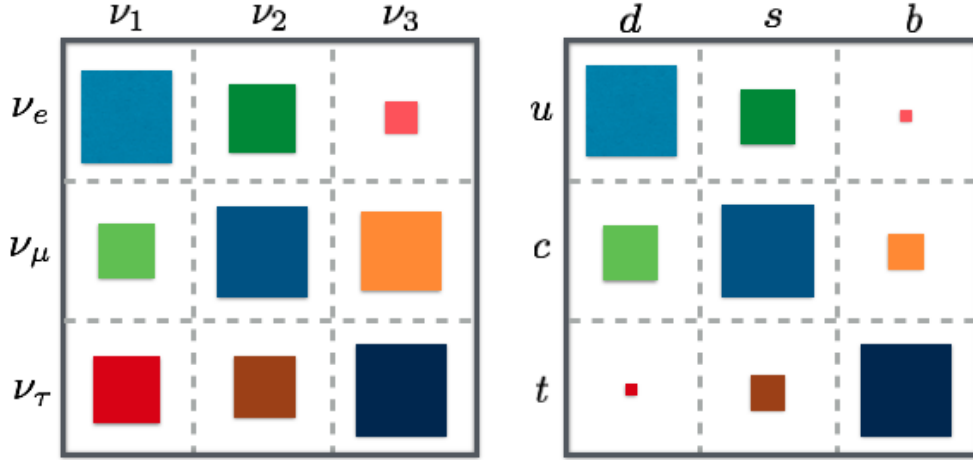


Figure 2.1: **Left:** neutrino mixing matrix elements, **Right:** quark mixing matrix elements. The surface of the squares represents the absolute value of the relative magnitudes of the matrix elements. In the quark CKM matrix a hierarchical pattern can be seen, in contrast to the present knowledge of the neutrino PMNS matrix.

a flavour $\alpha = (e, \mu, \tau)$ to a flavour $\beta = (e, \mu, \tau)$ is described by

$$\begin{aligned}
 P(\nu_\alpha \rightarrow \nu_\beta) &= \delta_{\alpha\beta} \\
 &- 4 \sum_{i>j} \Re(U_{\alpha i}^* U_{\beta i} U_{\alpha j} U_{\beta j}^*) \sin^2[1.27 \cdot \Delta m_{ij}^2 (L/E)] \\
 &+ 2 \sum_{i>j} \Im(U_{\alpha i}^* U_{\beta i} U_{\alpha j} U_{\beta j}^*) \sin[2.54 \cdot \Delta m_{ij}^2 (L/E)] \quad ,
 \end{aligned} \tag{2.11}$$

where $i,j=(1,2,3)$ label the mass eigenstates, L is the distance in km traveled by the neutrino, and E is its energy in GeV^2 .

From the measurement of the oscillation probabilities, the difference of the squared neutrino masses $\Delta m_{ij}^2 = m_i^2 - m_j^2$ and the mixing angles can be extracted. Oscillation experiments are sensitive to different mixing angles depending on the employed neutrino source. Neutrinos from the

²The km/GeV convention is particularly useful for designing neutrino oscillation experiments. For example, if the neutrino energy is of the order of 1 GeV, $\sin^2 2\theta \sim 0.8$ (assuming only one oscillation parameter in a simplified two-flavour model), and the neutrino mass difference is $\Delta m^2 \sim 3 \cdot 10^{-3} \text{eV}^2$, the maximum oscillation probability will be located at $L \sim 400$ km.

sun, the atmosphere, fission reactors or spallation sources at accelerators have been used for investigating neutrino properties.

The PMNS matrix can be conveniently parameterized with three angles $\theta_{12}, \theta_{13}, \theta_{23}$ (defined in the first quadrant $[0, \pi/2]$):

$$U = \underbrace{\begin{pmatrix} c_{12} & s_{12} & 0 \\ -s_{12} & c_{12} & 0 \\ 0 & 0 & 1 \end{pmatrix}}_{\text{Solar Neutrinos}} \underbrace{\begin{pmatrix} c_{13} & 0 & s_{13}e^{-i\delta} \\ 0 & 1 & 0 \\ -s_{13}e^{-i\delta} & 0 & c_{13} \end{pmatrix}}_{\text{Reactor Neutrinos}} \underbrace{\begin{pmatrix} 1 & 0 & 0 \\ 0 & c_{23} & s_{23} \\ 0 & -s_{23} & c_{23} \end{pmatrix}}_{\text{Atmospheric/Accel. Neutrinos}} \underbrace{\begin{pmatrix} 1 & 0 & 0 \\ 0 & e^{i\alpha_1/2} & 0 \\ 0 & 0 & e^{i\alpha_2/2} \end{pmatrix}}_{\text{Majorana Phases}}, \quad (2.12)$$

where $s_{ij} = \sin \theta_{ij}$, $c_{ij} = \cos \theta_{ij}$. For example, in this parameterization, $U_{e1} = \cos \theta_{12} \cos \theta_{13}$ (compare with Eq. 2.10). The most sensitive experiments to the different angles are highlighted under the matrices³. Besides the angles, there are also three phases δ and $\alpha_{1,2}$ related to the Dirac or Majorana nature of neutrinos.

If neutrinos ψ have Dirac nature, their mass will be described by a term like $m\psi\psi = m(\bar{\psi}_L\psi_R + \bar{\psi}_R\psi_L)$ in the SM lagrangian and the "Dirac phase" δ will describe CP violation in the lepton sector (in analogy with the CKM matrix).

Neutrinos admit another possibility for constructing their mass term. Unlike the other SM fermions, neutrinos carry no electric charge. They still carry lepton and flavour number but these can be violated by BSM physics. If the neutrino does not have conserved quantum numbers, it can be its own antiparticle. In this case neutrinos must be described by Majorana fermions and the only difference between ν and $\bar{\nu}$ is a spin flip. Mathematically, a Majorana neutrino is described by a two-component Weyl spinor instead of a 4-component Dirac spinor. In the case of Majorana neutrinos, two additional phases have to be present: α_1 and α_2 ⁴. For Majorana neutrinos, a different mass term is allowed:

$$\mathcal{L}_M = \underbrace{m_D \bar{\nu}_L \nu_R}_{\text{Dirac term}} + \underbrace{\frac{1}{2} m_L \nu_L^T \nu_L + \frac{1}{2} m_R \nu_R^T \nu_R}_{\text{Majorana terms}} + h.c. \quad (2.13)$$

In the case of a charged lepton (e.g. an electron), the fields e_R and e_L have the same mass, as showed by the Dirac term in Eq. 2.13. For a neutrino,

³Accelerator experiments can also access the CP phase δ comparing data produced with neutrino and antineutrino beams.

⁴In the Dirac case, these phases vanish. Neutrino oscillations are influenced only by a linear combination of Majorana phases.

all three terms in Eq. 2.13 are instead in principle allowed. The interesting feature of the two additional Majorana terms is that they induce lepton number violation (LNV). LNV gives rise to new phenomena, like neutrinoless double beta decay of nuclei ($0\nu\beta\beta$, e.g. for ^{130}Te , ^{76}Ge , ^{136}Xe) and SM-forbidden $\Delta L = 2$ decays like $B_c^- \rightarrow \pi^+ \mu^- \mu^+$ or $K^+ \rightarrow \pi^+ e^- \mu^+$.

Majorana neutrinos have the interesting feature of providing a possible explanation for the smallness of the neutrino mass. Rewriting Eq. 2.13 as

$$\mathcal{L}_M = \frac{1}{2} (\nu_L, \nu_R) \begin{pmatrix} m_L & m_D \\ m_D & m_R \end{pmatrix} \begin{pmatrix} \nu_L \\ \nu_R \end{pmatrix} + h.c. \quad , \quad (2.14)$$

and supposing that ν_R is a very heavy *sterile* neutrino (i.e. does not couple to SM forces), diagonalizing the mass matrix we obtain the effective masses

$$\begin{aligned} M_H &\approx m_R \\ M_L &\approx m_L - \frac{m_D^2}{m_R} \quad , \end{aligned} \quad (2.15)$$

where M_H and M_L are the masses of a "heavy" and a "light" state respectively. If $m_L \ll m_D \ll m_R$, then if $m_D \approx 200$ GeV and $m_R \approx 10^{15}$ then $M_L \approx 0.04$ eV, which is close to the mass scale observed for neutrinos. This is the so-called *seesaw mechanism* [55]: if m_R is large, M_H is pushed at high masses while M_L becomes small.

In conclusion, if neutrinos are Majorana particles, there is a possible explanation for their small mass if a very heavy right-handed sterile neutrino is introduced.

2.2 Pions in an Effective Field Theory of QCD

At low energies, QCD is computationally very complex but nevertheless, an Effective Field Theory (EFT) description is still possible in this regime [47]. Noting that the u, d , and s quarks are much lighter than the c, b and t :

$$\begin{pmatrix} m_u \\ m_d \\ m_s \end{pmatrix} \ll 1 \text{ GeV} \leq \begin{pmatrix} m_c \\ m_b \\ m_t \end{pmatrix} \quad , \quad (2.16)$$

and that the proton mass m_p is much larger than the mass of its constituent quarks ($m_p \gg 2m_u + m_d$), suggests that we can approximate QCD for the three lightest quarks in its massless limit ($m_{u,d,s} \rightarrow 0$).

In this limit, the quark fields can be decomposed in left and right chiral field components (q_L and q_R , respectively) and the new lagrangian reads:

$$\mathcal{L} = \sum_{f=u,d,s} (\bar{q}_{R,f} i \not{D} q_{R,f} + \bar{q}_{L,f} i \not{D} q_{L,f}) - \frac{1}{4} F_{\mu\nu}^A F^{A\mu\nu} \quad , \quad (2.17)$$

where the two chiralities are clearly decoupled. Such a lagrangian has a classical global $U(3)_L \times U(3)_R$ symmetry which leads through Nöther's theorem to 18 conserved currents:

$$L^{\mu,f} = \bar{q}_L \gamma_\mu \frac{\lambda^f}{2} q_L ; R^{\mu,f} = \bar{q}_R \gamma_\mu \frac{\lambda^f}{2} q_R ; L^\mu = \bar{q}_L \gamma_\mu q_L ; R^\mu = \bar{q}_R \gamma_\mu q_R \quad , \quad (2.18)$$

where λ^f are the Gell-Mann SU(3) matrices. The currents can be linearly combined forming currents having different properties under the parity operator:

$$V^{\mu,f} = R^{\mu,f} + L^{\mu,f} ; V^\mu = R^\mu + L^\mu \quad , \quad (2.19)$$

$$A^{\mu,f} = R^{\mu,f} - L^{\mu,f} ; A^\mu = R^\mu - L^\mu \quad , \quad (2.20)$$

which are called octet vector, singlet vector (positive parity), octet axial-vector and singlet axial-vector (negative parity) currents, respectively. Thus the global symmetries of the chiral lagrangian can also be described by $SU(3)_L \times SU(3)_R \times U(1)_V \times U(1)_A$. It turns out that $U(1)_A$ is not realized at the quantum level: we are in the presence of an anomaly.

This *axial anomaly* plays an important role in the description of the $\pi^0 \rightarrow \gamma\gamma$ decay: in fact in the low-energy limit the whole contribution to the decay amplitude comes from the anomaly [56, 57].

The group describing the global symmetries at the quantum level is therefore $SU(3)_L \times SU(3)_R \times U(1)_V$. It is possible to add to the lagrangian a mass term for the quarks: $\mathcal{L}_M = -\bar{q} M q$ with $M = \text{diag}(m_u, m_d, m_s)$. This term will explicitly break chiral symmetry leading to the non-conservation of the previously defined currents.

The case where $m_u = m_d = m_s$ leads to the conservation of the vector currents only and the theory is nothing else than the celebrated SU(3) symmetry case first discussed in the *eightfold way* of M.Gell-Mann and Y. Ne'eman [58].

Besides the explicit symmetry breaking induced by the quark masses, a spontaneous symmetry breaking can also be introduced. The idea is to break the axial group for generating 8 massless Goldstone bosons [59, 60]

which are interpreted as the 8 lightest mesons. The spontaneous symmetry breaking pattern is

$$SU(3)_L \times SU(3)_R \times U(1)_V \rightarrow SU(3)_V \times U(1)_V \quad . \quad (2.21)$$

In the chiral limit, the ground state is necessarily invariant under $SU(3)_V \times U(1)_V$ as showed in [61] and, by Coleman's theorem [62] also the hamiltonian must share the same symmetry. The axial charge operators derived from the axial currents do not annihilate the vacuum and the symmetry is spontaneously broken.

A sufficient condition for the spontaneous symmetry breaking is the presence of a non-vanishing vacuum expectation value of the scalar quark condensate $\langle q\bar{q} \rangle$.

At this point, it is possible to construct an effective lagrangian obeying the relevant symmetries at low energies and abandoning quarks as degrees of freedom in favor of the 8 lightest mesons.

Since the lagrangian must be invariant under the chiral transformations in the $m \rightarrow 0$ limit, and the relevant group is $SU(3)$, the idea is to parameterize the 8 meson fields with Gell-Mann matrices:

$$\phi(x) = \sum_{a=1}^8 \lambda_a \phi_a(x) = \begin{pmatrix} \pi^0 + \frac{1}{\sqrt{3}}\eta & \sqrt{2}\pi^+ & \sqrt{2}K^+ \\ \sqrt{2}\pi^- & -\pi^0 + \frac{1}{\sqrt{3}}\eta & \sqrt{2}K^0 \\ \sqrt{2}K^- & \sqrt{2}K^0 & -\frac{2}{\sqrt{3}}\eta \end{pmatrix} \quad . \quad (2.22)$$

Since the transformation property of $\phi(x)$ is non-linear, another idea is to define a new field

$$U(x) = \exp\left(i\frac{\phi(x)}{F_0}\right) \quad , \quad (2.23)$$

which has now linear transformation properties under the chiral transformations. F_0 is at this point a free parameter⁵. This is the usual procedure for implementing symmetry transformations on Goldstone fields [63]. The most general and chirally invariant Lagrangian with the minimal number of derivatives is

$$\mathcal{L}_2 = \frac{F_0^2}{4} \text{Tr}(\partial_\mu U \partial^\mu U^\dagger) = \frac{1}{2} \partial_\mu \phi_a \partial^\mu \phi_a + \dots \quad , \quad (2.24)$$

⁵ F_0 will be later interpreted as the pion decay constant.

where the expansion in the last term is performed expanding the exponential in Eq. 2.23 around zero. The first term represents free mesons and the following ones describe their interactions. The index in \mathcal{L}_2 denotes the number of derivatives. In general, in mesonic chiral perturbation theory, the effective lagrangian takes the general form

$$\mathcal{L}_{ChPT} = \mathcal{L}_2 + \mathcal{L}_4 + \mathcal{L}_6 + \dots \quad . \quad (2.25)$$

Masses are introduced with the chirally invariant term

$$\mathcal{L}_M = \frac{F^2}{B_0} \text{Tr}(MU^\dagger + UM^\dagger) = -\frac{B_0}{2} \text{Tr}(\phi^2 M) + \dots \quad , \quad (2.26)$$

with the introduction of the new constant B_0 . M is the diagonal mass matrix of the three lightest quarks. The first expansion term together with the $m_u = m_d$ approximation leads to the Gell-Mann-Oakes-Renner relation [64]

$$4M_K^2 = 3M_\eta + M_\pi^2 \quad . \quad (2.27)$$

All the terms in the chiral effective lagrangian can be organized systematically in decreasing order of importance according to a power counting scheme (for more details, see e.g. [47]).

2.3 The Pion Decay

The rate of pion decay to leptons can be calculated at the lowest order, coupling the chiral meson lagrangian \mathcal{L}_2 with external fields provided in this case by the electroweak interaction. The coupling happens through the covariant derivative $D_\mu = \partial_\mu + iU l_\mu$ where $l_\mu = -(g/\sqrt{2})(W_\mu^+ T_+ + h.c.)$, and the isospin operator T is reduced to the relevant elements:

$$T_+ = \begin{pmatrix} 0 & V_{ud} & V_{us} \\ 0 & 0 & 0 \\ 0 & 0 & 0 \end{pmatrix} \quad . \quad (2.28)$$

The final result for the coupling of an effective field theory Goldstone boson with the electroweak force is

$$\begin{aligned} \mathcal{L}_{W\phi} = & -\frac{g}{\sqrt{2}} \frac{F_0}{2} \text{Tr} \left[(W_\mu^+ T_+ + W_\mu^- T_-) \partial^\mu \phi \right] = \\ & -g \frac{F_0}{2} \left[W_\mu^+ (V_{ud} \partial^\mu \pi^- + V_{us} \partial^\mu K^-) + W_\mu^- (V_{ud} \partial^\mu \pi^+ + V_{us} \partial^\mu K^+) \right] \end{aligned} \quad (2.29)$$

We still need the coupling of the W bosons to leptons, which is given by the SM electroweak lagrangian (Eq. 2.6):

$$\mathcal{L}_{Wl} = -\frac{g}{\sqrt{2}} \left[W_\mu^+ \bar{\nu}_l \gamma^\alpha (1 - \gamma_5) l + W_\mu^- \bar{l} \gamma^\alpha (1 - \gamma_5) \nu \right] . \quad (2.30)$$

The previous lagrangians allow to write the matrix element for the charged pion decay $\pi^\pm \rightarrow l^\pm \nu_l$:

$$\mathcal{M} = i \left[-\frac{g}{2\sqrt{2}} \bar{u}_{\nu_l} \gamma^\beta (1 - \gamma_5) v_l \right] \frac{i g_{\beta\alpha}}{M_W^2} i \left[-g \frac{F_0}{2} V_{ud} (-i p^\alpha) \right] = \quad (2.31)$$

$$-G_F V_{ud} F_0 \bar{u}_{\nu_l} \not{p} (1 - \gamma_5) v_l$$

where p is the pion four-momentum, $G_F = g^2/4\sqrt{2}M_W^2 = 1.16639(1) \times 10^5 \text{ GeV}^{-2}$ is the Fermi constant, u_{ν_l} is the neutrino spinor, v_l the lepton spinor, and the free parameter F_0 can now be identified with the pion decay constant (in the chiral limit).

Since the mass scale of the W boson is much higher than the other scales in the decay, the W propagator can be approximated as

$$\frac{-g_{\mu\nu} + \frac{k_\mu k_\nu}{M_W^2}}{k^2 - M_W^2} = \frac{g_{\mu\nu}}{M_W^2} + \mathcal{O}\left(\frac{k^2}{M_W^4}\right) . \quad (2.32)$$

The differential pion decay rate can be written as

$$d\Gamma_{\pi \rightarrow l\nu} = \frac{1}{2m_\pi} |\mathcal{M}|^2 \frac{1}{E_l E_\nu} \frac{d^3 p_l}{(2\pi)^3} \frac{d^3 p_\nu}{(2\pi)^3} (2\pi)^4 \delta^4(q - p_l - p_\nu) . \quad (2.33)$$

After inserting Eq. 2.31 and performing the energy integrals we finally obtain

$$\Gamma_{\pi \rightarrow l\nu} = \frac{G_F^2 |V_{ud}|^2}{4\pi} F_0^2 m_\pi m_l^2 \left(1 - \frac{m_l^2}{m_\pi^2} \right) . \quad (2.34)$$

2.3.1 Helicity Suppression

The pion can decay either into electrons (positrons) or muons. Using Eq. 2.34 and taking the ratio for the two cases $l = e$ and $l = \mu$ we obtain

$$R_\pi^0 = \frac{\Gamma_{\pi \rightarrow e\nu}}{\Gamma_{\pi \rightarrow \mu\nu}} = \frac{m_e^2}{m_\mu^2} \left(\frac{m_\pi^2 - m_e^2}{m_\pi^2 - m_\mu^2} \right)^2 = 1.283 \times 10^{-4} . \quad (2.35)$$

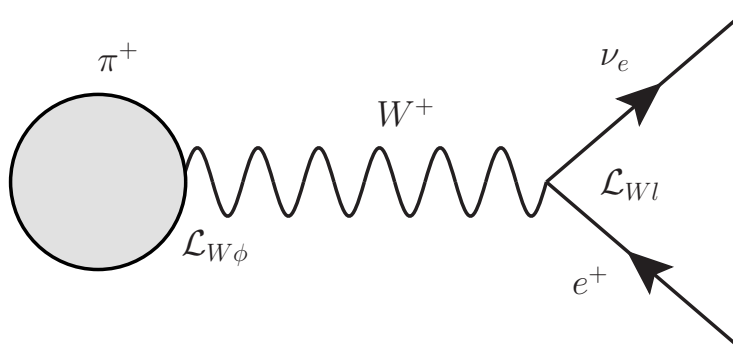


Figure 2.2: Lowest order diagram describing the pion decay. From a chiral effective field theory point of view, the pion is a structure-less Goldstone boson which couples with the external electroweak field W through the lagrangian $\mathcal{L}_{W\phi}$. The W decays into lepton-neutrino pairs with coupling described by \mathcal{L}_{Wl} .

This is the lowest order prediction for the branching ratio of leptonic decays of the pion and it shows that decays into electrons/positrons are 10^{-4} times less likely than decays into muons, contrary to the expectation from simple phase space considerations. This happens because of a *helicity suppression* mechanism due to the V-A nature of weak interactions.

The pion, being a pseudo-scalar particle, has spin zero: this means that the spins of the two decay products should be antiparallel (the black arrows on top of the particles in Fig. 2.3).

On the other side, the weak interaction is a chiral theory and forces massless particles to have a spin (equivalent to the helicity in this case) to be antiparallel to the momentum vector (and parallel for antiparticles), as indicated by the red arrows in Fig 2.3.

This constraint can be evaded by massive particles, since they move at a speed less than the speed of light and it is always possible to find a reference frame where the spin is not parallel/antiparallel to the momentum. While the neutrino is with good approximation massless, the muon and the electron are not.

The muon is about 200 times more massive than the electron and therefore the helicity suppression is less pronounced, as the m_e^2/m_μ^2 factor in Eq. 2.35 indicates.

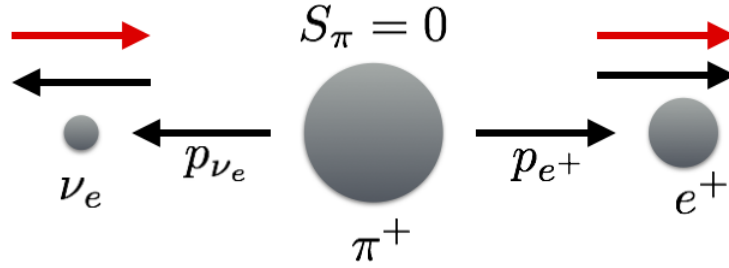


Figure 2.3: Helicity suppression mechanism in the pion decay. p_{e^+} and p_{ν_e} represent the particles' momenta. The horizontal arrows over the decay particles describe their spin state: black arrows are the spins according to angular momentum conservation, red arrows show the helicity state (in the case of massless particles) forced by the chiral V-A structure of the weak interactions.

In conclusion, if the decay products were massless, the weak interaction would prevent the pion to decay into leptons and neutrinos. What actually happens is that such a decay is more suppressed, the lighter the lepton is. Analogous helicity-suppressed decays exist also in the case of kaons and B-mesons (e.g. $K \rightarrow e\nu$, $B_s \rightarrow \mu^+\mu^-$).

2.3.2 Lepton Universality

In calculating the branching ratio $R_{\pi^0}^0$, the ratio of the decay amplitudes $\Gamma_{\pi \rightarrow l}$ was considered. This implied the assumption that the W boson couples with equal strength with every lepton generation (the coupling is flavour-independent). The coupling strength g is contained in the Fermi constant G_F .

In the SM, this assumption is known as *lepton universality*. If we introduce the hypothesis that the coupling might be different for each generation ($g \rightarrow g_e, g_\mu, g_\tau$), the branching ratio can be rewritten as

$$R_{\pi}^{\text{exp}} = \left(\frac{g_e}{g_\mu} \right)^2 R_{\pi}^{\text{SM}} . \quad (2.36)$$

Comparing the measured (R_{π}^{exp}) and calculated (R_{π}^{SM}) branching ratios, the ratio of the coupling constants can be extracted and compared with

Mode	Branching ratio	Notes
$\mu^+ \nu_\mu$	0.9998770 ± 0.0000004	
$\mu^+ \nu_\mu \gamma$	$(2.00 \pm 0.25) \times 10^{-4}$	$E_\gamma > 1 \text{ MeV}$
$e^+ \nu_e$	$(1.230 \pm 0.004) \times 10^{-4}$	
$e^+ \nu_e \gamma$	$(7.39 \pm 0.05) \times 10^{-7}$	$E_\gamma > 10 \text{ MeV}, \theta_{e\gamma} > 40^\circ$
$e^+ \nu_e \pi^0$	$(1.036 \pm 0.006) \times 10^{-8}$	
$e^+ \nu_e e^+ e^-$	$(3.2 \pm 0.5) \times 10^{-9}$	
$e^+ \nu_e \nu \bar{\nu}$	$< 5 \times 10^{-6}$	

Table 2.1: Pion decay modes and corresponding branching fractions.

the SM expectation $g_e/g_\mu = 1$. The current experimental situation concerning Lepton Universality tests is summarized in Sec. 2.6.

2.3.3 Pion Decay Modes

The pion decays mostly into muons and neutrinos and its lifetime is 26.033 ± 0.005 ns. The radiative version of this decay happens about as often as the helicity-suppressed decay into electrons or positrons, at the 10^{-4} level. Radiative decays are relevant for experiments like PIENU where the calorimetric system cannot discriminate between charged particles or photons. Theoretical calculations of the $\pi^+ \rightarrow e^+ \nu_e$ branching ratio take fully into account radiative effects and the experimental value can be directly compared with the experimental one. The radiative version of $\pi^+ \rightarrow e^+ \nu_e$ happens at the 10^{-7} level and it is therefore not significant at the level of precision targeted by PIENU.

The charged pion π^\pm is more than 4 MeV heavier than the π^0 and therefore it can decay into it, although the branching fraction is at the 10^{-8} level. A summary of the pion decay modes can be found in Tab. 2.1.

2.4 Precision Theoretical Calculations of R_π

The result for the pion decay branching ratio R_π^0 was obtained at the lowest order in perturbation theory and a more precise calculation re-

quires the inclusion of radiative and pion-structure dependent effects. The leading-order radiative corrections were first calculated by Berman [65] and Kinoshita [66] in the 1950s. They considered the diagrams in Fig 2.4 which are divided in two classes: Inner Bremsstrahlung diagrams (IB) involving real photons, and emission/re-absorption diagrams (ER) involving virtual photons. The diagrams require both infrared and ultraviolet cutoffs but the final result is cutoff independent. The infrared cutoff cancels exactly out after summing IB and ER diagrams and the ultraviolet cutoff cancels in the branching ratio. The branching ratio including the IB and ER diagrams is

$$R_{IB+IR} = R_0(1 + \delta)(1 + \epsilon) \quad , \quad (2.37)$$

$$\delta = \frac{3\alpha}{\pi} \ln \frac{m_\mu}{m_e} \quad , \quad \epsilon = 0.92 \cdot \frac{\alpha}{\pi} \quad .$$

The calculations were later checked and confirmed by T. Goldman and J. Wilson [67].

The pion is not a pointless particle and his substructure must bring additional corrections to the branching ratio. In 1976, W. Marciano and A. Sirlin calculated new corrections expanding the ratio in powers of the lepton mass and adding structure-dependent effects [68]. The new diagrams involved a photon, either real or virtual, emitted from the internal structure of the pion. They showed that the leading order term in m_l which does not cancel in the branching ratio does not depend on strong interactions. Another result of [68] is the first computation of the leading $\ln m_l$ term with structure-dependent ER corrections (SD-ER, see Fig. 2.5). They found also that the ER term exactly cancel the contribution of the interference term among the two last diagrams showed in Fig. 2.5. The full calculation leads to a -3.929% correction to R_π^0 . In 1993, they repeated the calculation with a more rigorous assessment of the theoretical uncertainty, obtaining $R_\pi^{\text{SM}} = (1.2352 \pm 0.0005) \times 10^{-4}$ [69]. The latest calculation of the pion branching ratio was performed by V. Cirigliano and I. Rosell in 2007 using Chiral Perturbation Theory at $\mathcal{O}(e^2 p^4)$ order [13, 70]. In this expansion, the branching ratio can be written as

$$R_\pi^{\text{SM}} = R_\pi^0 \left[1 + \Delta_{e^2 p^2} + \Delta_{e^2 p^4} + \Delta_{e^2 p^6} + \dots \right] [1 + \Delta_{LL}] \quad . \quad (2.38)$$

The $\Delta_{e^2 p^2}$ term represents the leading-order radiative effects. The $\Delta_{e^2 p^6}$ term arises from the emission of a photon by the pion. This higher-than- $\mathcal{O}(e^2 p^4)$ term has to be included since it is not helicity-suppressed. The

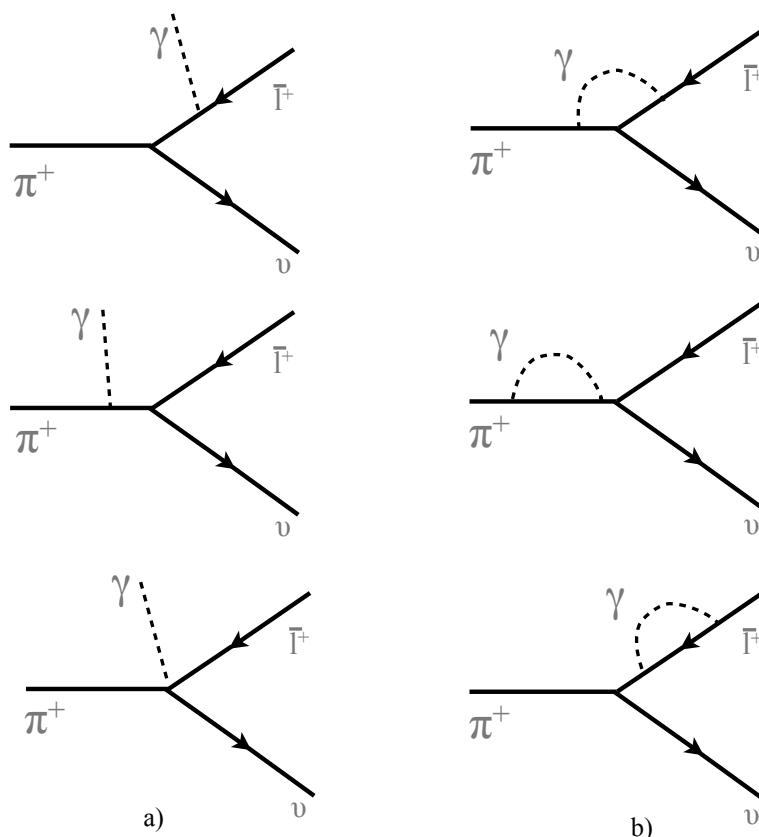


Figure 2.4: Feynman diagrams for the radiative corrections to pion decay, from real (a) and virtual (b) photons. \bar{l}^+ denotes an anti-lepton.

magnitude of the corrections are summarized in Tab. 2.2 and the final result is $R_{\pi}^{\text{SM}} = (1.2352 \pm 0.0001) \times 10^{-4}$. Later, it was shown in [71] that $\mathcal{O}(\alpha^2)$ two-loop diagrams contribute to the uncertainty, giving

$$R_{\pi}^{\text{SM}} = (1.2352 \pm 0.0002) \times 10^{-4} \quad . \quad (2.39)$$

The current theoretical uncertainty of the SM calculation is an order of magnitude smaller than the experimental result. This is the main motivation for the PIENU experiment, since an improvement of the experimental accuracy can provide constraints to models of physics beyond the SM.

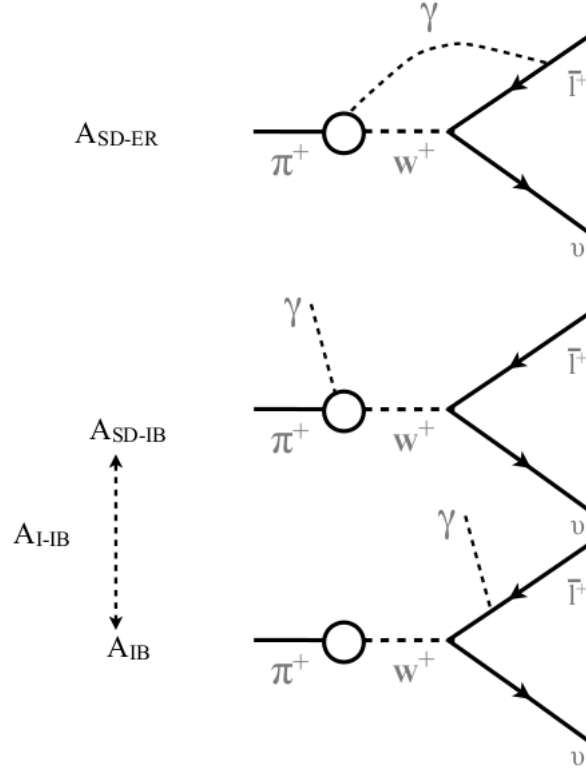


Figure 2.5: Leading Feynman diagrams contributing to the QED corrections of the branching ratio. A_{SD-ER} is the amplitude of the structure-dependent virtual correction. A_{I-IB} is the interference amplitude between structure-dependent and structure-independent IB corrections.

Term	Value (%)
$\Delta_{e^2 p^2}$	-3.929
$\Delta_{e^2 p^4}$	0.053 ± 0.011
$\Delta_{e^2 p^6}$	0.073
Δ_{LL}	0.054

Table 2.2: Corrections to the leading-order value for R_{π}^{SM} from [13, 70].

The presence of new physics can bring corrections to the branching ratio in the 0.01%–1% range [13] depending on the models considered.

2.4.1 Summary of the SM Calculations

Following [71], the branching ratio and its corrections can be parameterized with the following formula

$$R_{\pi}^{\text{SM}} = R_0 \left[1 + \frac{\alpha}{\pi} \left\{ \underbrace{F\left(\frac{m_e}{m_{\pi}}\right) - F\left(\frac{m_{\mu}}{m_{\pi}}\right)}_{\text{Kinoshita [66], } -3.929\%} + \underbrace{\frac{m_{\mu}^2}{m_{\rho}^2} \times 3.1 \ln \frac{m_{\rho}^2}{m_{\mu}^2}}_{\text{Terentev [72], } \sim 5.4 \times 10^{-4}} + \underbrace{\frac{m_{\mu}^2}{m_{\rho}^2} c_3 + 3.9(4) \times 10^{-3} \frac{m_{\pi}^6}{m_e^2 m_{\rho}^4}}_{\text{Cirigliano [73], } c_3 = -0.9 \pm 2.5} \right\} + \underbrace{\frac{7}{2} \left(\frac{\alpha}{\pi} \ln \frac{m_{\mu}}{m_e} \right)^2}_{\text{Two-loop, } +0.054(10)\%} \right], \quad (2.40)$$

where $m_{\rho} = 768 \text{ MeV}/c^2$ parameterizes the hadronic structure effects and the $F(x)$ function can be found in [66] and describes all the one-loop corrections for a structure-less pion. The values with percentages in Eq. 2.40 are expressed with respect to R_{π}^0 .

2.5 Physics Beyond the Standard Model

Despite the success of the SM in describing the interactions among the known particles, some of its features are not fully explained.

Examples are the existence of three families of quarks and leptons, the different mixing in the quark and lepton sectors, the nature of neutrinos and their masses, the large range of particle masses from $< \text{eV}$ to GeV , and the relative smallness of the Higgs boson mass. Moreover, the SM does not provide explanations for the presence of dark matter and dark energy and does not provide sufficient CP violation to explain the matter/antimatter asymmetry observed in the universe. Therefore, there are reasons to believe that the SM is an effective theory approximating at low energies a more fundamental theory. A new BSM theory can be potentially discovered producing new particles in high-energy collisions. However, such a theory can also manifest its effects in modifications of the SM predictions through virtual effects due to the presence of new

particles.

A recent renormalization group evolution analysis shows that the current precision in measuring and calculating meson decays such as $\pi^+ \rightarrow e^+ \nu_e$ sets a scale for BSM physics at $\mathcal{O}(500)$ TeV [74].

2.5.1 New Scalar and Pseudoscalar Interactions

Physics beyond the SM above the electroweak scale could give rise to new scalar interactions. Such effects might come from extra Higgs multiplets, leptoquarks or contact interactions coming from quark/lepton compositeness. Searches for new scalar couplings can be performed with precision β -decay experiments.

Measurements of pseudoscalar meson decays can provide instead higher precision on searches for new pseudoscalar interactions, since such decays are highly helicity suppressed and deviations due to new non-suppressed physics are larger. Meson decays can therefore provide indirect information on new scalar interactions since pseudoscalar interactions can be generated through loop corrections. New pseudoscalar interactions can also be generated by leptoquarks, supersymmetric particles at loop level and charged Higgs bosons [75].

The pion decay matrix element in Eq. 2.31 can be also be generally written in terms of the leptonic and hadronic currents $J_{l\pi}$ and J_{lv} . Approximating the propagator as in Eq. 2.32 the matrix element reads

$$\mathcal{M} = \frac{iG}{\sqrt{2}} \langle 0 | V - A | \pi \rangle \bar{u}(p_l) \gamma_\mu (1 - \gamma_5) v(p_\nu) \quad . \quad (2.41)$$

Since the matrix element $\langle 0 | V - A | \pi \rangle$ connects the vacuum with a pseudo-scalar particle, the vector part vanishes leaving only $\langle 0 | A | \pi \rangle$. More in general, in the presence of physics beyond the SM, we can consider the general case $\langle 0 | \mathcal{O} | \pi \rangle$ where \mathcal{O} can be a scalar (S), pseudoscalar (P), vector (V) or axial-vector (A) operator. Given the pseudo-scalar nature of the pion, only the P and A terms can give non-vanishing contributions [76]. The pseudo-scalar term can be written as

$$\langle 0 | \bar{u} \gamma_5 d | \pi \rangle = i\sqrt{2} \frac{F_\pi m_\pi^2}{m_u + m_d} \quad , \quad (2.42)$$

and the effective four-Fermi pseudoscalar contact interaction is described

by

$$\mathcal{L}_P = -i \frac{\rho}{2\Lambda^2} [\bar{l}(1 - \gamma_5)v_l] [\bar{u}\gamma^5 d] \quad , \quad (2.43)$$

where ρ is the pseudo-scalar coupling constant and Λ is the mass scale of the new particle. The final matrix element will be the coherent sum of the new pseudo-scalar matrix element \mathcal{M}_P and the SM (V-A) matrix element. In the final square of the matrix element, the largest contribution from new physics comes from the interference term proportional to $1/\Lambda^2$. Assuming the effect of the new interaction only in the $\pi^+ \rightarrow e^+ \nu_e$ decay, the deviation from the SM branching ratio can be parameterized by

$$1 - \frac{R^{exp}}{R^{SM}} \sim \pm \frac{\sqrt{2\pi}}{G} \frac{1}{\Lambda^2} \frac{m_\pi^2}{m_e(m_u + m_d)} \sim \left(\frac{1 \text{ TeV}}{\Lambda} \right)^2 \times 10^3 \quad . \quad (2.44)$$

From the above formula, a $\sim 0.1\%$ precision experiment like PIENU can be sensitive to new pseudoscalar interactions at the $\mathcal{O}(1000)$ TeV mass scale, well beyond the reach of present colliders.

2.5.2 Supersymmetry

Supersymmetric extensions of the SM can induce non-universal contributions and modify R_π^{SM} [77, 78]. In [78] contributions to R_π from the Minimal Supersymmetric Standard Model (MSSM) were considered. The MSSM can change R_π by a quantity ΔR_π^{SUSY} which can arise either at tree or loop level.

Considering R-parity conservation, the value of ΔR_π^{SUSY} turns out to be very small, and only in particular regions of the MSSM parameter space, the magnitude of the deviation might fall into the range of the sensitivity of PIENU.

Considering R-parity violation (RPV) with lepton number violation, the effects are larger and observable already at tree level. Contributions from RPV interactions can be expressed as

$$\frac{\Delta R_\pi^{SUSY}}{R^{SM}} = 2(\Delta_{11k} - \Delta_{21k}) \quad , \quad (2.45)$$

$$\Delta_{i1k} = \frac{\lambda_{i1k}}{4\sqrt{2}G_F m_f^2} \quad , \quad (2.46)$$

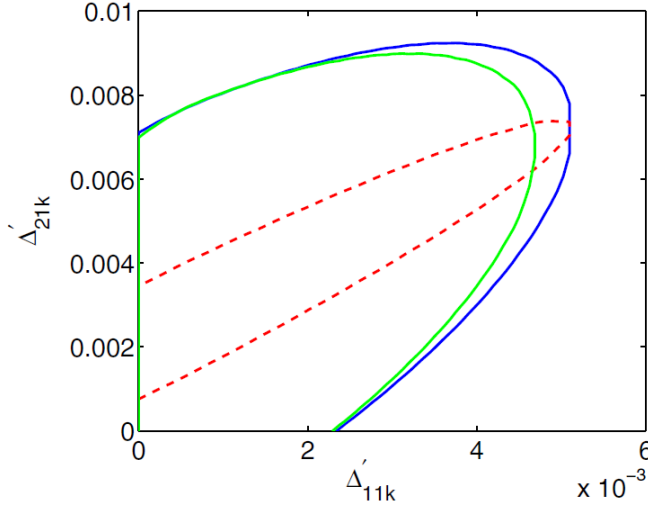


Figure 2.6: The curves enclose the allowed region for the RPV parameters given the available experimental data. The blue curve shows the constraint using the PDG (2007) value for the branching ratio, and the dashed red curve shows the projected constraint from a 0.1% precision measurement of the branching ratio, with the same central value as the blue curve. The green curve shows the expected limits from the Qweak experiment measuring the weak charge of the proton at Jefferson Lab [79].

where λ_{11k} and λ_{21k} are parameters related to the RPV interaction for the decay into an electron or a muon respectively and $m_{\tilde{f}}$ is the mass of the exchanged sfermion. In [78] a fit to precision experimental data was performed for extracting allowed bounds for λ_{11k} and λ_{21k} . The results are showed in Fig. 2.6 where the contribution of a 0.1% precision measurement of R_π is highlighted (red dashed contour). The existence of RPV supersymmetric interactions and lepton number violation would have profound implications, like the generation of a neutrino Majorana mass term and a lightest SUSY particle (LSP) decaying into SM states. In particular, the instability of the LSP would put into question its role as dark matter candidate (depending on its lifetime).

2.5.3 Charged Higgs

Extensions of the SM predict the existence of charged Higgs bosons H^\pm [80]. Considering a H^\pm coupling $g/2\sqrt{2}\lambda_{ud}$ to the $\bar{u}\gamma_5 d$ pseudoscalar current and $g/2\sqrt{2}\lambda_{lv}$ to the leptonic current $\bar{l}(1 - \gamma_5)v_l$ ($l=e,\mu$), with g the $SU(2)_L$ gauge coupling and λ the chirality-breaking factors, we have

$$R_\pi = R_\pi^{\text{SM}} \times \left[1 - \frac{2m_\pi^2}{m_e(m_u + m_d)} \frac{m_W^2}{m_{H^\pm}^2} \lambda_{ud} \left(\lambda_{ev} - \frac{m_e}{m_\mu} \lambda_{\mu\nu} \right) \right]. \quad (2.47)$$

A 0.1% precision measurement of the branching ratio would probe

$$m_{H^\pm} \sim 200 \text{ TeV} \times \sqrt{\lambda_{ud}} \sqrt{\lambda_{ev} - \frac{m_e}{m_\mu} \lambda_{\mu\nu}}. \quad (2.48)$$

In the SM with a Higgs doublet, $\lambda_{ev}/\lambda_{\mu\nu} = m_e/m_\mu$, then $R = R_{SM}$ and no experimental constraints can be provided. In more general multi-Higgs scenarios with H^\pm couplings $\lambda_{ud} \simeq \lambda_{\mu\nu} \simeq \lambda_{ev} \simeq \alpha/\pi$ induced by loops, $m_{H^\pm} \approx 400 \text{ GeV}/c^2$ and this can be probed at $\sim 0.1\%$ sensitivity level.

2.5.4 Leptoquarks

Leptoquarks are hypothetical particles carrying both lepton and baryon quantum numbers and represent thus a new interaction among quarks and leptons (for a review, see e.g. [81]). Leptoquarks are predicted by various models of BSM physics. One example is the Pati-Salam model [82] where the $SU(3)$ symmetry is extended to $SU(4)$ including the lepton number. $SU(5)$ and $SO(10)$ Grand Unification Theories (GUTs) predict vector leptoquarks [83, 84, 85] and R-parity violating SUSY models can also generate leptoquark Yukawa couplings.

Limits to leptoquarks come from production cross sections at colliders, while indirect limits are calculated from the bounds on induced four-fermion interactions obtained from low-energy experiments or from collider experiments below threshold.

Leptoquarks can be chiral or non-chiral and thus able to couple to both left- and right-handed leptons and quarks. The $\pi^+ \rightarrow e^+ \nu_e$ decay places strong constraints on non-chiral leptoquarks with bounds on the mass M_{LQ} and couplings g_L, g_R of $M_{LQ}^2/g_L g_R \geq (100 \text{ TeV})^2$ [86]. The same decay can place also constraints in the case of chirally coupled leptoquarks.

In a singlet representation and assuming a coupling similar to the strong coupling, $M_{LQ}/g \geq 12$ TeV bounds can be placed [87].

Direct searches at LHC (at $\sqrt{s} = 7$ TeV) place limits for first and second generation leptoquarks at the ~ 1 TeV level while third generation leptoquarks are excluded up to ~ 700 GeV [81].

2.5.5 Partial Compositeness

Usually with "compositeness" one refers to the existence of a substructure of a particle previously considered elementary. An important case is the possibility that the Higgs boson is not an elementary scalar particle which drives the electroweak symmetry breaking obtaining a non-zero vacuum expectation value. In compositeness scenarios, the Higgs boson is instead a pseudo-Nambu-Goldstone particle resulting from the formation of a condensate in a new strongly interacting sector (a new "force") [88].

An alternative model for explaining the fermion masses is *partial compositeness* [89]. In this model, SM fermions mix with new composite fermions and become massive.

The direct influence of partial compositeness to the $\pi^+ \rightarrow e^+ \nu_e$ branching ratio is not yet calculated, but its precision measurement provides important constraints to other processes.

In [89], the hints of disagreement with the SM in $B \rightarrow K^{(*)} ll$ and $B \rightarrow D^{(*)} \tau \nu$ decays measured at high-energy flavour experiments (see Sec. 2.6) are accommodated within a partial-compositeness model. The analysis in [89] employs the strong constraints provided by $\pi^+ \rightarrow e^+ \nu_e$ and $K^+ \rightarrow e^+ \nu_e$ decays for restricting the amount of $e - \mu$ universality violation allowed in flavour-changing neutral currents.

2.5.6 Heavy Neutrinos

Neutrinos show the remarkable effect of oscillations which clearly points to physics beyond the SM. What is their nature (Dirac or Majorana) and what are their masses is the subject of active current research, as discussed in Sec. 2.1.3. The current neutrino data can be described with 3 neutrino flavours and their mixing described by the 3×3 unitary PMNS matrix. In order to explain the relatively small observed neutrino masses

and to resolve some experimental anomalies [90], the existence of additional neutrino states is hypothesized. The idea is that the new states are electroweak singlets and therefore not interacting with SM particles ("sterile neutrinos"). If we assume the existence of k additional neutrino states, the mixing is described by

$$\nu_\alpha = \sum_{i=1}^{3+k} U_{\alpha i} \nu_i \quad . \quad (2.49)$$

Additional neutrinos can have a broad range of masses, from eV to TeV. A $k=3$ example is the Neutrino Minimal Standard Model (ν MSM, [91]), where three right-handed sterile neutrinos are added. This renormalizable model contains 18 new parameters: 3 Majorana masses, 3 Yukawa couplings, 6 mixing angles and 6 CP-violating phases. It is valid up to the Planck scale without introducing any other new fields. The ν MSM neutrino lagrangian for the new gauge-singlet neutrinos N_i ($i=1,2,3$) is

$$\mathcal{L}_\nu = \bar{N}_i i \partial_\mu \gamma^\mu N_i - F_{\alpha i} \bar{L}_\alpha N_i \phi - \frac{M_i}{2} \bar{N}_i N_i + h.c. \quad , \quad (2.50)$$

where ϕ is the Higgs field, L_α ($\alpha = e, \mu, \tau$) are the lepton doublets, M_i are the Majorana masses, $M_D = F\langle\phi\rangle$ the Dirac masses and $F_{\alpha i}$ is the matrix containing the Yukawa couplings. Mixing angles and phases are contained in F :

$$F = \tilde{U}_L f \tilde{U}_R^\dagger \quad , \quad (2.51)$$

with the Yukawa couplings $f = \text{diag}(f_1, f_2, f_3)$, $\tilde{U}_L = \text{diag}(e^{i\alpha_1}, e^{i\alpha_2}) \times U_L$ and $\tilde{U}_R = \text{diag}(e^{i\beta_1}, e^{i\beta_2}) \times U_R$. $U_{L/R}$ are two 3×3 matrices analogous to the PMNS mixing matrix containing each 3 angles and one CP-violating Dirac phase. The Majorana masses are assumed to be below the electroweak scale, so the model can be consistent with neutrino experiments only with very small Yukawa couplings, of the order of

$$f_i^2 = \mathcal{O}\left(\frac{m_\nu M_i}{v^2}\right) \quad , \quad (2.52)$$

where m_ν is the mass scale of the active neutrinos and $v \sim 174$ GeV is the vacuum expectation value of the Higgs field. At the same time, Majorana masses must be larger with respect to the Dirac masses, so that the seesaw mechanism (Sec. 2.1.3) can take place.

In the ν MSM, the two heavier states among three right-handed neutrinos are responsible for baryogenesis and the remaining lightest one can be a candidate for warm dark matter, since for small enough f_i the sterile neutrino lifetime can exceed the age of the universe. In the early universe sterile neutrinos are produced through their coupling with active neutrinos.

Searches for sterile neutrinos can be performed with astrophysical and cosmological data [92]. The presence of sterile neutrinos can also be investigated with meson decays. In [93] it is argued that in some cosmological scenarios (if the reheating temperature is $T_{RH} \ll 100$ MeV), direct searches at the MeV-scale can provide much more stringent limits than astrophysical measurements.

Depending on the choice of the parameters, the ν MSM predicts contributions of sterile neutrinos to π and K decays [94].

In [95], a simple renormalizable model for addressing small-scale structure formation problems in dark matter models is described. In this model, a dark matter candidate can couple to a sterile heavy neutrino via a new dark sector mediator. The model requires heavy neutrinos in the ~ 100 MeV mass range and ~ 10 MeV dark matter particles. In [96] the same model is systematically explored for addressing dark matter annihilation and thermalization via interactions with heavy neutrinos.

In the case of the $\pi^+ \rightarrow e^+ \nu_e$ decay, heavy neutrino states with masses below m_π can be searched for with a peak search on the decay lepton energy spectrum. On the other hand, the presence of a heavy neutrino will weaken the helicity-suppression mechanism and thus modify the R_π branching ratio.

2.5.7 Majorons

If neutrinos are Majorana particles, then the lepton number is not conserved and the associated original SM symmetry is broken. In [98] the case where the lepton number global symmetry is spontaneously broken was considered, resulting in the appearance of a massless Goldstone boson, called *Majoron*⁶.

⁶As mentioned in [98], the name "Majoron" was proposed by G. Gelmini, who in [99] comments: "We wish to make clear that, although it has been invented in Munich, its name does not come from the typical German name *Meyer*, but rather from the great

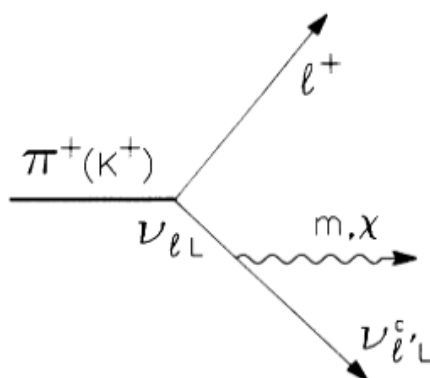


Figure 2.7: Majoron emission in a meson decay (figure from [97]).

In another model [99], Majorana neutrino masses are introduced extending the Higgs sector: after spontaneous symmetry breakdown, two new particles appear: the Majoron and a low-mass neutral Higgs boson. The new Higgs boson is coupled with leptons and very weakly to the other fermions.

Majorons J can be searched for in the decay $\pi \rightarrow e\nu_e J$ [97] investigating the features of the decay lepton energy spectrum. In this decay, the Majoron is radiated from the neutrino.

2.6 Status of Universality Violation Searches

According to Lepton Universality (LU), the SM leptons differ only by their mass, while their coupling to the electroweak current is the same. Precision tests of LU have been performed by many experiments with W bosons, meson and τ -lepton decays:

$$W, \pi, K \rightarrow l\nu_l \quad ,$$

$$\tau \rightarrow l\nu_\tau\nu_l \quad ,$$

Tab. 2.3 summarizes some of the results concerning these decays. More recently, with the advent of asymmetric e^+e^- B-factories (BaBar and Belle

Italian physicist Majorana."

Decay mode	g_μ/g_e
$\mathcal{B}_{\pi\rightarrow\mu}/\mathcal{B}_{\pi\rightarrow e}$	1.0004 ± 0.0012 [100]
$\mathcal{B}_{\tau\rightarrow\mu}/\mathcal{B}_{\tau\rightarrow e}$	1.0018 ± 0.0014 [101]
$\mathcal{B}_{K\rightarrow\mu}/\mathcal{B}_{K\rightarrow e}$	0.996 ± 0.005 [102]
$\mathcal{B}_{K\rightarrow\pi\mu}/\mathcal{B}_{K\rightarrow\pi e}$	1.002 ± 0.002 [103]
$\mathcal{B}_{W\rightarrow\mu}/\mathcal{B}_{W\rightarrow e}$	0.997 ± 0.010 [103]
	g_τ/g_μ
$\mathcal{B}_{\tau\rightarrow e\tau_\mu}/\tau_\tau$	1.0011 ± 0.0015 [101]
$\mathcal{B}_{\tau\rightarrow\pi}/\mathcal{B}_{\pi\rightarrow\mu}$	0.9963 ± 0.0027 [101]
$\mathcal{B}_{\tau\rightarrow K}/\mathcal{B}_{K\rightarrow\mu}$	0.9858 ± 0.0071 [101]
$\mathcal{B}_{W\rightarrow\tau}/\mathcal{B}_{W\rightarrow\mu}$	1.039 ± 0.013 [103]
	g_τ/g_e
$\mathcal{B}_{\tau\rightarrow\mu\tau_\mu}/\tau_\tau$	1.0029 ± 0.0015 [101]
$\mathcal{B}_{W\rightarrow\tau}/\mathcal{B}_{W\rightarrow e}$	1.036 ± 0.014 [103]

Table 2.3: Experimental results on lepton universality from π , K, τ , and W decays. \mathcal{B} represents the branching ratio of a specific decay mode.

experiments) and the LHC at CERN (with the LHCb experiment), the leptonic and semileptonic decays of the B meson were precisely studied:

$$B \rightarrow \tau \nu_\tau \quad ,$$

$$B \rightarrow D^{(*)} l \nu_l \quad ,$$

where $l = e, \mu, \tau$ and $D^{(*)}$ refers to the D and D^* charm mesons. The measurements from BaBar, Belle and LHCb all point towards larger than expected rates of B mesons decays involving τ leptons. Since these processes can be precisely calculated within the SM, these excesses might point towards Lepton Universality Violation (LUV). The SM predictions for the decay branching ratios are

$$\mathcal{B}_{SM}(B^- \rightarrow \tau^- \bar{\nu}_\tau) = (0.75 \pm_{0.05}^{0.10}) \times 10^{-4} \quad [104] \quad ,$$

$$\mathcal{R}_{SM}^D = \frac{\mathcal{B}(\bar{B} \rightarrow D \tau^- \bar{\nu}_\tau)}{\mathcal{B}(\bar{B} \rightarrow D e^- \bar{\nu}_e)} = 0.300 \pm 0.008 \quad [105, 106, 107] \quad ,$$

$$\mathcal{R}_{SM}^{D^*} = \frac{\mathcal{B}(\bar{B} \rightarrow D^* \tau^- \bar{\nu}_\tau)}{\mathcal{B}(\bar{B} \rightarrow D^* e^- \bar{\nu}_e)} = 0.252 \pm 0.003 \quad [105, 106, 107] \quad .$$

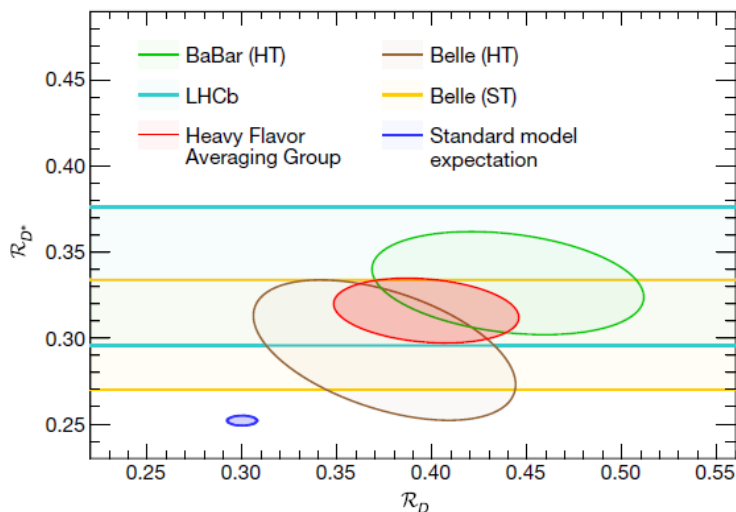


Figure 2.8: Experimental results for \mathcal{R}^{D^*} from BaBar, Belle and LHCb. The 1σ contours include statistical and systematic errors together with their correlations (figure from [108]).

The first fully leptonic branching ratio is normalized to all the other decays. The decay into μ or e is very small and it has not been observed so far. $\mathcal{R}_{SM}^{D^*}$ are ratios of branching fractions, considered for removing the dependence from the CKM matrix element $|V_{cb}|$ and in this way reducing both theoretical errors and experimental uncertainties.

The 2016 experimental average results are

$$\mathcal{B}_{Exp}(B^- \rightarrow \tau^- \bar{\nu}_\tau) = (1.06 \pm 0.19) \times 10^{-4} \quad [117] \quad ,$$

$$\mathcal{R}_{Exp}^D = \frac{\mathcal{B}(\bar{B} \rightarrow D \tau^- \bar{\nu}_\tau)}{\mathcal{B}(\bar{B} \rightarrow D e^- \bar{\nu}_e)} = 0.397 \pm 0.040_{\text{stat}} \pm 0.028_{\text{syst}} \quad [118] \quad ,$$

$$\mathcal{R}_{Exp}^{D^*} = \frac{\mathcal{B}(\bar{B} \rightarrow D^* \tau^- \bar{\nu}_\tau)}{\mathcal{B}(\bar{B} \rightarrow D^* e^- \bar{\nu}_e)} = 0.316_{\text{stat}} \pm 0.016_{\text{syst}} \quad [118] \quad .$$

The leptonic decay shows a 1.4σ deviation from the SM, while the semileptonic decays display a $\sim 4\sigma$ deviation. The results are summarized in Fig. 2.9 using the results from BaBar [109], Belle [110, 111] and LHCb [112].

The discrepancies of the experimental values with respect to the SM

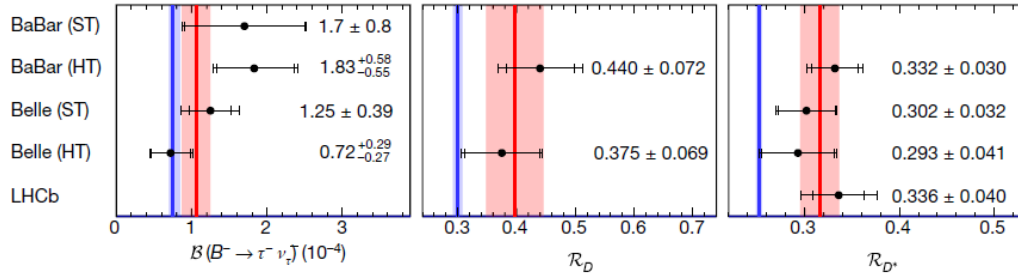


Figure 2.9: Single experimental results from BaBar [109], Belle [110, 111] and LHCb [112]. ST and HT refer to measurements with semileptonic and hadronic tags respectively (figure from [108]). The vertical red lines and bands are the average values with combined errors calculated by the Heavy Flavor Averaging group [113, 114]. The blue bands are SM calculations [115, 116, 106].

calculations can have an explanation in terms of BSM physics. Among the proposed solutions there are new vector bosons W' similar to the electroweak ones but heavier, which couple differently among generations and among quarks and leptons. Another possibility is a new charged, spin-0 Higgs boson. SUSY theories generically predict the presence of charged Higgs particles.

2.7 Summary

The pion decay amplitude can be calculated within the SM using Chiral Perturbation Theory and the result can be used to calculate the $\pi^+ \rightarrow e^+ \nu_e$ branching ratio. At tree-level, the calculation evidences the helicity-suppression effect of the V-A electroweak theory through the factor m_e^2/m_μ^2 . Higher-order calculations include radiative corrections and structure dependent corrections. This observable is the most precisely calculated quantity involving quarks in the SM and as such it is extremely interesting to measure for uncovering disagreements due to the presence of BSM physics. Many BSM theories predict deviations from the SM calculation within the reach of the PIENU experiment.

The branching ratio represents also a test of lepton universality. In light

of the most recent measurements showing interesting deviations from the SM predictions, a stringent test of lepton universality represents an important piece of information for testing BSM theories.

Chapter 3 | Experimental Setup

In this chapter, the PIENU experimental setup will be described. A beam of pions, muons, and positrons was provided by the TRIUMF cyclotron proton beam impinging on a primary beryllium target. Pions were selected and sent to the experiment with the M13 secondary beamline.

PIENU consists of different sub-detectors: wire chambers, silicon microstrip detectors, scintillators and crystal calorimeters. The different detectors will be described as well as the data acquisition system and software.

3.1 The TRIUMF Cyclotron

With the 18 m diameter of the 4000 tons main magnet, the TRIUMF cyclotron is still the largest ever built. The 0.56 T magnetic field is created by coils with 18500 A currents. It accelerates in 326 μ s negative hydrogen ions to a maximum energy of 520 MeV (3/4 of the speed of light) and the beam has a current of 300 μ A, divided among four primary beamlines. Acceleration is provided by a 23.05 MHz 93 kV RF field which corresponds to a bunch spacing of 43.4 ns, with a bunch width of 4 ns. Extraction from the cyclotron to the beamlines is accomplished by stripping foils which remove the electrons off the H^- ions, thus reversing the direction of the magnetic steering.

3.2 The M13 Beamline

For reducing the statistical error on the branching ratio R_π , a large sample of pion decays must be collected. To this end, the new PIENU setup has a

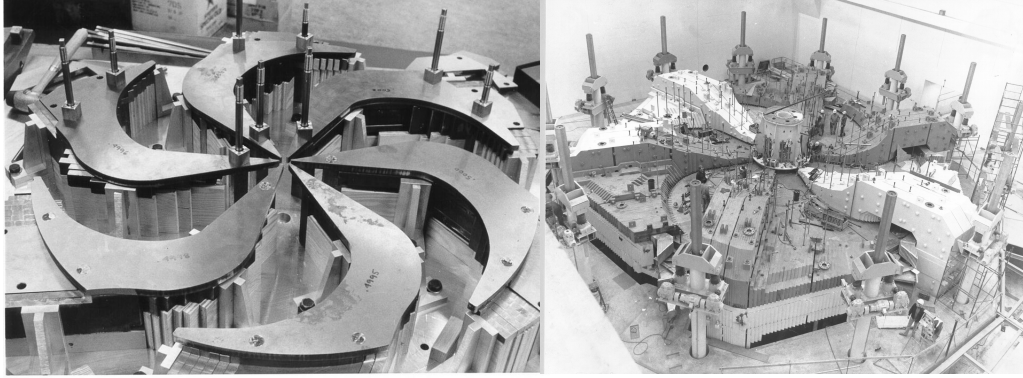


Figure 3.1: **(Left)** Shape of the TRIUMF cyclotron main magnet, which was designed for coping with the defocusing effects arising from the relativistic motion of particles on the spiral orbits [119]. **(Right)** Picture of the fully assembled cyclotron taken in March 1972.

larger acceptance with respect to the previous TRIUMF E248 experiment, where the calorimeter for e^+ detection was placed on the side of the beam to avoid excessive backgrounds. In the new setup, the acceptance to decay positrons is maximized placing the detectors directly on the beam axis. This new arrangement posed some challenges to the experiment, which had to cope with higher beam backgrounds.

In particular, positrons in the beam can place severe limitations to the data collection. The original M13 beamline [120] delivered a pion beam with $\sim 1/4$ contamination of positrons which severely increased detector and trigger rates, as well as backgrounds in the $\pi^+ \rightarrow e^+ \nu_e$ spectrum. In order to cope with this issue, an extension of M13 was designed adding a collimator and additional magnets.

Original M13 Beamline

In a test run performed in 2006 with a two plastic scintillator setup, it was showed that after offline analysis cuts, 2% of positrons with respect to $\pi^+ \rightarrow e^+ \nu_e$ events still remained in the data. Another background was identified in the form of neutrons and γ rays from the beamline that raised the energy of the $\pi^+ \rightarrow \mu^+ \nu_\mu \rightarrow e^+ \nu_e \bar{\nu}_\mu$ decay chain to $\pi^+ \rightarrow e^+ \nu_e$ energies adding another background [121].

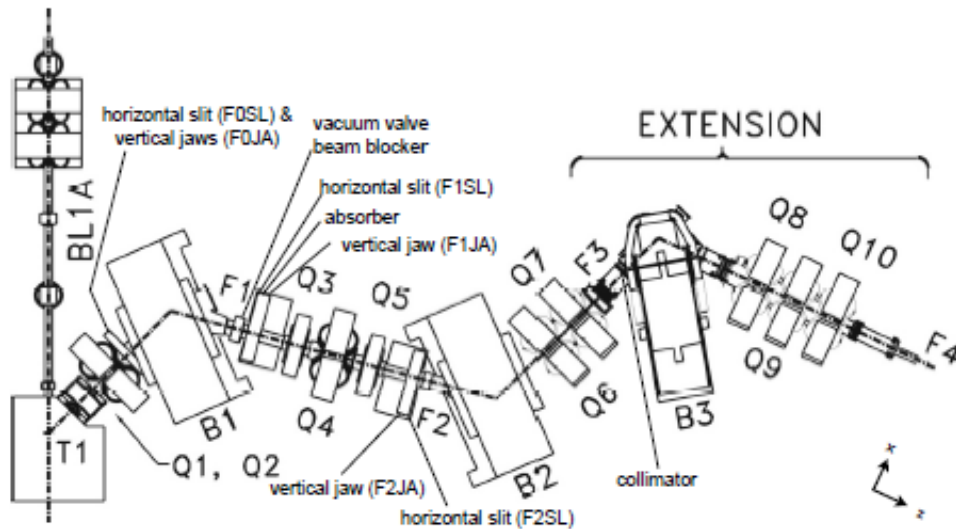


Figure 3.2: A schematic of the M13 beamline with the extension and the collimator constructed for the PIENU experiment in 2008.

All the previous considerations and experimental findings pointed toward the need of a modification of the M13 beamline for dealing with these unacceptably high levels of beam background. In Fig. 3.2, the old M13 beamline is showed, together with the new added components. The beamline started from the BL1A primary proton beamline at a 135° angle in correspondence of a 1-cm thick beryllium primary production target. M13 had a 29 msr acceptance and it was an achromatic beamline with -60° and $+60^\circ$ dipole magnets (called B1 and B2¹), a quadrupole doublet (Q1, Q2) between the beryllium target and B1 for large acceptance particle collection, a quadrupole triplet (Q3, Q4, Q5) between B1 and B2, and another quadrupole doublet after B2 for the final focusing. The magnetic optics defines three foci: F1 between B1 and Q3, F2 between Q5 and

¹The magnets were commissioned at the beginning of the 1980s and were conventionally called *Leander* (B1) and *Hector* (B2) with a weight of 22t and 17.2t respectively, with a maximum of ~ 300 A of current. The gap was 7.65" with maximum fields of 0.64T and 0.74T [122].

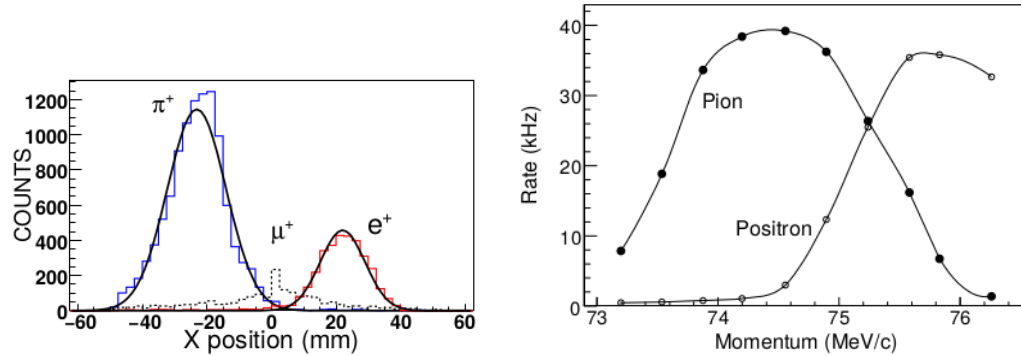


Figure 3.3: **Left:** Position distribution of π^+ , μ^+ and e^+ at F3 measured with wire chambers. Particle identification was achieved with a plastic scintillator giving energy loss and TOF measurements. Solid lines are Gaussian fits. **Right:** π^+ and e^+ rates at F4 as a function of the selected momentum.

B2, and F3 after the last quadrupole. Slits for acceptance definition SL1 and SL2 were placed at F1 and F2 respectively. After SL1 (~ 10 cm), there were two wheels holding different absorbers.

If one of the absorber materials was placed in the beam, M13 worked as an energy-loss based particle separator. If pions and positrons passed through a thin material, at 75 MeV/c momentum this is sufficient to obtain a clean separation of the particle species, as showed in Fig. 3.3 (left). The data were taken during a test for verifying beam dynamics calculations done with the REVMOC package [123] used for designing the beamline [124]. The test setup consisted in the NaI(Tl) calorimeter used for the PIENU experiment and a plastic scintillator for triggering and particle identification via energy and time-of-flight with respect to the cyclotron frequency. In front of the calorimeter there was a 3-layer wire chamber. The separator material was a 1.45 mm thick Lucite² absorber.

²Poly(methyl methacrylate), or PMMA. Lucite is one of the commercial names for this material, commonly referred as *acrylic*.

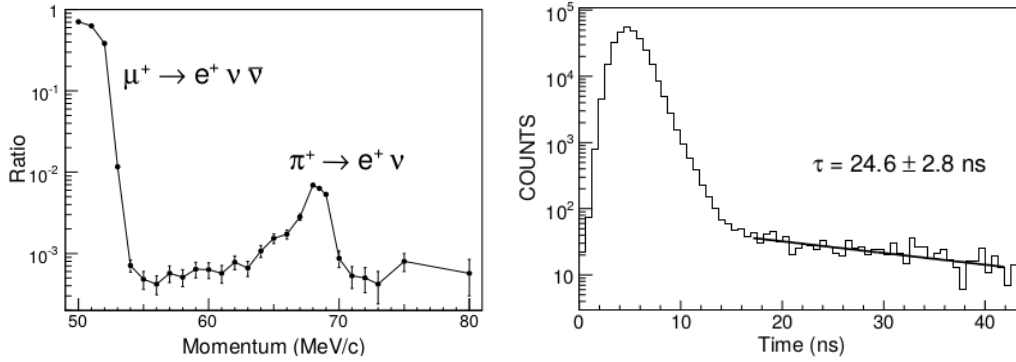


Figure 3.4: **Left:** fraction of beam positrons as a function of the selected momentum. **Right:** fit of the delayed component of the positrons' time-of-flight showing consistency with the pion decay time.

Beamline Extension

Once it was verified that a clean separation among pions and positrons can be achieved, an extension of the beamline was installed (Fig. 3.2 and pictures in Fig. 3.5). The extension started at the F3 focus and consisted of an additional -70° dipole (B3, or *Pacman*) and a 30 cm aperture quadrupole triplet (Q8, Q9, Q10) after B3. A lead collimator of 5 cm thickness with a 3 cm square hole was placed at F3, blocking the spatially separated positrons. The beamline extension defined a new focus F4 1.5 m after Q10 where the experiment was placed. The B3 magnet bent the beam for cleaning it from electromagnetic radiation arising from the collimator. In Fig. 3.3 (right) the obtained particle rates are showed as a function of the selected beamline momentum. The rates were consistent with beam dynamics calculations and it was showed that the positron rate can be suppressed by a factor ~ 60 with respect to the pion rate [125].

The momentum calibration of the beamline was difficult to achieve with high accuracy, due to the presence of fringe fields of the dipoles. A good calibration can be nevertheless achieved relying to physics processes like the endpoint of the muon decay spectrum $\mu^+ \rightarrow e^+ \nu_e \bar{\nu}_\mu$ and the peak of the $\pi^+ \rightarrow e^+ \nu_e$ decay. Positrons from the two decays came from decays happening in the primary target. Above 55 MeV/c, the major source of positrons is γ conversion from $\pi^0 \rightarrow \gamma\gamma$ decays inside the

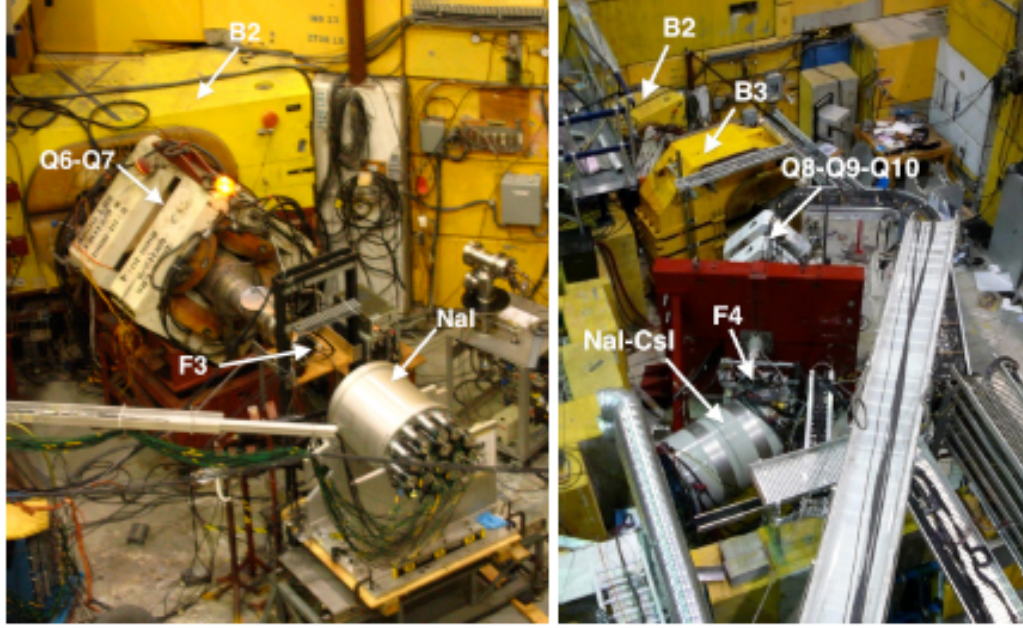


Figure 3.5: The end of the M13 beamline, before (left) and after (right) the extension. Part of the detector was in place to measure the particle content of the beam.

primary target. The momentum distribution of these prompt (with respect to the proton beam bunch) positrons was nearly flat [122]. Selecting instead positrons delayed with respect to the primary beam RF structure, it is possible to eliminate the prompt background and observe pion and muon decay products. The result of the momentum scan is showed in Fig. 3.4 (left), where the endpoint of the muon decay and the peak of the $\pi^+ \rightarrow e^+ \nu_e$ decay are clearly visible. In Fig. 3.4 (right), it is showed that the delayed positrons have indeed a time spectrum consistent with the pion decay time [126]. The beamline was also tested with negative polarity, finding a ratio of delayed to prompt positrons of $(3.4 \pm 0.4) \times 10^{-3}$, consistent with an estimate based on the yield ratio $N_{\pi^-} / N_{\pi^+} = 1/5$ in this energy region and the $\sim 1\%$ fraction of pion decays in flight in which muons stop in the target [127].

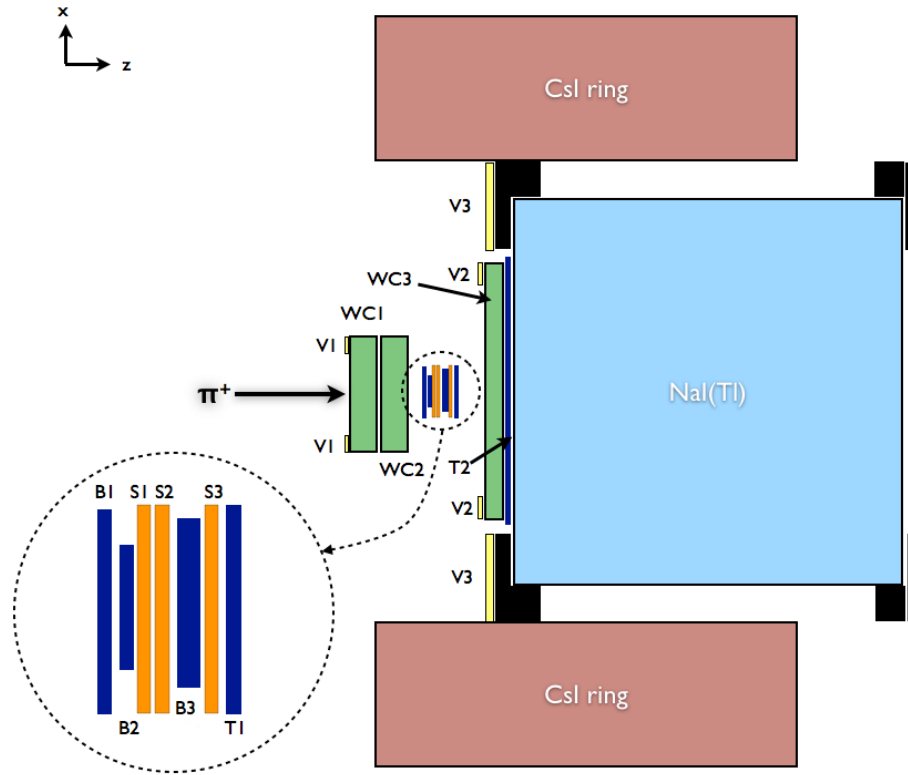


Figure 3.6: Schematic illustration of the PIENU detector. The target region is magnified in the insert.

The beamline extension ended with a steel wall for shielding the experiment from remaining γ and neutron backgrounds.

3.3 The PIENU Detector

The PIENU detector is sketched in Fig. 3.6, data about the single sub-detectors can be found in Tab. 3.1, and more in details in [128].

The detector consisted in two main assemblies conventionally called PIENU-1 and PIENU-2. PIENU-1 was mounted directly on the beam pipe af-

ter the steel wall and it was comprised by two 3-layer wire chambers (WC1, WC2) for pion beam tracking, two plastic scintillators (B1, B2), two double-sided silicon microstrip detectors (S1, S2) and the scintillator target (B3)³. After B3, there was another double-sided silicon microstrip detector (S3) and a scintillator for measuring the decay time of the positrons (T1). PIENU-2 was contained in a steel cylinder mounted on rails precisely aligned with the beamline. The detectors were a 3-layer wire chamber (WC3) and another scintillator (T2) covering the front face of a NaI(Tl) calorimeter (also called "BiNa"), which was surrounded by 97 pure CsI crystals. Veto scintillators were covering the beamline flange before the other detectors (V1), the wire chamber flange (V2) and the NaI(Tl) flange (V3).

3.3.1 Design Considerations

The detector design is driven by the technique employed also by previous experiment at TRIUMF and PSI: stopping pions in an active target and measure the time and energy spectra of positrons emerging from the it. The stopped pion technique allows the construction of a very compact experiment which is able to work with a high pion rate keeping the realization costs reasonable. An alternative technique is the decay-in-flight one which would require a more complex detector.

A relevant difference with respect of the previous TRIUMF experiment is the positioning of the calorimeter with respect to the beam. In the PIENU case, the calorimeter faces directly the beam and it is not placed on its side. The advantage is an increase of the acceptance by one order of magnitude with direct impact on the statistical error of the measurement.

The previous experiment was not able to cope with the beam background present with a calorimeter placed directly on the beam axis.

In PIENU the issue is not present, given the very low positron contamination in the beam (thanks to the new beamline) and faster electronics.

As mentioned in the previous section, the detector is divided into two sub-assemblies (PIENU-1 and PIENU-2). This design construction allows the easy removal of PIENU-1 and the possibility of measuring with

³For historical reasons and consistency with already published material, the notation for the scintillators (B1, B2, B3) is the same as the notation for the beamline dipole magnets but its use should be clear from the context.

CHAPTER 3. EXPERIMENTAL SETUP

Name	Z (mm)	Thickness (mm)	Shape	Dim. (mm)
Plastic Scintillators				
B1	-39.03	6.6	Square	100 x 100
B2	-30.02	3.07	Square	45 x 45
B3	0.00	8.05	Square	70 x 70
T1	19.92	3.04	Square	80 x 80
T2	72.18	6.6	Circular	171.45 diameter
Name	Z (mm)	Diameter	Wires per plane	Wire spacing (mm)
Wire Chambers				
WC1	-112.55	96.0	120	0.8
WC2	-74.41	96.0	120	0.8
WC3	55.86	230.4	96	2.4
Name	Z (mm)	Dim. (mm)	Chn. per plane	Strip pitch (mm)
Silicon Strips				
S1	-23.54	61 x 61	48	0.32
S2	-11.76	61 x 61	48	0.32
S3	10.50	61 x 61	48	0.32
Name	Z (front face, mm)	Thick. (mm)	Shape	Dim. (mm)
Crystal scintillators				
BINA		84	Cylinder	240 radius
CsI		-	Pentagon	90 x 80

Table 3.1: Characteristics of the PIENU detector. The z position is given with respect to the centre of the detector which was defined as the centre of the B3 scintillator. A more detailed data table can be found in [128].

PIENU-2 only. This last feature is relevant in the context of the low energy tail measurement. Removing most of the material in front of the calorimeter, this can be rotated with respect of the beam axis. This allows to measure the calorimeter response to positrons entering it at the various angles within the acceptance. Such measurement permits the reconstruction of the calorimeter response to positrons which comprehends also the low energy tail without any contamination from $\pi^+ \rightarrow \mu^+ \nu_\mu \rightarrow e^+ \nu_e \bar{\nu}_\mu$ decays. This is the most relevant aspect of the experimental design, since the knowledge of the low energy tail is the principal limitation to a pre-

cise measurement of the $\pi^+ \rightarrow e^+ \nu_e$ branching ratio.

In the following, the use of the various detectors listed in the previous section will be discussed.

- **Active Target B3:** The B3 scintillator is the stopping target for the pions. The amount of materials before it and the beamline momentum acceptance were adjusted for stopping pions in the middle of B3. The target is active in order to have a signal corresponding to the arrival of the pion. Another advantage of an active target is the possibility to identify pions and also detect the decay muons or positrons. This can be achieved recording the full digitized waveforms with high resolution: this is why B3 (and also the other scintillators) were digitized with 500 MHz sampling frequency. The ability of B3 to distinguish $\pi^+ \rightarrow e^+ \nu_e$ from $\pi^+ \rightarrow \mu^+ \nu_\mu \rightarrow e^+ \nu_e \bar{\nu}_\mu$ if the decay times of pions, muons, and positrons are not too close to each other, was also important in the study of the low-energy tail and in searches for massive neutrinos.
- **B1 and B2 scintillators:** Correlating the energy deposit in these two scintillators, pions could be identified before entering the target.
- **Wire Chambers 1 and 2:** The pion beam provided by the M13 beamline contained a halo of pions and decay products. In order to identify and reject these particles and isolate a centered pion beam spot on the target, WC1 and WC2 were used.
- **Silicon Detectors S1, S2, S3:** One of the irreducible backgrounds present in the previous TRIUMF experiment was the presence of pion decays in flight right before the target. These decay products could not be identified because they happened after the wire chambers and scintillators. PIENU was equipped with the silicon strip detectors S1 and S2 before the target for identify pion decays in flight. A third silicon detector S3 was placed after the target for precisely tracking the decay positrons.
- **T1 and T2 scintillators:** These two scintillators are placed after the target for providing the trigger signal from the decay positron following a valid pion stop trigger from B1, B2, and B3.

- **NaI(Tl) crystal:** This is the main detector for the measurement of the positron energy. NaI(Tl) was chosen for its sensitivity to photons (so that the radiative counterparts of the decays are directly measured) and for its high energy resolution. Energy resolution is critical for cleanly separating the $\pi^+ \rightarrow e^+ \nu_e$ decays from the $\pi^+ \rightarrow \mu^+ \nu_\mu \rightarrow e^+ \nu_e \bar{\nu}_\mu$ decays. The better the separation, the smaller will be the low-energy tail correction to be applied.
- **CsI crystal array:** The CsI calorimeter was added around the NaI(Tl) for containing the shower leakage, especially for positrons entering the NaI(Tl) at high angles. The choice of CsI was driven by the availability of a large number of crystals and although their energy resolution is not as high as for NaI(Tl), it was found by simulation to be adequate for the experiment. Shower leakage is the main cause for the presence of the low-energy tail and considering the energy measured by both the calorimeter systems permits a significant reduction of it. Strongly restricting the angular acceptance for positron tracks also reduces the low energy tail but statistics will be reduced too. The presence of the CsI calorimeter allows for a large acceptance while keeping the low energy tail small.
- **Wire Chamber 3:** A third wire chamber was installed before the calorimeter. Together with the silicon detector S3, it provides the tracking of the decay positrons and precisely defines the acceptance region.

In the following, each detector sub-system will be described in more details.

3.3.2 Plastic Scintillators

The plastic scintillators were made of Bicron BC-408 (polyvinyltoluene) scintillator⁴. B1 and B2 were placed after WC1 and WC2 covering their full aperture. B2 was smaller than B1 and B3 in order to ensure that particles impinged into the center of the target. T1 defined the positron timing with respect to the incoming pion time measured by B1. B3 and

⁴Light output: 10240 photons/MeV, attenuation 380 cm, decay time 2.1 ns, density 1.032 g/cm³ [129].

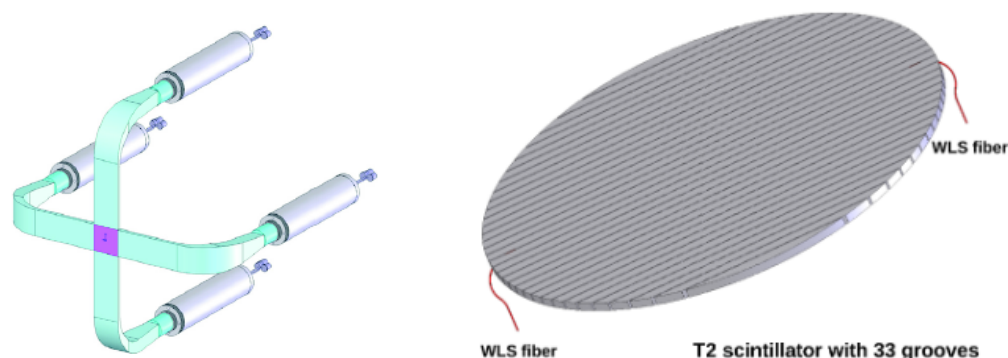


Figure 3.7: **(Left)** B1, B2, B3 and T1 plastic scintillators were read out with 4 PMTs (gray cylinders). Light was collected by four acrylic lightguides (light green). **(Right)** Readout scheme with wavelength-shifting fibers of the T2 plastic scintillator.

T1 were rotated with respect to B1 and B2 by an angle of 45° around the beam axis (given the space constraints). T2 was placed directly in front of the NaI(Tl) calorimeter. Due to limited space and its circular shape, T2 and the veto scintillators were read out by 1 mm diameter wave-length-shifting (WLS) fibers (Kuraray Y-11). Each scintillator, except the veto ones and T2, was read out by four PMTs through acrylic lightguides. The schematic configuration of the scintillator readouts is showed in Fig. 3.7.

3.3.3 Wire Chambers

The PIENU wire chambers were built at TRIUMF following the successful design [130] for the TWIST experiment [131]. The wire chambers (WC1, 2, 3) consisted of three wire planes rotated by an angle of 120° with respect to each other⁵. All the chambers were filled with a gas mixture of 80% tetrafluoromethane (CF_4) and 20% isobutane (C_4H_{10}) at atmospheric pressure. WC1 and WC2 (Fig. 3.8) had 120 wires for each of the three planes, read out by groups of three wires. The effective pitch was 2.4 mm and the total active diameter is 10.6 cm. WC3 (Fig. 3.9 (Left)) has an identical construction scheme, but it was larger, with 96 wires for each of the

⁵This configuration has the following property, useful for checking the correct working of the chambers: if the wires in a plane were progressively numbered, then at every "crossing point" of three wires, the sum of the wire numbers is a constant.

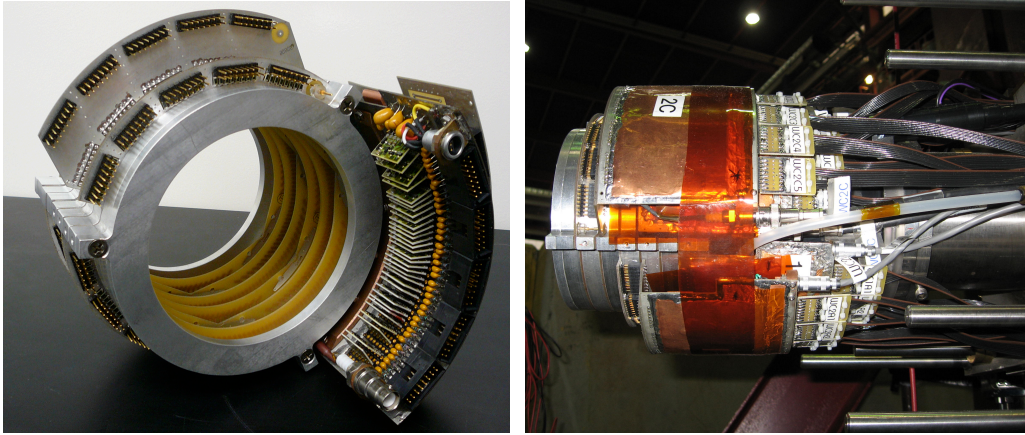


Figure 3.8: **(Left)** WC1/2 wire chamber plane and its preamplifier board. Each chamber consisted of three planes. **(Right)** W1/2 after installation on the beam pipe.

three planes, grouped and read out by two. The effective wire pitch was 4.8 mm for a total active diameter is 23.04 cm. Wire signals were fed to preamplifiers, discriminators, and time-to-digital converters (VT48 [132]). The efficiency of every plane was measured to be larger than 99% for beam positrons. WC1 and WC2 were used for tracking beam particles. WC3 was used to define the acceptance for decay positrons at the entrance of NaI(Tl). WC3 was mounted on the flange of the NaI(Tl) crystal enclosure.

3.3.4 Silicon Detectors

In the PIENU-1 setup, there were three silicon detectors (S1, S2 and S3). Each set consisted of two identical hybrids fixed back to back with a perpendicular orientation of the strips (along the X and Y coordinates. Z was the beam direction). S1 and S2 were placed immediately upstream of the target while S3 was placed immediately downstream of it to provide position information on the incoming pion and the outgoing positron, respectively. A picture of S1 and S2 with one silicon plane visible is showed in Fig. 3.9 (right)).

A plane of the silicon detector had an active volume of $61 \text{ mm} \times 61 \text{ mm} \times 285 \text{ }\mu\text{m}$. The silicon sensor was a single sided AC-coupled micro-strip

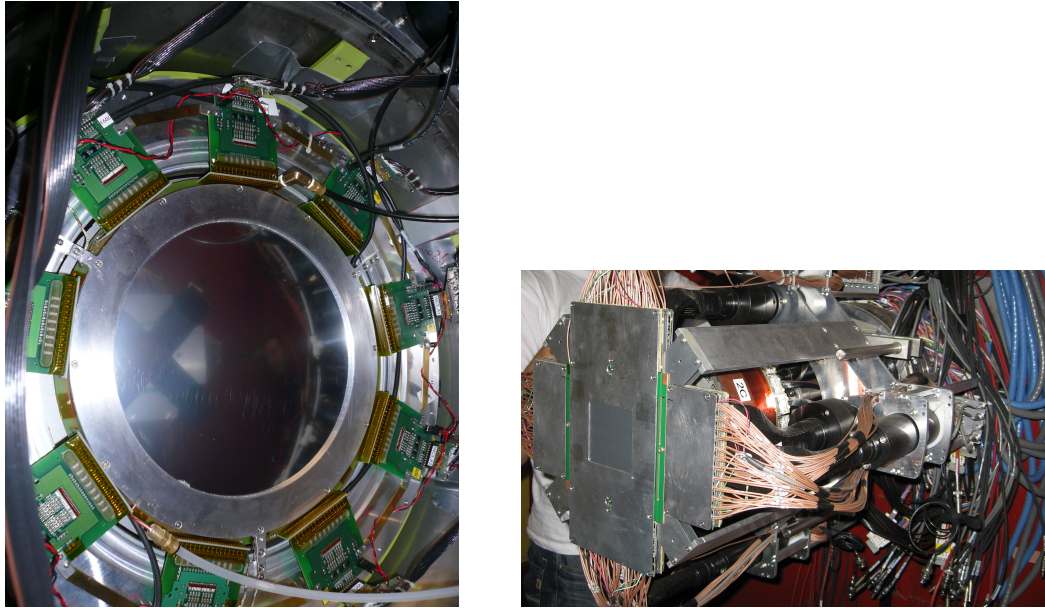


Figure 3.9: **(Left)** Picture of the wire chamber WC3 placed in front of the NaI(Tl) calorimeter. **(Right)** S1 and S2 assembly on their support structure.

detector of the same type as the ones used in the ATLAS central tracker [133].

In the original design, each strip had a pitch of $80 \mu\text{m}$. The required resolution for the PIENU experiment was of the order of $300 \mu\text{m}$, so the design has been modified binding four silicon strips to one read-out line. The readout channels were further reduced connecting the lines with capacitors and only one every fourth line was connected to an amplifier (Fig. 3.10).

A total of 48 channels per silicon plane were readout. The capacitive network formed a charge division line where the reconstruction of the amplitude and position was possible by properly weighting the channels that fire during an event (typically 2 or 3). In order to reduce the data size, a hardware threshold was set to suppress channels with no hits. The signals were read out by VF48 60 MHz ADCs [134].

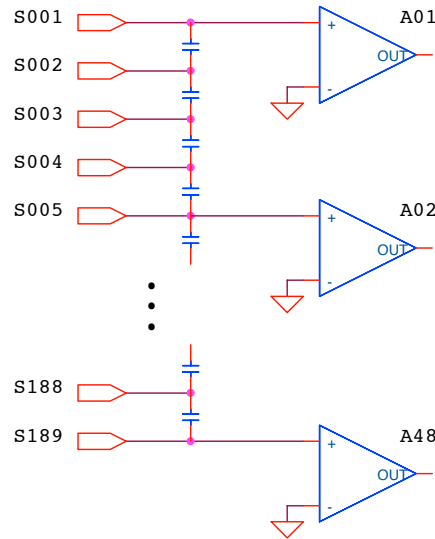


Figure 3.10: Schematic drawing of the silicon readout scheme. Four silicon strips were bonded together and these groups were further connected to a capacitor network. Every fourth group, the signal was fed to amplifiers. This readout scheme allowed the reduction of the number of channels to 48 per plane with a final resolution of about $300 \mu\text{m}$.

3.3.5 NaI(Tl) Crystal Calorimeter

The NaI(Tl) calorimeter was a single crystal of thallium-doped sodium iodide and it was the largest of this kind ever grown⁶. The crystal was enclosed in a 3 mm thick aluminum enclosure which had 19 circular quartz windows at the rear end (Fig.3.11 (left)). The aluminum front face was 0.5 mm thick for minimizing the amount of material crossed by the incoming particles. Each window was viewed by 3 inch diameter Hamamatsu R1911 PMTs (at the exception of the centre PMT which was of type R1911-07) which were surrounded by a μ -metal shield to reduce the impact of the cyclotron magnetic field. The bases of the phototubes were modified to allow the last two dynodes to have a fixed voltage (ca. $\times 0.21$

⁶The NaI(Tl) was on loan from the Brookhaven National Laboratory (Upton, NY, USA) where it was used by the LEGS collaboration [135, 136].



Figure 3.11: **(Left)** Back side of the NaI(Tl) crystal on the test bench. **(Right)** The NaI(Tl) crystal and the 97 pure CsI crystals while the calorimeter assembly was under construction in a low-humidity clean room at TRIUMF.

and $\times 0.37$ of the high voltage applied to the resistor chain) This modification was needed to improve the performance at high count rates in the BNL experiment. Two tubes were restored to their original configuration and no difference in the response was found at the typical count rates of the PIENU experiment. The surface of the crystal was covered with a reflective material. An optical simulation was performed with the software Detect2000 [137] and the results showed that light was uniformly reflected [138] independently from the scintillation centre. This was confirmed within 2% by bench tests using a ^{22}Na radioactive source [139].

3.3.6 CsI Crystal Calorimeter

The CsI calorimeter⁷ consisted of 97 pure CsI crystals 25 cm long (13.5 radiation length) with a pentagonal cross section and about 9 radiation lengths radially, arranged in two concentric layers around the NaI(Tl). A picture of the calorimeter assembly can be seen in Fig. 3.11 (right). Each of the two layers were divided in an upstream and downstream

⁷The crystals and PMTs were on loan from Brookhaven National Laboratory (Upton, NY, USA) and were previously used for the endcap photon-veto detector [140] in the E949 experiment [141].

part, making a total of 4 rings [142]. Each crystal was read out by a fine-meshed, 3 inch diameter Hamamatsu R5543 PMT [143] which was designed to operate in high magnetic fields. The magnetic field in the M13 area was at maximum 2 Gs at the location of the detector and it was within specifications of the PMTs.

Each crystal had a $\text{YAlO}_3:\text{Ce}^{245}\text{Am}$ light pulser attached to it [144] producing light pulses at 50 Hz with similar wavelength and pulse width as the CsI scintillation. These signals could be used to monitor the light output of the crystals and the PMT gain. Each crystal was connected via a quartz fiber to the output of a Xenon lamp pulser triggered at 2Hz during data taking [145]. The Xenon lamp flashes did not excite the CsI crystal and therefore were used only for monitoring the PMT gains. A comparison between the $\text{YAlO}_3:\text{Ce}^{245}\text{Am}$ and Xenon lamp data gave information on changes in the light collection efficiency of the crystals.

The Xenon lamp sent light to the crystals and also at seven reference PMTs of the same type as the ones used in the calorimeter. The reference PMTs were enclosed in an incubator maintained at a constant temperature of 24.0°C. The Xenon-lamp itself was located in an identical incubator. These PMTs gave reference measurements for correcting from light-output changes of the lamp (Fig. 3.12). The CsI crystals were constantly flushed by Nitrogen gas to maintain low humidity levels, since pure CsI is slightly hygroscopic.

3.3.7 Tracking

The PIENU tracking system consisted of three subsystems ("trackers"): the beam wire chambers WC1/2 (Trk1), the first two silicon detectors (Trk2), and S3 with WC3 (Trk3). Trk1 provided 6 position informations (6 wires), Trk2 four (2 x-y points) while Trk3 five (one x-y point and 3 wires).

Track Definition

Without magnetic fields, tracks are straight lines parameterized as:

$$\begin{cases} x = x_0 + v_x \cdot t \\ y = y_0 + v_y \cdot t \\ z = z_0 + v_z \cdot t \end{cases} \quad (3.1)$$

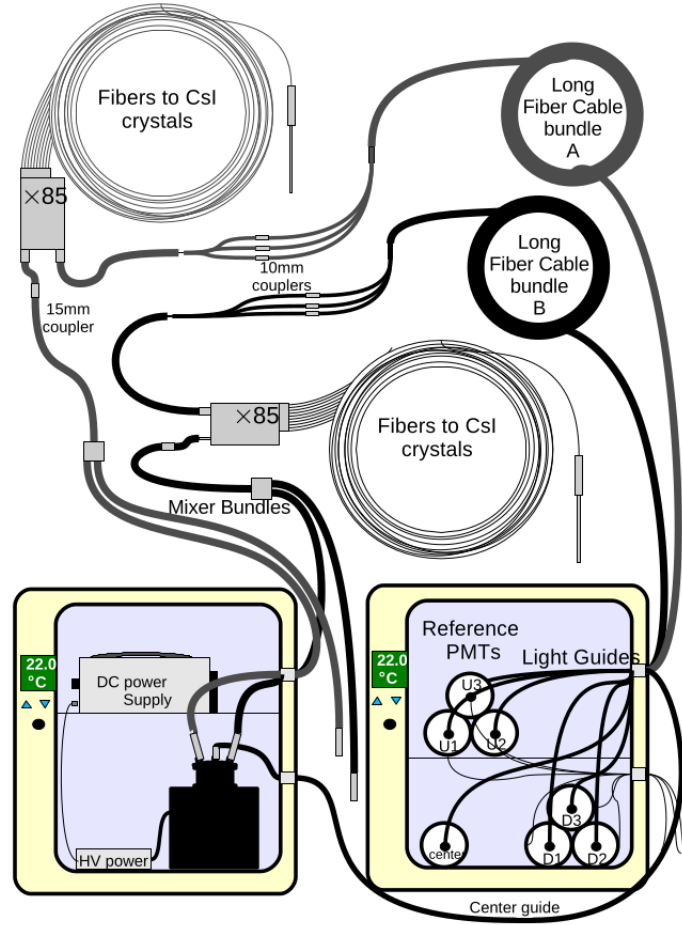


Figure 3.12: Schematic view of the xenon lamp monitoring system for the CsI calorimeter (from [145]).

The number of parameters is 6, however only 4 are independent. We can choose $z_0 = 0$ and set a normalization for the vector $v = (v_x, v_y, v_z)$ choosing $v_z = 1$:

$$v = \left(t_x = \frac{v_x}{v_z}, t_y = \frac{v_y}{v_z}, 1 \right) . \quad (3.2)$$

With these choices, and $z = t$ we get the new parameterization:

$$\begin{cases} x = x_0 + t_x \cdot z \\ y = y_0 + t_y \cdot z \end{cases} . \quad (3.3)$$

The parameterization choice is convenient, since the particles are mainly going in one direction, which we choose to be the beam direction z , and the parameters x_0 and y_0 identify the point where the track intersect the plane defined by $z = 0$ (the center of the target). A drawback of the chosen parameterization is that it is not able to describe lines parallel to the xy plane, but this situation is not relevant in the present case.

Track Fitting

The measurement of one hit in a tracking detector plane corresponds ideally to one wire chamber wire or to a silicon detector channel, for which the position is known. In reality, more wires and/or strips can be active and the tracking software used only "hits" which were consistent with the correct trigger timings. Let us consider now a coordinate system (u, v) in a tracker's plane (z is fixed) where the axis u is orthogonal to the wires/strips. In this way, the coordinate u is proportional to the wire/strip number. With a rotation, it is possible to transform the (u, v) system to the (x, y) system of the experimental hall:

$$u_i = x \cos \theta_i - y \sin \theta_i = (x_0 + v_x z_i) \cos \theta_i - (y_0 + v_y z_i) \sin \theta_i \quad , \quad (3.4)$$

where the index i identifies the plane and θ_i the angle of rotation of the specific plane with respect to the y axis. For example, in the PIENU WC1 and WC2 wire chambers, the planes are six, so $i = 0..5$ and $\theta_i = n_i \pi / 3$ (with n_i the right integer factor for each plane). It is useful to introduce a vector representation for the rotated tracks, defining the parameters vector

$$p = (x_0, y_0, v_x, v_y) \quad , \quad (3.5)$$

and the matrix of rotation vectors:

$$C_i = \begin{pmatrix} \cos \theta_i & -\sin \theta_i \\ \cos \theta_i z_i & -\sin \theta_i z_i \end{pmatrix} \quad . \quad (3.6)$$

In this way we have (repeated indices are summed):

$$u_i = C_{ij} p_j \quad . \quad (3.7)$$

From the last expression, it is possible to construct the χ^2 function, which is the squared deviation of the tracks from the measurements, weighted

with the errors in each measurement ω_i :

$$\chi^2 = \frac{1}{2} \sum_{i=0}^5 \omega_i (u_i - C_{ij}p_j)^2 \quad . \quad (3.8)$$

The χ^2 can be minimized analytically:

$$\frac{\partial \chi^2}{\partial p_i} = -\omega_i (u_i - C_{ij}p_j) C_{ij} = 0 \quad . \quad (3.9)$$

Solving the last equation for p_i and introducing

$$M_{jk} = \omega_i C_{ij} C_{ik} = (\omega C^T C)_{jk} \quad , \quad (3.10)$$

which is a 4x4 symmetric matrix, and

$$V_j = \omega_i u_i C_{ij} \quad , \quad (3.11)$$

we get the closed form solution

$$p = M^{-1} V \quad . \quad (3.12)$$

The full error correlation matrix is given by

$$\sigma_{ij}^2 = M_{ij}^{-1} \quad . \quad (3.13)$$

Tracking Quantities

Tracking was relevant in the PIENU experiment mainly for two reasons:

- Trk3 was used for tracking decay positrons entering the calorimeter and thus it defines the acceptance radius. This information was important in connection to the estimation of the low energy tail and the acceptance correction to the branching ratio.
- One tool for estimating the low energy tail was the "suppressed spectrum", which was the decay positron energy spectrum with tight cuts applied in order to suppress the $\pi^+ \rightarrow \mu^+ \nu_\mu \rightarrow e^+ \nu_e \bar{\nu}_\mu$ component. Part of these decays were due to pions decaying in flight or muon leakage from the target. To suppress pion decays in

flight, Trk1 and Trk2 can be used for detecting pion decays before the target. Further suppression and removal of pion/muon leakage events can be achieved matching the tracks from Trk1 and Trk2 with the positron tracks from Trk3 and checking if the decay vertex laid within the target. $\pi^+ \rightarrow \mu^+ \nu_\mu \rightarrow e^+ \nu_e \bar{\nu}_\mu$ events had also a broader vertex distribution with respect to $\pi^+ \rightarrow e^+ \nu_e$ events, given the presence of the muon.

For defining the acceptance and suppress the $\pi^+ \rightarrow \mu^+ \nu_\mu \rightarrow e^+ \nu_e \bar{\nu}_\mu$ background in the suppressed spectrum, the following variables were constructed:

- **Acceptance Radius:**

$$R = \sqrt{(t_x z_{WC3} + x_0)^2 + (t_y z_{WC3} + y_0)^2} \quad , \quad (3.14)$$

where Z_{WC3} was the location of the center of WC3 along the beam direction z .

- **Kink Variable:**

$$KV = \arccos \frac{t_{xA} t_{xB} + t_{yA} t_{yB} + 1}{\sqrt{(t_{xA}^2 + t_{yA}^2 + 1) \cdot (t_{xB}^2 + t_{yB}^2 + 1)}} \quad , \quad (3.15)$$

where the track A was reconstructed by Trk1, while the track B was reconstructed by Trk2.

- **Z-vertex:**

$$Z_V = - \frac{(x_{0A} - x_{0B}) \cdot (t_{xA} - t_{xB}) + (y_{0A} - y_{0B}) \cdot (t_{yA} - t_{yB})}{(t_{xA} - t_{xB})^2 + (t_{yA} - t_{yB})^2} \quad , \quad (3.16)$$

where track A was reconstructed by Trk2 and track B by Trk3 (see App. D for the derivation of this formula).

Track Topologies

Being pions and muons unstable particles, both or one of them can decay before stopping in the target. Depending on which particles decay, there were different relevant track topologies:

1. πev : The pion stops in the target and decays as $\pi^+ \rightarrow e^+ \nu_e$.
2. $\pi\text{DAR}-\mu\text{DAR}$: Both the pion and the muon in the $\pi^+ \rightarrow \mu^+ \nu_\mu \rightarrow e^+ \nu_e \bar{\nu}_\mu$ channel decay at rest in the target.
3. $\pi\text{DAR}-\mu\text{DIF}$: In $\pi^+ \rightarrow \mu^+ \nu_\mu \rightarrow e^+ \nu_e \bar{\nu}_\mu$, the muon decays in flight in the target. This particular case cannot be detected and eventually requires a correction to the branching ratio, since the timing of this event resembles $\pi^+ \rightarrow e^+ \nu_e$.
4. $\pi\text{DIF}-\mu\text{DAR}$: The pion decays in flight before stopping in the target. Part of these decays can be detected with tracking through the kink variable KV.
5. $\pi\text{DIF}-\mu\text{DIF}$: Both the pion and the muon decay in flight: the probability of this case is negligible.

The probability of decays in flight with respect to the decays at rest were about 6% for pion decays in flight before the target, 6% for pions decaying in flight in the target and 0.002% for muon decays in flight in the target.

3.3.8 Trigger

The PIENU trigger system was built largely using NIM modules. The trigger logic implemented different selection criteria for detector calibration and physics data collection.

The identification of an incoming pion was based on a B1·B2·B3 coincidence, together with a high threshold on B1 for excluding muons and positrons. A small amount of positrons and muons were selected by the trigger logic using specific energy thresholds for the calibration of the scintillators (with positrons and muons) and the NaI(Tl) calorimeter (with positrons).

A coincidence among T1 and T2 scintillators defined the decay-positron signal. The basic trigger condition for accepting a valid decay was a coincidence between a valid incoming pion and a decay-positron within a time window of -300 to 500 ns. The prompt time $t_0 = 0$ was defined by the pion signal. Since the $\pi^+ \rightarrow \mu^+ \nu_\mu \rightarrow e^+ \nu_e \bar{\nu}_\mu$ decay happened $\sim 10^4$ more often than the $\pi^+ \rightarrow e^+ \nu_e$ decay, special trigger conditions were defined for enriching the data sample of $\pi^+ \rightarrow e^+ \nu_e$ events.

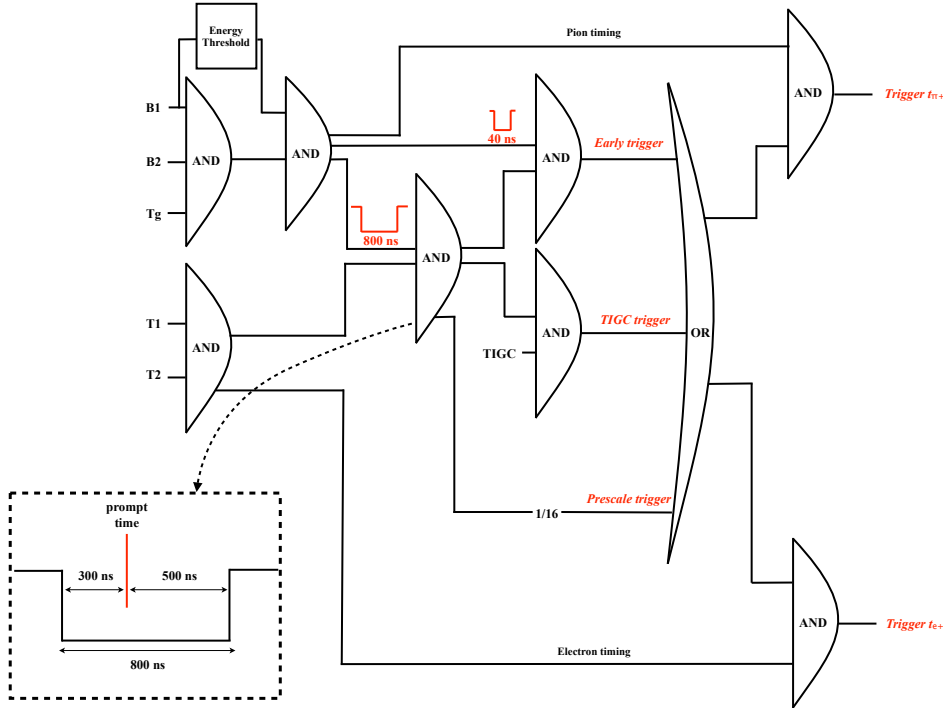


Figure 3.13: Simplified scheme of the PIENU trigger system. The complete diagram is showed in App. B (from C. Malbrunot [146]).

Physics Triggers

The *physics triggers* collecting data for the branching ratio analysis were

1. **Prescale Trigger:** This is an unbiased trigger which recorded all the events with valid pion and positron signals within the -300 to 500 ns time window. These events were mainly $\pi^+ \rightarrow \mu^+ \nu_\mu \rightarrow e^+ \nu_e \bar{\nu}_\mu$ events and were prescaled by a factor 16.
2. **Early Trigger:** This trigger condition selects events in the 4 – 40 ns time window. Since the pion decays in ~ 26 ns, this trigger was biased towards $\pi^+ \rightarrow e^+ \nu_e$ events.
3. **TIGC Trigger:** Another feature of the $\pi^+ \rightarrow e^+ \nu_e$ decay besides the faster timing with respect to $\pi^+ \rightarrow \mu^+ \nu_\mu \rightarrow e^+ \nu_e \bar{\nu}_\mu$ was a larger

energy deposit in the calorimeters. TIGC was a special VME module (see Sec. 3.3.9) which summed the energies of the NaI(Tl) and CsI calorimeters for each event. A trigger based on the TIGC summed energy selected events exceeding a threshold typically set below the Michel edge.

The Early and TIGC triggers recorded mainly all the $\pi^+ \rightarrow e^+ \nu_e$ events without prescaling.

A simplified diagram of the trigger logic is shown in Fig. 3.13.

Calibration Triggers

The triggers devoted to the calibration of the detectors were

- **Cosmics trigger:** Muons from cosmic rays were minimum ionizing particles selected by requiring a high energy deposit in the CsI outer layer or the coincidence of inner and outer layers. A prescaling factor of 16 was applied to reduce the rate of this trigger. These events were used for the calibration of the CsI calorimeter, since it was the only detector not directly exposed to the beam. This trigger provided an energy calibration for the crystals as well as the monitoring of the crystal+PMT gain.
- **Xe-lamp trigger:** A Xenon lamp provided light to all the CsI crystals at a frequency of 2 Hz. This trigger was used to monitor PMT gain variations.
- **Beam positron trigger :** Beam positrons were accepted by this trigger with pre-scaling by a factor of 32. This trigger was used for plastics scintillators and NaI(Tl) calibration.

During a normal run, all of these 6 triggers were turned on and more of them could be fulfilled at the same time. Typical rates of the triggers are shown in Table 3.2. The total trigger rate was about 600 Hz.

3.3.9 Data Acquisition

The PIENU data acquisition system was comprised by a combination of NIM and VME modules integrated in three racks which were placed in a

Trigger	Rate (Hz)
<i>Physics Triggers</i>	
Early trigger	160
TIGC trigger	170
Prescale trigger	240
<i>Calibration Triggers</i>	
Cosmics trigger	15
Beam Positron trigger	5
Xe lamp trigger	2
Total Trigger	600

Table 3.2: Typical rates of each trigger in normal datataking conditions.

temperature-controlled enclosure. In the following, a brief description of the main VME modules is given.

COPPER

All the plastic scintillators' PMTs were readout by a 500 MHz flash-ADC waveform digitizer. This system was based on the COPPER (COMmon Pipelined Platform for Electronics Readout) platform [148] originally developed by KEK for the Belle experiment, consisting in a 9U-size VME board. The detailed characteristics of the COPPER system can be found in [149]. One COPPER board had four frontend modules called "FINESSE" (see Fig. 3.14). Each FINESSE can receive two analog input signals, therefore, each COPPER board can digitize a maximum of 8 channels. On each FINESSE card, two 250-MHz flash-ADCs were operated on alternating phases for realizing the final 500-MHz sampling. The gain of the two flash-ADCs were monitored and corrected on a run-by-run basis using beam particle signals. An important feature of COPPER was the possibility to perform data-processing on-board. Each board had an embedded CPU running Linux and data-suppression was realized by the software running on it. The COPPER system was completed by a 250 MHz clock distribution module and a GPIO module (General Purpose Input Output) developed by KEK for providing gate, reset and busy signals to the

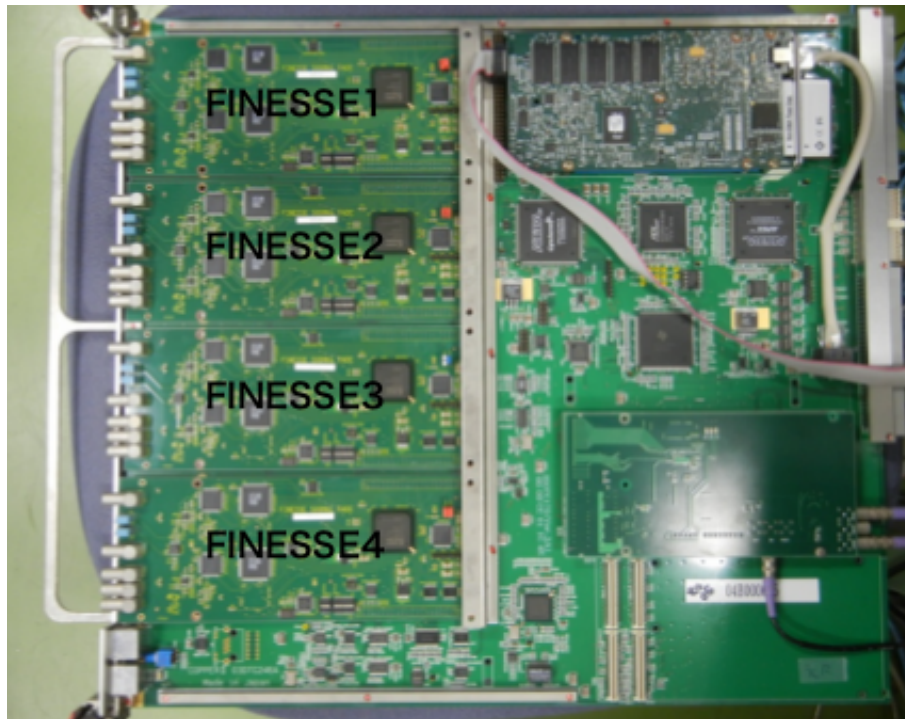


Figure 3.14: Picture of a COPPER board with in the four FINESSE front-end cards [147].

boards. In Fig. 3.15 a typical digitized waveform from a PMT obtained with COPPER is showed, together with a fit to the sampled points.

The PIENU experiment was initially equipped with 4 COPPER boards digitizing the signals from the 23 PMTs reading out the plastic scintillators. The analog sums of the NaI(Tl) calorimeter PMTs, of the four T1 PMTs, and of the inner and outer CsI rings were also digitized. In a later phase (2012 datataking run), a fifth COPPER board was added to the setup in order to digitize groups of CsI crystals and the central PMT of the NaI(Tl) calorimeter.

VF48

The VF48 was a 60 MHz flash-ADC, 6U-size VME module which was designed at the University of Montreal in 2004 [150]. It had a resolu-

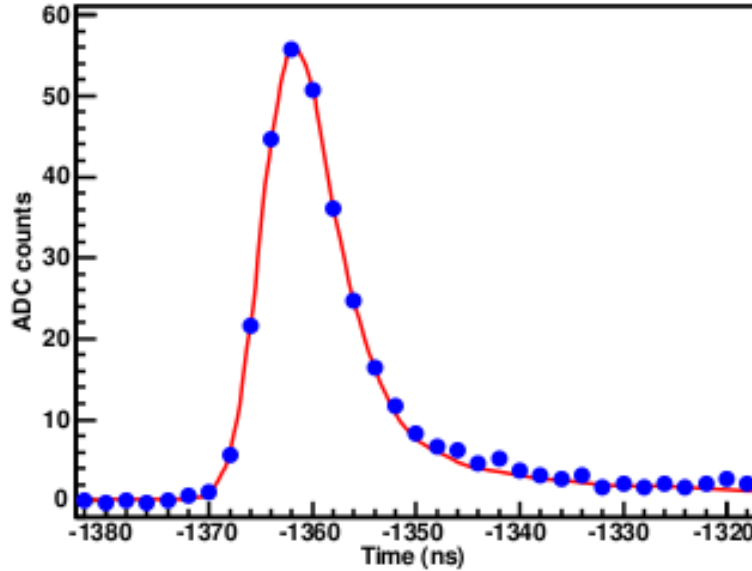


Figure 3.15: COPPER data samples fitted by a waveform template.

tion of 10 bits and a dynamic range of ± 250 mV. All the NaI(Tl) and CsI PMT signals as well as all the silicon detectors channels were read out by VF48 modules. A total of 404 channels (NaI: 19, CsI: 97, Silicon: 288) were readout by 10 VF48 modules. All VF48 modules received a 20-MHz clock signal provided by the TIGC module. This clock was multiplied internally to reach 60-MHz. Due to the large number of channels, zero-suppression was implemented with the following logic: only if two consecutive samples had a pulse height difference higher than a given threshold, the full waveform was recorded. With the exception of the NaI(Tl) signals which were always recorded, all the other channels implemented the zero-suppression logic. Since the NaI(Tl) signal was relatively slow ($\sim 1\mu\text{s}$), the sampling frequency was reduced to 30 MHz for this detector.

TIGC

The Tigress Collector (TIGC) is a VME module built and developed by the University of Montreal and TRIUMF for the TIGRESS experiment

[151]. This module allowed on-the-fly summing of VF48 signals before the read-out. Every 250 ns, the highest sample of each waveform of all CsI and BINA channels was sent to TIGC which then summed them and compared the result to a predefined threshold. Before the sum, a multiplicative factor was applied to take into account different gains of the detectors. This threshold was set to be about 2 MeV below the Michel edge. If the threshold was passed, TIGC issued a signal which, if in coincidence with a valid pion/positron-decay signal, will trigger the read-out. TIGC also provided the synchronized clock to all the VF48 modules.

VT48

The Wire Chambers's wires and all the signals issued by the PMTs after discrimination and some trigger logic signals were readout by the VT48 multi-hit TDC modules. The VT48 was a single width VME 6U-size module [152] designed at TRIUMF in 2006 for the KOPIO experiment [153]. In this module, the AMT3 chip [154] was employed: it was originally developed for reading out ATLAS muon detector's channels. An on-board 25-MHz clock was multiplied to achieve 0.625 ns resolution. All VT48s were also fed with an external 25-MHz clock to synchronize all the modules. One board can readout 48 channels for up to 20 μ s. To optimize the dead-time only one channel was read out with the full time window while the other channels were read out with a 8.0 μ s window before the trigger signal.

Data Acquisition, Slow Control and Software

The PIENU data acquisition system consisted of 3 VME crates (two for the VF48 and VT48 modules, one mostly for slow control modules and modules for COPPER) controlled by VME master modules and 4 COPPER boards with a CPU each. Each CPU ran the associated frontend programs to transfer data to a host computer.

Data collection was realized by the MIDAS data acquisition system [155] which incorporated an integrated slow control system with an on-line database and a history system. The main MIDAS server computer was controlled with a web interface. The web page displayed the overall status of the data acquisition system: trigger rates, error messages from the boards and information from the online data-quality system (Fig. 3.16).

CHAPTER 3. EXPERIMENTAL SETUP

MIDAS experiment "pienu"		Fri Dec 14 14:19:11 2012 Refr:60			
<input type="button" value="Stop"/> <input type="button" value="Pause"/> <input type="button" value="ODB"/> <input type="button" value="CNAF"/> <input type="button" value="Messages"/> <input type="button" value="ELog"/> <input type="button" value="Alarms"/> <input type="button" value="Programs"/> <input type="button" value="History"/> <input type="button" value="Config"/> <input type="button" value="Help"/>					
monitor					
VME0_settings VME1_settings B1_Setpt B2_Setpt B3_Setpt Shifts Cameras Histos Operators Runlog HV_PIENU HVBertan					
Run #82584	Running	Alarms: On	Restart: Yes	Data dir: /home/pienu/online/data	
Start: Fri Dec 14 14:03:40 2012			Running time: 0h15m31s		
Equipment	FE Node	Events	Event rate[/s]	Data rate[MB/s]	Analyzed
Vme0	feVme0@lxpienu01.triumf.ca	86890	105.8	0.467	N/A
Vme1	feVme1@lxpienu02.triumf.ca	87085	107.3	0.576	N/A
Copper1	feCopper01@copper1	86908	107.7	0.071	N/A
Copper2	feCopper02@copper2	86849	107.7	0.038	N/A
Copper3	feCopper03@copper3	87085	108.3	0.055	N/A
Copper4	feCopper04@copper4	87018	103.5	0.025	N/A
Copper5	feCopper05@copper5	86864	107.7	3.202	N/A
EB	Ebuilder@pienu01.triumf.ca	87018	88.4	3.675	N/A
PostAmp	PostAmp@pienu01.triumf.ca	0	0.0	0.000	N/A
u_Beam	fe3hp@pienu01.triumf.ca	0	0.0	0.000	N/A
NMR	fenmr@pienu01.triumf.ca	0	0.0	0.000	N/A
Epics	feepics@pienu01.triumf.ca	0	0.0	0.000	N/A
M13DVM	fem13dvm@pienu01.triumf.ca	0	0.0	0.000	N/A
GASDVM	fegasdvm@pienu01.triumf.ca	0	0.0	0.000	N/A
ScalerN	feScalerN@lxpienu03.triumf.ca	0	0.0	0.000	N/A
LRS1440	FeLrs1440@pienu03.triumf.ca	0	0.0	0.000	N/A
RunLog	feRunLog@pienu01.triumf.ca	0	0.0	0.000	N/A
QOD	feqod@pienu02.triumf.ca	0	0.0	0.000	N/A
Temperature	FeTemperature@pienu01.triumf.ca	90	0.0	0.000	N/A
scbertan	scbertan@lxpienu03.triumf.ca	0	0.0	0.000	N/A
Channel	Events	MB written	Compression	GB total	
#0: run82584.mid.gz	86976	1170.957	67.7%	116315.892	
Lazy Label	Progress	File Name	# Files	Total	
Dcache	0 %	run82581.mid.gz	20206	0.0 %	

Figure 3.16: Web interface of MIDAS. The green boxes show the different front-end programs and the name of the device on which they were running. The corresponding collected events and rates are showed on the right. MIDAS integrated also an E-log and a history system.

The offline data processing was performed using a software called `proot`, which was based on the `R00T` [156] libraries. `proot` converted MIDAS files to `R00T` format files while applying the calibration procedures and a preliminary data analysis for the calculation of high-level variables. The final data analysis was done with a software package called `Clark`

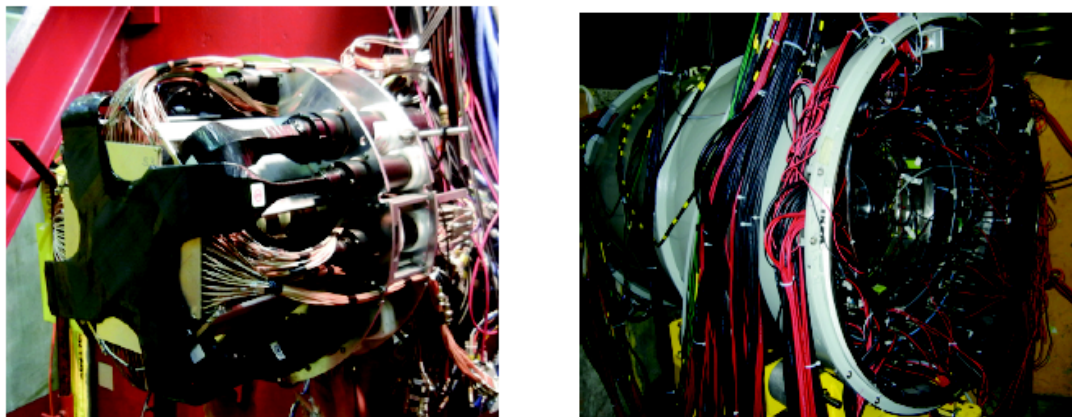


Figure 3.17: **(Left)** PIENU-1 and **(Right)** PIENU-2 detector assemblies. PIENU-1 was comprised of the beam wire chambers WC1/2, the B1, B2, B3, T1 scintillators, and the silicon microstrip detectors S1 and S2. The PIENU-2 assembly contained the NaI(Tl) and CsI calorimeters, the T2 scintillator, and the WC3 wire chamber.

which was also based on ROOT and was developed in its original version by A. Hillaret for the TWIST experiment.

The data analysis and MC simulations were done on computing resources provided by the Westgrid consortium⁸ which was a regional partner of ComputeCanada⁹.

3.3.10 Final Detector Assembly

The final detector assembly is showed in Fig. 3.17 and 3.18. Following the 2009 datataking, it was noticed that temperature variations in the experimental hall resulted in high gain variations in the PMTs. In order to keep the gain variations within acceptable limits, a temperature-controlled enclosure housing the detector was constructed. The temperature was maintained at 20°C within $\pm 0.5^\circ\text{C}$. PIENU-2 was mounted on a supporting structure on wheels which were guided by rails to ensure a correct alignment with respect to PIENU-1 and the beamline. The rails could be taken

⁸<https://www.westgrid.ca/>

⁹<https://www.computecanada.ca/>

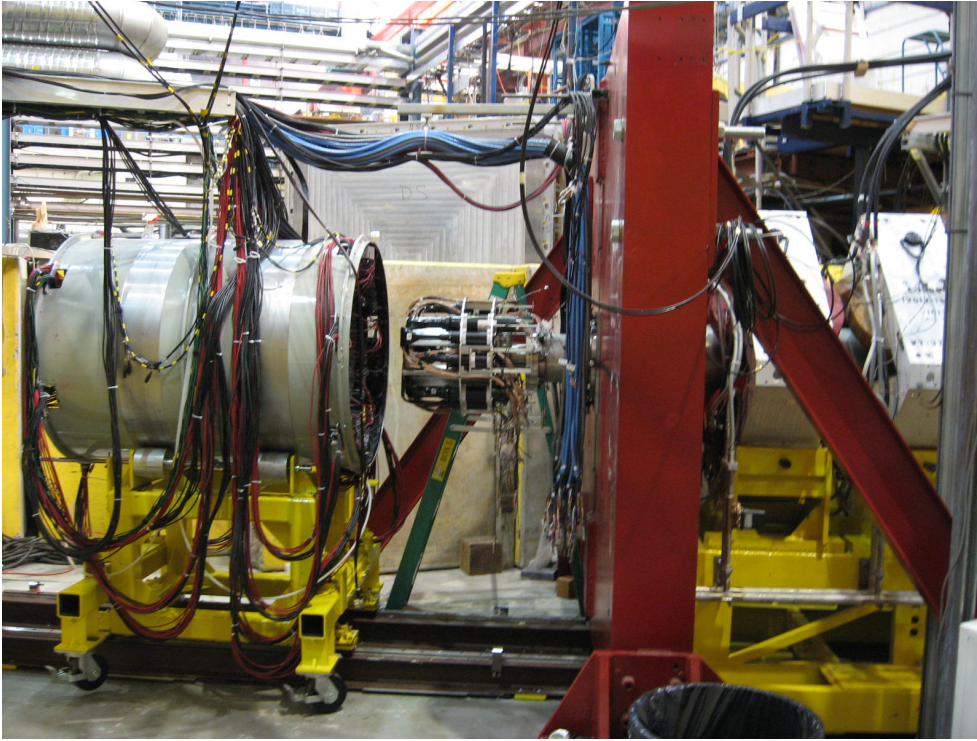


Figure 3.18: The PIENU detector and beamline after the last bending magnet, showing the steel wall used for radiation shielding.

away for removing the PIENU-1 assembly and rotate PIENU-2 with respect to the beam axis. This flexible system allowed the investigation of the calorimeter response to a positron beam at different entrance angles. This information was crucial for the determination of the $\pi^+ \rightarrow e^+ \nu_e$ low energy tail. A detailed detector setup description can be found in [128].

3.4 Datataking History

In the following, the relevant datataking periods of the PIENU experiment are briefly described, and a summary is presented in Tab. 3.3. Every data run was taken in about 10 min and consisted in a MIDAS file of about 1.8 GB size. MIDAS format files were then processed with the PIENU analysis framework producing ROOT [156] trees of about 250 MB

Year	Runs used	Special runs
2009	0	One week positron beam data
2010	2400	Eight hours per week muon beam data
2011	3600	One month positron beam data
2012	13000	One week beamline tests

Table 3.3: Datataking periods with the special runs taken for calibration and detector studies.

size. The number of events in one file was $\sim 3 \times 10^5$.

3.4.1 2009 Run

This was the first stable run where physics data were collected. The TIGC module was not available at that time so a discriminator was used to determine the pulse height of the sum of the NaI(Tl) and CsI PMTs. The output signal was an analog sum without gain correction, so the threshold of the trigger was not stable, leading to a potential loss of $\pi^+ \rightarrow e^+ \nu_e$ events. In this run, an automatic energy calibration procedure for the CsI array was still not in place and the trigger for recording cosmic rays did not exist.

3.4.2 2010 Run

The final trigger configuration was available in 2010. The high-quality data taken in November led to the PhD thesis of C. Malbrunot [146] and to the first publication of an improved value of the branching ratio [100]. The branching ratio uncertainty was 0.24% with an about equal contribution from statistical and systematic uncertainties. With only one month of data, it was achieved a factor of two improvement over the old measurements, proving the validity of the new detector concept.

3.4.3 2011 Run

The cyclotron was unavailable until September due to a failure in the vacuum system. In September and part of October, data were taken to measure the response function of the NaI(Tl) and CsI crystals. Physics

data were taken in stable conditions until the end of the year. Preliminary results of the analysis of the 2011 dataset were published in the PhD thesis of S. Ito [147].

3.4.4 2012 Run

The largest data set was recorded in 2012. At the start of this run, the energy threshold of the TIGC trigger was lowered, to ensure that no $\pi^+ \rightarrow e^+\nu_e$ decays were being missed. This resulted in more $\pi^+ \rightarrow \mu^+\nu_\mu \rightarrow e^+\nu_e\bar{\nu}_\mu$ events causing TIGC triggers. Since these events were not used in the analysis, the number of events per run was about 1.5 times lower by in 2012 compared with 2010 and 2011. Preliminary results of the analysis of the 2012 dataset were published in the PhD thesis of T. Sullivan [157].

3.5 Summary

The PIENU detector was designed for maximizing the data collection and for achieving a reduction of the systematic error with respect to the previous experiment.

The statistics goal was achieved placing the detector directly along the beam direction to maximize the acceptance. This choice posed a challenge to the reduction of the beam backgrounds, which was solved extending the existing M13 secondary beamline and achieving a $<1\%$ positron contamination. This has been possible installing a collimator and operating the beamline as an energy-loss magnetic spectrometer. The third magnet cleaned the beam from the electromagnetic radiation coming from the collimator.

The systematic goal was achieved foreseeing the possibility to rotate the detector with respect to the beam. This allowed a careful characterization of the calorimeter response and the accurate knowledge of the $\pi^+ \rightarrow e^+\nu_e$ low energy tail.

Chapter 4 | Data Analysis

Analyzing the data involved the development of calibration procedures, the identification of suitable cuts for rejecting backgrounds and isolating good events. In this chapter, these procedures are described, together with an algorithm for *blinding* the data. The main analysis strategy is based on obtaining the positron energy spectrum and dividing it in low energy (LES) and a high-energy (HES) spectra. The extraction of the branching ratio is done fitting simultaneously the time spectra corresponding to LES and HES.

4.1 Blind Analysis Technique

It is common in nowadays precision experiments to introduce *blind analysis* techniques in order to remove, or at least reduce, human bias while analyzing the data. Blinding a dataset means for example hiding part of the data containing the signal from the analyzer. Other techniques consist in presenting an altered result to the analyzer (the case of the PIENU experiment) or introducing false signals into the data (like in gravitational wave searches [158] or dark matter searches, with the so-called *salting* technique [159]). In the case of the PIENU experiment, the result of the data analysis is a branching ratio. In order to "blind" it, a procedure was developed for artificially change the value of the branching ratio: this can be done randomly removing either $\pi^+ \rightarrow e^+\nu_e$ or $\pi^+ \rightarrow \mu^+\nu_\mu \rightarrow e^+\nu_e\bar{\nu}_\mu$ events. In practice, this was achieved using the total energy deposit measured in the target: in this way the positron spectrum in the calorimeter will not be distorted and nothing will be noticeable to the analyzer. The two pion decay modes deposited different amounts of energy in the target, since in the $\pi^+ \rightarrow \mu^+\nu_\mu \rightarrow e^+\nu_e\bar{\nu}_\mu$ case also the muon contributes. By

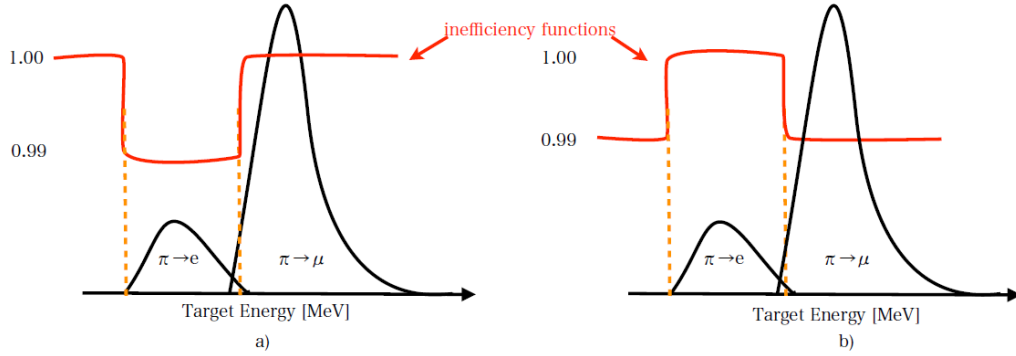


Figure 4.1: Blind analysis technique. On a random basis, events are removed from one of the two regions of the target energy spectrum corresponding to either $\pi^+ \rightarrow e^+ \nu_e$ or $\pi^+ \rightarrow \mu^+ \nu_\mu \rightarrow e^+ \nu_e \bar{\nu}_\mu$ events.

applying the inefficiency function sketched in Fig. 4.1, events from one of the two energy regions in the target can be randomly discarded. Concretely, the procedure works as follows:

1. An algorithm generates randomly the amplitude parameters of the function

$$f(E) = A \pm B \cdot [b \cdot \text{erf}((E - a)) + d \cdot \text{erf}((-E + c))] \quad , \quad (4.1)$$

where erf is the error function $\text{erf}(x) = (2/\sqrt{\pi}) \int_0^x e^{-t^2} dt$, and E is the total energy deposited in B1, B2, S1, S2, and the target B3.

2. The randomly chosen parameters were stored in a file which was not accessible to the analyzers.
3. When the data were analyzed, on an event-by-event basis the decision to discard an event (or not) was taken using the hidden function as a probability distribution.
4. The function parameters were generated for biasing the branching ratio to a maximum of 1%.

4.2 Calibration Procedures

4.2.1 Scintillators

The plastic scintillators were read out by the COPPER waveform digitizers which employed two 250 MHz ADCs in counterphase realizing an effective 500 MHz sampling frequency. The gain of the two ADCs had to be calibrated for a correct sampling procedure. The gain correction factor calculation was based on the height of a pulse corresponding to a real signal. For each ADC channel, the pedestal was assumed as the mean of the distribution of the first three samples of the waveforms calculated over an entire run. This procedure was insensitive to pileup, as instead it would be a pedestal calculated on an event-by-event basis. The pedestal was subtracted from the waveforms before the extraction of charge and pulse-height variables. For all the plastic scintillators and the NaI(Tl) crystal, beam particles were used for gain calibration. Beam positrons (for the NaI(Tl)), beam pions (for B1 and B2) and beam muons (for the target B3 and T1) energy distributions were considered on a run-by-run basis to automatically correct for gain fluctuations. Due to the strong position dependence of the signal in T2, the gain calibration of this scintillator was achieved with decay positrons from the $\pi^+ \rightarrow \mu^+ \nu_\mu \rightarrow e^+ \nu_e \bar{\nu}_\mu$ decay chain selecting their entrance position with WC3. ADC counts were converted in MeV using the simulation, which included a Birks' correction [160]. The light yield per path length is generally proportional to the the energy loss per path length: $dY/dx \propto dE/dx$. Birks' law takes into account saturation and quenching effects with the correction

$$\frac{dY}{dx} = S \frac{dE/dx}{1 + k_B(dE/dx)} \quad , \quad (4.2)$$

where S is the scintillation efficiency and k_B is the Birks' constant (which is typically of the order $10^{-1} - 10^{-2}$ mm/MeV).

4.2.2 Silicon Detectors

A pulser was connected to the amplifiers of all silicon detector channels. Run-by-run, a correction factor equal to the ratio of the calibration pulse signal to the calibration pulse signal from a reference run was calculated

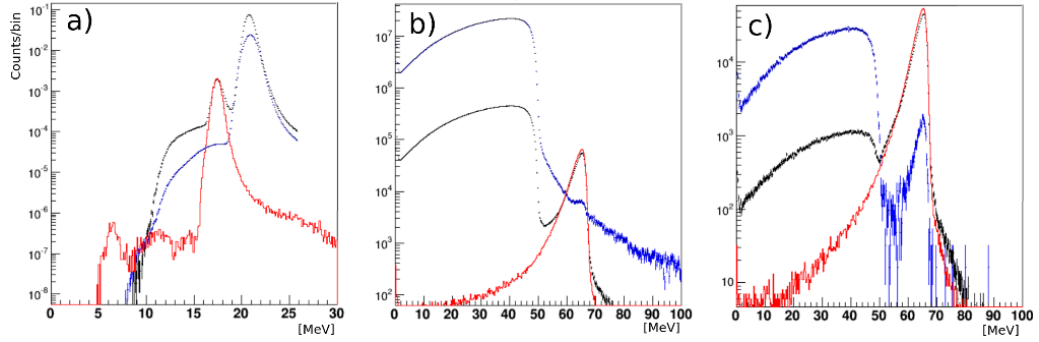


Figure 4.2: Calibration of the scintillators and NaI(Tl) crystal via the Monte Carlo simulation. **a)** Spectrum of the energy sum in the scintillators B1, B2, B3 and silicon detectors S1 and S2. The red histogram represents the MC generated $\pi^+ \rightarrow e^+ \nu_e$ events. The blue histogram shows events happening 200 ns after the pion stop (almost only $\pi^+ \rightarrow \mu^+ \nu_\mu \rightarrow e^+ \nu_e \bar{\nu}_\mu$ events). The black histogram is enriched with $\pi^+ \rightarrow e^+ \nu_e$ events selecting an early time window (< 20 ns) after the pion stop. After calibration, the $\pi^+ \rightarrow e^+ \nu_e$ peak in the data results aligned with the one in the simulation. **b)** The histograms have the same cuts as in a), but refer to the energy deposit in the whole calorimeter system (NaI(Tl)+CsI). **c)** Same as b), but with a cut around the $\pi^+ \rightarrow e^+ \nu_e$ peak in the target. This cut strongly suppresses the $\pi^+ \rightarrow \mu^+ \nu_\mu \rightarrow e^+ \nu_e \bar{\nu}_\mu$ background. In the red and black histograms, the $\pi^+ \rightarrow e^+ \nu_e$ peaks were normalized to the same number of events for direct comparison.

and multiplied to the measured signal. In total, 288 correction factors corresponding to all the silicon detector channels were calculated every run. This calibration procedure corrected only changes in the amplification electronics and was therefore not sensitive to changes in the silicon detector itself. The energy scale calibration was expected to change because of temperature fluctuations, voltage fluctuations or degradation in the silicon due to radiation damage. Voltages and temperatures in the area were recorded for every run so that such residual fluctuations could be identified and corrected during the offline analysis.

4.2.3 NaI(Tl) Crystal

The energy calibration in the NaI(Tl) was based on the total energy deposited in the detectors downstream of the target by the $\pi^+ \rightarrow e^+\nu_e$ events. The total energy should be equal to 70.3 MeV: the positron kinetic energy is 69.3 MeV, plus the 0.511 MeV mass of the positron and 0.511 MeV mass of the electron with which the positron annihilated. The energies recorded by S3, T1, T2 amount to ~ 2.5 MeV, while the mean energy deposited in the target (~ 1 MeV) and in the front aluminum face of the NaI(Tl) were obtained from MC. The sum of all these energies was used to fix the energy calibration for the NaI(Tl) calorimeter. The NaI(Tl) calibration was checked against the MC simulation. The results are showed in Fig. 4.2, where the simulation of the $\pi^+ \rightarrow e^+\nu_e$ decay is compared with data. For better comparison, the employed dataset was enriched with $\pi^+ \rightarrow e^+\nu_e$ events selecting an early time window after the pion stop signal (< 20 ns). This cut also strongly suppresses the $\pi^+ \rightarrow \mu^+\nu_\mu \rightarrow e^+\nu_e\bar{\nu}_\mu$ component in the data.

4.2.4 CsI Crystals

Since the CsI crystals were not directly exposed to the beam, they were calibrated using cosmic rays. A cosmic ray trigger was operating in parallel to the other triggers, enabling a new calibration every 20 runs (needed to collect sufficient statistics). The peak due to the passage of minimum ionizing cosmic muons in each crystal was compared with the energy deposit predicted by a simulation made with the CRY package [161]. CRY generated cosmic-rays at the altitude and geographic latitude of the PIENU experiment (sea level, 49° -north) and the resulting particles were injected in the Geant4 simulation of the detector. The energy deposited by minimum ionizing particles in a single CsI crystal was ~ 50 MeV. In Fig. 4.3, the comparison between simulation and the data is showed. The peak positions varied up to 20% in energy with the position of the crystal in the detector and it was reasonably reproduced by the MC. With reference to Fig. 4.3, the MC peaks appear sharper than the data. This discrepancy happens for multiple reasons:

- The influence of the $\text{YAlO}_3:\text{Ce}^{245}\text{Am}$ radioactive sources contributes to the background present in the data only.

- The electronic noise was not included in the simulation.
- The effect of the ADC thresholds and integration time were not included in the simulation.
- The simulation included only cosmics events, while the data contained also beamline related backgrounds.
- The exact position in space of the single CsI crystals was known only with few cm accuracy.

Although the width of the distributions were not correctly reproduced, the peak position is consistent between data and MC: given the large difference in energy resolution between NaI(Tl) and CsI (one order of magnitude worse for CsI), the automatic cosmics-based calibration was appropriate for correcting for the shower leakage and track the drift of the PMT gains.

4.3 Event Selection

The list of runs analyzed was the result of many checks done on the data concerning detector, DAQ, slow control, and beam stability. The data analysis aimed at isolating clean events while rejecting backgrounds. The main output of the analysis was the positron energy decay spectrum and the time spectra corresponding to low-energy and high-energy events.

4.3.1 Pion Identification

The identification of incoming pions was realized using the energy deposit information in B1/B2 and the time of flight (TOF) information from B1 relative to the cyclotron RF frequency (Fig. 4.4 (left)). A cut on the beam profile in WC1 and WC2 was applied to remove particles (mostly positrons and muons) from the beam halo (Fig. 4.4 (right)). This cut also minimized the tail of the pion momentum distribution. Additionally, using tracking in WC1 and WC2, a cut was made on the position of pion stops at the center of the target to exclude pion events stopping near the edge of the scintillator.

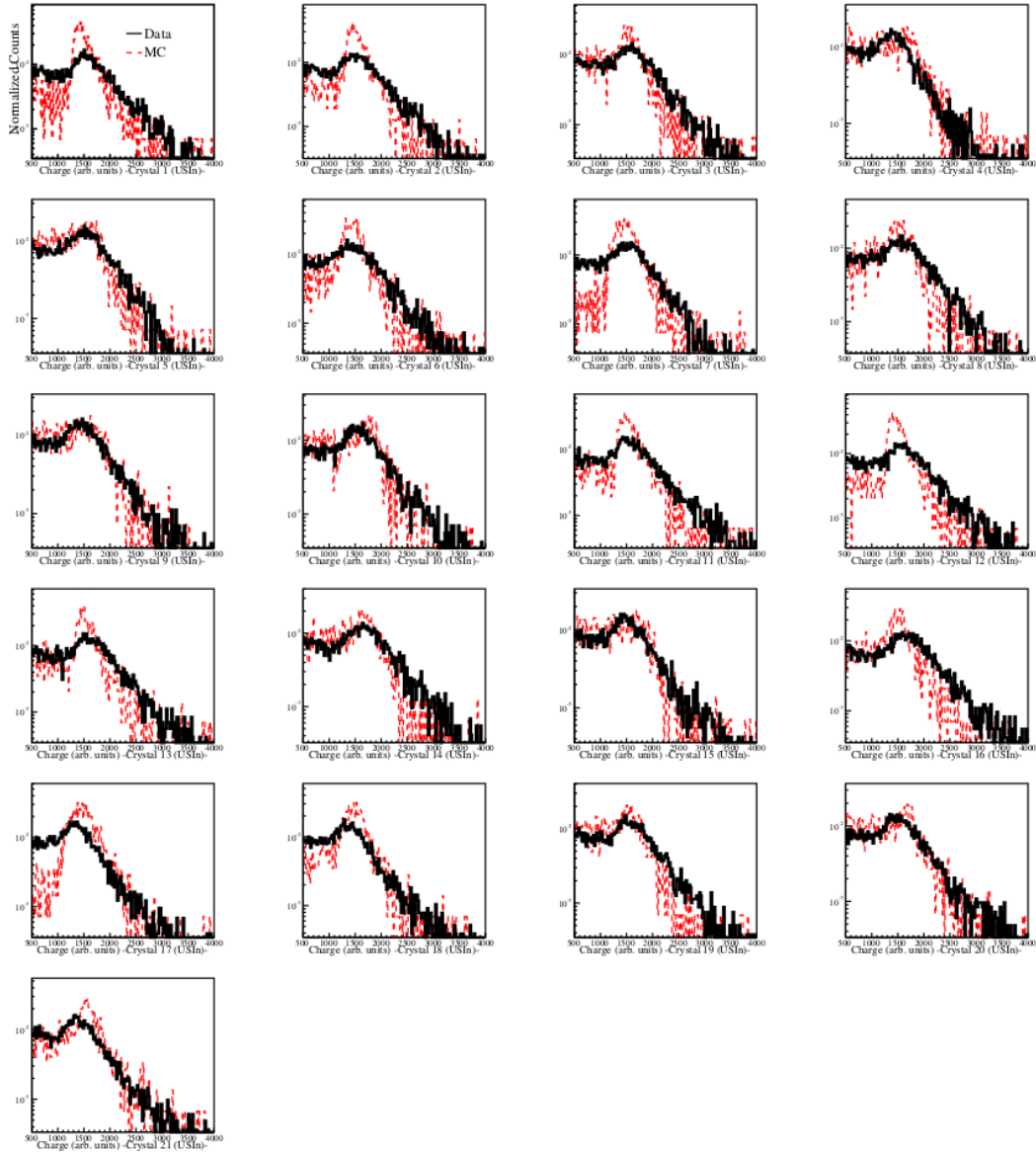


Figure 4.3: Comparison between data taken with the cosmic ray trigger (black) and a MC simulation (red) based on the CRY [161] simulation package. The spectra are relative to the 21 crystals in the inner-upstream CsI ring.

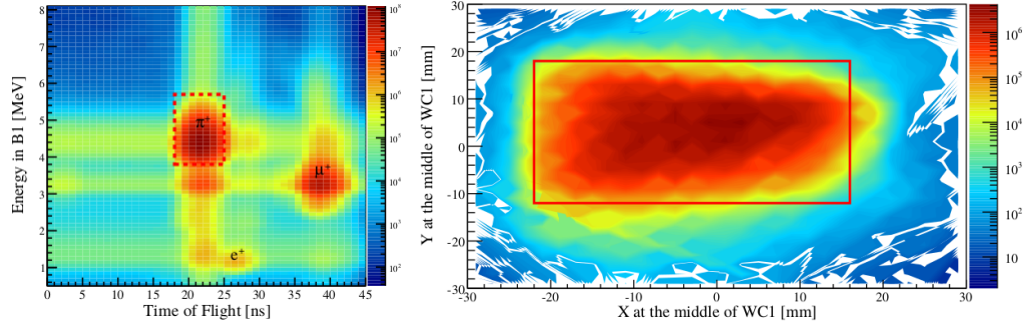


Figure 4.4: **(Left)** Energy deposit in B1 versus time of flight. **(Right)** Beam profile in the transverse direction as measured by WC1 and the corresponding selection cut (red box).

4.3.2 Positron Identification

Cuts for identifying positrons were carefully designed for not biasing the branching ratio selecting preferentially positrons with a certain energy. A low energy cut was applied on T1 ($E_{T1} > 0.3$ MeV) to remove events produced by particles hitting the light guides.

Pion interactions with nuclei in the target may lead to the emission of protons which had a broad energy distribution in the NaI(Tl). Protons deposited also a large amount of energy in the scintillators after the target. This energy deposit was anticorrelated with the energy deposited in the NaI(Tl) crystal, as showed in Fig. 4.5. Events containing protons had prompt timing (with respect to the pion arrival time) and only 0.008% of them happened at later times. The energy dependence of this cut can therefore be safely neglected.

Events in which at least one T1 pulse was in coincidence with the pion time were also rejected. This cut removed muons coming from pions decaying in flight which then stopped in T1. These muons can decay and produce a trigger if the decay positron hit T2 within the trigger window. In this case, the trigger time was defined by T2 instead of T1 and this resulted in a change of the trigger gate time by up to 200 ns. This effect gave rise to a distortion of the time spectrum in the early time region.

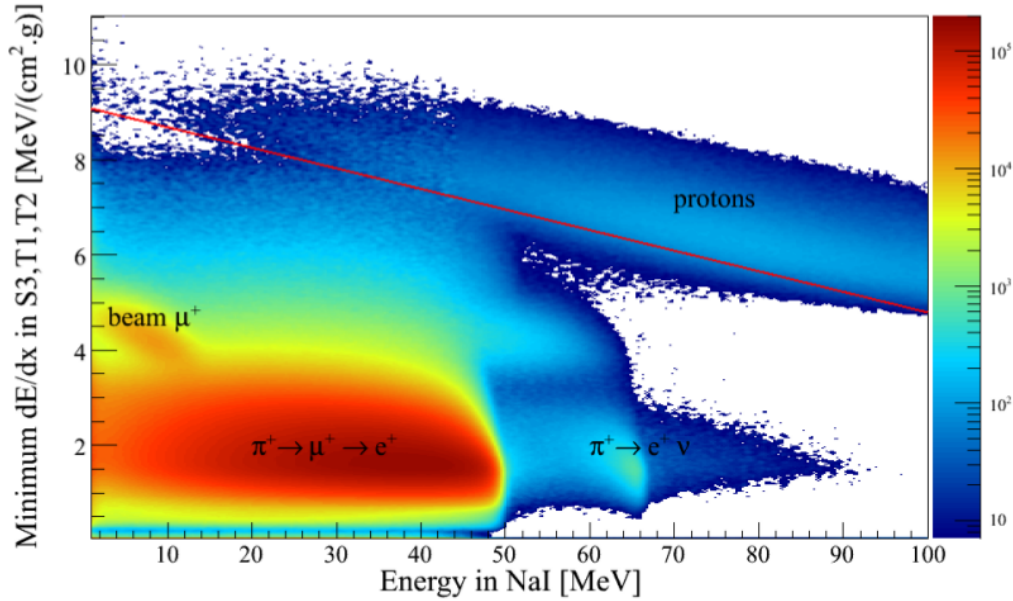


Figure 4.5: Energy deposit in S1, T1 and T2 as a function of the energy deposited in the NaI(Tl) crystal. The proton band is clearly visible. The red line is the cut applied to the data.

4.3.3 Pileup Rejection

The waveforms digitized by COPPER in the plastic scintillators were used for reconstructing timing, energy deposits and for detecting the presence of multiple pulses generated by different particles (pileup). In order to reject pileup events, only single pulse (or "hit") events were accepted. However, some waveforms presented additional pulses due to noise or optical reflections. In order to avoid rejecting events with no true pileup, each scintillator was required to have at least one PMT (and not all four at the same time) with a single hit in the signal region. This requirement was used for B1, B2 and T1. The target presented multiple hits from pion decays and therefore no hits requirements were made on this scintillator. T2 had a fiber readout which generated more hits with respect to light-guides and requiring a single hit for each PMT may introduce unwanted position dependence inefficiencies.

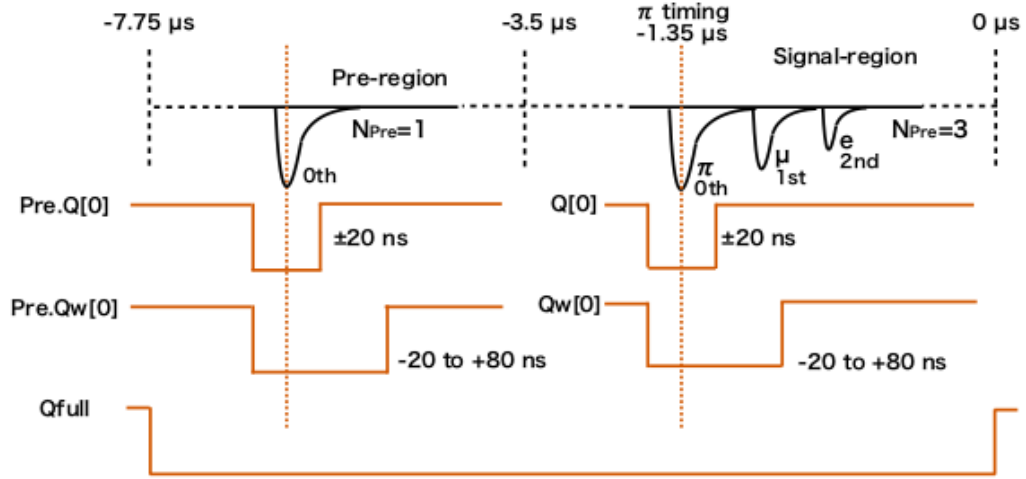


Figure 4.6: Time regions of the waveform digitized by COPPER for the charge integration (figure from S.Ito [147]). The signal region was defined by the trigger signal arrival time, corresponding to $-1.35\mu\text{s}$ in the COPPER timing window. The times before $-1.35\mu\text{s}$ constituted the "pre-region" and contained for example old muon decays. An event was discarded if hits in the pre-region were present (pre-pileup cut). Pile-up hits were searched for $t > -1.35\mu\text{s}$ and an event was rejected if all the four PMTs reading the same scintillator saw more than one hit.

When pulses were too close to be identified, a hit-based pileup rejection cut would not be effective. This type of pileup events were rejected using the ratio between the charge Q measured in a short time range (20ns) and the one measured in a longer range Qw (80ns, refer to Fig. 4.6). Pileup events will tend to have a smaller Q/Qw ratio. This cut was applied to B1 and B2 for enhancing beam pileup rejection.

For rejecting backgrounds from stopped beam muons or from decay of beam pions, all plastic scintillators were required to have no hits in the "pre-region" (see Fig. 4.6).

The timings of the trigger-defining scintillators must also be consistent with the generated trigger signal.

To this end a timing cut made sure that the timing in B1 was consistent

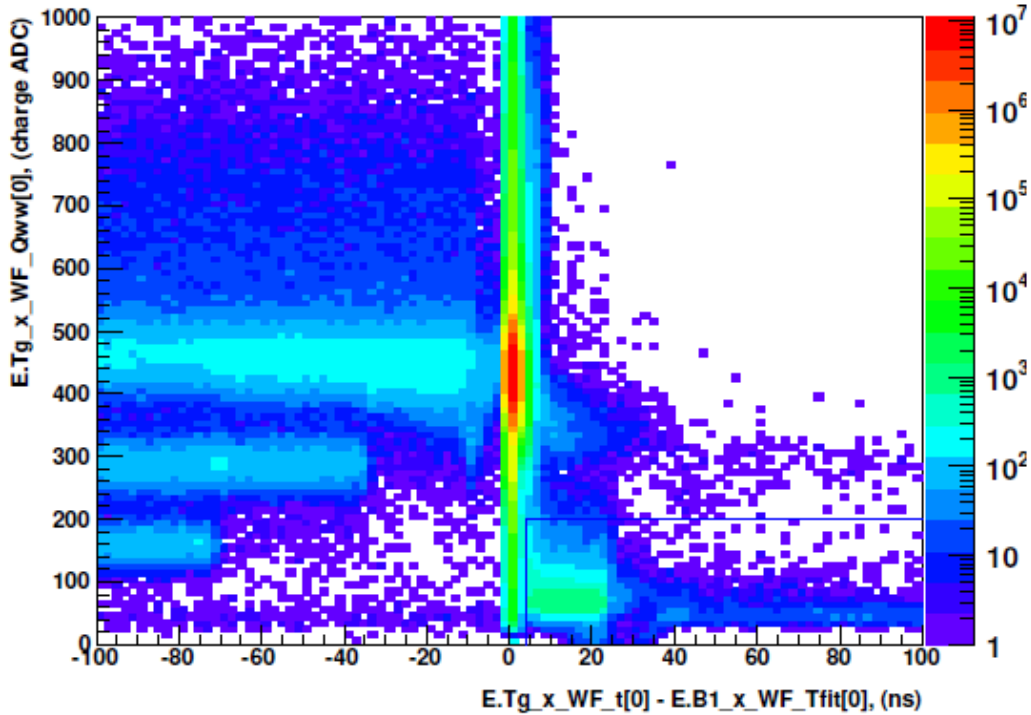


Figure 4.7: Wide-gate integrated charge in the target B3 as a function of the time difference between the target and B1. False triggers (due to positrons from pions decaying before the Target) are visible in the blue box (corresponding to the values of the cut) in the lower-right part of the 2d-histogram.

with the trigger timing. Additionally, the time difference between T1 and T2 was also checked in order to avoid accidental pileup events where for example decay positrons hit T1 and missed T2 while a background particle (e.g. a decay positron from an old muon) hit T2.

4.4 Additional Cuts

Sometimes beam pions stopped in B2 due to range straggling, low momentum, or π DIF events. If those events occur within the coincidence

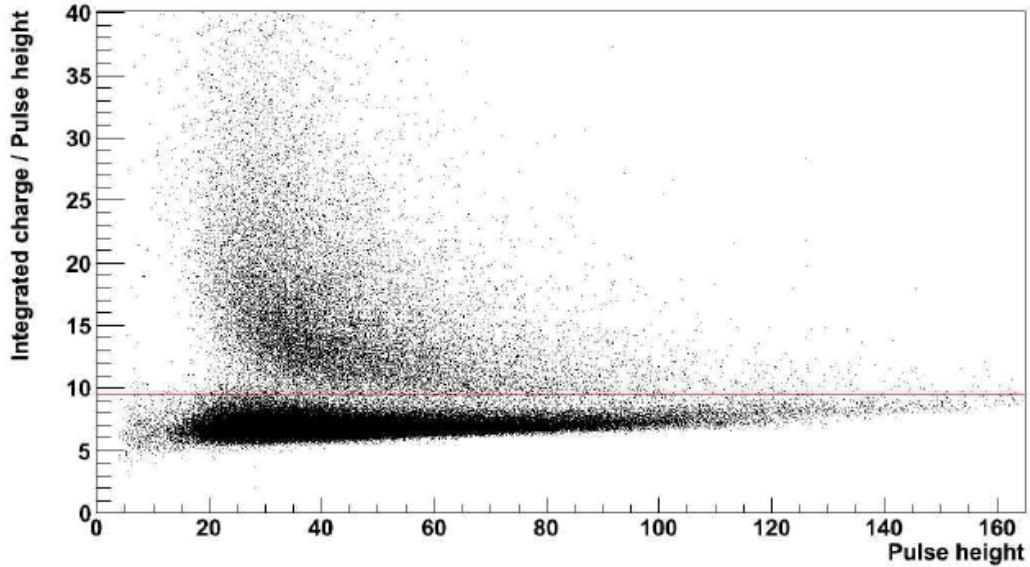


Figure 4.8: Ratio of the integrated charge and the fitted amplitude as a function of the amplitude. The real pileup events are above the red line which represent the value of the applied cut.

window of B1, B2, and B3, this false trigger would be accepted. Such events can be removed with an appropriate cut: the energy deposit in B3 by a decay positron will be smaller than that of a π DAR event. Moreover, π DAR events had a small timing difference between B1 and B3. The false-trigger events can be seen in the blue box in Fig. 4.7.

Another cut ensured that the positron trigger was caused by the first hit in each PMT of T1, and that the triggering hits in T1 and T2 are coincident within 20 ns (the coincidence window in the hardware trigger itself was 100 ns). An additional cut was designed in order to avoid discarding events which looked like pileup. The idea was considering the ratio between the integrated charge and the fitted pulse height. If pileup was really present, the integrated charge will result larger than expected for a given fitted amplitude. The correlation between the ratio and the pulse height can be seen in Fig. 4.8 together with the cut applied.

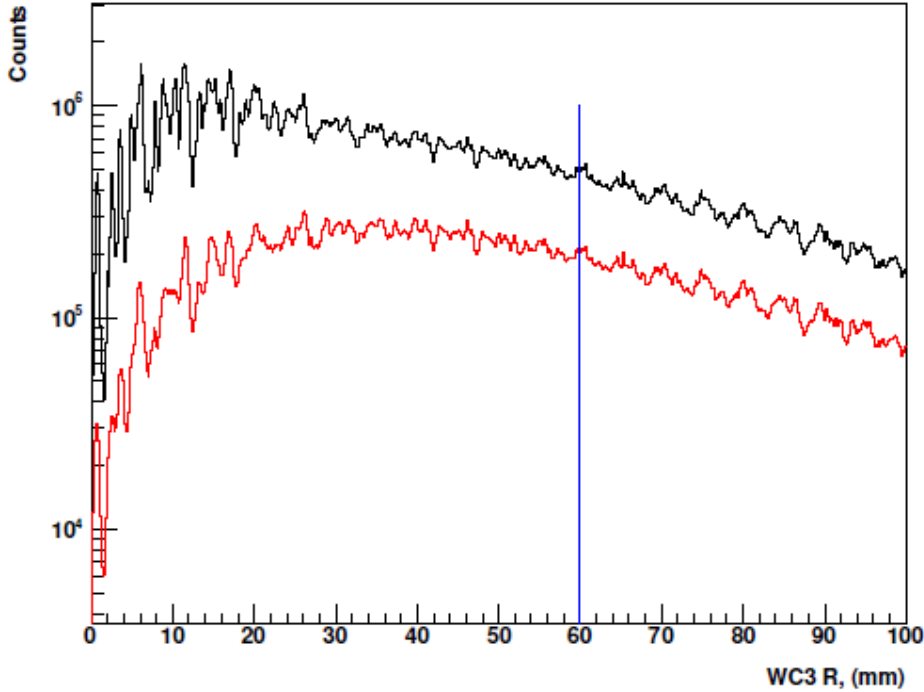


Figure 4.9: Radius at the center of WC3 reconstructed with the tracking. The vertical blue line shows the cut adopted in [100]. The black spectrum represents the distribution of all events, while the red spectrum is the result after the cuts. The wiggles in the spectra correspond to the wire positions in WC3.

4.5 Acceptance Definition

The distance between the centre of WC3 and the positron track reconstructed using S3 and WC3 (tracker Trk3), is showed in Fig. 4.9. This distance is referred to as track radius R . The measured energy spectrum was highly dependent on the angle and position at which decay positrons entered the calorimeter assembly. For events with multiple tracks, the track with the minimum distance from the centre was considered. The choice of the cutoff value for R resulted from a trade-off between the increasing systematic error as the low energy tail of the $\pi^+ \rightarrow e^+ \nu_e$ decay increases, and the decreasing statistical error as more events were

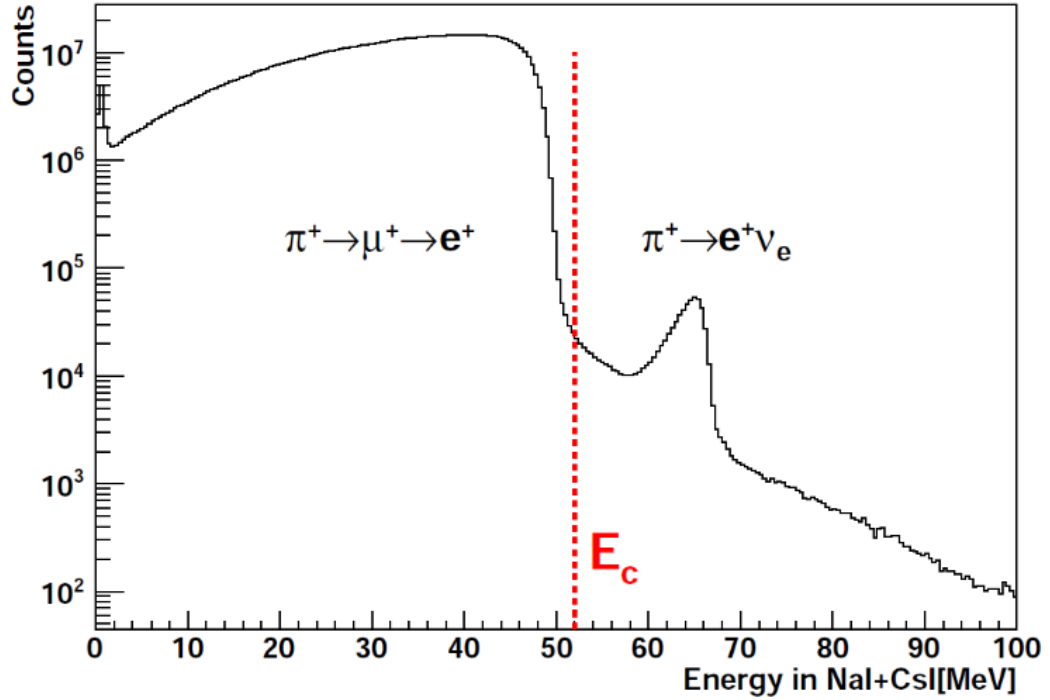


Figure 4.10: Positron energy spectrum after all the analysis cuts (with the prescale factor of the $\pi^+ \rightarrow \mu^+ \nu_\mu \rightarrow e^+ \nu_e \bar{\nu}_\mu$ events taken into account). The spectrum is divided in low-energy and high-energy regions by a cut-off energy E_c (vertical red dashed line).

included at higher values of R . The determined value was $R = 40$ mm, while in the first analysis published in [100] it was $R = 60$ mm.

4.6 Energy Spectrum

After all the described selection cuts, the positron energy spectrum was obtained (Fig. 4.10). The spectrum combines the calibrated energies of the NaI(Tl) and the CsI calorimeters. The high-energy part contains mainly $\pi^+ \rightarrow e^+ \nu_e$ events, while the low-energy part contains mainly $\pi^+ \rightarrow \mu^+ \nu_\mu \rightarrow e^+ \nu_e \bar{\nu}_\mu$ events. The events in the energy spectrum were divided

in two energy regions by a cutoff $E_C = 52$ MeV. In the following, the time spectra corresponding to these two regions will be considered for the extraction of the branching ratio.

4.7 Time Spectrum Fit

After dividing the events in two energy classes, the branching ratio could be calculated in principle. In practice, due to the presence of backgrounds and corrections, a more complex procedure had to be used. Since the time shapes of the signals and of some backgrounds were known analytically, time spectra instead of energy spectra were considered.

4.8 Fitting function

4.8.1 Low energy time spectrum

In the low energy time spectrum (LES) two backgrounds were present at a non-negligible level: decays from old muons ($O\mu$) and pion decays-in-flight (π DIF). The time dependence of $O\mu$ was an exponential with the muon lifetime, starting at the beginning of the trigger window (-300 ns). π DIF events were events where the pion decayed before the target and the muon passed through and stopped in S3 or T1. If it stopped in T1, the event was prompt, and thus outside the fitting range. The only π DIF events included in the fit were those for which there was a muon in the target or S3 (*i.e.* before T1) at $t=0$. In this case, the time dependence of these events was also an exponential with the muon lifetime, but starting at $t=0$ instead from the beginning of the trigger window. The $\pi^+ \rightarrow \mu^+ \nu_\mu \rightarrow e^+ \nu_e \bar{\nu}_\mu$ signal shape was $\propto e^{-t/\tau_{\pi i}} - e^{-t/\tau_\pi}$, as results from the two-step decay process (see App. C). The fitting function used in the low energy time spectrum was the sum of the three described shapes

$$f_{LES}(t) = H(t) \left[\underbrace{A \frac{1}{\tau_\mu - \tau_\pi} \left(e^{\frac{t-t_0}{\tau_\mu}} - e^{\frac{t-t_0}{\tau_\pi}} \right)}_{\pi \rightarrow \mu \rightarrow e} + \underbrace{B \frac{1}{\tau_\mu} e^{\frac{t-t_0}{\tau_\mu}}}_{\pi \text{DIF}} + \underbrace{C \frac{1}{\tau_\mu} e^{\frac{t-t_0}{\tau_\mu}}}_{O\mu} \right], \quad (4.3)$$

where H is the Heaviside function, t_0 is the offset in the time spectrum (determined from beam particles traversing the apparatus), τ_μ and τ_π are the muon and pion lifetimes, A is the amplitude of the $\pi^+ \rightarrow \mu^+ \nu_\mu \rightarrow e^+ \nu_e \bar{\nu}_\mu$ shape, B is the amplitude of the π DIF shape, and C is the amplitude of the $O\mu$ background.

4.8.2 High energy time spectrum

The high energy time spectrum (HES) contained more contributions since several processes can add extra energy which was eventually deposited in the calorimeters. Mechanisms that can add energy to a single decay were old muon pileup, neutrons from the cyclotron (which are time independent relative to the decay), energy resolution effects, and radiative pion decay. There were also two mechanisms by which old muon pileup events can reach the high-energy region.

In the first mechanism, if both decay positrons hit T1, the event was rejected by the T1 pileup cut, unless they were sufficiently close in time (within about 15 ns) to be recorded as a single hit.

In the second mechanism, if the decays were separated in time, one of the positrons can miss T1 and reach the calorimeters. In the following, these processes will be described and time shapes derived.

Time-independent addition of energy

Time-independent mechanisms (like for example neutron background from the cyclotron) result in components of the LES being present in the HES. The term included in the fit is thus Eq 4.3 multiplied by a free parameter r .

Old-muon pileup I: T1 time resolution

The pileup cut in T1 did not reject events where two positrons were sufficiently close in time. The time spectrum for this component depended on whether the trigger was caused by the positron from an old muon or the positron from the primary pion since the latter can only occur at positive time while the former can occur at any time in the trigger window. Defining ΔT as the minimum time difference for which T1 is able to resolve hits, the shape for the old-muon trigger case is given by the

product of the amplitude of the $\text{O}\mu$ shape and the probability that the $\pi^+ \rightarrow \mu^+ \nu_\mu \rightarrow e^+ \nu_e \bar{\nu}_\mu$ positron will come within a time ΔT . This component is called T1res and its form is

$$f(t) = \begin{cases} 0 & t < -\Delta T \\ \frac{\exp(-\frac{t}{\tau_\mu})}{\tau_\mu} \int_0^{t+\Delta T} \frac{\exp(-\frac{y}{\tau_\mu}) - \exp(-\frac{y}{\tau_\pi})}{\tau_\mu - \tau_\pi} dy & -\Delta T < t < 0 \\ \frac{\exp(-\frac{t}{\tau_\mu})}{\tau_\mu} \int_t^{t+\Delta T} \frac{\exp(-\frac{y}{\tau_\mu}) - \exp(-\frac{y}{\tau_\pi})}{\tau_\mu - \tau_\pi} dy & t > 0 \end{cases} \quad (4.4)$$

If the trigger was caused by the $\pi^+ \rightarrow \mu^+ \nu_\mu \rightarrow e^+ \nu_e \bar{\nu}_\mu$ positron, the shape was given by the product of the $\pi^+ \rightarrow \mu^+ \nu_\mu \rightarrow e^+ \nu_e \bar{\nu}_\mu$ shape and the probability that the old muon will decay within ΔT

$$f(t) = \begin{cases} 0 & t < 0 \\ \frac{\exp(-\frac{t}{\tau_\mu}) - \exp(-\frac{t}{\tau_\pi})}{\tau_\mu - \tau_\pi} \int_t^{t+\Delta T} \frac{\exp(-\frac{y}{\tau_\mu})}{\tau_\mu} dy & t > 0 \end{cases} \quad (4.5)$$

For obtaining the time resolution ΔT , the time difference between consecutive T1 hits was histogrammed, and the edge fitted with an error function. The fitted histograms for the four T1 PMTs are shown in Fig. 4.11. The average result is $\Delta T = 15.7$ ns and the final normalized shape is shown in Fig. 4.12.

Old-muon pileup II: Double decays

Old-muon pileup events can also appear in the HES if one of the decay positrons missed T1, but still hits one of the two calorimeters. The shape of this component was influenced by the requirement of the BinaHigh trigger, which employed a running sum of the NaI(Tl)+CsI pulse height with a window of 250 ns. The integration time used for the NaI(Tl) energy was 1 μs , which means that if hits were sufficiently separated in time, the energy could be above E_c event without a BinaHigh trigger.

The shape was determined using a MC simulation where $\pi^+ \rightarrow \mu^+ \nu_\mu \rightarrow e^+ \nu_e \bar{\nu}_\mu$ events caused by a positron and events caused by a positron from an old muon decay were generated. If only one positron hit T1, the acceptance cut was passed, and the BinaHigh trigger requirement was met, the time of the event was included in the shape. The presence or absence of the BinaHigh trigger condition was determined using NaI(Tl) and CsI

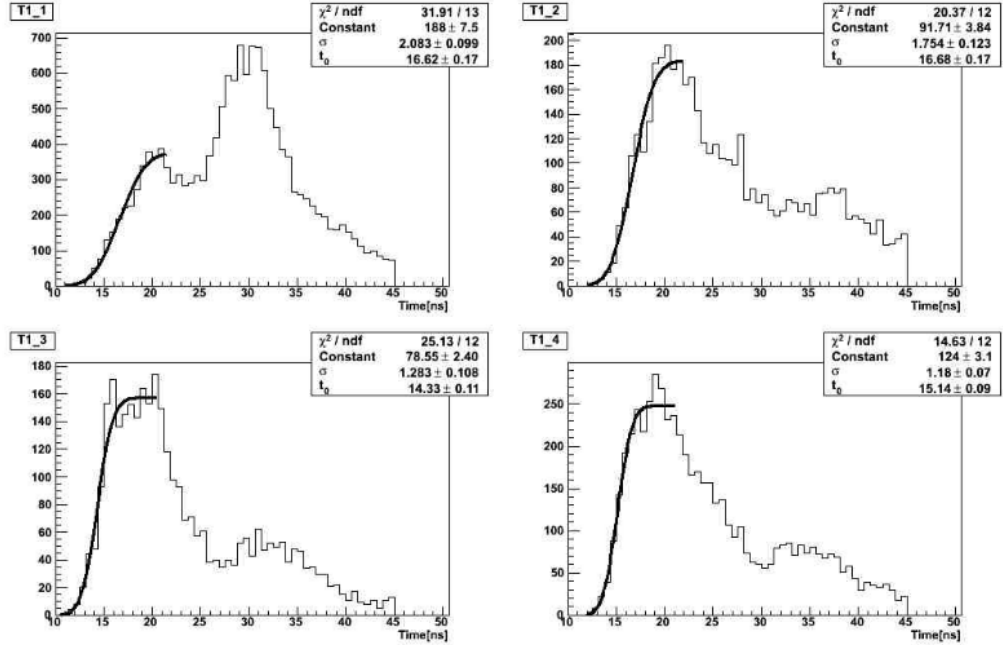


Figure 4.11: Time difference between consecutive hits in T1 for each PMT. The edge of the distributions were fitted with an error function. The peaks around 30 ns are due to fake hits at a characteristic time after the real hit.

waveform template shapes together with the energy deposited found in the simulation. This background shape is called `oldmu_both` and it is shown in Fig. 4.13.

Radiative decay

If the decay positron was produced in association with a photon from $\mu^+ \rightarrow e^+ \nu_e \bar{\nu}_\mu \gamma$ the energy spectrum of the positron was altered, but not the time dependence. However, if the pion decayed to a muon and a photon ($\pi^+ \rightarrow \mu^+ \nu_\mu \gamma$), followed by the $\mu^+ \rightarrow e^+ \nu_e \bar{\nu}_\mu$ decay, the measured energy could be above E_c . The probability for this process is dependent on the relative time of the photon and the positron because of

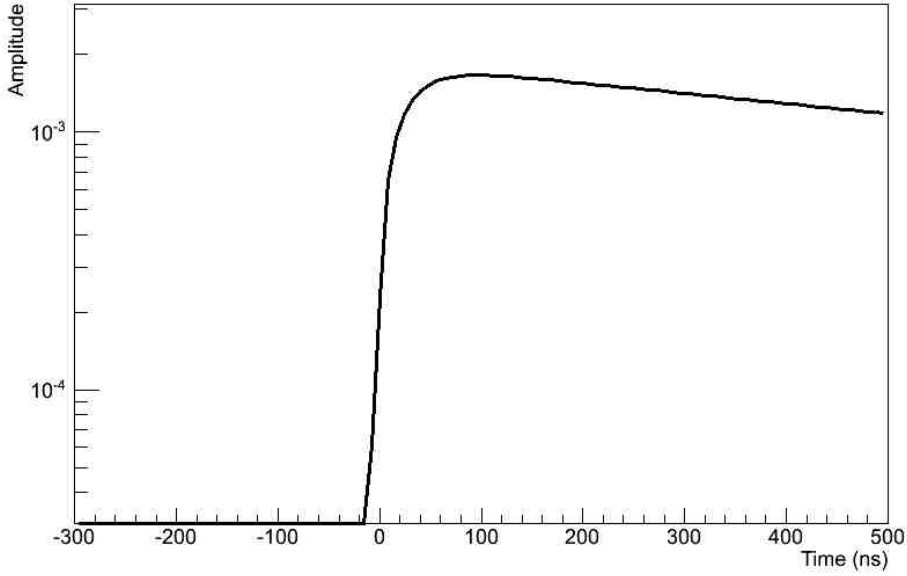


Figure 4.12: The T1res shape arising from the finite time resolution of T1.

the BinaHigh trigger requirement. This shape was also determined from a simulation and the result is showed in Fig. 4.14.

The final HES function consisted of all of the shapes previously discussed, plus the $\pi^+ \rightarrow e^+ \nu_e$ signal shape with amplitude $(A - A \cdot r) \cdot BR$, where A is the $\pi^+ \rightarrow \mu^+ \nu_\mu \rightarrow e^+ \nu_e \bar{\nu}_\mu$ amplitude, r is the proportion of the low energy time spectrum present in the HES, and BR is the $\pi^+ \rightarrow e^+ \nu_e$ branching ratio. The fitting function is

$$f_{HES}(t) = H(t) \left[(A - A \cdot r) \cdot BR \cdot \frac{1}{\tau_\pi} e^{\frac{t-t_0}{\tau_\pi}} \right] + r \cdot \mathcal{L} + \mathcal{F}_1 + \mathcal{F}_2 + \mathcal{F}_3 \quad , \quad (4.6)$$

where \mathcal{F}_1 , \mathcal{F}_2 , and \mathcal{F}_3 are the radiative decay shape and the two old muon pileup shapes respectively, and \mathcal{L} is the low energy fitting function given in Eq. 4.3.

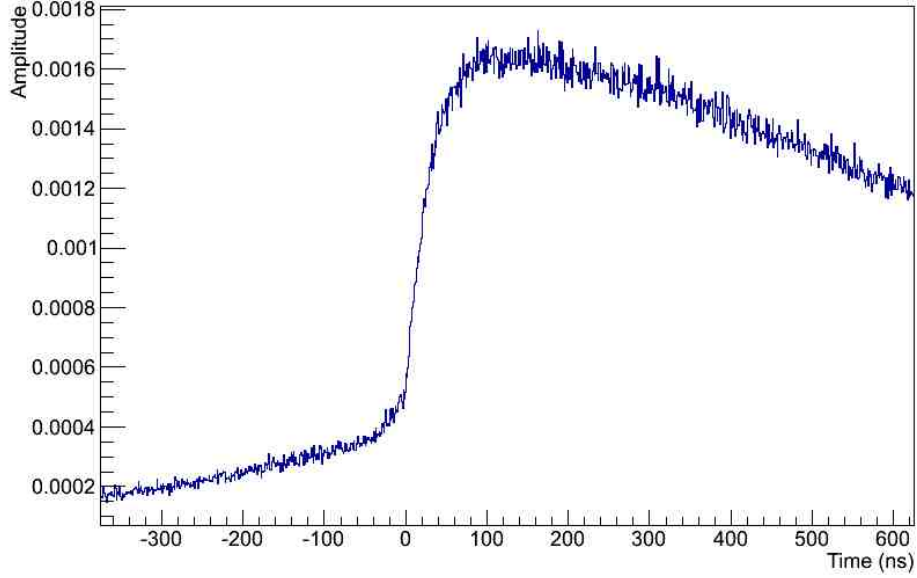


Figure 4.13: The `oldmu_both` shape used in the fit for pileup events where only one positron hits T1.

4.9 Summary

The extraction of the branching ratio was done in two steps: first a raw branching ratio was extracted from the time spectra and then corrections (described in the next chapter) were applied. The raw branching ratio was extracted in the following way: the positron energy spectrum was divided into a low-energy and in a high-energy part and the corresponding time spectra were obtained.

The low-energy part contained mostly $\pi^+ \rightarrow \mu^+ \nu_\mu \rightarrow e^+ \nu_e \bar{\nu}_\mu$ and πDIF events, plus the low-energy tail (LET) of the $\pi^+ \rightarrow e^+ \nu_e$ decay. The LET was too small with respect to the other components and the fit was not sensitive to it. The LET had to be treated as a correction to the raw branching ratio.

The high-energy part contained mostly $\pi^+ \rightarrow e^+ \nu_e$ events and back-

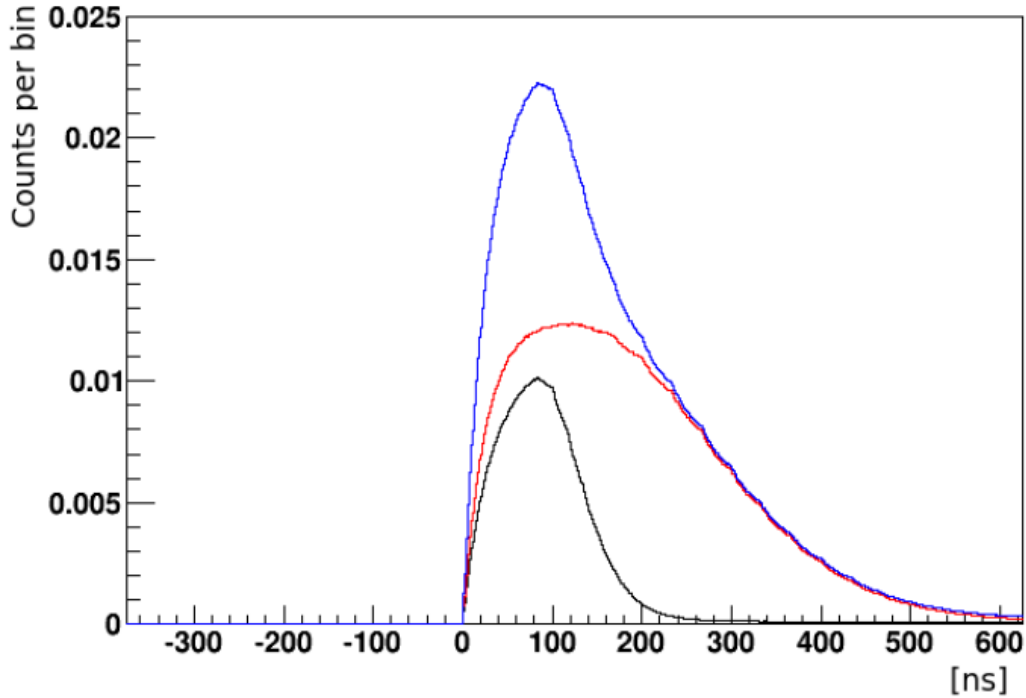


Figure 4.14: The simulated distribution of the radiative decays $\pi^+ \rightarrow \mu^+ \nu_\mu \gamma$. The contribution from the NaI(Tl) calorimeter corresponds to the red histogram, while the black histogram is relative to the CsI. The blue histogram is the total time spectrum for the radiative decay.

ground components originating from pileup effects. The fit of the time spectrum allows the extraction of the branching ratio automatically subtracting the different background components.

The advantage of fitting the time spectra is that the larger components are known analytically (like for example the exponential decays of the pion and the muon). This is not true for the energy spectra, where a simulation should have been used to a large extent. In particular, while the energy spectra of the decays can be quite accurately simulated, the background shapes are more difficult and subject to higher uncertainties.

This analysis strategy is the same as the one used in the previous TRIUMF experiment and it is allowed by the excellent energy resolution of the NaI(Tl) crystal. The high energy resolution allows the separation into

low- and high-energy parts leaving a relatively small LET: without this feature, the correction would have been larger, like the corresponding systematic error.

Chapter 5 | Corrections

With *corrections* are intended all the factors which have to be multiplied to the *raw* branching ratio to obtain the final result. The largest corrections comes from the low energy tail of the $\pi^+ \rightarrow e^+ \nu_e$ decay (LET). The LET originates from detector effects, energy leakage from the calorimeter, and radiative decays. Since the LET is made by $\pi^+ \rightarrow e^+ \nu_e$ events and their radiative counterparts, its amount must be known for extracting the correct branching ratio. The LET extends below the overwhelming $\pi^+ \rightarrow \mu^+ \nu_\mu \rightarrow e^+ \nu_e \bar{\nu}_\mu$ background and it cannot be accessed directly. The technique used to reliably extract the LET was to inject a positron beam in the calorimeter at various angles mimicking in this way positrons from pion decays. The positron beam data were then compared with the MC which in turn was accurately tuned for reproducing the data. The MC was eventually used to calculate the LET.

A second correction comes from energy-dependent processes in the various detectors and materials which leads to different acceptances for the two decay modes.

A third correction comes from the presence of muons decaying in flight in the target. These events cannot be distinguished from $\pi^+ \rightarrow e^+ \nu_e$ decays in the time spectra and the branching ratio had to be corrected accordingly.

Another correction comes from energy-dependent effects in the determination of the timing between the two decay modes.

5.1 The Low Energy Tail Correction

The LET of the $\pi^+ \rightarrow e^+ \nu_e$ peak extended to very low energies and it was covered by the $\pi^+ \rightarrow \mu^+ \nu_\mu \rightarrow e^+ \nu_e \bar{\nu}_\mu$ background. Since the number of

events in the LET was very small, the time fit of the low-energy region was not sensitive to it. This is why a separate correction had to be applied to the raw branching ratio BR_{raw} extracted from the time fit. The LET is defined as the fraction of events below a cutoff energy E_c

$$LET = \frac{\int_0^{E_c} N(E)dE}{\int_0^{\infty} N(E)dE} \quad , \quad (5.1)$$

where $N(E)$ is the energy spectrum (the number of events in the bin of energy E) and E_c had the nominal value $E_c = 52$ MeV. The branching ratio BR_{raw} was corrected as

$$BR = \frac{BR_{raw}}{1 - LET} \quad , \quad (5.2)$$

and BR is the corrected branching ratio.

The amount of events lost in the LET and corrected with Eq. 5.2 should be compensated with a corresponding change in the $\pi^+ \rightarrow \mu^+ \nu_\mu \rightarrow e^+ \nu_e \bar{\nu}_\mu$ amount of events. This correction was included in the fit procedure without obtaining any effect on the branching ratio value.

5.1.1 Estimation of the Low Energy Tail with a Positron Beam

The idea for accessing the LET was to inject positrons directly into the calorimeter for studying its response. In the normal operation mode, the target was located at about 8 cm from the NaI(Tl) crystal face and the positrons coming from it had a large angular distribution ($\sim 50^\circ$). The larger the angle of a positron track, the larger the probability to have shower leakage contributing to the LET.

Since the positron beam could not be rotated, the entire setup was rotated instead, in order to mimic the decay positrons. For rotating the calorimeter with respect to the beam, the whole PIENU-1 assembly (silicon detectors, B1, B2, B3 scintillators) and the rails had to be removed. The remaining detectors (the calorimeters, WC3, the T2 scintillator) were rotated with respect to the beam (the WC1/2 were still mounted on the beampipe). A steel shaft connected the calorimeter's cart to the experimental hall's floor allowing the rotation of the assembly. The rotation

point defined by the shaft corresponded to the location of the target scintillator B3.

Comparing the positron beam spectra measured at various angles to a detailed simulation of the experimental setup resulted in the possibility to accurately tune the simulation which was then used to estimate the LET with all the other detectors in place.

5.1.2 Positron Beam Data Analysis

The angular position of the detectors was measured with a theodolite and markers placed on the beamline and on the detector itself resulting in an error $< 0.1^\circ$.

T2 was used as a trigger and a loose cut on the cyclotron RF timing helped in reducing the backgrounds and discard beam pions. Most of the events not caused by beam particles were removed with cuts in WC1/2 which were also used as timing detectors for further background reduction. After these preliminary cuts, the spectrum contained mostly beam positrons and beam muons (Fig. 5.1 (left)).

Muons could be fully removed with an energy cut in T2, but such a cut would also remove positrons in an energy-dependent way, thus biasing the LET estimation. The energy spectrum in T2 was further complicated by the presence of back-splash events from the NaI(Tl) calorimeter (as verified with the simulation). A two-dimensional cut in the NaI(Tl) energy deposit below 35 MeV and 400 ADC counts in T2 removed most of the beam muons [162]. Since the LET below 35 MeV was negligibly small, there is no bias in this cut. For example, at 0° the impact of the cut on the tail was 0.04%. Above 35 MeV, there were still some contributions from muons decaying in the NaI(Tl) where the decay positron was also integrated.

In principle, this contamination could be estimated with the simulation, but a data-driven approach was preferred.

The correction due to muons will be described in the next section.

The final spectrum (as example for the 0° case) is showed in Fig. 5.2.

The additional peaks at energies lower than the beam energy were due to photonuclear reactions inside the NaI(Tl) crystal [37]. Photons can be captured by iodine nuclei in the giant resonance region and emit one or more neutrons. If neutrons were not recaptured, they could eventually escape the crystal (after a series of elastic and inelastic scatterings). Ad-

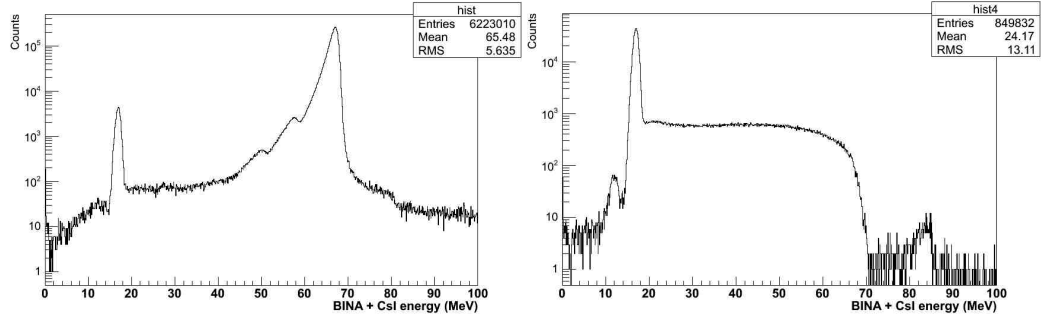


Figure 5.1: **(Left)** Positron spectrum for the 0° case after the RF positron and WC1/2 selection cuts. The peak due to beam muons is visible at ~ 18 MeV. **(Right)** Muon events selected with the RF cut. The muon peak is visible, together with the high-energy tail due to the integration of the decay positron energy.

ditionally, more than one photon in a shower could be captured. These processes resulted in an unmeasured energy which showed up as as peaks in the energy spectrum corresponding to 1-neutron escape at ~ 57 MeV, and to 2-neutron escape at ~ 50 MeV. More neutron escape events were in principle present but not clearly visible with the available data sample. These processes were well reproduced by the simulation.

5.1.3 Muon Correction

Muons can be isolated with an RF cut. The resulting spectrum (see Fig. 5.1 (right)) was composed by a peak due to the energy deposit of the muon and a tail towards higher energy deposits. The high-energy events were due to the long ($\sim 1\mu\text{s}$) integration time of the NaI(Tl) calorimeter which can add energy from the decay positrons. The beam-positron contamination under the muon peak is $< 10^{-5}$ and can be neglected. This means that the spectrum was composed essentially by muons only and the number of muons can be estimated from the size of the peak.

The peak region was defined between 15 and 19 MeV. Due to energy loss, the region's width changed with the entrance angle of the positrons. In order to correct the LET in Eq. 5.1, the number of muons in the spectrum and in the tail must be estimated.

Defining $N_\mu(E)$ as the energy spectrum of the muons (Fig. 5.1 right), the

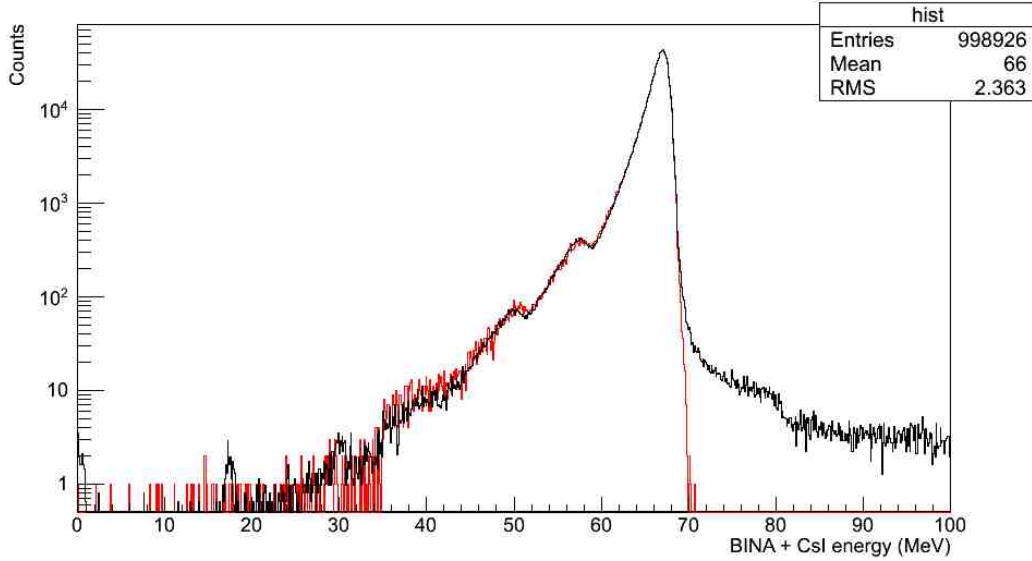


Figure 5.2: (Black) Lineshape for the 0° case after subtraction of the muon contribution. The step at 35 MeV is due to the two-dimensional muon cut, which was well reproduced by the simulation (red). The additional peaks at lower energies were due to neutron escapes from from the crystal. Neutrons were emitted by iodine nuclei after capture of a photon from the positron-initiated shower.

total number of events in the muon peak, the number of muons up to E_c and the total number of muons are respectively

$$N_{peak}^\mu = \int_{15 \text{ MeV}}^{19 \text{ MeV}} N_\mu(E) dE \quad , \quad (5.3)$$

$$N_{tail}^\mu = \int_{0 \text{ MeV}}^{E_c} N_\mu(E) dE \quad , \quad (5.4)$$

$$N_{tot}^\mu = \int_{0 \text{ MeV}}^{\infty} N_\mu(E) dE \quad . \quad (5.5)$$

Considering now the positron spectrum $N(E)$, we can define the analogue quantities N_{peak} , N_{tail} , and N_{tot} .

If N_1 is the number of muons present in $N(E)$ and N_2 the muons present

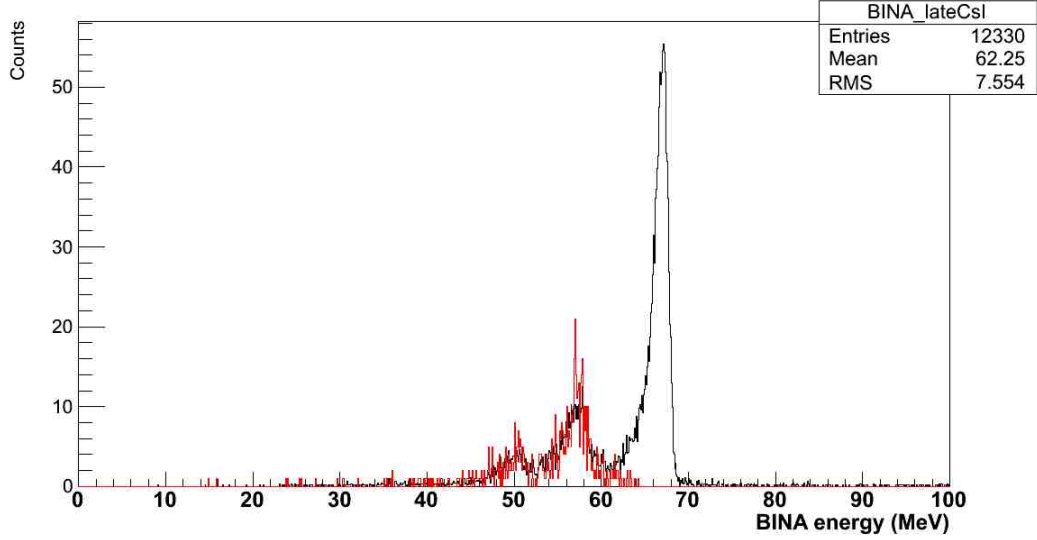


Figure 5.3: NaI(Tl) energy spectrum for events with late timing hits in the CsI with respect to the trigger. The photonuclear peaks are clearly isolated in the data (black) and well reproduced by the rescaled Geant4 simulation (red). The higher peak in the data histogram is due to beam background in the CsI crystals.

below E_c in $N(E)$, their values are

$$N_1 = N_{peak} \times \frac{N_{tot}^\mu}{N_{peak}^\mu} , \quad (5.6)$$

$$N_1 = N_{peak} \times \frac{N_{tail}^\mu}{N_{peak}^\mu} . \quad (5.7)$$

The corrected formula for the tail fraction is finally

$$LET = \frac{\int_0^{E_c} N(E)dE - N_1}{\int_0^\infty N(E)dE - N_2} . \quad (5.8)$$

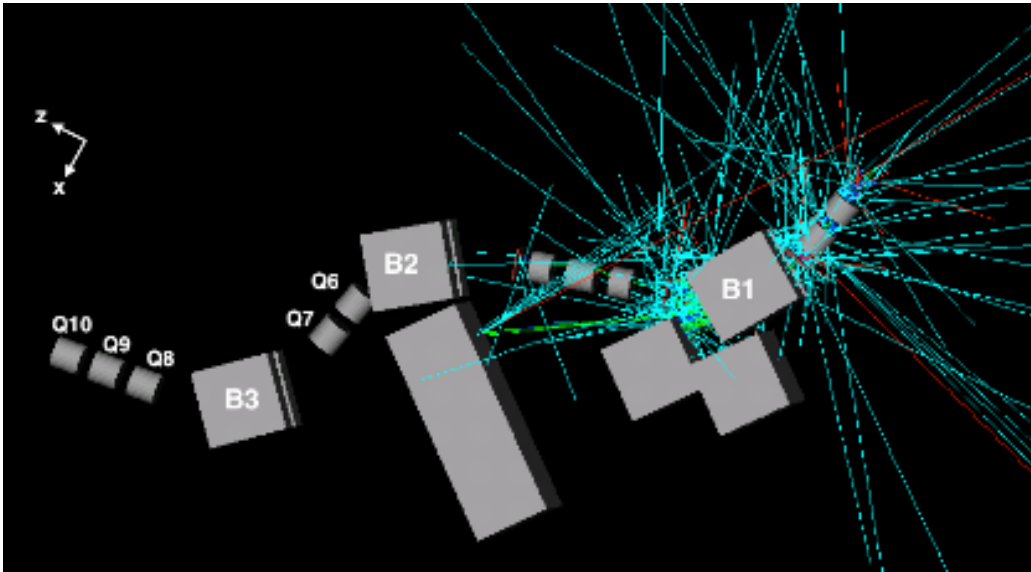


Figure 5.4: `G4beamline` simulation of the extended M13 beamline. The color lines are particle tracks, mainly coming from the initial part of the beamline.

5.1.4 Simulation of the Photonuclear Reactions

`Geant4` was able to reproduce and explain the presence of the peaks due to photonuclear reactions well. In order to reach a satisfactory agreement, the cross section of the process in the simulation had to be tuned to the data by a factor 1.1 (the effect predicted by `Geant4` was thus smaller). The scaling factor was determined isolating photonuclear events. This was achieved selecting events with late timing in the CsI crystals. The resulting spectrum after this selection is showed in Fig. 5.3.

Using a cross section scaling of 1.1 ± 0.1 was sufficient to cover the error coming from the residual disagreement between data and simulation up to 41.6° , which is equivalent to a 50 mm radial cut in the acceptance-defining detector WC3. For larger acceptances, the LET could not be estimated with enough precision with the positron beam method given the detector's geometrical constraints [157].

5.1.5 Systematic Uncertainties

The stability of the muon correction as the RF cut varied was used to assign a systematic error [157]. Backgrounds can also influence the LET and their level can be estimated from the spectrum in Fig. 5.1 (left). The events to the right of the main peak were caused by a normal positron event coincident with a positron from a muon decay. This kind of events could affect the LET only in the case where an event that would have been in the <52 MeV region ended up above 52 MeV due to the presence of the extra positron. Events where a decay positron made the trigger were almost completely removed by the cut requiring hits consistent in time in all three WC1/2 wire planes. The presence of additional flat backgrounds could also influence the LET but for example, at 0° the fraction of events < 10 MeV was $< 10^{-5}$, which was not sufficient for significantly contribute to the LET.

Other backgrounds coming from the beamline were studied with a full G4beamline simulation [163], finding no significant contributions to the tail. The beamline was simulated in a variety of settings where the positions of slits and magnetic field strengths were varied, obtaining a negligible tail of $(2.8 \pm 0.5) \times 10^{-2}$ % at the final focus F4.

The energy calibration of the calorimeter assembly was verified as accurate within 0.1 MeV. The calibration uncertainty was used for varying E_c , obtaining a corresponding systematic uncertainty.

The $\pm 0.1^\circ$ error on the angle of the calorimeter assembly was also taken into account for deriving a systematic error, since the LET was dependent from it.

The beam phase-space distribution used in the simulation was derived from data and its influence on the LET was also studied [157].

5.1.6 Calculation of the Low Energy Tail

The positron data were essential for validating the Geant4 simulation, but they could not be used alone for estimating the LET. During normal data taking, also other detectors were present along the positron tracks (the target B3, T1, and the silicon detectors). The full validated simulation was finally used to determine the LET of the $\pi^+ \rightarrow e^+ \nu_e$ events, including the radiative decays $\pi^+ \rightarrow e^+ \nu_e \gamma$. The full simulation took into account also the important contribution coming from Bhabha scattering,

R_{max} (mm)	LET (%)	Stat. Error (%)	Syst Error (%)
30	2.174	0.023	0.028
40	2.572	0.020	0.045
50	3.061	0.019	0.068
60	3.613	0.018	0.095
70	4.253	0.018	0.115
80	4.996	0.018	0.154
90	5.886	0.091	0.198

E_c (MeV)	LET (%)	Stat. Error (%)	Syst Error (%)
50	2.806	0.016	0.063
51	3.160	0.017	0.076
52	3.613	0.018	0.095
53	4.172	0.020	0.116
54	4.887	0.021	0.142
55	5.784	0.023	0.173

Table 5.1: Estimated low energy tails for different values of the angle and cut-off energy E_c .

multiple scattering in the detectors, and the beam conditions (see next section). The results for the LETs at various angles and cut-off energies are summarized in Tab. 5.1.

5.1.7 Simulation of the Pion Beam

For simulating the correct pion stopping distribution (which has an influence on the LET), the pion beam phase space should be reproduced.

In the Geant4 simulation, the pion beam particles were parameterized by the two transverse coordinates (x, y) at $z = 0$, the normalized momentum components p_x, p_y, p_z , and the energy E . The pions were started at the position (x_s, y_s, z_s) 60 cm before B3:

$$\begin{cases} x_s = -60 \frac{p_x}{p_z} + x \\ y_s = -60 \frac{p_y}{p_z} + y \\ z_s = -60 \end{cases} \quad (5.9)$$

Using the data and the tracking while applying the same analysis cuts used in the branching ratio analysis, the distributions for the variables

$$\begin{cases} x \\ y \\ t_x = p_x/p_z \\ t_y = p_y/p_z \end{cases} , \quad (5.10)$$

can be extracted.

The total energy distribution can be approximately estimated summing the full energy deposited in B1, B2, S1, S2, and B3. Having the distributions for the single variables of the beam phase space, it is possible in principle to randomly sample them and simulate the beam. This procedure neglects correlations among the variables, like for example the relatively strong correlation between x and the energy.

For taking into account the correlations, the following method was employed. First, the 5×5 correlation matrix C_{ij} was calculated and then a *Choleski decomposition* was performed [164].

The decomposition finds a matrix U such that

$$C_{ij} = U_{ik}^T \cdot U_{kj} \quad . \quad (5.11)$$

The Choleski matrix can thus be seen as a "square root" of the correlation matrix. The decomposition can be done for symmetric and positive-definite matrices (which are indeed properties of a correlation matrix) with the following iterative procedure

$$\begin{aligned} U_{ii} &= \sqrt{C_{ii} - \sum_{k=1}^{i-1} U_{ik}^2} \\ U_{ji} &= \frac{1}{U_{ii}} \left(C_{ij} - \sum_{k=1}^{i-1} U_{ik} U_{jk} \right) ; j = i + 1, i + 2, \dots, N \quad . \end{aligned} \quad (5.12)$$

The problem is now the generation of a vector v of *correlated* random numbers. If a 5-dimensional vector w is constructed sampling independently the phase space variables distributions, the correlated random vector will be

$$v_i = w_j U_{ji} \quad . \quad (5.13)$$

The result of the transformation on the sampled variables used in the MC are showed in Fig. 5.5.

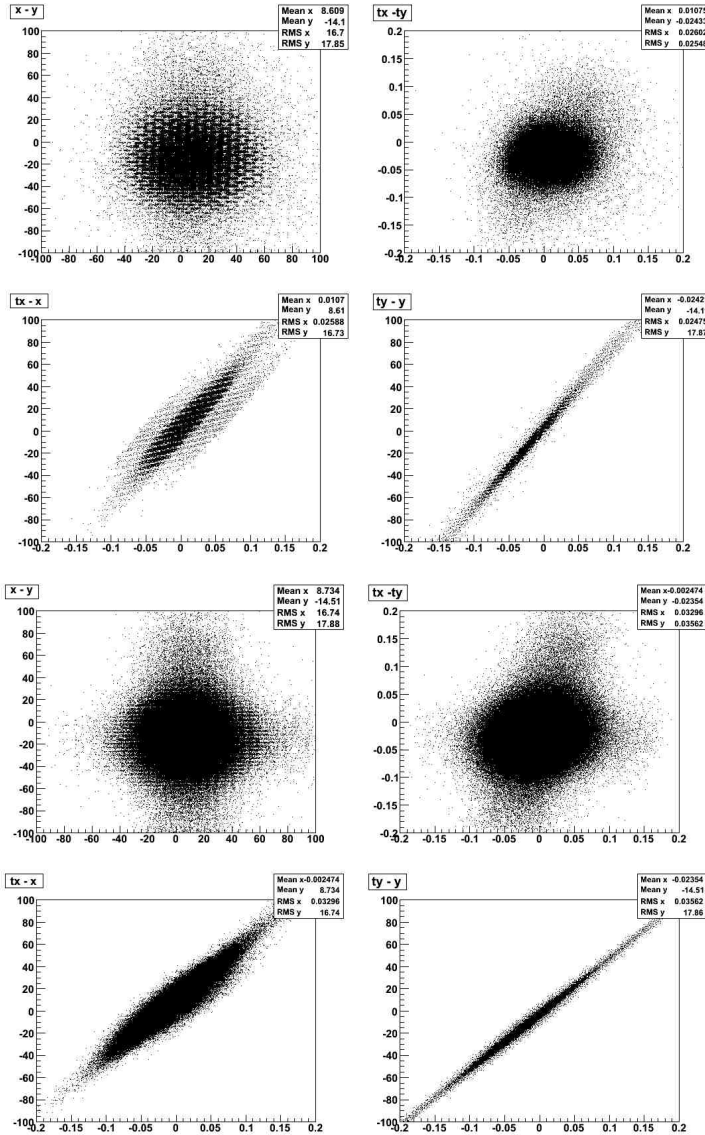


Figure 5.5: (Top four histograms) Correlations among independently sampled beam variables. (Bottom four histograms) Correlations among sampled beam variables after applying the Choleski transformation.

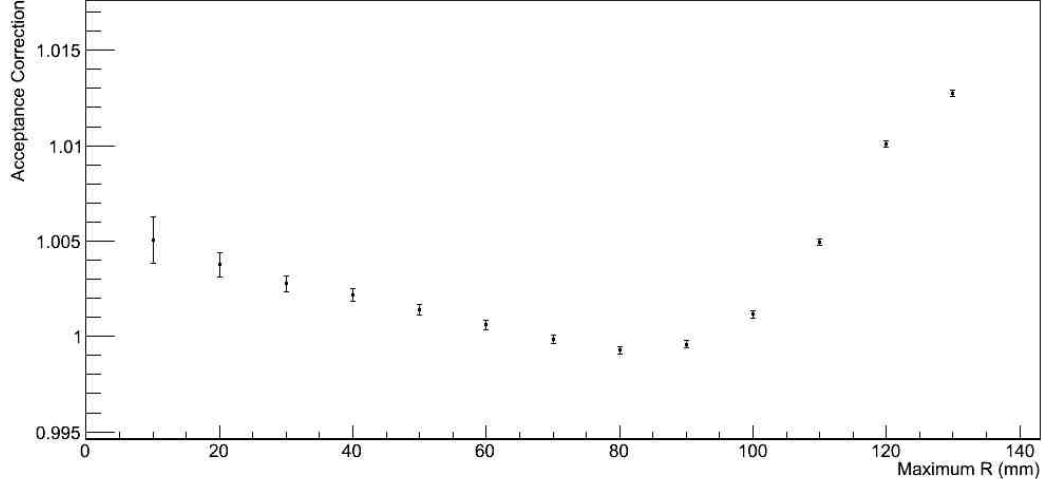


Figure 5.6: Acceptance correction A_{corr} as a function of the WC3 radius for the 2012 dataset (the errors are statistical only).

5.2 Acceptance Correction

At first approximation, the acceptance for the $\pi^+ \rightarrow e^+ \nu_e$ and $\pi^+ \rightarrow \mu^+ \nu_\mu \rightarrow e^+ \nu_e \bar{\nu}_\mu$ decays is the same, since they are both measured at the same time with the same apparatus. Processes happening in materials traversed by the decay positrons (like multiple scattering, Bhabha scattering, pair production) are energy dependent, and since the two decay modes produce positrons in different energy ranges, they can alter the acceptance.

The acceptance correction quantifying this small difference was estimated with the Geant4 simulation separately for the three datataking periods since the beam conditions were slightly different (a different beam momentum changes the pion stopping distribution and therefore the acceptance).

A total of 10^9 events for each decay mode and datataking period were simulated and the correction factor

$$A_{corr}(R) = \frac{N(\pi^+ \rightarrow e^+ \nu_e)}{N(\pi^+ \rightarrow \mu^+ \nu_\mu \rightarrow e^+ \nu_e \bar{\nu}_\mu)} \quad , \quad (5.14)$$

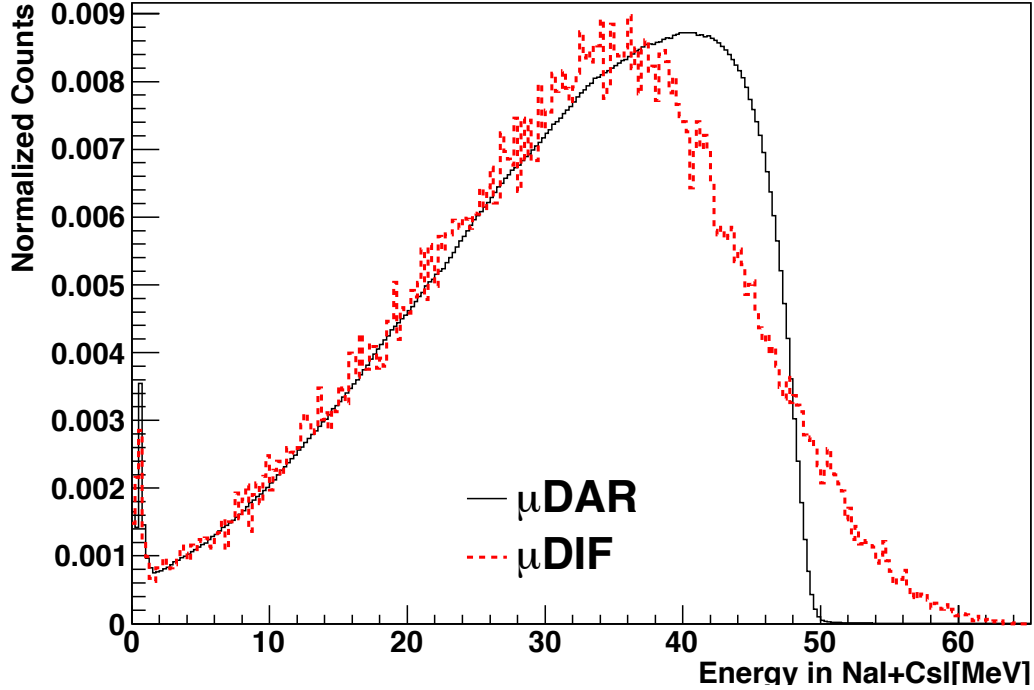


Figure 5.7: Simulated energy distributions of positrons coming from the $\pi^+ \rightarrow e^+ \nu_e$ decay chain. The black histogram corresponds to positrons from stopped muons, while the red histogram corresponds to events where the muon decayed in flight in the target.

was calculated. N is the number of events in the energy spectrum for a maximum value of the radius R . The results are showed in Fig. 5.6 for the 2012 data set. The systematic error on A_{corr} was obtained by varying several parameters in the simulation: the position and width of the pion stopping distribution, the positions and thicknesses of various detectors, and the trigger thresholds in T1 and T2. All the uncertainties (both statistical and systematic) are at the 10^{-8} level, and thus negligible in their impact on the branching ratio error.

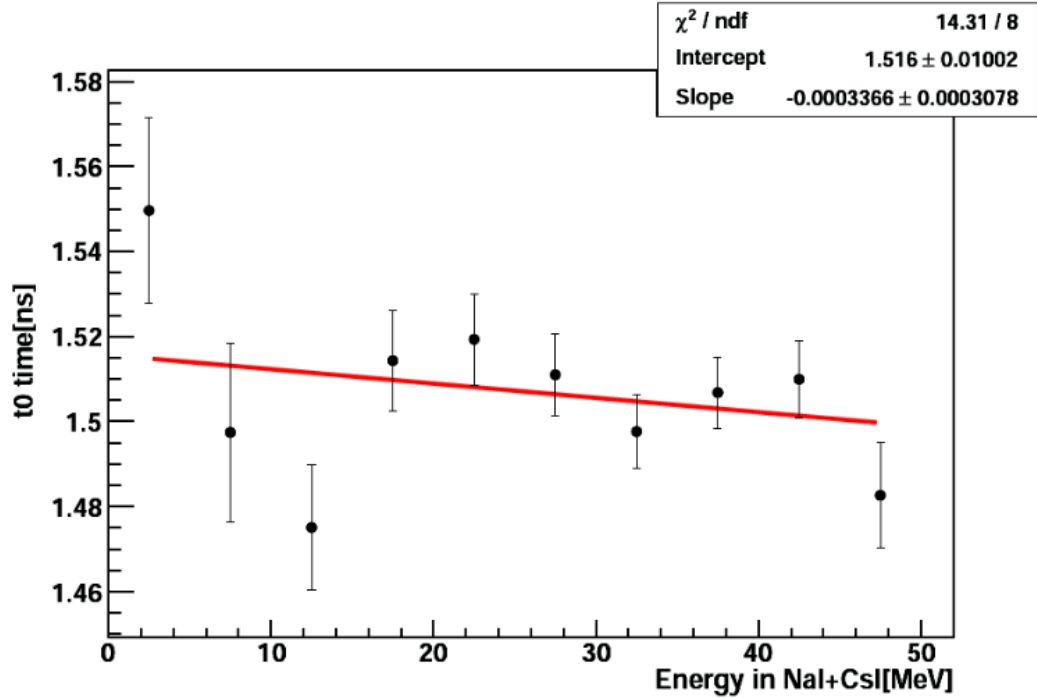


Figure 5.8: Fitted value of t_0 as a function of the positron energy.

5.3 Muon Decay in Flight Correction

Muons can decay in flight in the target and mimic the timing of the $\pi^+ \rightarrow e^+ \nu_e$ decay. These events cannot be detected and separated from the $\pi^+ \rightarrow e^+ \nu_e$ events and a correction was needed. The MC simulation showed that the decay time distribution of muons which were not at rest in the target was approximately flat between 0 and 19 ps. The probability of a muon decay in flight can be estimated as

$$1 - e^{-\frac{19\text{ps}}{2197\text{ns}}} = 8.3 \times 10^{-6} \quad . \quad (5.15)$$

The proportion of these events above $E_c = 52$ MeV was estimated with the simulation to be 2.37% (see Fig. 5.7), giving a total correction factor

$$C_{\mu DIF} = 0.0237 \times 8.3 \times 10^{-6} = 1.97 \times 10^{-7} \quad . \quad (5.16)$$

Taking into account the level of agreement of the energy spectra between data and simulation (few percent), the error on $C_{\mu DIF}$ is negligible.

5.4 t_0 Correction

The timing of the positrons was calculated fitting the waveforms from the T1 scintillator. If the shape of the waveform depended from the positron energy, also the extracted time could be energy-dependent, affecting ultimately the branching ratio.

To investigate this effect, time spectra for different energy regions were constructed and t_0 (the starting point of the spectrum) was obtained by fitting the edge with a step function with Gaussian resolution (see Fig. 5.8). Using 2010 data, a correction of 1.0004 ± 0.0005 was obtained. Using 2011, the obtained correction was 1.0006 ± 0.0003 .

5.5 Summary

After the extraction of the raw branching ratio with the fit of the time spectra corresponding to low- and high-energy regions, corrections were applied. The largest correction was due to the presence of the low-energy tail (LET) of the $\pi \rightarrow e\nu$ events. The LET could not be extracted from the time fits and had to be estimated in another way. The method employed was based on injecting a positron beam in the calorimeter at different angles for characterizing its response and comparing it with the simulation. In turn, the simulation was accurately tuned to the data and then used to simulate the whole experiment and estimate the LET.

A detailed simulation showed that no additional low energy tail was added by the beamline elements. The second correction was due to the presence of muons decaying in flight into the target. This component had the same time structure of the $\pi^+ \rightarrow e^+\nu_e$ decays and thus it cannot be subtracted with the fit.

The third correction came from time-walk effects in the time determination: the timing of an event could have been correlated with its energy (waveform amplitude).

Another correction was due to acceptance differences between the two decays. These differences came from energy-dependent processes in the detector materials.

Chapter 6 | Results

Results from the branching ratio analysis as well as from searches of BSM particles will be presented. The previous two chapters described the fitting technique of the time spectra for the extraction of the branching ratio and its corrections. Here the results of the fits are reported together with the (blinded) results for the branching ratio. Searches for majorons and massive neutrinos in pion and muon decays will also be described.

6.1 The $\pi^+ \rightarrow e^+ \nu_e$ Branching Ratio

The simultaneous fit to the high-energy and low-energy timing spectra allowed for the extraction of the branching ratio (BR). The BR is the ratio of the $\pi^+ \rightarrow e^+ \nu_e$ and $\pi^+ \rightarrow \mu^+ \nu_\mu \rightarrow e^+ \nu_e \bar{\nu}_\mu$ components with the automatic subtraction of the backgrounds. The radiative counterparts of the processes were taken into account.

The BR extracted from the fit is called *raw* branching ratio (BR_{raw}), which had to be corrected with the corrections described in the previous chapter for obtaining the final branching ratio.

At the time of writing, the analysis is in its final stages and the blinding has not been removed yet.

A first analysis of the 2010 dataset was already published [100] with a nominal acceptance of $R=60$ mm and a different procedure for estimating the LET. Here we present the results of an improved re-analysis of the 2010 data and the results for the 2011 and 2012 datasets. In this analysis, the acceptance was set to $R = 40$ mm, which was determined as the optimal choice for minimizing the systematic errors (mainly from the LET) while keeping the statistical error sufficiently low.

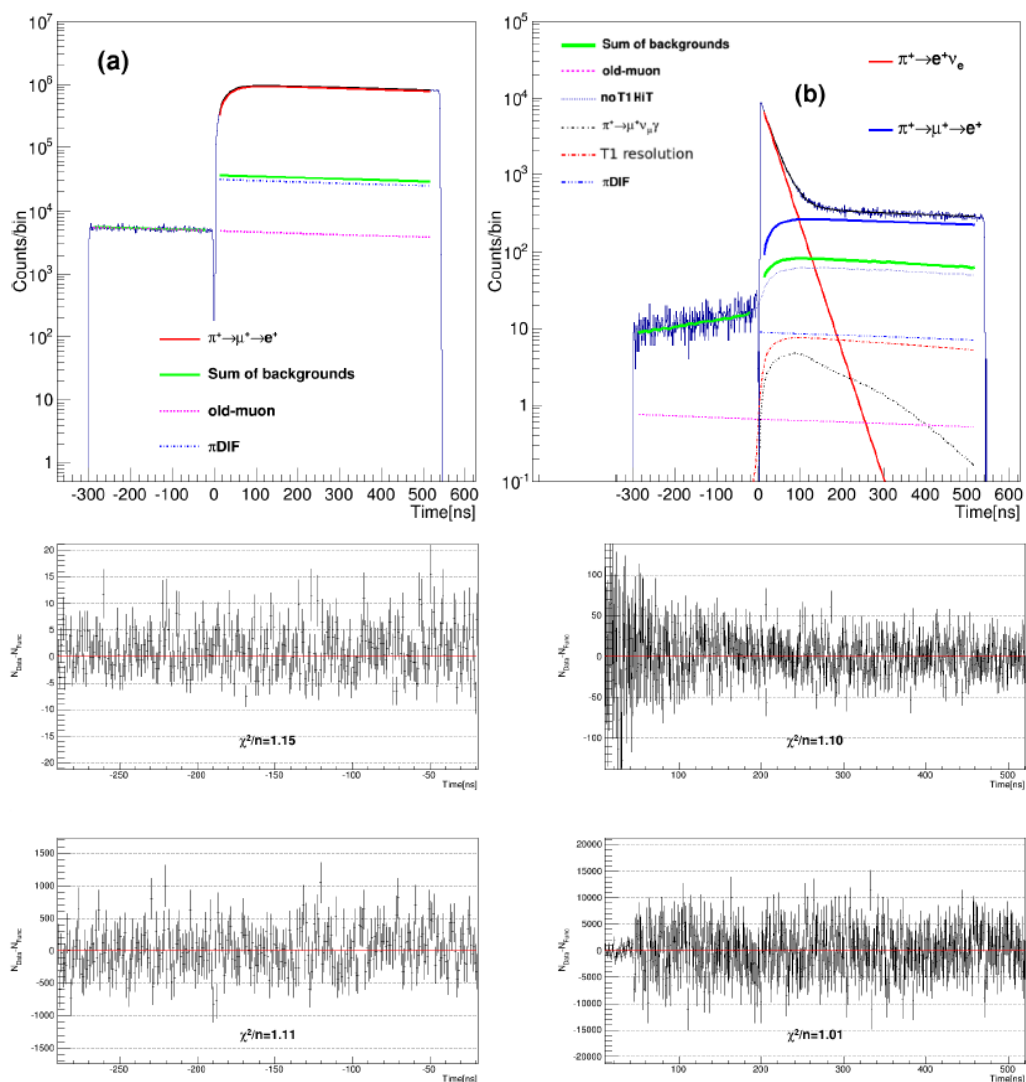


Figure 6.1: **2010 Dataset results.** (Top) Fit of the LE (a) and HE (b) time spectra. HE fit residuals for the time before (center left) and after the prompt time (center right). LE fit residuals for the time before (bottom left) and after the prompt time (bottom right).

CHAPTER 6. RESULTS

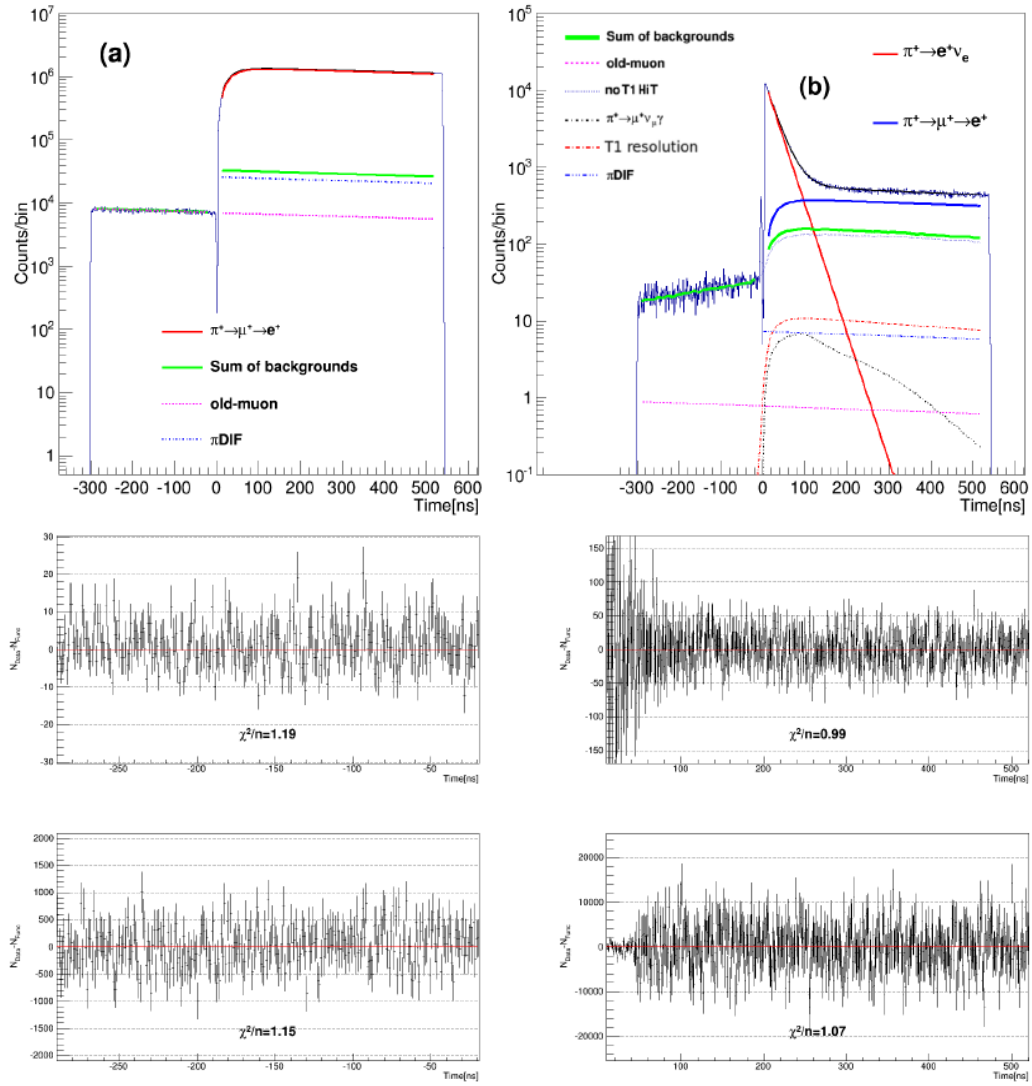


Figure 6.2: **2011 Dataset results.** (Top) Fit of the LE (a) and HE (b) time spectra. HE fit residuals for the time before (center left) and after the prompt time (center right). LE fit residuals for the time before (bottom left) and after the prompt time (bottom right).

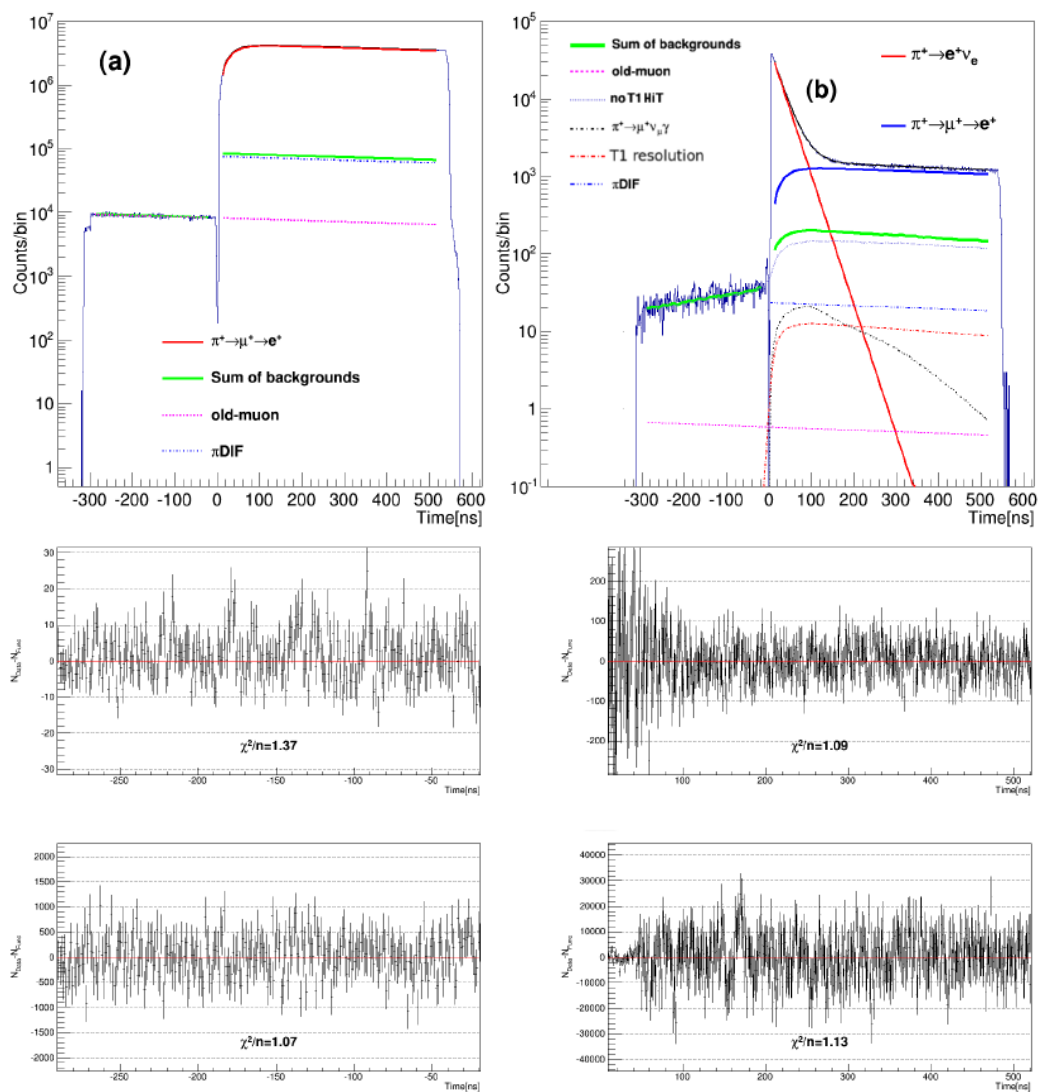


Figure 6.3: **2012 Dataset results.** (Top) Fit of the LE (a) and HE (b) time spectra. HE fit residuals for the time before (center left) and after the prompt time (center right). LE fit residuals for the time before (bottom left) and after the prompt time (bottom right).

	2010	2011	2012
$A_{\pi \rightarrow \mu \rightarrow e}$	$2.13 \cdot 10^9 \pm 8.98 \cdot 10^5$	$3.04 \cdot 10^9 \pm 1.10 \cdot 10^6$	$0.95 \cdot 10^{10} \pm 2.00 \cdot 10^6$
r	$2.92 \cdot 10^{-4} \pm 5.0 \cdot 10^{-6}$	$2.83 \cdot 10^{-4} \pm 5.30 \cdot 10^{-6}$	$3.09 \cdot 10^{-4} \pm 1.80 \cdot 10^{-6}$
t_0 (fixed)	2.15 ns	2.15 ns	2.15 ns
$O\mu$ (LE)	$1.07 \cdot 10^7 \pm 4.01 \cdot 10^4$	$1.55 \cdot 10^7 \pm 4.10 \cdot 10^4$	$1.81 \cdot 10^7 \pm 5.00 \cdot 10^4$
BR_{raw} $\times 10^{-4}$	1.2 *** ± 0.0031	1.2 *** ± 0.0026	1.2 *** ± 0.0014
τ_μ (fixed)	2197.03 ns	2197.03 ns	2197.03 ns
τ_π (fixed)	26.033 ns	26.033 ns	26.033 ns
$O\mu$ (HE)	$1.44 \cdot 10^3 \pm 1.97 \cdot 10^3$	$1.72 \cdot 10^3 \pm 3.01 \cdot 10^3$	$1.28 \cdot 10^3 \pm 3.14 \cdot 10^3$
oldmu_both	$1.81 \cdot 10^4 \pm 1.67 \cdot 10^3$	$3.77 \cdot 10^4 \pm 2.43 \cdot 10^3$	$5.29 \cdot 10^4 \pm 2.74 \cdot 10^3$
$\pi^+ \rightarrow e^+ \nu_e \gamma$ (fxd)	$4.8 \cdot 10^{-7}$	$4.8 \cdot 10^{-7}$	$4.8 \cdot 10^{-7}$
T1res (fixed)	$4.08 \cdot 10^{-4}$	$4.08 \cdot 10^{-4}$	$4.08 \cdot 10^{-4}$
ΔT	15.7 ns	15.7 ns	15.7 ns
πDIF	$6.7 \cdot 10^7 \pm 7.0 \cdot 10^5$	$5.7 \cdot 10^7 \pm 8.0 \cdot 10^5$	$1.67 \cdot 10^8 \pm 1.4 \cdot 10^6$
χ^2/dof	1.07	1.06	1.13

Table 6.1: Results from the timing spectra for the three datataking periods. The exact fit values are truncated for a more compact presentation. The errors are statistical only as obtained by the MINUIT [165] fit and the parameters marked as *fixed* (or *fxd*) were kept fixed during the fit. The statistical errors on the BR reflect the magnitude of the data samples collected in the three periods. The complete value of the branching ratio is not reported, since the datasets are still blinded. The first unblinded result referring to the 2010 dataset was published in [100].

If Fig. 6.1, 6.2, and 6.3 the results of the fits are showed. The upper panels show the fitted amplitudes superimposed on the timing spectra. The four lower panels show the residuals of the fit for the LE and HE spectra, which are further divided in two regions before and after the prompt timing (the time of arrival of the pion). The prompt time region was removed from the fit range since it was composed by beam particles (electrons and muons) traversing all the detectors and generating a sharp peak at $t=0$ ns which was removed also from Fig. 6.1, 6.2, and 6.3 for clarity.

The fit results for the three datataking periods are reported in Tab. 6.1.

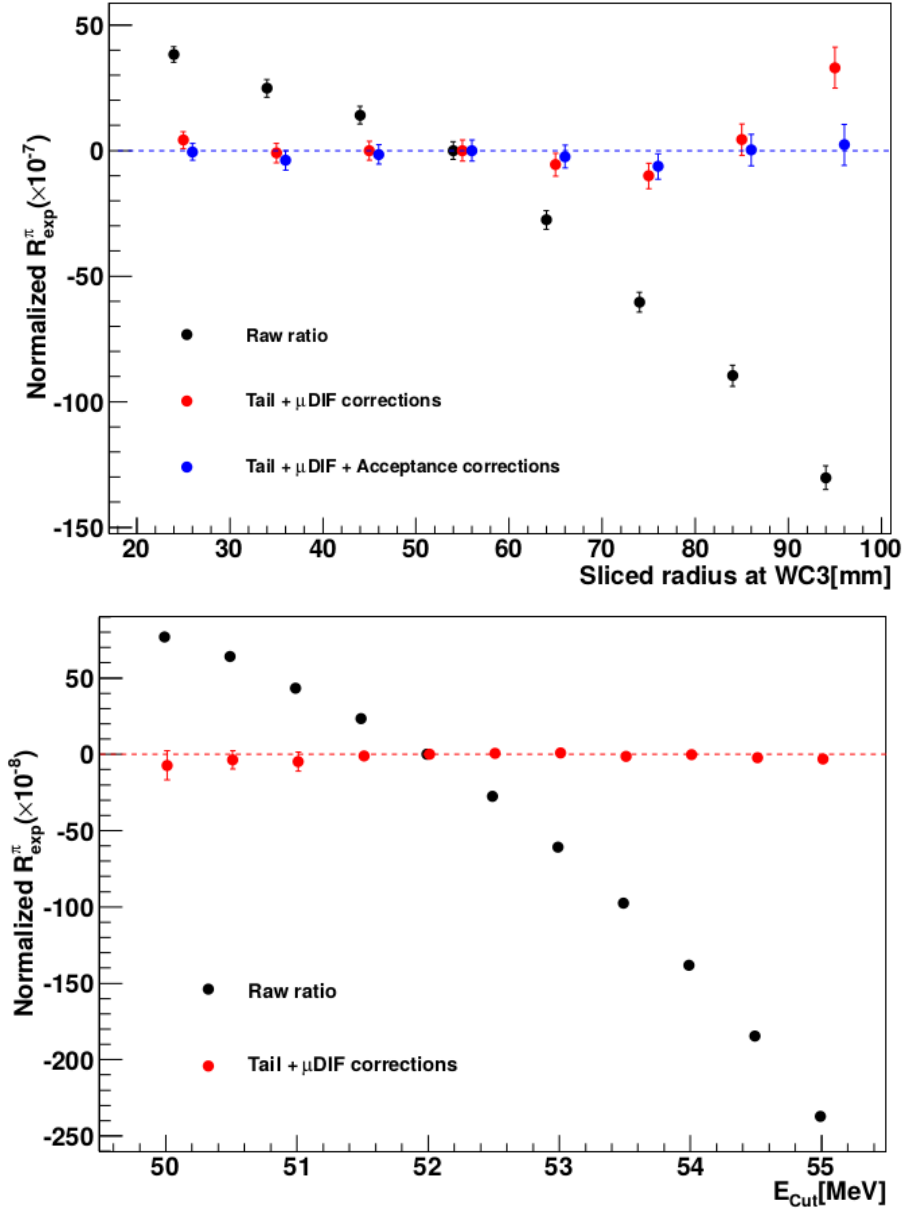


Figure 6.4: **(Top)** Dependence of the BR from the choice of the acceptance radius set with WC3 before (black) and after (red) the LET correction and the (blue) μ DIF correction. **(Bottom)** Dependence of the BR from the choice of the cut-off energy E_c before (black) and after (red) corrections (figure from S. Ito, 2011 dataset).

6.2 Systematic Checks

Before unblinding the data, some crucial tests on the BR stability had to be made. The tests involve the validity of the fit and of the LET correction.

LET tests

Since the LET is the main correction to the BR, two tests involving it are particularly important. The LET changes if a different acceptance radius R is chosen, as well as a different energy threshold E_c for separating the two energy regions. If the BR is calculated with different R and E_c , a different LET correction has to be applied. If the LET-corrected BR is stable against the change in R and E_c , there is confidence that the LET is globally well known.

The stability of the BR with respect to variations of R and E_c has been already demonstrated in the first published results [100] and it is almost finalized for the other datasets. In Fig. 6.4 the stability of the BR is showed as example for the 2011 dataset [147].

Fit stability

The BR must be stable against changes in the fit conditions. The fit results were tested changing the fitting range around the prompt region and at the two extreme limits.

Fit parameters

The stability of the BR was checked when the parameters of the fit were changed. This includes changing the pion and muon lifetimes with respect to the known values, changing the contribution of the radiative decay, and the T1 resolution shape.

Fit shapes

The shapes derived from MC were modified in order to assess the dependence of the BR from them. Additional background shapes were included in the fit for checking the sensitivity of the BR to small unaccounted backgrounds. The shapes tested were: a flat background, and a faster ($\tau_\mu/2$) decay time component.

Prepileup Window

An important diagnostic test was the stability of the BR as more pileup is allowed in the trigger window. To this end, the PrePileup window identified by the PrePileup cut was varied. This cut normally rejects events in a $6.6 \mu\text{s}$ to $2.2 \mu\text{s}$ window *before* the arrival of the pion. The rejection win-

$\Delta R \pm \Delta e [10^{-8}]$	2012	2011	2010
Fit stability tests			
Fitting range, t			
positive limit: 520 \rightarrow 490	0.5 ± 0.7	-0.3 ± 1.3	0.2 ± 1.6
prompt positive: 10 \rightarrow 8	-2.9 ± 4.3	2.2 ± 7.6	9.3 ± 9.1
prompt negative: -20 \rightarrow -30	0.0 ± 0.1	0.2 ± 0.3	0.1 ± 0.2
negative limit: -290 \rightarrow -250	-0.1 ± 0.1	0.0 ± 0.3	0.0 ± 0.1
Lifetimes			
$\tau_{\mu}^{fit} - \tau_{\mu}^{PDG}$ [ns]	1.4 ± 3.7	-8.2 ± 6.4	-1.8 ± 7.7
$\tau_{\pi}^{fit} - \tau_{\pi}^{PDG}$ [ns]	0.0 ± 0.0	0.1 ± 0.0	0.0 ± 0.0
Syst. errors (shape variation)			
Parameters fixed in the fit			
$\pi \rightarrow \mu\gamma$ ($\pm 20\%$)	$\pm 2.9 \pm 0.0$	$\pm 2.8 \pm 0.1$	$\pm 2.8 \pm 0.0$
T1 resolution ($\pm 50\%$)	$\pm 0.9 \pm 0.0$	$\pm 2.3 \pm 0.1$	$\pm 2.2 \pm 0.0$
Old-muon MC shape			
2 ns bin	-0.3 ± 0.1	-0.9 ± 0.2	-0.7 ± 0.1
3 ns bin	-1.0 ± 0.1	-2.8 ± 0.2	-1.8 ± 0.2
-1 ns shift	-1.2 ± 0.1	-3.3 ± 0.3	-2.2 ± 0.2
+1 ns shift	1.1 ± 0.1	3.2 ± 0.3	2.1 ± 0.3
Other backgrounds			
Flat component	-0.8 ± 0.5	-3.5 ± 1.6	-4.5 ± 1.8
Fast decay component	0.0 ± 0.0	0.2 ± 0.3	0.2 ± 0.4

Table 6.2: Preliminary systematic tests for the time spectrum fits.

dow was varied in the B1, B2, and B3 scintillators and the dependence of the BR from the window width was studied, without finding a significant dependence.

The results of the systematic checks are reported in Tab. 6.2.

6.3 Combination of the Datasets

The three different datasets were collected in similar conditions but differences were present besides the statistics collected. The differences did not allow for a global fit of all the data available and thus the three branching

ratios had to be combined after the separate fits to the timing spectra. In this section a procedure for combining the BRs is outlined, assuming that the various systematic uncertainties were not correlated.

In the following, the superscript *raw* indicates the BR extracted from the fit, *st* statistical errors and *sy* systematic errors.

Defining the raw BR as $R^{raw} \pm \delta R_{st}^{raw} \pm \delta R_{sy}^{raw}$ and the multiplicative corrections with their uncertainties as $C_j \pm \delta C_j$, the total systematic error is

$$\delta R_{sy} = R^{raw} \prod_j C_j \sqrt{\left(\frac{\delta R_{sy}^{raw}}{R^{raw}}\right)^2 + \sum_j \left(\frac{\delta C_j}{C_j}\right)^2} , \quad (6.1)$$

and the final corrected BR is

$$R = (R^{raw} \pm \delta R_{st}) \prod_j C_j \pm \delta R_{sy} . \quad (6.2)$$

The multiplicative corrections in this case are three:

$$j = 1, 2, 3 = (LET, \text{Acceptance}, t_0) . \quad (6.3)$$

Labeling the datataking periods with the index

$$i = 1, 2, 3 = (2010, 2011, 2012) , \quad (6.4)$$

we can define the raw BRs for the different periods as $Y_i \pm \delta Y_i^{st} \pm Y_i^{sy}$ with dataset-dependent corrections $C_{ij} \pm \delta C_{ij}^{st} \pm C_{ij}^{sy}$, common corrections $C_k \pm \delta C_k^{st} \pm C_k^{sy}$, and common systematic uncertainties $\pm \delta S$.

The BR corrected by dataset-dependent corrections is R_i , w_i is a set of weights, $R_s \pm \delta R_s^{st} \pm R_s^{sy}$ is the weighted average before common corrections, and $R_f \pm \delta R_f^{st} \pm R_f^{sy}$ is the final BR.

The BR for one dataset with its corresponding corrections is thus

$$R_i = Y_i \prod_j C_{ij} . \quad (6.5)$$

Defining the weights

$$w_i = \frac{1}{(\delta Y_i^{st})^2 + R_i^2 \left[\left(\frac{\delta Y_i^{st}}{Y_i}\right)^2 + \sum_j \left(\frac{\delta C_{ij}^{st}}{C_{ij}}\right)^2 + \sum_j \left(\frac{\delta C_{ij}^{sy}}{C_{ij}}\right)^2 \right]} , \quad (6.6)$$

the BR error-weighted average before common corrections is

$$R_s = \sum_i \frac{R_i \cdot w_i}{\sum_j w_j} , \quad (6.7)$$

with errors

$$(\delta R_s)^2 = \sum_i \left(\frac{\delta R_i \cdot w_i}{\sum_j w_j} \right)^2 ; \quad (\delta R_i)^2 = R_i^2 \cdot \left[\left(\frac{\delta Y_i^{st}}{Y_i} \right)^2 + \sum_j \left(\frac{\delta C_{ij}^{sy}}{C_{ij}} \right)^2 \right] . \quad (6.8)$$

Following the previous formulas, we can now write separately the statistical and systematic errors on R_s

$$\delta R_s^{st} = \sqrt{\frac{\sum_i R_i^2 \cdot \left[\left(\frac{\delta Y_i^{st}}{Y_i} \right)^2 + \sum_j \left(\frac{\delta C_{ij}^{st}}{C_{ij}} \right)^2 \right] \cdot w_i^2}{(\sum_i w_i)^2}} , \quad (6.9)$$

$$\delta R_s^{sy} = \sqrt{\frac{\sum_i R_i^2 \cdot \left[\left(\frac{\delta Y_i^{sy}}{Y_i} \right)^2 + \sum_j \left(\frac{\delta C_{ij}^{sy}}{C_{ij}} \right)^2 \right] \cdot w_i^2}{(\sum_i w_i)^2}} . \quad (6.10)$$

The statistical and systematic errors on the final corrected branching ratio are

$$\delta R_f^{st} = R_s \cdot \prod_k C_k \cdot \sqrt{\underbrace{\left(\frac{\delta R_s^{st}}{R_s} \right)^2}_{\text{Datataking-dep.}} + \sum_k \underbrace{\left(\frac{\delta C_k^{st}}{C_k} \right)^2}_{\text{common err.}}} , \quad (6.11)$$

$$\delta R_f^{sy} = \sqrt{(R_s \cdot \prod_k C_k)^2 \cdot \left[\left(\frac{\delta R_s^{sy}}{R_s} \right)^2 + \sum_k \left(\frac{\delta C_k^{sy}}{C_k} \right)^2 \right] + \underbrace{(\delta S)^2}_{\text{common syst.}}} . \quad (6.12)$$

The final expression for the branching ratio is

$$R_f = R_s \cdot \prod_k C_k \pm \delta R_f^{st} \pm \delta R_f^{sy} . \quad (6.13)$$

	BR	Stat. Error	Syst. Error
Fit			
$R_{raw} \times 10^{-4}$	Υ	δY^{st}	δY^{sy}
2010	1.2***	0.0031	0.0008
2011	1.2***	0.0025	0.0007
2012	1.2***	0.0014	0.0003
Common Corrections			
	C	δC^{st}	δC^{sy}
LET	1.0264	0.0002	0.0005
Acceptance	0.9978	0.0002	
t_0	1.0006	0.0003	
Common Systematics			δS
$\sqrt{\sum S^2}$			0.0005
Beamtime Combinations			
$R \times 10^{-4}$			
2010	1.2***	0.0031	0.0012
2011	1.2***	0.0026	0.0011
2012	1.2***	0.0015	0.0009
Total Weighted Avg.	1.2***	0.0013	0.0009

Table 6.3: Preliminary (blinded) results for the branching ratio. All the numbers are in units of 10^{-4} .

6.4 Branching Ratio Results

The final (blinded) results for the branching ratio are showed in Tab. 6.3. The results are presented for the single datataking periods with the corresponding statistical and combined systematic errors. The systematic errors of the fit were obtained combining the systematic uncertainties coming from the stability tests of the fit described in Sec. 6.2 together with the analysis systematic tests.

The combination of the results was done using the equations described in Sec. 6.3.

6.5 Search for Heavy Neutrinos in the $\pi^+ \rightarrow e^+ \nu_e$ Decay

The motivations for the search for heavy neutrino searches were given in Sec. 2.5.6. Pion, Kaon and B meson decays can be used for heavy neutrino searches. In particular, leptonic two-body decays like $\pi \rightarrow e \nu$ have a fixed kinematics which results in a precise final state energy for the lepton, given the pion four-vector. In the case of the PIENU experiment, the pion is at rest and therefore the lepton energy was fixed by energy-momentum conservation

$$E_{e^+} = \frac{m_\pi^2 + m_e^2 - m_\nu^2}{2m_\pi} . \quad (6.14)$$

In the SM case where $m_\nu \approx 0$ we have $E_{e^+} \sim 70$ MeV. If the neutrino mixes with heavy states where $m_\nu > 0$, E_{e^+} will be smaller. The experimental signature will be a peak in the positron energy spectrum with $E_{e^+} < 70$ MeV. Thus a peak search on the low-energy tail of the $\pi \rightarrow e \nu$ decay could potentially detect such a peak or set limits to its existence.

Unfortunately, the LET is hidden by the massive $\pi^+ \rightarrow \mu^+ \nu_\mu \rightarrow e^+ \nu_e \bar{\nu}_\mu$ background, which can be only partially removed. To this end, very tight cuts were set for removing as much background as possible and suppress the $\pi \rightarrow \mu \rightarrow e$ contribution:

- A timing cut between 3 and 35 ns selected most of the $\pi^+ \rightarrow e^+ \nu_e$ events, given the $\tau_\pi = 26.03$ ns pion decay constant.
- A cut on the total energy seen by B1, B2, B3, S1, and S2. B3 used a longer (100 ns) integration window with respect to the branching ratio analysis. This choice allowed to integrate also the muon energy deposit. Because of the presence of the muon, the $\pi^+ \rightarrow \mu^+ \nu_\mu \rightarrow e^+ \nu_e \bar{\nu}_\mu$ decay deposits more energy in B3 with respect to the $\pi^+ \rightarrow e^+ \nu_e$ decay (Fig. 6.5 (left)). This was the most powerful cut for rejecting the unwanted background.
- Using tracking before and after the target, the Z position of the decay vertex can be estimated. Given the presence of the muon, the $\pi^+ \rightarrow e^+ \nu_e$ decay had a wider distribution for the Z coordinate of the decay vertex (Fig. 6.5 (right)). This information can be used to reject the unwanted events.

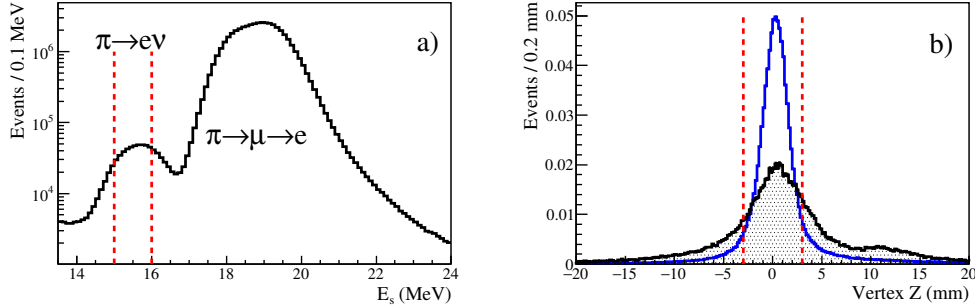


Figure 6.5: **a)** Sum of the energies in B1, B2, S1, S2, and B3. **(b)** Z vertex for events with positron energy $E_{e^+} < 52$ MeV (shaded histogram) and $E_{e^+} > 52$ MeV (blue full line). The two distributions are normalized to the same number of events, and cuts applied are indicated by the red vertical dashed lines.

Besides these specialized suppression cuts, the other analysis cuts were the same as for the branching ratio analysis. The acceptance radius was fixed at $R = 80$ mm for maximizing the acceptance, since no LET correction was needed in this case.

The final data sample contained about 10^7 $\pi^+ \rightarrow e^+ \nu_e$ decays, about 10 times more than the dataset used in a previous search [166]. The final suppressed spectrum is showed in Fig. 6.6 .

Although the $\pi^+ \rightarrow \mu^+ \nu_\mu \rightarrow e^+ \nu_e \bar{\nu}_\mu$ component was strongly suppressed, backgrounds still remain and have to be subtracted. The following background and signal shapes were simultaneously fitted to the energy spectrum:

- A shape representing the remaining $\pi^+ \rightarrow \mu^+ \nu_\mu \rightarrow e^+ \nu_e \bar{\nu}_\mu$ decays was derived from the data selecting late-time events ($t > 200$ ns) where the $\pi^+ \rightarrow e^+ \nu_e$ component is negligibly small.
- A shape derived from MC where the muon in the $\pi^+ \rightarrow \mu^+ \nu_\mu \rightarrow e^+ \nu_e \bar{\nu}_\mu$ decay chain decays in flight in the target, mimicking the $\pi^+ \rightarrow e^+ \nu_e$ timing.
- A shape representing the $\pi^+ \rightarrow e^+ \nu_e$ LET. This shape was a triple-exponential fit to the simulated LET.

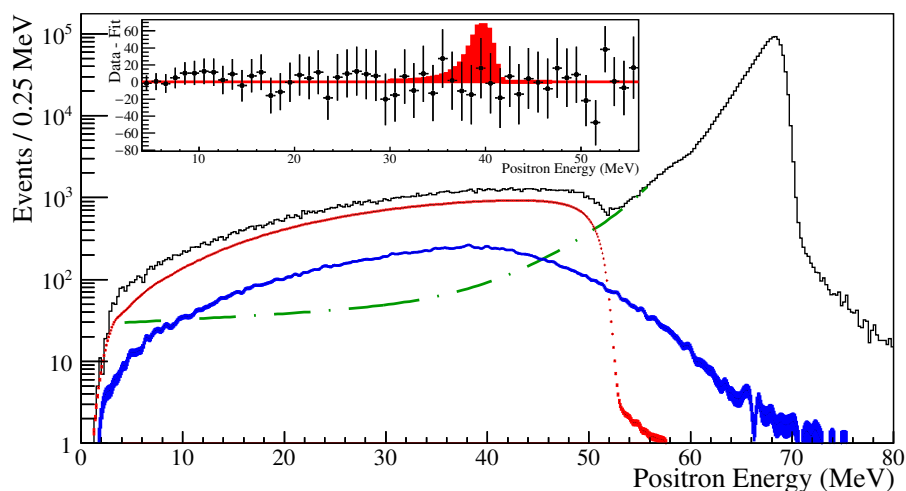


Figure 6.6: Suppressed positron energy spectrum (black histogram). Fitted components: muon decays in flight (blue line, from MC), $\pi^+ \rightarrow e^+ \nu_e$ (green, dot-dashed line, fit to MC), and $\pi^+ \rightarrow \mu^+ \nu_\mu \rightarrow e^+ \nu_e \bar{\nu}_\mu$ (red dashed line, from late-time data events). The top insert shows the residuals (Data-Fit) with statistical error bars and the signal shape in the example case of $E_{e^+} = 40$ MeV and $|U_{ei}|^2 = 10^{-8}$.

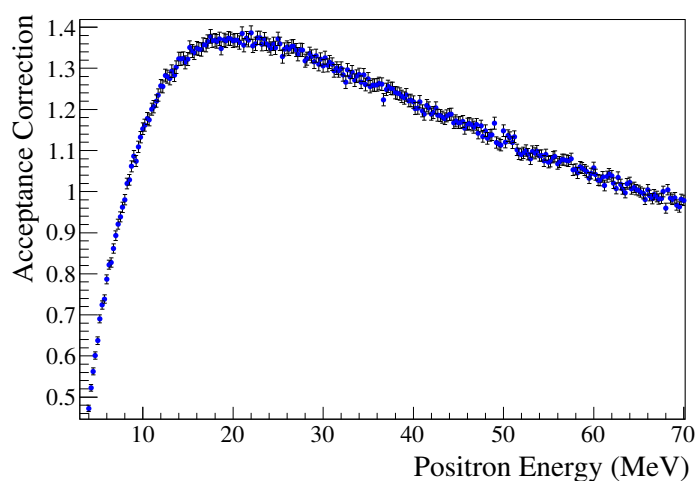


Figure 6.7: Acceptance correction $Acc(E_{e^+})$ determined via MC simulation with statistical error bars.

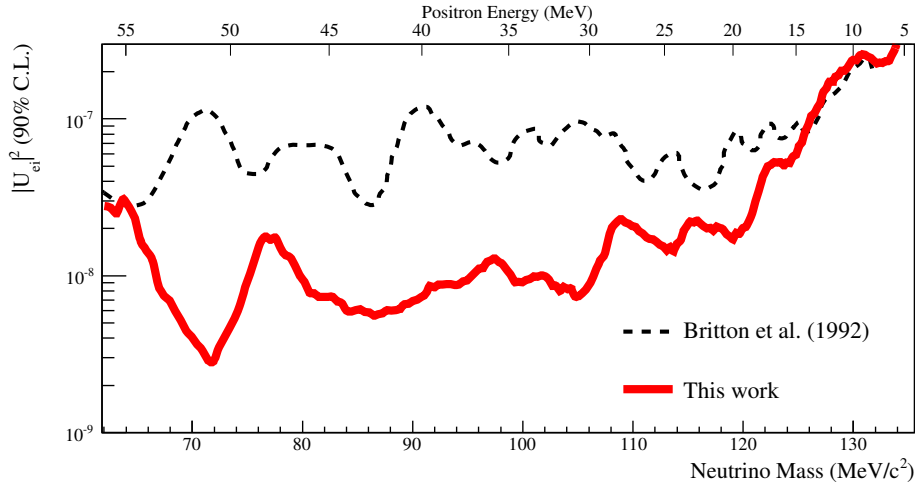


Figure 6.8: 90% C.L. upper limits on the square of the mixing matrix elements $|U_{ei}|^2$ of heavy neutrinos coupled to electrons (thick red line). The black dashed line shows the results from [166].

- A signal shape derived from MC. The shape is similar to the $\pi^+ \rightarrow e^+ \nu_e$ shape but it is peaked to a different E_{e^+} according to Eq. 6.14. An example of the signal shape can be seen in the insert of Fig. 6.6 for the case of $E_{e^+} = 40$ MeV and $|U_{ei}|^2 = 10^{-8}$.

The fit to the spectrum between 4 to 56 MeV using only the background shapes described the data well, yielding $\chi^2/\text{ndof} = 197.2/203 = 0.97$ (Fig. 6.6). The fit was repeated introducing the signal shape and shifting it by 0.25 MeV from 4 to 56 MeV. The fit returned the signal yield as the integral of the signal shape $N(\pi^+ \rightarrow e^+ \nu_e)$. The number of $\pi^+ \rightarrow e^+ \nu_e$ events $N(\pi^+ \rightarrow e^+ \nu_e)$ was obtained fitting a simulated shape to the experimental spectrum using as fitting region only the peak. A 90% upper limit $N(\pi \rightarrow e \nu_i)_{UL}$ to the existence of the signal was calculated with a Bayesian procedure assuming a flat prior for positive peak amplitudes (and zero otherwise) and assuming a Gaussian distribution for the likelihood.

An upper limit $|U_{ei}|_{UL}^2$ on the squared matrix element describing the mix-

ing with a massive sterile neutrino state was obtained using

$$\frac{1}{Acc(E_{e^+})} \frac{N(\pi^+ \rightarrow e^+ \nu_i)_{UL}}{N(\pi^+ \rightarrow e^+ \nu_e)} = |U_{ei}|_{UL}^2 \rho_e(E_{e^+}) \quad , \quad (6.15)$$

where $\rho_e(E_{e^+})$ is a phase space and helicity-suppression factor [167]

$$\rho_e(E_{e^+}) = \frac{\sqrt{1 + \delta_e^2 + \delta_i^2 - 2(\delta_e + \delta_i + \delta_e \delta_i)}}{\delta_e(1 - \delta_e)^2} \times (\delta_e + \delta_i - (\delta_e - \delta_i)^2) \quad ,$$

with

$$\delta_e = \left(\frac{m_e}{m_\pi} \right)^2 \quad , \quad \delta_i = \left(\frac{m_{\nu_i}}{m_\pi} \right)^2 \quad , \quad m_{\nu_i} = \sqrt{m_\pi^2 - 2m_\pi E_{e^+} + m_e^2} \quad .$$

The notation $|U_{ei}|_{UL}^2$ was used for indicating a generic mixing with a massive sterile neutrino without specifying the number of additional states. If only one additional neutrino is assumed (as e.g. in [168, 169]), then $i=4$. The factor $Acc(E_{e^+})$ is an acceptance correction arising from the suppression cuts which are energy-dependent. This correction was estimated using the MC simulating uniformly distributed positron tracks at a given energy E_{e^+} with the suppression cuts. The relative acceptance correction was taken as the ratio between the number of events obtained and the number of events at the $\pi^+ \rightarrow e^+ \nu_e$ energy $E_{e^+} \sim 70$ MeV. The obtained acceptance correction is showed in Fig. 6.7 and the final 90% upper limits on $|U_{ei}|^2$ are in Fig. 6.8. The obtained limits can be compared with the global analysis presented in Fig. 6.9 taken from [168].

6.6 Other BSM Searches

The large data sample collected by the PIENU experiment enables more searches of particles predicted by BSM theories. In the following, two examples will be discussed: a search for massive neutrinos using the muon decay and a search for majorons.

6.6.1 Search for Heavy Neutrinos in the $\pi^+ \rightarrow \mu^+ \nu_\mu$ Decay

The search presented in Sec. 6.5 can be performed also in the more common pion decay $\pi^+ \rightarrow \mu^+ \nu_\mu$ for extracting limits to the mixing matrix

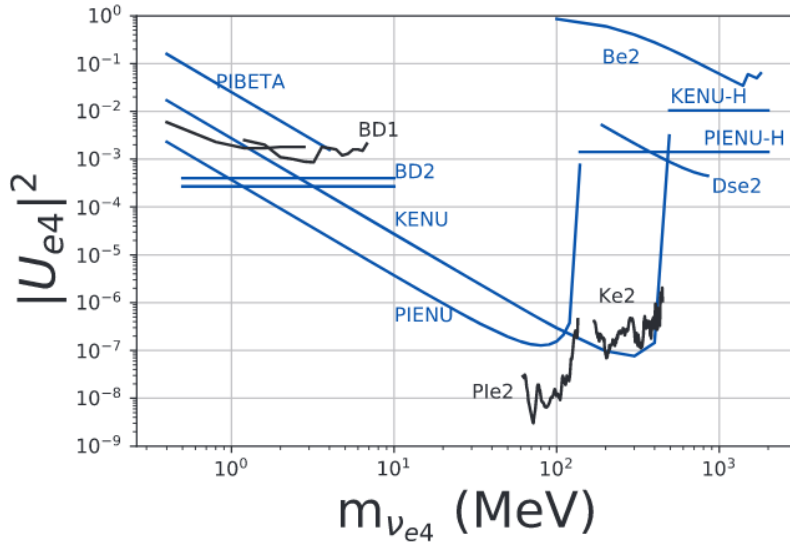


Figure 6.9: Global analysis of sterile neutrino limits from [168] (see also [169]) where for simplicity only one additional sterile neutrino was assumed ($i=4$). The black line marked with PIe2 is the latest peak-search PIENU result [170], while the one marked with Ke2 is the peak-search from the NA62 experiment [171, 172]. Other limits are from pion beta decay (PIBETA experiment [173]), previous limits from beta decay (BD1, and the re-analysis of [168] BD2), PIENU and PIENU-H using the $\pi^+ \rightarrow e^+ \nu_e$ branching ratio (see Sec. 7.5), KENU and KENU-H using the $K^+ \rightarrow e^+ \nu_e$ branching ratio. The Dse2 and Be2 lines come from the $D_s^+ \rightarrow e^+ \nu_e$ and $B_s^+ \rightarrow e^+ \nu_e$ decays, respectively.

element $|U_{\mu i}|^2$.

Having to tag the presence of a muon, the most important information is provided by the target B3. After the pion decay at rest in the target, the muon remained almost always fully contained there and thus this scintillator can provide information on the total energy deposit.

The analysis used the same datasets of the previous branching ratio analysis, plus the 2009 dataset, where no information from the CsI was recorded. The muon energy peak in the target was calibrated to 4.12 MeV energy deposit as predicted by the simulation with quenching effects for all the datasets, and then all the data were merged together. The data collected with the prescaled trigger were used, resulting in a final statistics of $\sim 10^9$ muon decays. Saturation effects in the PMTs and other electronics were

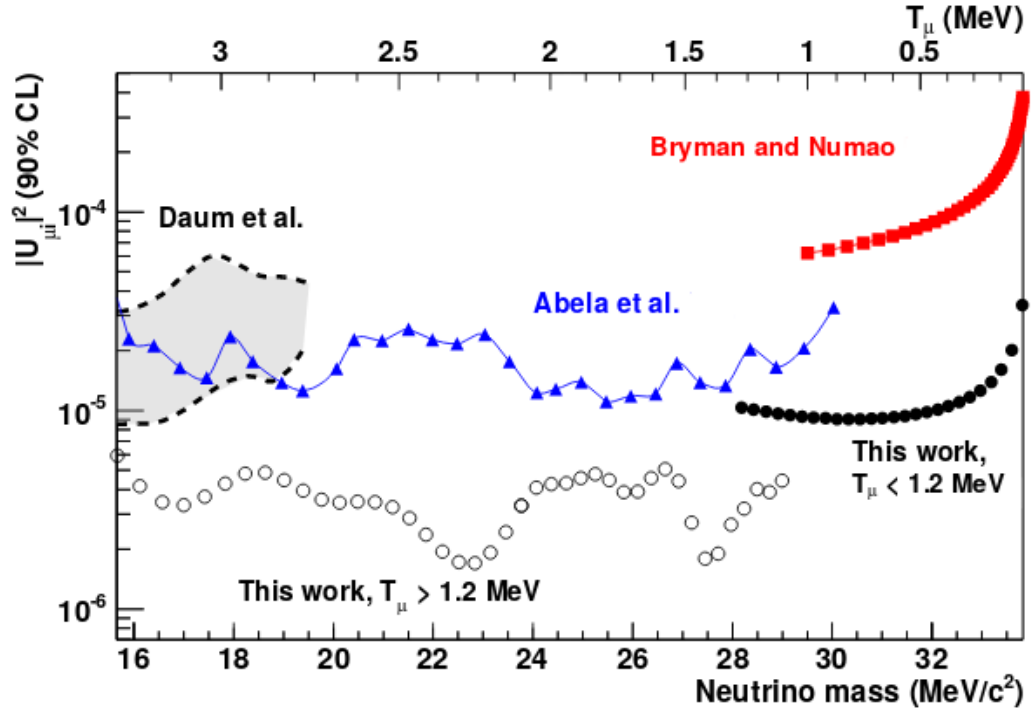


Figure 6.10: Summary of the 90% C.L. upper limits to $|U_{\mu i}|^2$. The blue and red lines are the results of [174] and [175], respectively. The gray shaded region is the result of [176]. The black full circles are the PIENU results for $0 < E_{\mu} < 1.2$ MeV, while the black open circles refer to $1.1 < E_{\mu} < 3.3$ MeV [177].

also studied and found negligible.

The $\pi^+ \rightarrow \mu^+ \nu_{\mu}$ events were identified with the requirements

- $E(\text{NaI(Tl)}+\text{CsI}) < 55$ MeV,
- $R < 80$ mm,

and the same main cuts of the branching ratio analysis for rejecting pile-ups and identify incoming pions were applied.

The data analysis was divided into two parts corresponding to two muon energy regions:

1. $E_{\mu} > 1.2$ MeV. In this region, it was possible to clearly see the pulse

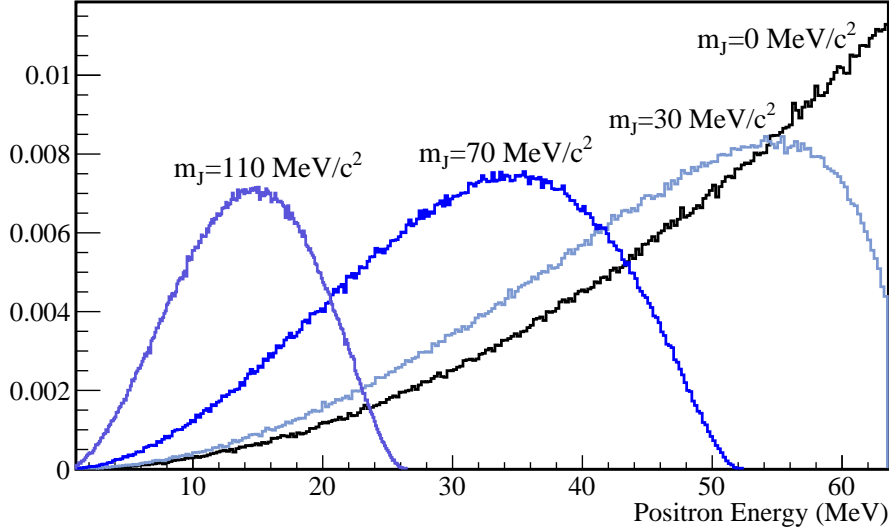


Figure 6.11: Simulated positron spectra for the $\pi^+ \rightarrow e^+ \nu_e J$ decay for different m_J cases.

given by the muon. Accidental backgrounds are the major component besides the muon signal.

2. $E_\mu < 1.2$ MeV. In this region, the pulse detection logic was not efficient enough. The presence of the muon was sought considering the integrated charge in a long gate up to 600 ns, which includes also the pion pulse. The main background in this energy region was π DIF very close to B3, and the low-energy tail of very early pion decays contributing to the 4.12 MeV peak via energy resolution effects.

The obtained result (see Fig. 6.10) was published in [177], improving by about one order of magnitude over the previous searches in the same mass region.

6.6.2 Search for Majorons in the $\pi^+ \rightarrow e^+ \nu_e$ Decay

In Sec. 2.5.7 Majorons were introduced. Under the hypothesis that a Majoron J with mass m_J is emitted in the three-body decay process $\pi^+ \rightarrow$

$e^+ \nu_e J$, the positron energy spectrum would be¹

$$\begin{aligned} \frac{d\Gamma_{\pi \rightarrow e\nu J}}{dE_e} &= \frac{|y|^2 G_F^2 f_\pi^2 |V_{ud}|^2}{32\pi^3} m_\pi \sqrt{E_e^2 - m_e^2} \\ &\times \left(\frac{m_\pi E_e - 2E_e^2 + m_e^2}{m_\pi^2 - 2m_\pi E_e + m_e^2} \right) \left(1 - \frac{m_J^2}{m_\pi^2 - 2m_\pi E_e + m_e^2} \right)^2, \end{aligned} \quad (6.16)$$

where y is a coupling constant, G_F the Fermi constant, f_π the pion decay constant, and $|V_{ud}|$ the CKM matrix element. The spectra for $m_J = 0, 30, 70,$ and 110 MeV are showed in Fig.6.11. Normalizing to the $\pi^+ \rightarrow e^+ \nu_e$ decay amplitude

$$\begin{aligned} \frac{1}{\Gamma_{\pi \rightarrow e\nu}} \frac{d\Gamma_{\pi \rightarrow e\nu J}}{dE_e} &= \frac{|y|^2}{4\pi^2} \frac{\sqrt{E_e^2 - m_e^2}}{(1 - m_e^2/m_\pi^2)^2} \\ &\times \left(\frac{m_\pi E_e - 2E_e^2 + m_e^2}{m_\pi^2 - 2m_\pi E_e + m_e^2} \right) \left(1 - \frac{m_J^2}{m_\pi^2 - 2m_\pi E_e + m_e^2} \right)^2. \end{aligned} \quad (6.17)$$

A search for Majorons using the PIENU data is currently undergoing. The search strategy is similar to the massive neutrino searches, with the complication that Majorons are produced in 3-body decays and the broad distribution of the signal can have large correlations with the shape of the backgrounds.

6.7 Summary

The branching ratio data analysis was divided into three datataking periods and for each of them the raw branching ratio was extracted with a combined fit of the low-energy and high-energy time spectra.

The statistical error on the raw BR came from the χ^2 minimization procedure, while systematic errors came from the variation of the fitting range, bins size, MC shapes, and the variation of fixed parameters.

Other sources of systematic errors were the variation of the analysis cuts. The corrections applied to the raw BR (LET, muon decays in flight in B3 and t_0 variations) have also corresponding statistical and systematic errors.

¹D. McKeen, private communication (2018).

The combination of the three datasets in a final branching ratio was done through a standard error propagation procedure and a weighted sum where the weights were proportional to the single dataset errors.

The 2010 dataset analysis was already finalized and published in [100]. The presented BR is still blinded as the final values of the systematic uncertainties are being finalized. A factor of ~ 2 improvement on the statistical error was obtained including the full dataset, while the systematic error was kept under control with improvements in the estimation methods.

Chapter 7 | Limits on New Physics

Using the results presented in Ch. 6, limits on the presence of new physics beyond the Standard Model can be calculated. Limits can be obtained starting from an upper limit to the branching ratio R_{UL} , which can be calculated for example with the Feldman-Cousins "unified approach" frequentist method [178].

Calculating $(R_{\pi}^{exp} - R_{\pi}^{SM})/\sigma$ where R_{π}^{exp} is the measured branching ratio, σ the total error, and R_{SM} is the SM prediction, and consulting Tab. X of [178], an upper limit to R_{exp} can be obtained.

For the 2010 dataset, with a combined (statistical+systematic) error $\sigma = 0.03$, the upper limit at 95% confidence level is 1.67 standard deviations above the SM value

$$R_{UL} = 1.2402 \times 10^{-4} \quad . \quad (7.1)$$

For comparison, using the combined error of all the data available ($\sigma \simeq 0.02$) and the 2010 value for R_{exp} , the upper limit at 95% confidence level is 1.58 standard deviations above the SM value, or $R_{UL} = 1.2384 \times 10^{-4}$.

7.1 Lepton Universality

Lepton universality is the assumption that the W boson couples with the same strength to each lepton generation. If there is a difference in the couplings, we can quantify it with the three different coupling constants g_e , g_{μ} , and g_{τ} . In the case of the $\pi^+ \rightarrow e^+ \nu_e$ branching ratio we have

$$R_{\pi}^{exp} = \left(\frac{g_e}{g_{\mu}} \right)^2 R_{\pi}^{SM} \quad , \quad (7.2)$$

where R_{π}^{exp} is the measured branching ratio and R_{π}^{SM} is the SM prediction. Since the yields depend on the square of the coupling constants, the

measurement of the branching ratio is a particularly powerful test of lepton universality: for example a 1% precision in the measurement would translate in a 0.05% precision on the test. Using the published result with the 2010 dataset, the following result was obtained

$$\frac{g_e}{g_\mu} = 0.9996 \pm 0.0012 \quad , \quad (7.3)$$

which has to be compared with the SM prediction $g_e/g_\mu = 1$. Using the current estimates for the errors with the full dataset, the error on the ratio of the coupling constants becomes ± 0.0008 .

7.2 New Pseudo-Scalar Interactions

The BR is very sensitive to the presence of new pseudoscalar interactions. Using Eq. 2.44, and the upper limit of the BR from Eq. 7.1 we have

$$1 - \frac{R^{exp}}{R^{SM}} = \frac{1.2402}{1.2352} \sim \left(\frac{1\text{TeV}}{\Lambda} \right)^2 \times 10^3 \quad , \quad (7.4)$$

which gives the estimate

$$\Lambda \sim 497 \text{ TeV} \quad . \quad (7.5)$$

The result implies that new pseudoscalar interactions must have a mass scale $\gtrsim 497 \text{ TeV}$ at 95% C.L. . Using the upper limit derived with the estimated error of the whole dataset gives the estimate $\Lambda \sim 621 \text{ TeV}$.

7.3 R-Parity violating SUSY

Eq. 2.45 relates the branching ratio to the R-parity violating parameters Δ_{11k} and Δ_{21k} :

$$\frac{\Delta R_\pi^{SUSY}}{R^{SM}} = 2(\Delta_{11k} - \Delta_{21k}) \quad .$$

If $\Delta_{11k} = \Delta_{21k}$, no constraints can be provided. Considering the limiting cases where one of the two parameters is zero

$$\begin{aligned} \Delta_{11k} = 0 &\Rightarrow \Delta_{21k} < 0.0020 \quad (95\%C.L.) \\ \Delta_{21k} = 0 &\Rightarrow \Delta_{11k} < 0.0028 \quad (95\%C.L.) \end{aligned}$$

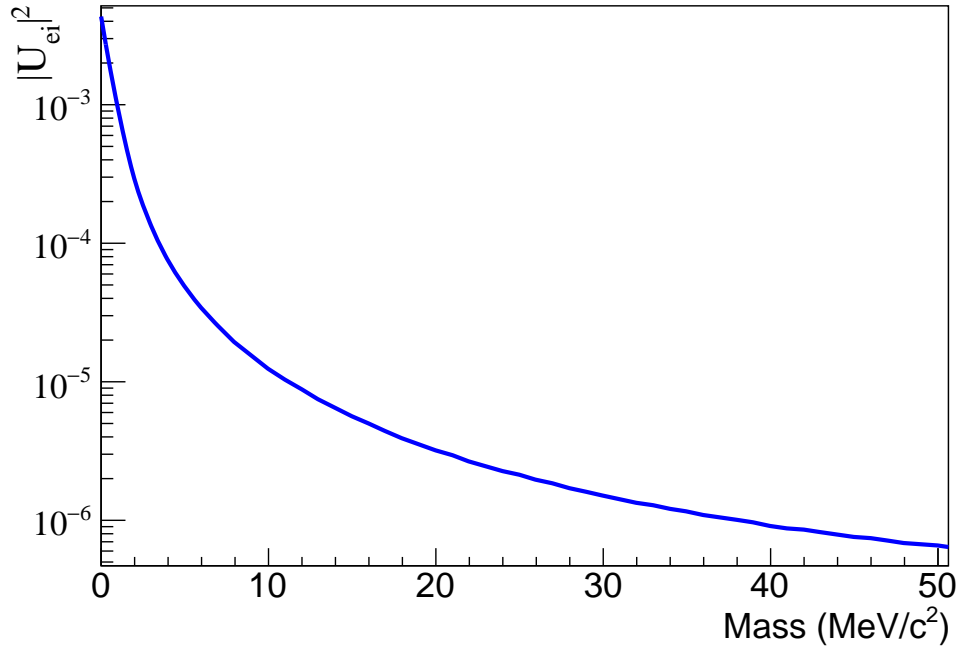


Figure 7.1: 95% upper limits for the mixing matrix element $|U_{ei}|^2$ derived from the $\pi^+ \rightarrow e^+\nu_e$ branching ratio.

7.4 Charged Higgs Bosons

If the coupling to a charged Higgs boson H^\pm is not proportional to the lepton masses, then Eq. 2.47 can provide limits on m_{H^\pm} . Assuming couplings of the order $\lambda_{ud} \sim \lambda_{ev} \sim \lambda_{\mu\nu} \sim \alpha/\pi$ we have

$$m_{H^\pm} \sim \frac{m_\pi m_W \alpha}{\pi} \sqrt{\frac{2}{m_e(m_u + m_d)} \left(1 - \frac{m_e}{m_\mu}\right) \frac{R_{SM}}{R_{SM} - R_{exp}}} , \quad (7.6)$$

which leads to the 95% C.L. limit

$$m_{H^\pm} \gtrsim 144 \text{ GeV} . \quad (7.7)$$

7.5 Massive Neutrinos

Using data taken in 2009 and a peak-search, a first limit on the massive neutrino mixing matrix element $|U_{ei}|^2$ with the $\pi^+ \rightarrow e^+ \nu_e$ decay was obtained [179]. The upper limit was improved by a factor up to four in the 55–129 MeV/ c^2 mass range. In 2018, the PIENU collaboration published an improved new limit in the 60–135 MeV/ c^2 range using the full available dataset [170]. The detailed results were presented in Sec. 6.5. Below 50 MeV/ c^2 (where a peak-search would be ineffective), limits can be derived directly using the result for the branching ratio.

In the presence of mixing with one single massive neutrino state ($i=4$) and considering the following kinematical factors and definitions

$$\delta_{e/\mu} = \left(\frac{m_{e/\mu}}{m_\pi} \right)^2, \quad \delta_4 = \left(\frac{m_{\nu_4}}{m_\pi} \right)^2, \quad \rho(x, y) = [x + y - (x - y)^2] \sqrt{\lambda(1, x, y)},$$

$$\lambda(z, x, y) = x^2 + y^2 + z^2 - 2(xy + yz + zx), \quad \bar{\rho}(x, y) = \frac{\rho(x, y)}{\rho(x, 0)} = \frac{\rho(x, y)}{x(1-x)^2},$$

the ratio $r = R_\pi^{\text{exp}} / R_\pi^{\text{SM}}$ can be written as

$$r = \frac{1 - |U_{e4}|^2 + |U_{e4}|^2 \bar{\rho}(\delta_e, \delta_4)}{1 - |U_{\mu 4}|^2 + |U_{\mu 4}|^2 \bar{\rho}(\delta_\mu, \delta_4)}. \quad (7.8)$$

Three mass intervals can be identified:

- I_1 : $m_{\nu_4} < m_\pi - m_\mu$, ν_4 contributes to both decays channels.
- I_2 : $m_\pi - m_\mu < m_{\nu_4} < m_\pi - m_e$, ν_4 contributes to $\pi^+ \rightarrow e^+ \nu_e$ only.
- I_3 : $m_{\nu_4} > m_\pi - m_e$, ν_4 cannot be emitted in both channels.

The I_1 case is complex to treat, but for the I_2 one, if from a peak-search is known that $|U_{\mu 4}|^2 \ll 1$, the denominator of Eq. 7.8 can be approximated to 1, and an upper limit on $|U_{e4}|^2$ can be obtained:

$$|U_{e4}|^2 < \frac{r - 1}{\bar{\rho}(\delta_e, \delta_4) - 1} \approx \frac{r - 1}{\bar{\rho}(\delta_e, \delta_4)}, \quad (7.9)$$

where the last approximation comes from $\bar{\rho} \gg 1$ over the considered mass range. Taking the Feldman-Cousins [178] upper limit to the ratio at 95%

C.L, $r \leq 1.0047$, an upper limit to the matrix element can be obtained (Fig. 7.1). This procedure follows closely the one used in [168] (where the PDG value for R_π^{exp} was used) which produced the curve marked as PIENU in Fig. 6.9.

In the I_3 case, by definition it is assumed that $\rho(x, y) = 0$ and therefore $\bar{\rho} = 0$ and thus

$$r = \frac{1 - |U_{e4}|^2}{1 - |U_{\mu4}|^2} . \quad (7.10)$$

If $|U_{\mu4}|^2 \ll 1$, then another upper limit can be derived

$$|U_{e4}|^2 < 1 - r . \quad (7.11)$$

With the last formula, the constant limit in Fig. 6.9 marked as PIENU-H was derived.

7.6 Summary and Outlook

The large data sample collected of $\pi^+ \rightarrow e^+ \nu_e$ and $\pi^+ \rightarrow \mu^+ \nu_\mu \rightarrow e^+ \nu_e \bar{\nu}_\mu$ decays allows for a variety of new physics searches besides the precision determination of the branching ratio. The two-body decay $\pi^+ \rightarrow e^+ \nu_e$ fixes completely the energy of the positron. If the neutrino were massive, the energy will be different and a peak will appear at lower energies. This allowed for a peak-search which was able to improve the limits on the mixing matrix element of massive neutrinos with the electron neutrino at the $\sim 10^{-8}$ level.

A similar search using the $\pi^+ \rightarrow \mu^+ \nu_\mu$ decay was performed using the information provided by the active target.

The presence of a massive neutrino weakens the helicity-suppression mechanism enhancing the measured branching ratio. Thus the branching ratio itself, compared with theoretical calculations, can provide further limits to the presence of massive neutrinos.

Another possible search is looking for the $\pi^+ \rightarrow e^+ \nu_e J$ decay, where J is a Majoron. In this case, the sensitivity of a peak search will be smaller, since in a three-body decay the energy distribution will be significantly broader, making the signal shape more difficult to distinguish from the background ones.

A key result related to the branching ratio is the precise test of lepton

universality. This is an important test for the SM and many BSM theories, also in light of discrepancies in recent observations by LHCb and B-Factories.

Part II

Search for Dark Matter with Electron Beams

Chapter 8 | Introduction

Dark Matter (DM) is the name assigned to one of the most important contemporary challenges that fundamental physics research is facing. There is now overwhelming evidence of gravitational interaction between normal (baryonic) matter and an invisible form of *dark* matter. A wealth of astrophysical observations at different length scales points to the existence of DM.

Nowadays, the quest for the nature of DM drives a broad variety of research programs, both in theoretical as well as in experimental physics. DM might point to modifications to our understanding of gravity or to extensions of the SM ¹.

In the latter case, it is commonly assumed that DM is constituted by one (or more) new particle(s). If these new particles can interact with SM particles, there is an opportunity to detect them.

Over the past decade, many different experiments have been designed with the task of directly detecting DM particles. Usually these experiments employ very low-background detectors placed in extremely well shielded locations, like underground laboratories. One of the leading candidates for DM are weakly interacting massive particles (WIMPs), generically predicted by many extensions of the SM. WIMPs have typical mass scales $\gtrsim 10$ GeV up to the multi-TeV range.

Although WIMPs still represent excellent candidates for DM, other theoretical paradigms are actively explored. In particular, in recent years the hypothesis that DM might be "light" ($\lesssim 1$ GeV) is gaining interest (light DM, or LDM in the following). The idea is that DM particles belong to a new, unexplored *dark sector* communicating with the SM through one (or more) *dark mediator* particles. Since LDM would be difficult to de-

¹Even both possibilities at the same time are logically possible.

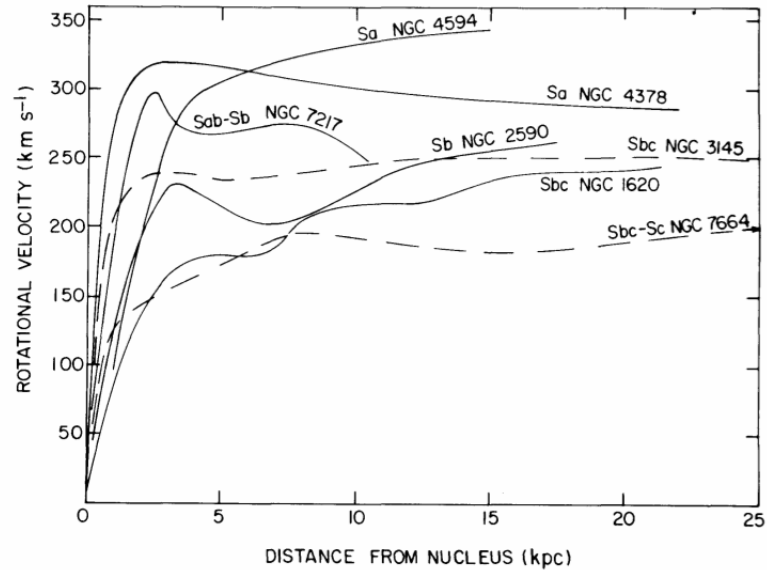


Figure 8.1: Rotational curves for different galaxies as measured by Rubin *et al.* in [181].

tect in direct detection experiments (extremely low thresholds would be needed), accelerator-based DM searches are becoming a new important tool for trying to solve this long-standing puzzle.

8.1 A Brief Historical Account

Already in 1932, Jan Hendrik Oort found some discrepancies between the observed rotation curve (the velocity of the stars as a function of the galactic radius) of our own galaxy and the expected one from luminous matter [180]. From this observation, he was not able to exclude that this discrepancy may have been caused by an underestimate of luminous matter due to the presence of absorbing matter.

In 1933, Fritz Zwicky's studies of the Coma cluster [182] pointed to a significant discrepancy between the amount of matter deduced from the knowledge of the typical mass-to-light ratio of galaxies, and the gravitation properties of the system. Under the hypothesis that the Coma system

has reached mechanically a stationary state, the virial theorem implies

$$\langle E_{kin} \rangle = \frac{1}{2} \langle V_g \rangle \quad , \quad (8.1)$$

where $\langle E_{kin} \rangle$ and $\langle V_g \rangle$ denote the average kinetic and potential energies. Zwicky assumed an uniform mass distribution and a cluster radius $R \sim 1$ Mly with 800 galaxies with $M \sim 10^9$ solar masses. The total mass estimate was $\sim 1.6 \times 10^{45}$ g. The average gravitational potential energy was therefore $\langle V_g \rangle = (3/5)GM/R$. Using the virial theorem (Eq. 8.1), the average mean squared velocity can be extracted:

$$\sqrt{\langle v^2 \rangle} \approx 80 \frac{\text{km}}{\text{s}} \quad . \quad (8.2)$$

This result has to be compared to the observed value of the average Doppler effect of ~ 1000 km/s. The conclusion was that the average density of the Coma system would have to be at least 400 times larger than that derived from the observations on luminous matter. Zwicky himself commented:

*If this would be confirmed we would get the surprising result that **dark matter** is present with much greater density than luminous matter.²*

In the last quote, the *dark matter* term was not used in today's acception, but was referring to normal, non-luminous matter. Until the 1970s, there was not much progress towards the understanding of this discrepancy, until Vera Rubin and coworkers published their work on rotation curves of spiral galaxies [181]. The measurements showed convincingly that the rotational velocities of stars as a function of the radius R of galaxies did not follow the expected Kepler's law

$$v(R) = \sqrt{\frac{GM(R)}{R}} \quad , \quad (8.3)$$

but rather stayed about constant out to very large R , as showed in Fig. 8.1. This implied that galaxies were surrounded by a large amount of invisible matter.

Besides the properties of galaxies and clusters of galaxies, also cosmo-

²In the original paper [182] : *Falls sich dies bewahrheiten sollte, würde sich also das überraschende Resultat ergeben, dass dunkle Materie in sehr viel grösserer Dichte vorhanden ist als leuchtende Materie.*

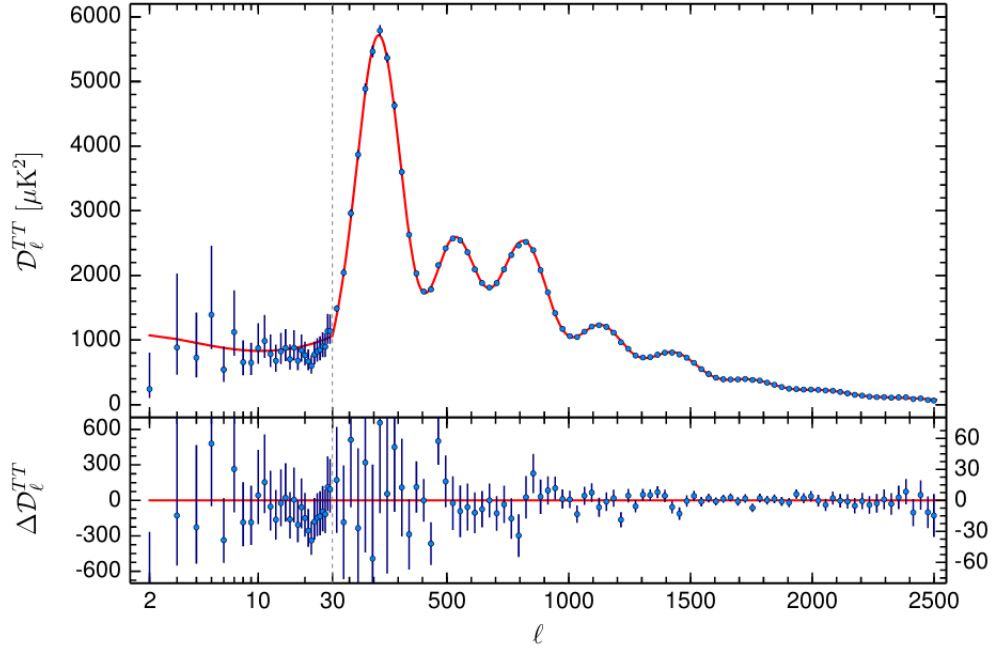


Figure 8.2: Power spectrum from the Planck satellite mission [8]. This is the so-called *TT spectrum*, which is the power spectrum of the angular temperature fluctuations $(T - T_0)/T_0$ as a function of the spherical harmonics number ℓ . The position and relative amplitude of the peaks can be directly related to cosmological models and the matter content of the Universe. For example, the position of the first peak is approximately $\ell_1 \sim \Omega_m / \sqrt{220}$ and thus gives information about the total matter content.

logical measurements point to the existence of dark matter.

In particular, studies of the Cosmic Microwave Background (CMB) favor cosmological models with dark matter and another component called *dark energy*. To date, the most precise CMB measurement is provided by the Planck satellite [8] and a fit to the Λ CDM cosmological model yields a rather precise description of the observed fluctuation spectrum. The Λ CDM model contains a cosmological constant Λ describing dark energy and a large amount of *cold* (*i.e.* non-relativistic) dark matter. The model is based on the Friedmann-Lemaître-Robertson-Walker (FLRW) metric which follows from the assumed homogeneity and isotropy of the universe at large scales (the so-called *cosmological principle*). With a

convenient choice of coordinates, the FLRW metric is

$$ds^2 = -dt^2 + R(t)^2 \left(\frac{dr^2}{1 - kr^2} + d\theta^2 + \sin^2 \theta d\phi^2 \right) , \quad (8.4)$$

where $R(t)$ is a time-dependent scale parameter, r , θ , and ϕ space coordinates and k is the curvature. Since the metric has the following rescaling invariance

$$\begin{cases} R \rightarrow \frac{R}{\lambda} \\ r \rightarrow \lambda r \\ k \rightarrow \frac{k}{\lambda^2} \end{cases} , \quad (8.5)$$

the curvature k can assume the values $k = -1, 0, 1$ corresponding to an open, flat, and closed Universe respectively. The scale parameter $R(t)$ is usually rescaled to the new parameter $a(t) = R(t)/R_0$ where R_0 is today's value. After substitution of the FLRW metric into the Einstein equations, the resulting *Friedmann equations* can be written as

$$\begin{cases} \frac{\ddot{a}}{a} = -\frac{4\pi G}{3}(\rho + 3P) \\ \left(\frac{\dot{a}}{a}\right)^2 = \frac{8\pi G}{3}\rho - \frac{k}{a^2} \end{cases} . \quad (8.6)$$

Introducing the appropriate equation of state³, the behavior of the density from energy-momentum conservation is,

$$\rho(t) \propto a(t)^{-3(1+w)} , \quad (8.7)$$

and the second Eq. 8.6 can be rewritten as

$$\left(\frac{\dot{a}}{a}\right) = H = H_0 \sqrt{\frac{1}{a^3}(\Omega_c + \Omega_b) + \frac{\Omega_r}{a^4} + \frac{\Omega_k}{a^2} + \Omega_\Lambda} , \quad (8.8)$$

where $H = \dot{a}/a$ is the Hubble parameter, and H_0 is the present-day value of H . The dynamics of the universe depends from the density parameters⁴ Ω and $\Omega_c + \Omega_b + \Omega_k + \Omega_\Lambda = 1$ where Ω_c is the cold DM density,

³The equation of state $P = w\rho$ for pure pressure-less matter is $w = 0$, and for radiation, $w = 1/3$.

⁴A density parameter $\Omega = \rho/\rho_c$ is the density ρ in units of the *critical density* $\rho_c = 3H^2/(8\pi G) \sim 10^{-29} \text{ g/cm}^3 = 1.05 \times 10^{-4} \text{ eV/cm}^3$.

Ω_b the baryonic density, Ω_r the radiation density, Ω_k is due to the global curvature, and Ω_Λ is the dark energy density.

The fit to the Planck data, consistent also with previous measurements from WMAP [7], describes an almost flat universe $\Omega_k \sim 0$, with the presence of a cosmological constant term. The baryonic density $\Omega_b = 0.0486 \pm 0.0010$ turns out to be much smaller than the cold DM density $\Omega_c = 0.2589 \pm 0.0057$ and the dark energy density $\Omega_\Lambda = 0.6911 \pm 0.0062$. The radiation density, made by photons and relativistic neutrinos gives an even smaller contribution $\Omega_r \sim 10^{-4}$ dominated by the CMB.

8.2 Summary

The most accurate CMB measurements point towards the existence of dark matter which contributes to about 25% of the total mass of the universe. This result is consistent also with other astrophysical observations, like galactic rotational curves, galaxy clusters dynamics, gravitational lensing [183], Type Ia supernova distance measurements⁵ [184, 185], structure formation studies, and spectroscopic methods [186].

Another strong argument in favour of the existence of DM is the problem of structure formation. The structures we observe today (galaxies and clusters of galaxies) should represent inhomogeneities in the early Universe which acted as *seeds* for gravitational instability and aggregation of matter.

These density inhomogeneities $\delta\rho/\rho$ could be observed measuring the $\delta T/T$ anisotropies in the CMB. It turns out that $\delta\rho/\rho \sim a \sim 10^{-4}$ where a is the FLRW scale factor. The scale factor (the size of the Universe) has grown by a factor equal to the red-shift since recombination time, which is $z \sim 1100$.

For structures to form, we need large enough inhomogeneities $\delta\rho/\rho \gg 1$ but since recombination, not enough time has passed for going from $\delta\rho/\rho = 10^{-4}$ to the needed size for the perturbations.

This tells us that considering only baryons, there was not enough time for structures to form and create what we observe today. Therefore, some kind of additional matter is needed, which decoupled from the primor-

⁵Type Ia supernova measurements yield information on the accelerated expansion of the universe due to dark energy. Comparing this result with estimates of the baryonic density, the DM component can be estimated.

dial plasma much earlier and started to clump and form in time the required density perturbations.

If DM is constituted by a new particle, its mass might be in a very large mass range. Simply estimating the de Broglie wavelength for a particle confined on galactic scales (kpc) with a typical escape velocity of 100 km/s, we can derive a lower limit of 10^{-22} eV.

Such a particle must also be *dark*, in the sense that it does not interact electromagnetically. The SM does not contain a particle which can play the role of DM and this forces to consider BSM theories for explaining the observations.

Another approach could be to alter the laws of gravity for example modifying General Relativity.

Chapter 9 | Dark Matter Models

Most models assume that DM and SM particles interact and were in equilibrium in the early Universe. The following expansion lowered the DM annihilation/creation rate to a level where the comoving DM density remained fixed: this process is called *freeze out*, and this DM origin is called *thermal*. A thermal origin imposes a requirement on the DM mass, which must be above ~ 10 keV, otherwise it remains relativistic until late times, erasing the observed small scale structures in the universe. On the other side, thermal DM heavier than ~ 10 TeV can violate perturbative unitarity in many models [187]. Thermal DM is then restricted in the ~ 10 keV–10 TeV mass range.

DM models can be further approximately divided in two classes: "WIMP" DM and "Light" DM (LDM). WIMPs (Weakly Interacting Massive Particles) are particles with masses above few GeV and arise in a variety of different models of physics beyond the SM. Searches for WIMP DM are mainly performed with collider or direct detection experiments (see Fig. 9.1 and Fig. 9.2).

LDM is very difficult to detect with high-energy colliders because of backgrounds and also with direct detection experiments, since recoil energies are too small.

LDM searches, depending on the exact mass range, have to be performed with dedicated experiments. LDM below the MeV mass range can be constituted for example by *axions* [188, 189] or new massive neutrino states. In this chapter, some of the leading DM models are reviewed (without pretending to be exhaustive, given the size of the field), with particular emphasis on WIMP dark matter and dark sector models.

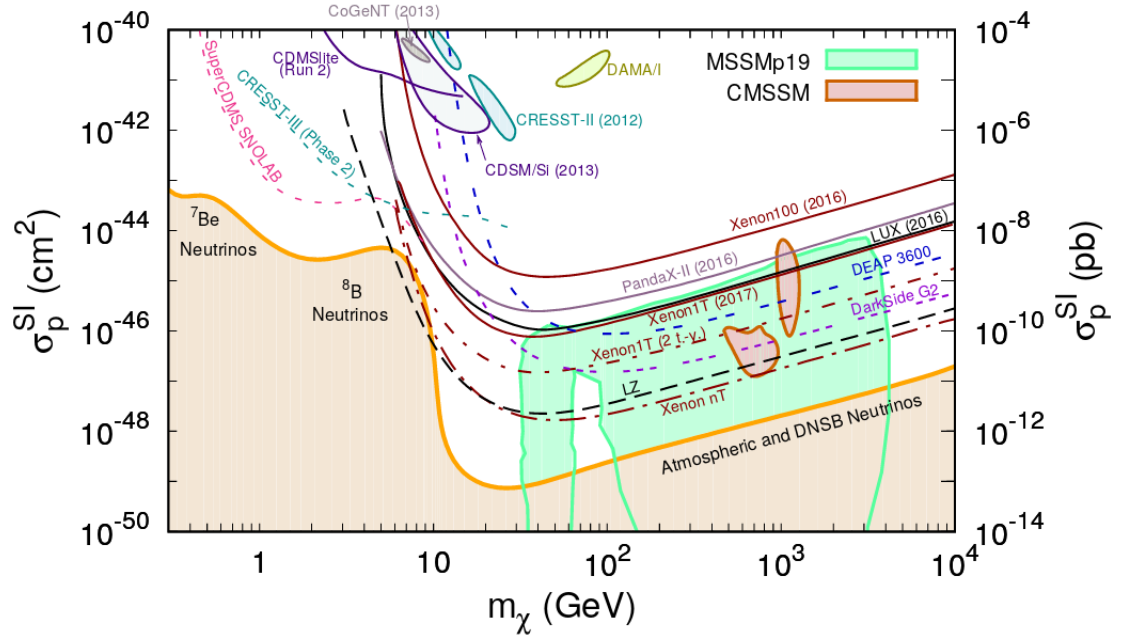


Figure 9.1: Summary of DM direct searches for spin-independent DM-nucleus scattering. Solid lines are experimental results, while dashed lines are projected sensitivities of future experiments. The shaded area below the orange line is the "neutrino floor". The current best limits are provided by LUX [190], Panda-X II [191], XENON1T [192] and CDMSlite-II [193]. (Figure from [194]).

9.0.1 WIMPS

WIMPs, or weakly interacting massive particles, are since long time leading candidates for describing the nature of DM in terms of new particles. An argument in favor of WIMPs is the so-called *WIMP miracle* and the thermal origin of DM. This argument is based on the hypothesis that in the early universe expanding at rate $H(t)$, at some temperature $T(t)$, DM particles χ were in thermal equilibrium with SM particles until

$$n_\chi \langle \sigma(\chi\chi \rightarrow SM)v_\chi \rangle > H \quad , \quad (9.1)$$

where n_χ is the DM number density, $\Gamma = \langle \sigma(\chi\chi \rightarrow SM)v_\chi \rangle$ the thermally averaged χ annihilation rate and v_χ the DM velocity. When the expansion rate becomes larger than Γ , we have the *freeze-out* of DM particles,

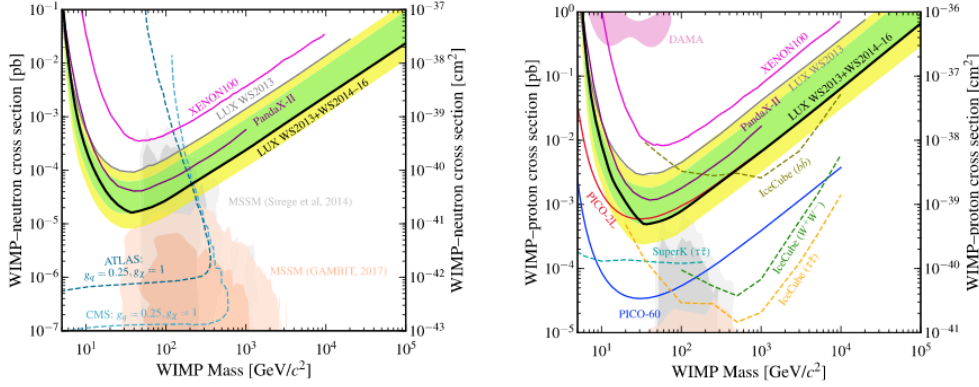


Figure 9.2: Summary of DM direct searches for spin-dependent DM-nucleus scattering [195]. **Left:** DM-neutron limits. **Right:** DM-proton limits. LHC limits are reported only in the DM-neutron limits since they are derived from processes involving Z^0 decays. The DAMA signal is present only in the DM-proton case, since in the DM-neutron case the cross section is smaller and out from range. Comparisons with selected SUSY models are also reported.

which cannot anymore efficiently annihilate (see Fig. 9.3). The *freeze-out* condition $n_\chi \Gamma = H$ fixes the *relic abundance* of DM.

For most interesting cases, up to a factor 3-4, we can assume $v \sim c$. The DM number density in a thermal bath at temperature T has two asymptotic regimes

$$n_{rel} \sim T^3 \quad \text{if} \quad m_\chi \ll T \quad , \quad (9.2)$$

$$n_{nrel} \sim (m_\chi T)^{3/2} e^{-m_\chi/T} \quad \text{if} \quad m_\chi \gg T \quad . \quad (9.3)$$

Eq. 9.2 describes the case of relativistic (or *hot*) DM, while Eq. 9.3 describes non-relativistic (or *cold*) DM.

The Hubble parameter as a function of the temperature $H(T)$ comes from the Friedmann equation

$$H^2 = \frac{8\pi G}{3} \rho \quad , \quad (9.4)$$

and in the radiation-dominated era $\rho \sim T^4$. For *cold* DM relics, the freeze-out condition $n\sigma \sim H$ gives

$$n_{fo} \sim \frac{T_{fo}^2}{M_{p\sigma}} \quad , \quad (9.5)$$

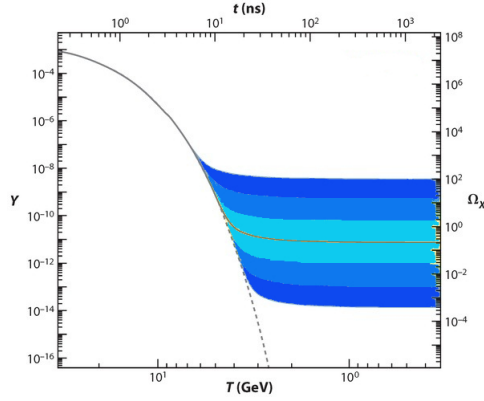


Figure 9.3: Graphical representation of the freeze-out process. The DM number density (normalized to the entropy density: $Y = n/s$) is showed as a function of the temperature (or time) of the Universe. Initially the DM is in equilibrium and the expansion of the Universe dilutes it causing the exponential drop of the annihilation rate. When $n_\chi \Gamma \sim H$, the DM freezes out (blue curves). The plot represents solutions of the Boltzmann equation for the expanding universe $\dot{Y} = \langle \sigma v \rangle s (Y_{eq}^2 - Y^2)$ (see e.g. [196]).

with the Planck mass $M_P = 1/\sqrt{8\pi G} \sim 2.4 \times 10^{18}$ GeV.

Defining $x = m_\chi/T$, and taking into account Eq. 9.3, we can rewrite the freeze-out condition as

$$\sqrt{x}e^{-x} = \frac{1}{m_\chi \cdot M_P \cdot \sigma} \quad . \quad (9.6)$$

This equation can be solved only numerically, and its graphical representation is showed in Fig. 9.4.

Knowing that the DM density parameter is $\Omega_\chi \sim 0.2$, we can write

$$\Omega_\chi = \frac{n_\chi(T = T_0) \cdot m_\chi}{\rho_c} = \frac{T_0^3 \cdot x_{f_0}}{\rho_c \cdot M_P \cdot \sigma} \quad , \quad (9.7)$$

where ρ_c is the critical density, $T_0 = 2.75 \text{ K} \sim 10^{-4}$, and we have used the iso-entropic condition $aT \sim \text{const.}$ (a is the scale factor) which implies $(n_o/T_0^3) = (n_{f_0}/T_{f_0}^3)$.

Substituting the numeric values of the constants we obtain the suggestive

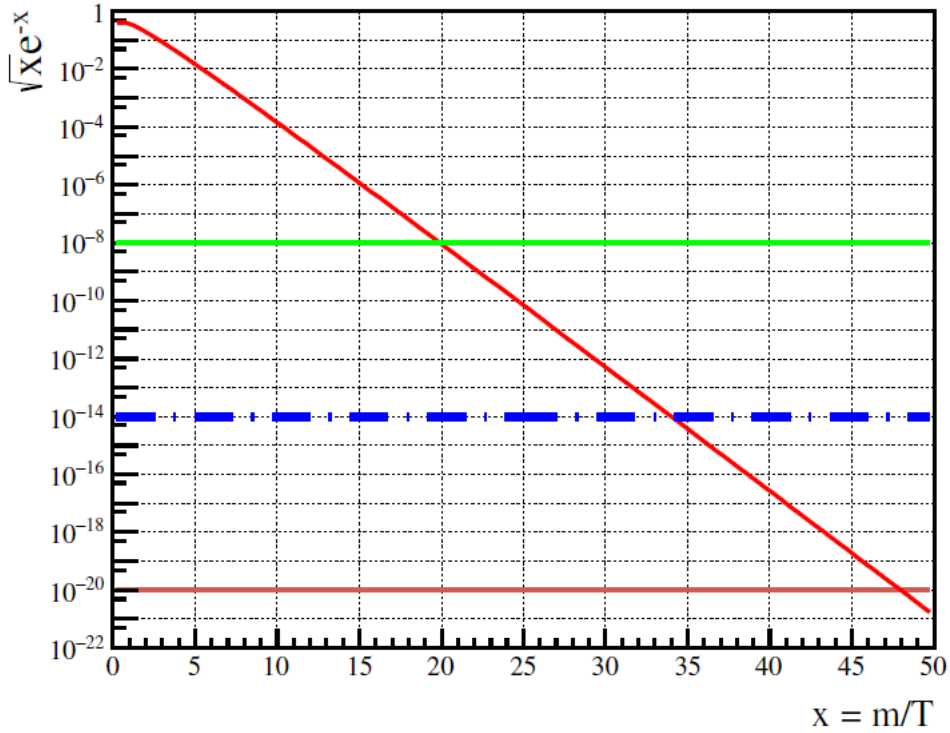


Figure 9.4: Graphical representation of the two sides of Eq. 9.6. The dashed blue line corresponds to $1/(m \cdot M_P \cdot \sigma) = 10^{-14}$ calculated with the weak scale "miracle" values $m_\chi = 100$ GeV and $\sigma = G_F^2 m_\chi^2$. Other two horizontal lines at 10^{-8} and 10^{-20} are added for reference.

equation [196]

$$\frac{\Omega_\chi}{0.2} \simeq \frac{x_{fo}}{20} \left(\frac{10^{-8} \text{GeV}^{-2}}{\sigma} \right) . \quad (9.8)$$

This result is often associated to the so-called **WIMP miracle**, which consists in the following coincidence. For various theoretical reasons, new physics is expected at the electroweak scale $m \sim E_{EW} \sim 200$ GeV. If we calculate the electroweak pair-annihilation cross-section at freeze-out temperature

$$\sigma_{EW} \sim G_F^2 T_{fo}^2 \sim \left(\frac{E_{EW}}{20} \right)^2 \sim 10^{-8} \text{ GeV}^{-2} , \quad (9.9)$$

we obtain a value which leads to the observed DM density parameter. In a more exact treatment of the problem, the cross-section of the last equation should be the thermally-averaged cross section $\langle\sigma v\rangle$ for reasons connected to the Boltzmann equation.

Using the equipartition theorem $(3/2)T = (1/2)mv^2$, we can estimate that $v \sim c/3$ for $x \sim 20$ and this leads to the estimate

$$\langle v\sigma \rangle \sim 3 \times 10^{-26} \frac{\text{cm}^3}{\text{s}} \sim 10^{-8} \text{GeV}^{-2} \times \frac{c}{3} . \quad (9.10)$$

Is all this really a "miracle"?

The previous result was obtained under the assumption of electroweak cross-sections and the cold relic condition $x \gg 1$. In general, following a dimensional argument, a DM annihilation cross-section can be written as $\sigma \sim g^4/m_\chi^2$, where g is some coupling constant. Using Eq. 9.6,

$$x \gg 1 \Rightarrow m_\chi M_p \sigma \gg 1 , \quad (9.11)$$

and therefore $m_\chi \gg 0.1$ eV if $\sigma \sim 10^{-8} \text{GeV}^2$.

This means that as long as the cross-section is the right one for explaining the DM abundance, the cold relic mass can be very small. The conclusion is that the supposed "miracle" can be realized also without appealing to the electroweak scale.

The argument for understanding the WIMP paradigm can also be restated noticing that

$$\Omega_\chi \propto \frac{1}{\langle v\sigma \rangle} \sim \frac{m_\chi^2}{g_\chi^4} . \quad (9.12)$$

The WIMP miracle states that if we use weak-scale masses and coupling constants, we can roughly reproduce the observed DM abundance. The last equation (*i.e.* the thermal paradigm) though fixes only the ratio between couplings and masses and thus also other combinations might in principle obtain the correct abundance [197].

9.0.2 Other Dark Matter Candidates

The WIMP paradigm has driven DM searches in the past decades and it is still a strong motivation for present and future experiments. SUSY theories provide good candidates for DM particles, like the **lightest neutralino** [198], which is a combination of the superpartners of the neutral

gauge bosons and Higgs particles. There are many supersymmetric models which predict different masses/cross sections for candidate DM particles. Another WIMP candidate is the **Kaluza-Klein photon or neutrino** [199, 200]. These DM candidates come out from theories which introduce new physics at the electroweak breaking scale and also possibly explain why that scale is so much lower than the Planck scale (the "hierarchy problem").

Axions are other DM candidates but are generally very light. Axions emerge as solution to the strong CP problem [188, 189].

While SUSY neutralinos are good candidates, also **gravitinos** can play the role of DM in particular versions and phase space locations of the theory [201]. Besides new particles, other ideas are pursued for the explanation of the nature of DM, like the presence of black holes, normal-matter non-luminous compact objects, modifications of the laws of gravity [202], and the corresponding relativistic extensions [203]. More recently, theories describing DM as an emergent phenomenon analog to condensed matter effects were also proposed [204, 205].

9.0.3 Light Dark Matter and The Dark Sector

If thermal DM interacts via the weak interaction (as the "WIMP miracle" might suggest), then the Lee-Weinberg bound [206] says that the DM mass must be larger than ~ 2 GeV for being able to reproduce the observed relic abundance. If DM interacting weakly were too light, its annihilation cross section $\langle\sigma v\rangle \sim G_F^2 m_\chi^2$ will be too small and this will result in DM overproduction.

The way out from this problem is to introduce new interactions with light (\lesssim GeV) force mediators to achieve the right abundance. At the same time, the new carriers must be neutral under the SM gauge groups, otherwise they would have been already discovered. DM and mediators are therefore part of an yet undiscovered *dark sector* which might have an even richer particle content.

The gauge and Lorentz symmetries of the SM as well as the renormalizability requirement restrict the possible new interactions which can be introduced in the lagrangian. The ways the new interaction can be introduced are called *portals*, represented by SM gauge singlet operators

$\hat{\mathcal{O}}$ with dimension < 4 :

$$\hat{\mathcal{O}} = H^\dagger H , LH , B_{\mu\nu} , \quad (9.13)$$

where H is the Higgs boson, L a lepton doublet and B the hypercharge field strength tensor. The new force-carrier or mediator field (SM-neutral) can be a scalar ϕ , a fermion N , or a vector particle A' .

In principle, higher-dimensional effective operators are possible, but direct searches for resolving such operators require suppression scales larger than the electroweak scale: this will reintroduce the DM overproduction problem.

Higgs Portal

If the force carrier is a scalar ϕ , the only renormalizable interactions are $\phi H^\dagger H$ and $\phi^2 H^\dagger H$. After electroweak symmetry breaking, these terms induce a mass mixing between the Higgs boson and the dark scalar. Assuming a fermionic DM particle χ , a simple model based on the Higgs portal is

$$\mathcal{L}_\phi = g_D \phi \chi \bar{\chi} + \frac{1}{2} m_\phi^2 \phi^2 + a H^\dagger H \phi \frac{m_f}{v} \bar{f}_L f_R + h.c. , \quad (9.14)$$

where f is a SM fermion, a is a coupling constant, v the Higgs vacuum expectation value, and g_D the DM-scalar coupling. After symmetry breaking, the mixing between SM fermions and the scalar is $g_{mix} = \sin \theta_{H\phi}/v$ where $\theta_{H\phi}$ is the Higgs-scalar mixing angle.

In the case where $m_\chi < m_\phi$, the relic density is reached with **direct annihilation** into couples of SM fermions mediated by the scalar: $\chi\chi \rightarrow \phi \rightarrow ff$. If $m_\chi \lesssim 1$ GeV and $m_f \ll v$ (LDM requires annihilation into light SM fermions), then $\sin \theta_{H\phi} \sim \mathcal{O}(1)$. This large mixing angle translates in too large branching ratios for rare decays like $B \rightarrow K\nu\bar{\nu}$ and $K \rightarrow K\nu\bar{\nu}$.

The conclusion is that scalar mediators are ruled out by precision meson decay experiments.

The case where DM is heavier than the mediator ($m_\chi > m_\phi$) allows the so-called **secluded annihilation** $\chi\chi \rightarrow \phi\phi$ with subsequent decay of the scalars into SM particles. The problem with this scenario is that it does not offer a precise thermal target to test experimentally. This happens because since in this case $\langle\sigma v\rangle \sim g_D^4/m_\chi^4$, there is no dependence from g_{mix}

which can assume arbitrarily small values and still be consistent with the thermal relic scenario. On the contrary, in the case of direct annihilation we have

$$y = g_D^2 \sin \theta_{H\phi} \left(\frac{m_f}{v} \right)^2 \left(\frac{m_\chi}{m_\phi} \right)^4 > \langle \sigma v \rangle_{relic} m_\chi^2 \quad , \quad (9.15)$$

where we introduced the "thermal target" variable y which scales like the annihilation cross-section. The above condition gives a clear experimental target to investigate.

Fermion Portal

If the force carrier is a fermion, the coupling to the SM can be realized with a term like

$$\mathcal{L}_L \sim a_\nu LHN \quad , \quad (9.16)$$

where a_ν is a Yukawa coupling and the fermion N is a right-handed neutrino. A thermal origin for DM requires a sub-GeV mass for N which in turn requires $a_\nu \lesssim 10^{-12}$: this value is too small for achieving thermalization in the early universe [207]. Giving up a thermal origin for DM, there is a narrow mass range where N can play the role of DM [208].

Vector Portal

If the force carrier is a new vector particle A' , it might come from an additional $U(1)_D$ gauge group under which the DM particle is charged. This group belongs to a *dark* sector which communicates with the SM particles through the new vector mediator (a *dark photon*, DP). A simple model is the following:

$$\begin{aligned} \mathcal{L}_{A'} \sim & \underbrace{-\frac{1}{4} F'_{\mu\nu} F'^{\mu\nu}}_{\text{DP Field}} + \underbrace{\frac{\epsilon_Y}{2} F'_{\mu\nu} B^{\mu\nu}}_{\text{Kinetic Mixing}} + \underbrace{\frac{m_{A'}^2}{2} A'_\mu A'^\mu}_{\text{DP Mass}} \\ & + \underbrace{g_D A'_\mu J_\chi^\mu}_{\text{DP-DM Interaction}} + \underbrace{g_Y B_\mu J_Y^\mu}_{\text{SM Hypercharge}} \quad . \end{aligned} \quad (9.17)$$

In analogy to the SM photon, the dark photon field $F'_{\mu\nu} = \partial_\mu A'_\nu - \partial_\nu A'_\mu$ and the DM current J_χ^μ are introduced. The DP coupling constant can be related to a *dark* fine structure constant: $g_D = \sqrt{4\pi\alpha_D}$. Particularly

important is the kinetic mixing term which couples the DP to the SM photon with the SM hypercharge ϵ_Y .

After electroweak symmetry breaking, the kinetic mixing term induces a mixing of the DP with the photon and the Z boson:

$$\frac{\epsilon_Y}{2} F'_{\mu\nu} B_{\mu\nu} \xrightarrow{\text{EWSB}} \frac{\epsilon}{2} F'_{\mu\nu} F_{\mu\nu} + \frac{\epsilon_Z}{2} F'_{\mu\nu} Z_{\mu\nu} \quad , \quad (9.18)$$

with

$$\begin{aligned} \epsilon &= \frac{\epsilon_Y}{\cos \theta_W} \quad , \\ \epsilon_Z &= \frac{\epsilon_Y}{\sin \theta_W} \quad . \end{aligned} \quad (9.19)$$

After mass diagonalization, the dark photon interactions with dark and visible matter can be obtained:

$$g_D A'_\mu J_\chi^\mu + g_Y B_\mu J_Y^\mu \xrightarrow{\text{Diag.}} A'_\mu (g_D J_\chi^\mu + \epsilon e J_{EM}^\mu) \quad , \quad (9.20)$$

where J_{EM}^μ is the SM electromagnetic current¹. Note that the coupling of the DP to the electromagnetic current happens through the "millicharge" coupling ϵe .

As seen in the scalar case, only the *direct annihilation* regime provides a clear thermal target for experimental searches, therefore, assuming $m_{A'} > m_\chi$ we have

$$y = \epsilon^2 \alpha_D \left(\frac{m_\chi}{m_{A'}} \right)^4 \quad . \quad (9.21)$$

The exact value of the thermal target depends on the choice of the DM candidate (*i.e.* its current J_χ). More in general, different couplings to the DP are possible (elastic, inelastic), as well as particle-antiparticle asymmetric versions of DM.

9.1 Light Dark Matter and Vector Mediators

From the previous discussion, vector mediators are promising candidates for coupling LDM to the SM and it is worth exploring the different possibilities they allow regarding the exact nature of DM.

¹High order terms in ϵ are omitted.

In the case where **DM is a fermion particle**, its current can be written as $J_\chi^\mu = \bar{\chi}\gamma^\mu\chi$ where χ is a Dirac fermion with mass m_χ in complete analogy with e.g. an electron. In this case, the DM abundance is the same for DM χ or anti-DM particles $\bar{\chi}$ (symmetric fermion DM) and the thermal constraint $\langle\sigma v\rangle \approx 10^{-26} \text{ cm}^3/\text{s}$ must be satisfied for reproducing the observed DM abundance. Assuming s-wave annihilation, for Dirac fermions we have (compare with Eq. 9.21):

$$\langle\sigma v\rangle \propto \epsilon^2 \alpha_D \frac{m_\chi^2}{m_{A'}^4} \sim \frac{y}{m_\chi^2} . \quad (9.22)$$

Since fermionic symmetric DM can leave imprints in the CMB through hydrogen re-ionization effects [209], present data can be compared with this scenario. The result is that it is ruled out by CMB measurements [207].

The case of **asymmetric DM** instead is not ruled out [210]. If the abundance of χ is set by a primordial matter/antimatter asymmetry mechanism, then the abundance of $\bar{\chi}$ can be suppressed by factors of $\sim e^{-\langle\sigma v\rangle}$ and the re-ionization bound can be evaded. Another attractive feature of asymmetric models is their similarity to the case of SM particles, where matter/antimatter asymmetry indeed exists.

Another possibility is considering **Majorana fermions** as DM particles. Since the DP has a mass, the $U(1)_D$ symmetry is somehow broken. The idea is to introduce Dirac and Majorana mass terms: the first one preserves $U(1)_{A'}$, while the second breaks it. This results in a split $\Delta = m_2 - m_1$ in mass between the two Weyl spinors in the χ four components $\chi \sim (\chi_1, \chi_2)$. The DP will couple predominantly to the off-diagonal terms:

$$J_\chi^\mu = \bar{\chi}_1 \gamma^\mu \chi_2 + h.c. . \quad (9.23)$$

In such a theory, χ_2 is unstable and decays via $\chi_2 \rightarrow \chi_1 f \bar{f}$ if $m_{A'} > m_1 + m_2$, as required for direct annihilation (f indicates a SM fermion). Moreover, direct annihilation requires both DM particles: $\chi_1 \chi_2 \rightarrow A' \rightarrow f \bar{f}$. For $\Delta \ll m_{\chi_{1/2}}$, the annihilation cross section has the same scaling of the Dirac case. The Majorana fermion DM is included in a general class of DM models called **inelastic Dark Matter** [211].

Exhausted the fermionic cases, it remains the possibility that DM is constituted by a **scalar particle**. In this case the current will be

$$J_\chi^\mu = i(\chi^* \partial^\mu \chi - \chi \partial^\mu \chi^*) . \quad (9.24)$$

The direct annihilation $\chi\chi \rightarrow A' \rightarrow ff$ proceeds via a p-wave interaction giving the thermal target

$$\langle\sigma v\rangle \propto \epsilon^2 \alpha_D \frac{m_\chi^2 v^2}{m_{A'}^4} \sim \frac{yv^2}{m_\chi^2} . \quad (9.25)$$

The presence of the velocity v in this case enhances (for the same m_χ) the thermal target by a factor ~ 10 with respect to the fermion case.

9.2 Modified Gravity

We end this brief summary on DM models mentioning non-particle DM candidate theories. One of them is called Modified Newtonian Dynamics (MOND, [202]).

The basic idea is to modify Newton's law introducing a minimal acceleration scale a_0 :

$$F = ma \rightarrow F = ma \cdot f\left(\frac{a}{a_0}\right) ,$$

where $f(a/a_0)$ is an "interpolating function" which bridges MOND to the normal dynamics in the limit if $a_0 \rightarrow 0$. An example of interpolating function is

$$f = \frac{1}{\left(1 + \frac{a_0}{a}\right)} .$$

The introduction of this modification can explain with only one new parameter the flat galaxy rotation curves, while such a model has problems in describing the CMB and some aspects of structure formation. MOND appears also to explain well the baryonic Tully-Fisher relation (an empirical relation between baryonic mass and rotation velocity in disk galaxies) [212, 213].

Fig. 9.5 shows the measured acceleration parameter for various astrophysical systems over a large range of scales as a function of the baryonic mass: the data suggest the existence of a common characteristic acceleration scale. This result is naturally explained by MOND and Λ CDM models require instead a large fine-tuning.

A relativistic and covariant extension of MOND is TeVeS (Tensor-vector-scalar gravity, [203]) which is a modification of general relativity with the addition of a scalar and a vector field. General relativity (GR) is

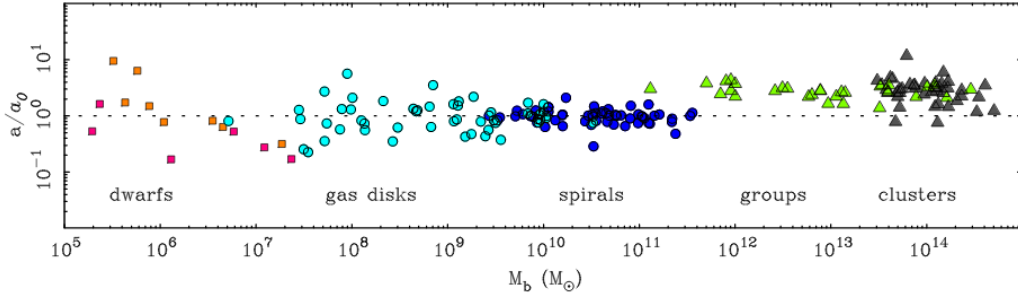


Figure 9.5: Acceleration parameter for various astrophysical systems as a function of the baryonic mass M_b . The data show a common characteristic acceleration scale which is natural in MOND models but requires large fine-tuning in Λ CDM models. Figure from [213].

constrained by many experimental results and it is not easy to modify. MOND requires modifications in the weak-field limit but since in GR the role of acceleration is played by the Christoffel symbols (which are not tensors), it is not possible to make the theory depend on them. Scalar-tensor theories add a scalar field which can act as an additional potential with its gradient playing the role of acceleration for realizing MOND-like effects [214]. Scalar-tensor theories provided a proof of principle that relativistic versions of MOND can be constructed. The ability of modified gravity scenarios to model DM and other observational features (like *e.g.* the CMB) is still controversial and subject of active research.

9.3 Summary on Dark Matter Models

In this chapter we briefly discussed some of the models describing particle DM. The DM mass range can be divided into ultra-light DM (sub-keV masses, for example axions), light DM (for example dark sector models) and WIMP DM (for example SUSY particles). The mass range is thus quite broad and generally not well constrained.

For example, for cold thermal DM, the requirement of unitarity in the calculation of cross-sections places the approximate bound

$$\sigma < \frac{4\pi}{m_\chi^2} \quad , \quad (9.26)$$

and this, together with Eq. 9.8 approximately implies

$$\frac{\Omega_\chi}{0.2} > 10^{-8} \text{GeV}^{-2} \times \frac{m_\chi^2}{4\pi} . \quad (9.27)$$

Since $\Omega_\chi < 0.2$ we have

$$\left(\frac{m_\chi}{120 \text{ TeV}} \right)^2 < 1 . \quad (9.28)$$

For a lower limit for WIMPs ($\sigma \sim G_F^2 m_\chi^2$), choosing $x_{fo} \sim 20$ we have

$$\Omega_\chi h^2 \sim 0.1 \frac{10^{-8} \text{GeV}^{-2}}{G_F^2 m_\chi^2} \sim 0.1 \left(\frac{10 \text{ GeV}}{m_\chi} \right)^2 . \quad (9.29)$$

This lower limit is the already mentioned **Lee-Weinberg** limit [206]. The overall mass range allowed for WIMPs goes thus from ~ 10 GeV to several TeVs.

The Lee-Weinberg limit is valid only for WIMPs and we have seen already that if we consider other types of interactions we can have $m_\chi < 10$ GeV. There are also theoretical models predicting super-heavy DM of cosmological (inflationary) origin with masses in the 10^{13} GeV range ("WIMPzillas" [215]).

The latter considerations motivate a very wide and diverse experimental research program which should be able to complementary probe different models of DM on the whole mass range. The mature field of direct searches in underground laboratories is now complemented by high-energy colliders, low-energy precision experiments, asymmetric B-factories, resonating cavity and NMR experiments, neutrino experiments, space-based experiments, high-energy telescopes, and small-scale experiments investigating intriguing anomalies.

Chapter 10 | Search for Dark Matter with a Beam-Dump Experiment

 Searching for dark matter requires highly sensitive and almost background-free experiments. Depending from the investigated mass range, different detection techniques have been developed. The so-called *direct detection experiments* try to detect DM through its recoil against nuclei which in turn are detected by different low-background techniques [216].

Since DM particles in the galactic halo move with velocities of order $v \sim 200$ km/s, the momentum transfer p in a DM scattering event is typically $p = \mu v$ with

$$\mu = \frac{m_{DM}m_N}{(m_{DM} + m_N)} \lesssim 100 \text{ MeV}/c^2$$

the DM-nucleus reduced mass. At this energies, DM particles interact coherently with the nucleus as a whole. There are two main types of DM-nucleus scattering: spin-independent and spin-dependent ¹.

In the spin-independent case, DM particles couple to the mass A or charge Z of the entire nucleus and scattering rates receive a coherent enhancement proportional to A^2 or Z^2 . In the spin-dependent case, DM couples dominantly to unpaired nucleons, and there is no enhancement

¹For a more accurate discussion about the different possible non-relativistic operators entering the DM-nucleus scattering see [217].

factor. Direct spin-independent searches have very high sensitivity (see Fig 9.1), while spin-dependent searches are more difficult, and the sensitivity is comparable to that of collider searches. At the time of writing, the leading result in spin-independent DM direct detection was set in May 2018 by the XENON-1T experiment [218] with a cross section exclusion limit of $4.1 \times 10^{-47} \text{ cm}^2$ at a WIMP mass of $30 \text{ GeV}/c^2$ at 90% confidence level.

Nuclear recoils can have different signatures depending from the detection technique. Common sought signals are light, ionization or phonons (or combinations of them). Nuclear recoils are sensitive to DM down to about 1 GeV (possibly even less with the latest cryogenic detector techniques [219, 220]). For masses below $\sim 1 \text{ GeV}$, recoil energies are too low and hardly detectable. Improvements can be achieved considering DM recoils against electrons and the feasibility of this approach has been already demonstrated [221].

A different approach is to try to produce DM directly with an accelerator. With particle production at an accelerator, DM particles can acquire a higher energy with respect to halo DM and thus overcome the limitation of direct detection techniques.

At high DM masses, LHC experiments have already produced remarkable results [222]. If DM couples to quarks or gluons, LHC can test the thermal freeze-out paradigm on a wide mass range. At low DM masses, dedicated experiments at high-intensity accelerators are the most promising path forward. In general, the comparison among direct detection and accelerator-based experiments is complicated by the presence of quantities which are not accurately known, like the DM local density, DM velocity distribution and nuclear form and structure factors.

DM can also be detected *indirectly* if it annihilates ($\chi\chi \rightarrow \text{SM particles}$) or decays ($\chi \rightarrow \text{SM particles}$). Promising sites for these searches are for example high-density regions in space, such as galaxy nuclei, neutron stars, the Sun, accretion disks, the galactic halo or galaxy clusters. Another DM "messenger" can be constituted by cosmic rays, although DM contribution is subdominant in this case and its effects are estimated at the $\mathcal{O}(1\%)$ level [196].

Since astrophysical backgrounds are small in the case of neutrinos, these extremely weakly interacting particles can also be used for DM searches. The basic idea is that if DM is concentrated in dense regions (for example in star cores) and if DM can decay into neutrinos, these are the only

particles that can easily escape a star and reach a detector on Earth.

In connection to SUSY models, DM candidates such as neutralinos have decay modes in W^+W^-/ZZ pairs with high branching ratios, which in turn produce neutrinos in their decays. Large neutrino experiments like SuperKamiokande [223], IceCube [224, 225] or future even larger experiments (DUNE [226] or HyperK [227]) will be able to perform DM searches based on neutrino signals [228, 229, 230, 231].

10.1 Experiments for LDM Detection

Among direct detection experiments, some are designed specifically for LDM detection, trying to achieve record-low detection thresholds. The most successful designs involve cryogenic detectors made of different materials and read-out technologies.

The CRESST experiment is based on CaWO_4 crystals with both scintillation and phonon read-outs in order to separate nucleon recoils (NR) from electron recoils (ER) [232].

SuperCDMS employs silicon and germanium targets with ionization and phonon readouts, again for separating WIMP-like NR from ER [233]. After an experimental campaign at the Soudan Underground Laboratory [234], an improved SuperCDMS experiment will be built at SNOLab [235]. The new location will provide improved shielding against cosmic background and an improved detector design will result in record-low sensitivities for LDM down to $\sim 0.5 \text{ GeV}/c^2$ masses [236].

New emerging technologies based on (skipper) CCD silicon detectors are used by the DAMIC [237] and SENSEI [238] collaborations. An increasing experimental effort is ongoing at high-intensity accelerators. Prominent examples are the various experiments taking place at the Thomas Jefferson National Accelerator Facility (JLab): APEX [239], HPS [240], and DarkLight [241].

10.2 Beam-Dump Experiments

The idea behind beam-dump experiments is to send an intense particle beam (protons or electrons) towards a thick target where the beam will deposit most of its energy. In such a process, depending on the beam

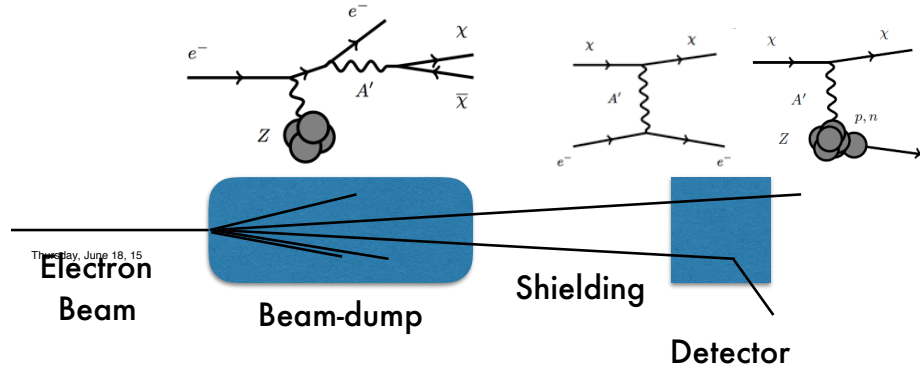


Figure 10.1: Beam-Dump experimental concept. A beam is impinging into a thick target (beam-dump) where dark photons are produced with a bremsstrahlung-like process. A detector shielded from the SM background can detect DM particles from dark photon decay. The detection proceeds through a dark photon-mediated interaction with nuclei or electrons in the detector.

energy, a large number of particles can be produced. Potentially, among them there are also DM particles which, being weakly interacting, can escape the target. If an appropriate detector is placed behind the beam-dump, and it is shielded by the SM background, it would be able to detect DM particles via re-scattering against nuclei or electrons.

The basic idea is sketched in Fig. 10.1 in the case of a dark photon decaying into DM pairs.

One of the first notable experiments using the beam-dump concept was aimed at searching for short-lived axions [242]. Particles emerging from the dump were drifting in a shielded 32m beam pipe and analyzed by a spectrometer.

Another experiment (E137) was performed at SLAC [243] using a 20 GeV electron beam for looking for neutral particles produced in a beam-dump. The detector was placed after 200 m of earth shielding (see Fig. 10.2) and consisted of plastic scintillators and wire chambers.

A higher energy electron beam experiment (275 GeV) was realized at FermiLab (E774) [244]. After these pioneering experiments, recent theoretical activity in dark sector models motivated new searches in this field.

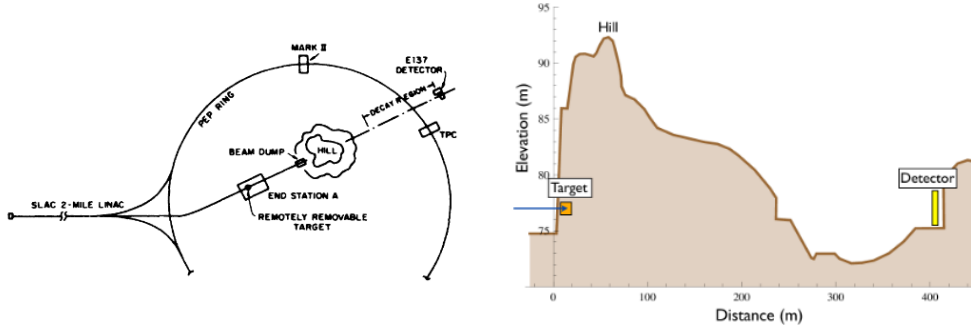


Figure 10.2: The SLAC beam-dump experiment E137 [243]. The plastic scintillator and wire chambers detector was located after 200 m of earth shielding provided by a hill after the beam-dump (Figures from [243] and [248]).

Recently, short-baseline neutrino experiments were used for dark matter searches using the beam-dump technique. In [245], the sensitivity of the LSND and MiniBooNE experiments were studied for using their data in order to search for LDM particles. In [246], the data of the E137 SLAC experiment were re-interpreted as limits on the dark photon mass and coupling constant.

The MiniBooNE collaboration performed a targeted search for DM [247]. MiniBooNE used a 8 GeV proton beam at FermiLab, usually directed towards a beryllium target followed by a magnetic horn for focusing the neutrino beam. For the DM search experiment, the horn was off, and the beam was directed towards a steel beam-dump for minimizing neutrino production. MiniBooNE set 90% C.L. exclusion limits to DM in the < 1 GeV mass range.

10.3 Beam-Dump Experiments: Theoretical Background

We focus on a simple dark sector model where the mediator is a massive vector particle (a dark photon) with mass $m_{\gamma'}$ decaying in pairs of Dirac DM particles with mass m_{χ} .

The dark photon is produced in a process similar to photon bremsstrahlung.

For an on-shell production, we assume $m_{\gamma'} > 2m_\chi$.

In most theoretical works [249], the production cross section is estimated using the Weizsäcker-Williams approximation (WW) [250, 251] in its improved formulation [252, 253, 254].

The physical idea behind the WW approximation is that the electromagnetic field generated by a fast-moving charge is mostly transverse to the direction of motion and resembles a plane wave which can be approximated by a real photon. Thus in the WW approximation the incoming electrons are approximated by an effective photon flux. This allows to simplify the phase space integrals and reduce $2 \rightarrow 3$ particle diagrams to $2 \rightarrow 2$ ones.

In this formulation, with $m_e \ll m_{\gamma'} \ll E_0$ and $x\theta_{\gamma'}^2 \ll 1$ the cross section is

$$\frac{d\sigma}{dx d\cos\theta_{\gamma'}} \approx \frac{8Z^2\alpha^3\epsilon^2 E_0^2 x}{U^2} \mathcal{L} \left[\left(1 - x + \frac{x^2}{2}\right) - \frac{x(x-1)m_{\gamma'}^2 E_0^2 x\theta_{\gamma'}^2}{U^2} \right] , \quad (10.1)$$

where E_0 is the incoming electron energy, $x = E_{\gamma'}/E_0$, Z is the atomic number of the beam-dump, $\alpha \sim 1/137$, $\theta_{\gamma'}$ is the lab-frame angle between the electron and the dark photon. The factor \mathcal{L} ($\mathcal{O}(1)$ for $m_{\gamma'} < 500$ MeV) depends on the kinematics, atomic screening, and nuclear effects. U is the virtuality of the electron in the initial state bremsstrahlung

$$U = E_0^2 x\theta_{\gamma'}^2 + m_{\gamma'}^2 \frac{1-x}{x} + m_e^2 x . \quad (10.2)$$

Neglecting the electron mass and integrating on the angle, the cross section is

$$\frac{d\sigma}{dx} \approx \frac{8Z^2\alpha^3\epsilon^2 x}{m_{\gamma'}^2} \left(1 + \frac{x^2}{3(1-x)}\right) \mathcal{L} . \quad (10.3)$$

The former result allows to draw some kinematical considerations about the dark photon bremsstrahlung process:

1. The dark photon production rate is proportional to the $\alpha^3\epsilon^2/m_{\gamma'}^2$ factor, as is physically expected: the rate drops with smaller coupling constants or larger masses.
2. The production of the dark photon is peaked at $x \sim 1$, where most of the electron energy is converted into dark photon energy (U has a minimum at $x = 1$).

3. At large angles, the cross section drops rapidly as $\sim 1/\theta_{\gamma'}^4$. An average estimate of the emission angle is

$$\theta_{\gamma'} \sim \max \left(\frac{\sqrt{m_{\gamma'} m_e}}{E_0}, \frac{m_{\gamma'}^{3/2}}{E_0^{3/2}} \right) . \quad (10.4)$$

This angle is generally smaller than the opening angle of the DM pairs produced in the dark photon decay

$$\theta_{\chi} \sim \frac{m_{\gamma'}}{E_0} . \quad (10.5)$$

When electrons ("electrons on target", EOT) of energy E_0 scatter on a target with T radiation lengths, the number of produced dark photons is

$$\frac{dN}{dx} = EOT \frac{N_A X_0}{A} \int_{E_{\gamma'}}^{E_0} \frac{dE}{E} \int_0^T dt \mathcal{I}(E; E_0, t) E_0 \frac{d\sigma}{dx'} \Big|_{x'=E_{\gamma'}/E} , \quad (10.6)$$

where X_0 is the beam-dump radiation length, N_A the Avogadro number, A is the atomic mass (g/mol), and the function \mathcal{I} describes the energy distribution of electrons after t radiation lengths.

In the case of a beam-dump, it is possible to take the limit $T \gg 1$ (thick target approximation) and the number of produced dark photons scales as

$$N_{\gamma'} \sim EOT \times C \times \epsilon^2 \frac{m_e^2}{m_{\gamma'}^2} , \quad (10.7)$$

where C is a $\mathcal{O}(10)$ factor which depends on the target nuclei in the dump.

Although the WW approximation allows for useful formulas and estimates of the dark photon production, it was argued (see e.g. [255]) that a complete calculation can lead to different results for projected experimental exclusion limits. In particular, if $m_{\gamma'} < 2m_e$, the results are very different. In the other cases, the WW approximation can be trusted within an order 10 with respect to the exact calculation.

It is therefore important for estimating the experimental sensitivity of an experiment to employ exact calculations without the WW approximation.

10.4 Expected Experimental Yield

From an experimental point of view, it is interesting to estimate how the DM production scales with the parameters of the theoretical model. There are two distinct regimes to consider

- If $m_{\gamma'} < 2m_\chi$, the DM production mechanism proceeds with an off-shell (virtual) dark photon and the DM yield Y scales as $Y_\chi \sim \alpha_D \epsilon^2 / m_\chi^2$ and the DM scattering rate in the detector scales as $Y_D \sim \alpha_D \epsilon^2 / m_{\gamma'}^2$. Therefore, the total expected DM yield scales as

$$Y = Y_\chi \times Y_D \sim \frac{\alpha_D^2 \epsilon^4}{m_\chi^2 m_{\gamma'}^2} . \quad (10.8)$$

- If $m_{\gamma'} > 2m_\chi$ the dark photon is on-shell: there is a real production followed by the decay $\gamma' \rightarrow \chi\chi$. In this case, $Y_\chi \sim \epsilon^2 / m_{\gamma'}^2$ and $Y_D \sim \alpha_D \epsilon^2 / m_{\gamma'}^2$, and

$$Y = Y_\chi \times Y_D \sim \frac{\alpha_D^2 \epsilon^4}{m_{\gamma'}^4} . \quad (10.9)$$

The latter yields scale as the fourth power in the coupling constant ϵ . This scaling is in general not favorable, but the high density of the target combined with the high currents of modern CW electron accelerators can still deliver stringent limits on this parameter.

Chapter 11 | The darkMESA Experiment

DarkMESA is a beam-dump experiment planned to be installed at the new Mainz Energy-recovery Superconducting Accelerator (MESA) facility. The new accelerator will be constructed at the Institute for Nuclear Physics at the Johannes-Gutenberg University in Mainz (Germany). The darkMESA experiment [256] will be one of the three experiments served by the new accelerator which will provide a CW electron beam with an energy in the 100-200 MeV range with mA currents.

11.1 A Beam-Dump Experiment at MESA

11.1.1 The MESA Accelerator

The Institute for Nuclear Physics at Mainz University is building a new CW multi-turn energy recovery linac for precision particle physics experiments with a beam energy range of 100-200 MeV. MESA will operate in two modes: energy recovery mode (ERM) and external beam mode (XBM). In ERM, the accelerator will provide a beam current of up to 1 mA at 105 MeV for the MAGIX internal target experiment with multi-turn energy recovery capability. In XBM, a polarized beam of 150 μA will be provided to the P2 experiment [257]. In this mode, the initial design energy is up to 155 MeV. The linac will provide an energy gain of 50 MeV/pass by using four ELBE-like 9-cell cavities [258] installed in two cryomodules. The existing beam-dump which was used by the A4 experiment [259] will also be used for darkMESA. It consists of a steel cylin-

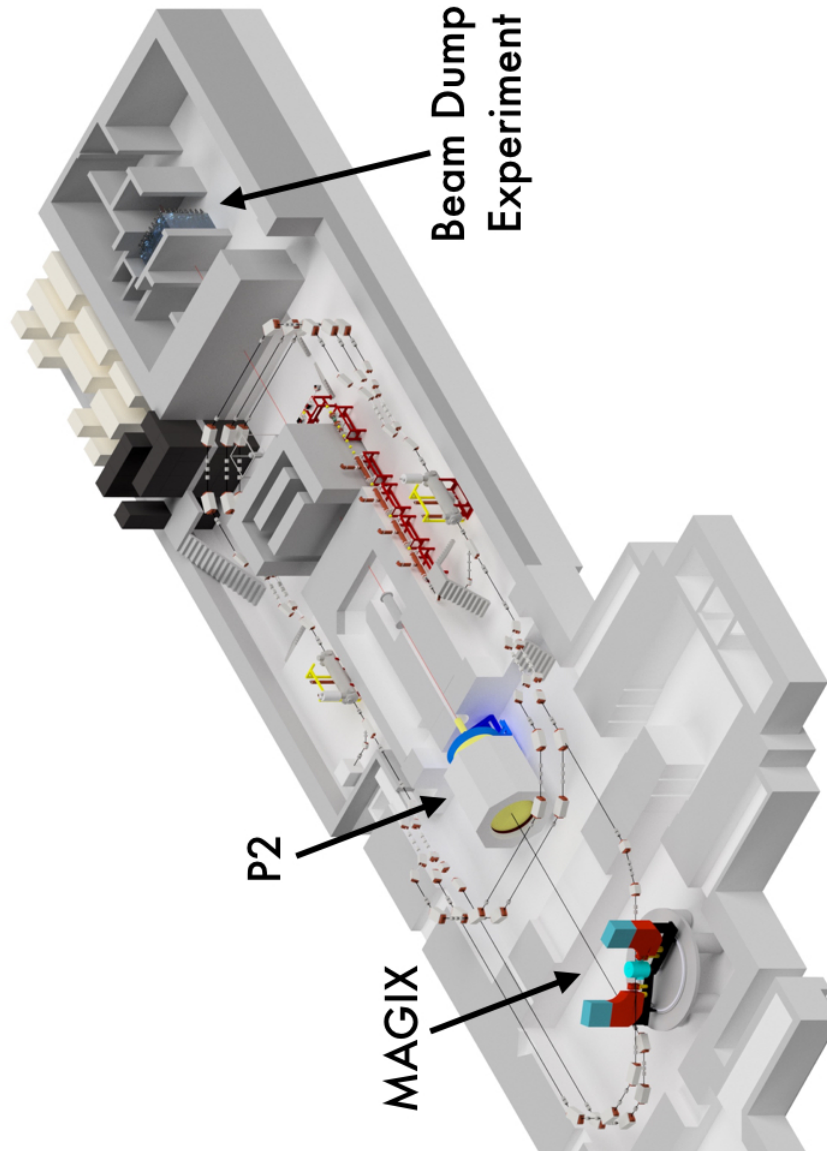


Figure 11.1: The MESA (Mainz Energy-Recovery Superconducting Accelerator) complex with the three foreseen experiments.

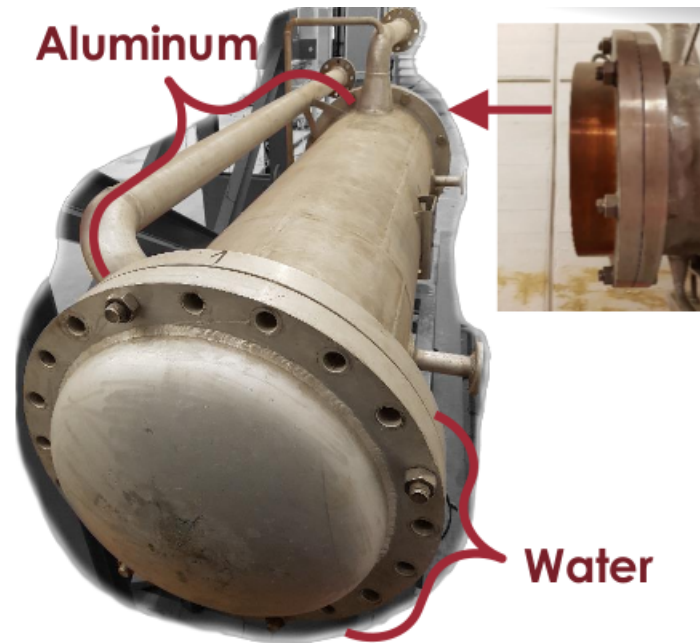


Figure 11.2: Picture of the existing aluminum beam-dump, previously used by the A4 experiment.

der filled with aluminum spheres (~ 16.5 radiation lengths) immersed in cooling water (see Fig. 11.2). Water is injected in the forward part of the beam-dump and extracted in the backwards part. The beam-dump will be placed at a distance of ~ 12 m from the P2 hydrogen target.

11.2 Simulation of the darkMESA Experiment

A full simulation study was performed for assessing the sensitivity of a beam-dump experiment at MESA. As discussed in the previous chapter, it is important to avoid approximations as much as possible for obtaining a reliable sensitivity prediction.

The simulation employs Geant4 [260] and a modified version of the MadGraph4 [261] event generator. The Geant4 simulation implements the geometry of the experimental halls, the relevant details of the P2 experiment (liquid hydrogen target and magnetic field), the (mainly aluminum) beam-

dump, and the detector. MadGraph4 is used for generating the dark photon bremsstrahlung process and the dark photon decay. The number of produced $\chi\bar{\chi}$ pairs per EOT is

$$N_{\chi\bar{\chi}} = \frac{N_A \rho_{BD} X_0}{A} \int_0^{T_{BD}} dt \int_{E_{min}}^{E_B} dE \cdot \sigma(E) \cdot \frac{dN}{dE}(t) \quad , \quad (11.1)$$

where ρ_{BD} and X_0 are the beam-dump density and radiation length, respectively. T_{BD} is the beam-dump length in radiation length units, $\sigma(E)$ the $eN \rightarrow eN\gamma' \rightarrow eN\chi\bar{\chi}$ cross-section, E_B the beam energy, and E_{min} the minimum detection threshold energy. Defining the *differential track length* (DTL) (t is the distance in radiation lengths)

$$\left\langle \frac{dN}{dE} \right\rangle = \int_0^{T_{BD}} dt \frac{dN}{dE}(t) \quad , \quad (11.2)$$

Eq. 11.1 becomes

$$N_{\chi\bar{\chi}} = \frac{N_A \rho_{BD} X_0}{A} \int_{E_{min}}^{E_B} dE \sigma(E) \left\langle \frac{dN}{dE} \right\rangle \quad . \quad (11.3)$$

A common simplifying approximation, referred as *single-radiation length approximation* assumes $\left\langle \frac{dN}{dE} \right\rangle = \delta(E - E_B)$, which neglects all the showering effects in the beam-dump. These effects are important in assessing the experimental sensitivity, since they can substantially reduce the dark photon production. Effectively, accounting for showering effects in the beam-dump shifts the final energy spectrum of the DM particles towards lower energies.

In the present simulation, the DTL was reconstructed using Geant4. The beam dump was divided in thin slices along the beam direction and at every slice the e^+ and e^- flux (number of particles per unit surface) was calculated. The sum of the fluxes allowed a numerical evaluation of the integral in Eq. 11.2 which results in an energy spectrum characterizing the beam dump and the incident beam.

Fixing the parameters of the theoretical model ($m_{\gamma'}$, m_{χ} , ϵ , α_D), $\sigma(E)$ and the final state four-vectors were calculated with MadGraph4 for each bin of the DTL spectrum ¹. The initial angle of the electron (or positron) in

¹The dark photon production through electron-positron annihilation was neglected. The effects of this additional process were studied in [248]

the beam dump as calculated by Geant4 was also taken into account. This effect is important, since it has a direct influence on the final aperture cone of the emerging DM "beam". The simulated electron/positron energy spectrum was divided in bins and for each energy a MadGraph4 simulation was performed. In a second step, the results were summed with the respective weight given by the DTL spectrum.

The final state four-vectors for the $\chi/\bar{\chi}$ particles were re-introduced in the Geant4 simulation where they were tracked through the various materials up to the detector location.

The $\chi/\bar{\chi}$ interaction with electrons or protons in the detectors was calculated with a custom code embedded into Geant4 implementing the $e\chi$ and $p\chi$ cross-sections at first order in the exchange of a dark photon. For example, for the $e\chi$ case (both particles are Dirac particles with spin 1/2) in the CM frame if $E \ll m_\chi, m_e$ at $\mathcal{O}(m_e^2)$

$$\frac{d\sigma_{e\chi}}{dE_f} = 4\pi\epsilon^2\alpha\alpha_D m_e \frac{4m_e m_\chi^2 E_f + \left[m_\chi^2 + m_e(E - E_f) \right]^2}{(m_{\gamma'}^2 + 2m_e E_f)^2 \cdot (m_\chi^2 + 2m_e E)^2} , \quad (11.4)$$

where E is the initial χ energy, and E_f is the electron recoil energy [262]. The complete formulas can be found in App. E. The simulation implements the $e\chi$ and $p\chi$ cross-sections at first order without approximations. In the $p\chi$ case, the nucleon form factor is taken into account using the dipole parameterization. The total number of detected $N_{\chi\bar{\chi}}$ particles (Eq. 11.3) is calculated as

$$N_{\chi\bar{\chi}} = EOT \times N_D \times N_{DET} \times N_{BD} \\ \times X_0 \times \frac{\sigma_{MG}}{N_{SIM}} \times \sum_{i=0}^{i=N_D} L_i \sigma_i , \quad (11.5)$$

where EOT are the number of electrons on target, N_D is the number of $\chi/\bar{\chi}$ within the detector acceptance, X_0 the beam-dump radiation length, L_i the track length in the detector of the i -th DM particle track, σ_i the $e\chi \rightarrow e\chi$ or $p\chi \rightarrow p\chi$ cross section of the i -th DM particle track, σ_{MG} the $eA \rightarrow eA\gamma' \rightarrow \chi\bar{\chi}$ cross-section calculated with MadGraph4, and N_{SIM} the total number of simulated events. For a detector with a combination of materials with average atomic number Z , mass number A , and density ρ_D , the total number of scattering centers (number of electrons or protons)

is $N_{DET} = Z\rho_D N_A / A$, where N_A is the Avogadro number. With the same notation, the number of nuclei in the beam dump is $N_{BD} = \rho_{BD} N_A / A$.

11.3 Detector Concept

The concept for the darkMESA detector consists in the construction of a calorimeter which should have the following properties

1. High acceptance. Since at MESA energies the DM particles are produced over a wide angle (the boost given from higher energy beams would tend to collimate the particles in the forward direction), the detector should have large enough transverse dimensions. In the case of on-shell dark photon production, the acceptance A scales approximately as

$$A = \frac{1}{1 + m_{\gamma'}^2 / (E_0^2 \frac{D}{2d})} \quad , \quad (11.6)$$

where E_0 is the beam energy, D the distance of the detector from the beam-dump, and d is the detector width. In the case of off-shell production, $m_{\gamma'}$ should be substituted by m_χ .

2. High density. The number of detected DM particles is directly proportional to the density.
3. High thickness. The number of detected DM particles is proportional to the length of the path in the detector.
4. Segmentation. A high detector segmentation can help in identifying the backgrounds.
5. Speed. A fast detector can help in distinguishing signals from backgrounds.
6. A veto system for removing cosmic rays or contributions from the environment has to be designed.

Given the previous requirements, the baseline design for the detector is a calorimeter based on dense inorganic crystals. Two choices can be made for the crystals types

Material	CsI(Tl)	PbF ₂	BGO	SF-5 (51% PbO)
Density (g/cm ³)	4.53	7.77	7.13	4.08
Rad. Length (cm)	1.85	0.93	1.13	2.54
Light yield (γ /MeV)	50 000	\sim 300	10000	\sim 300
Peak emission (nm)	565	350	480	450
Decay time (ns)	680 (64%) 3340 (36%)	< 20	300	< 20
Refraction Index	1.80	1.85	2.19	1.67
References	[263, 264]	[265, 266]	[267, 268]	[269]

Table 11.1: Comparison among candidate materials for the construction of the darkMESA calorimeter.

- Scintillation crystals: the main advantage is the high light yield and a wide range of possible materials with different scintillation speeds and light output.
- Čerenkov crystals: the advantage is the high speed and the relatively low sensitivity to neutron backgrounds. The cost is also in general lower with respect to scintillation crystals.

In Tab. 11.1 are listed candidate materials initially selected for their characteristics and availability from previous experiments.

11.4 Experimental Tests for the Calorimeter Material

For evaluating the response of candidate materials for the calorimeter, experimental tests were made with the following crystals

1. A **BGO** crystal on loan from Frascati National Laboratories (Italy), originally employed in the L3 experiment [270].
2. **PbF₂** crystals, originally used in the A4 experiment [259].

Crystal Type	X(mm)	Y(mm)	Length Z(mm)	Density (g/cm ³)
SF 5	30.3	30.3	150	4.07
SF 6	31	29	149	5.18
SF 57 HTultra	30	30	150	5.51
BGO	21	21	230	7.13
PbF ₂	(30×30 / 26×26)		150	7.77

Table 11.2: Crystals tested with the MAMI 14 MeV electron beam. The two PbF₂ crystals are truncated pyramids with bases 30×30 mm and 26×26 mm.

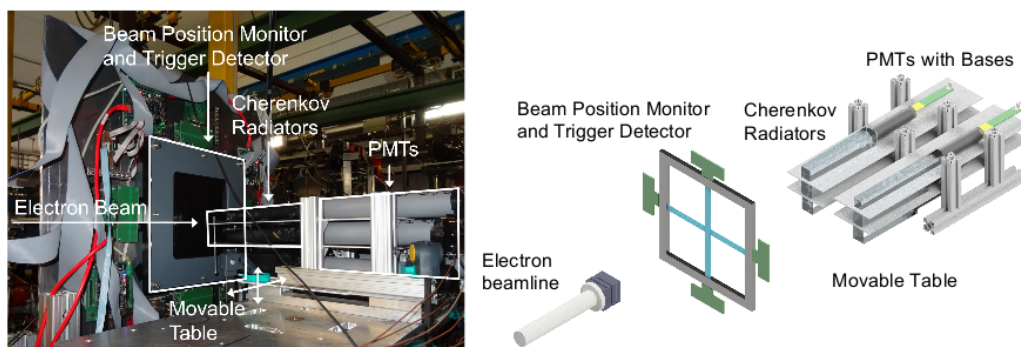


Figure 11.3: Experimental test stand for the investigation of the crystals response to the MAMI electron beam (photo and figure from M. Christmann).

3. **SF5, SF6, and SF57-HTultra Pb-Glass** crystal samples provided by the company Schott AG ².

Particularly interesting are the PbF₂ Čerenkov crystals since over 1000 of them are readily available at the Institute of Nuclear Physics in Mainz and have very high density. The characteristics of the crystals tested are reported in Tab 11.2. The experimental test consisted in exposing the crystals to the electron beam of the MAMI accelerator at different beam energies up to 14 MeV and at different entrance angles.

²SCHOTT AG, Hattenbergstrasse 10, 55122 Mainz, <https://www.us.schott.com>

Before the experimental test, a Geant4 optical simulation was performed. The simulation had as input the dimensions of the crystals, the characteristics of the PMT used for the readout (Photonis XP2900/01, 29 mm diam.), as well as the optical properties of the crystals (emission spectrum, absorption, transmission, and refraction). The experimental setup (Fig. 11.3) consisted on an adjustable table on which the crystals were installed. Before the table, a fiber detector was mounted for triggering and beam tracking. The PMT readout was realized with a CAEN V965 16 Channel Dual Range Multievent QDC (charge-to-digital converter) with variable integrating gate.

The comparison among simulation and the experimental results is the following

Crystal	Experiment		Simulation	
	p.e.	σ	p.e.	σ
PbF ₂	27.20	2.55	23.58	3.76
SF 5	21.28	1.79	19.96	7.09
SF 6	17.97	2.13	14.11	5.56
SF 57 HTultra	16.46	2.34	14.01	6.01

where p.e. is the average number of photoelectrons and σ is the width of the photoelectron distribution (see also Fig. 11.4 for a graphical representation of the table and Fig. 11.5 for the experimental spectra fitted with a Gaussian function). The differences with respect to the Montecarlo were due to the roughness of the surfaces and the transmission properties which were not yet precisely modeled.

The results of the beam scan along the crystals side revealed a rather homogeneous response, since the number of produced photoelectrons seems not to be dependent on the position hit by the beam. This can be explained with the high level of multiple scattering under which the low-energy electron underwent entering the crystal. Multiple scattering causes the loss of the initial direction information spreading the Čerenkov photons in all directions.

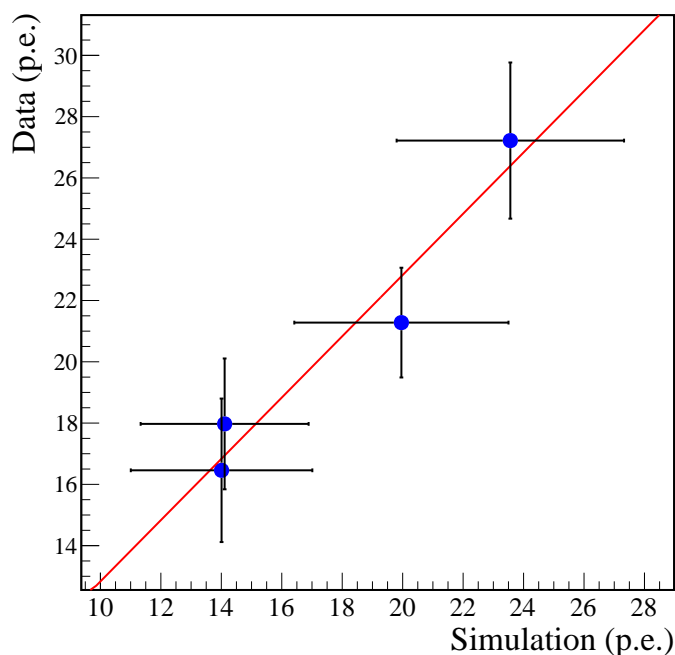


Figure 11.4: Calibrated data in photoelectrons (p.e.) versus the simulated number of photoelectrons. Points indicate the (Gaussian distribution) fitted averages and the error bars indicate the fitted widths of the energy spectra.

11.5 Simulation Results

The experimental tests on the crystal responses allowed confidence in the selection of a realistic low energy threshold which was conservatively chosen as $E_{\min}=14$ MeV.

At this stage, the backgrounds were not yet studied, thus they were not considered in the exclusion limits calculation.

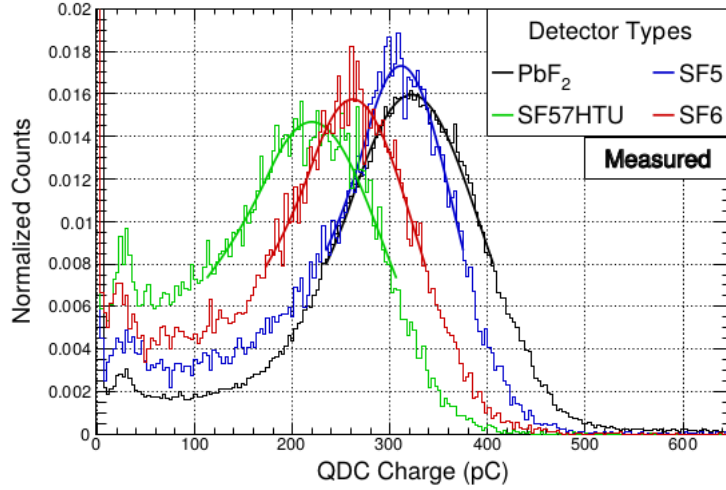


Figure 11.5: QDC spectra obtained at MAMI for the different crystal types (figure from M. Christmann).

11.5.1 Simulation Parameters

The limits on the thermal target variable y at the 3σ level were calculated under the following conditions

1. $m_\chi/m_{\gamma'} = 1/3$. This condition conservatively takes into account the direct annihilation and on-shell requirement $m_{\gamma'} > 2m_\chi$ (if the two DM particles have the same mass).
2. $\alpha_D = 0.5$. This choice (assumed in most of the recent works) is conservative in the sense that a smaller value would exclude more parameter space. Moreover, it is close to the perturbative limit for abelian dark sectors [271].
3. EOT = 3.7×10^{22} (or 5400 C of total deposited charge) with a beam energy of 155 MeV, 1mA current and 10000h of beamtime.
4. Based on the results from the beam tests, the low energy threshold for the detector was set at 14 MeV. The possibility to lower the threshold is currently under study and it will involve the construction of a detector prototype.

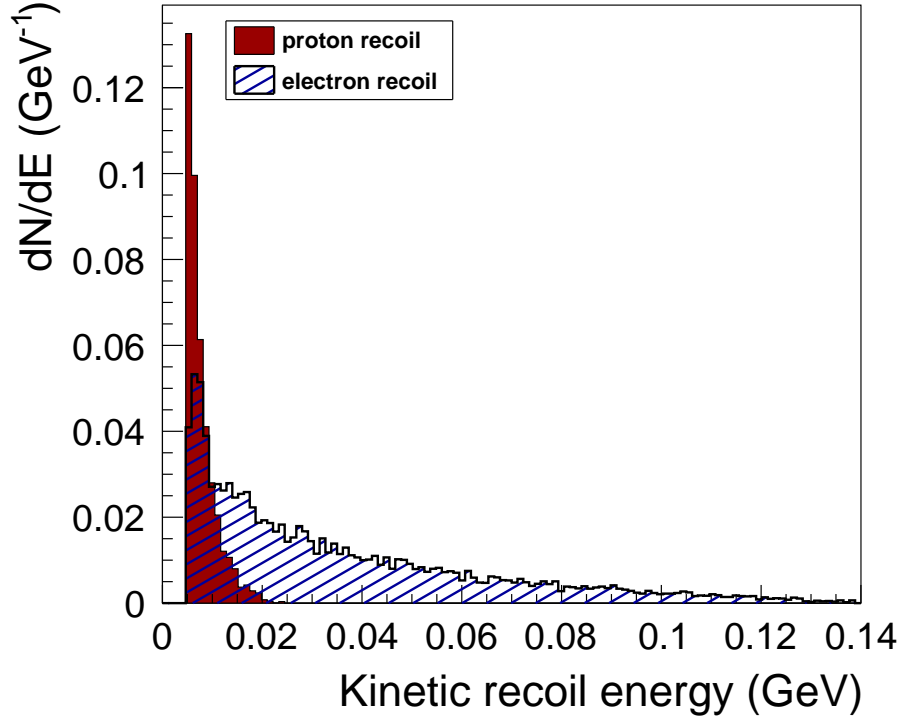


Figure 11.6: Proton and electron energy spectra after recoiling against a DM particle.

11.5.2 Interactions in the Detector

DM particles can in principle interact with nucleons and electrons in the detectors. The energy recoil spectra for the two cases are showed in Fig. 11.6. Assuming a low-energy threshold of 14 MeV for the two Čerenkov crystals, the electron recoil case is the most favorable in terms of detected signals. The following simulation results will therefore conservatively use only the $e\chi$ scattering process for modeling the DM detection.

11.5.3 Exclusion Limits

The minimal dark photon model has four parameters. With the introduction of the thermal target variable y , the model space is effectively reduced from 4 to two parameters. A physically interesting choice is to choose to represent the model in the $y - m_\chi$ space.

In order to produce conservative exclusion limits, the idea is to construct a physically motivated value of y which is the largest possible:

$$y_{\max} = \underbrace{\epsilon^2}_{\text{experiment}} \times \underbrace{\left[\alpha_D \left(\frac{m_\chi}{m_{\gamma'}} \right)^4 \right]}_{\text{maximize}} . \quad (11.7)$$

The choice α_D is already large and close to theoretical limits, while $m_{\gamma'} = 3m_\chi$ is also large with respect to the maximum value fixed by $m_{\gamma'} = 2m_\chi$. The coupling constant ϵ has to be fixed by the experiment or the simulation as in this case.

The simulation was performed with a fixed value $\epsilon = \epsilon^0$ and then the number of detected DM interactions N_χ^0 was scaled according to the scaling of the yield ($Y \sim \epsilon^4$) until the number of detected events corresponded to a 3σ exclusion limit:

$$N_\chi^{LL} = N_\chi^0 \times \left(\frac{\epsilon_{LL}}{\epsilon^0} \right)^4 . \quad (11.8)$$

Assuming Poisson statistics and zero backgrounds, we choose the lower limit ϵ_{LL} for which $N_\chi^{LL} = 9$ events.

The results are reported in Fig. 11.7 for three detector configurations foreseen in a staged approach:

- **Phase A:** Realization of a calorimeter based on the already available ~ 1000 PbF₂ crystals (0.13 m³ volume).
- **Phase B:** Addition of Pb-Glass blocks for reaching 1 m² volume.
- **Phase C:** More Pb-Glass blocks are added reaching a volume of about 10 m³, which is the maximum available within the MESA infrastructure.

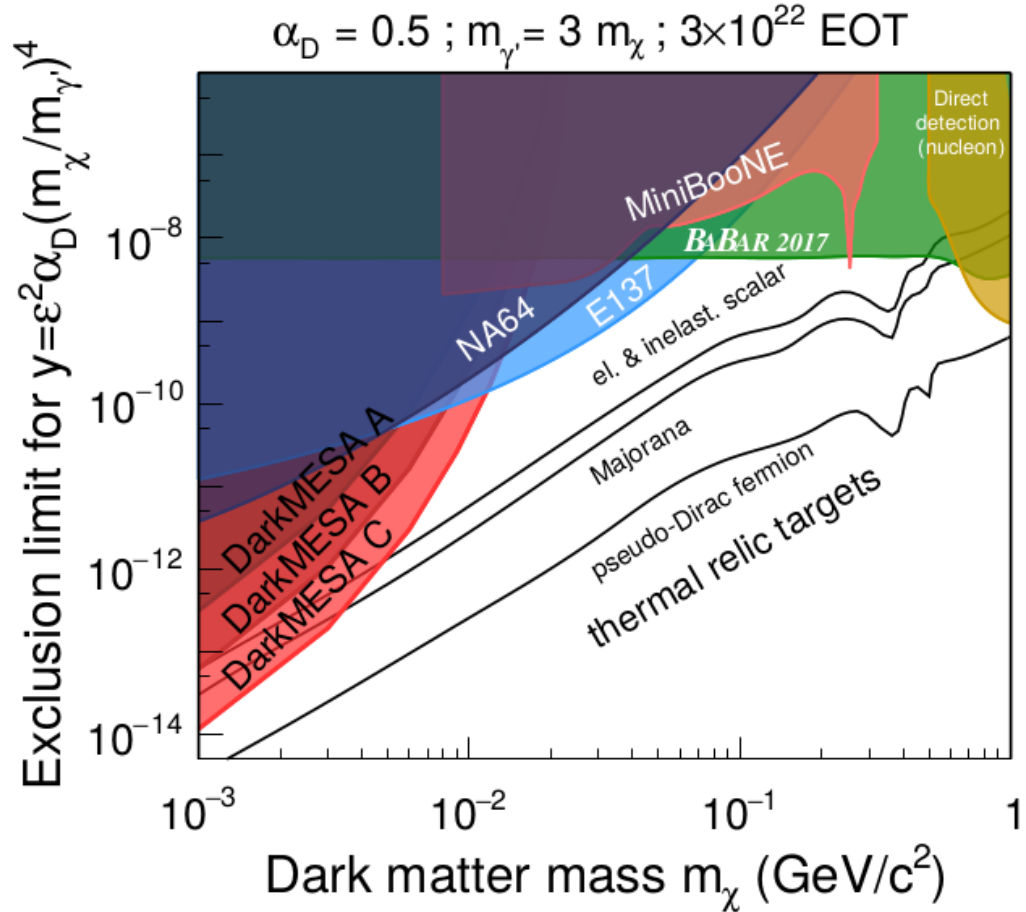


Figure 11.7: Simulated exclusion limits for the three foreseen construction phases of the darkMESA experiment compared to the existing limits from NA64 [272, 273], E137 [243], BaBar [274], MiniBooNE [275], and CRESST (direct detection) [276].

Existing experimental limits are also reported [272, 273, 274, 275, 276].

The downward peak visible in the MiniBooNE exclusion contour is located approximately at $m_\chi \sim m_{\gamma'}/2 \sim m_\rho/3 \sim 258 \text{ MeV}$ (m_ρ is the mass of the ρ meson.) Around this mass there is a resonant enhancement on the production of DM via proton bremsstrahlung near the ρ and ω mass regions. The same structure is visible also in the thermal lines, but in this case it appears at $m_\rho/2 \sim 388 \text{ MeV}$, since this is associated with DM annihilation [277].

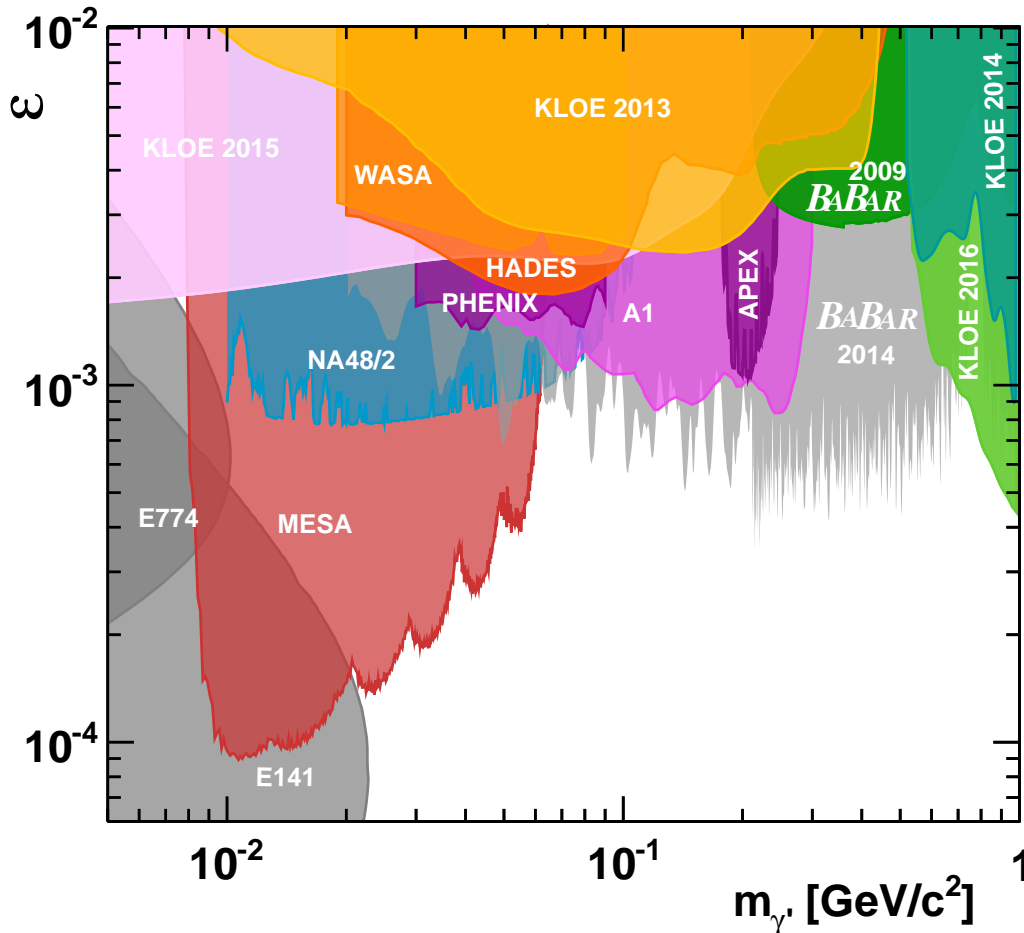


Figure 11.8: Projected exclusion limits for the MAGIX experiment in the case of $\gamma' \rightarrow e^+e^-$ visible decays. The reported existing limits are from the re-analysis [278] of the E774 [279] data, APEX [280], WASA [281], KLOE-2 [282], HADES [283], BABAR [284, 285], A1 [286], PHENIX [287], E141 [242, 288] (Figure from H. Merkel).

In Fig. 11.8, the expected limits for the other MESA experiment MAGIX are showed in comparison with the existing ones. These limits refer to a dark photon decaying into electron-positron pairs which are detected in coincidence with two magnetic spectrometers.

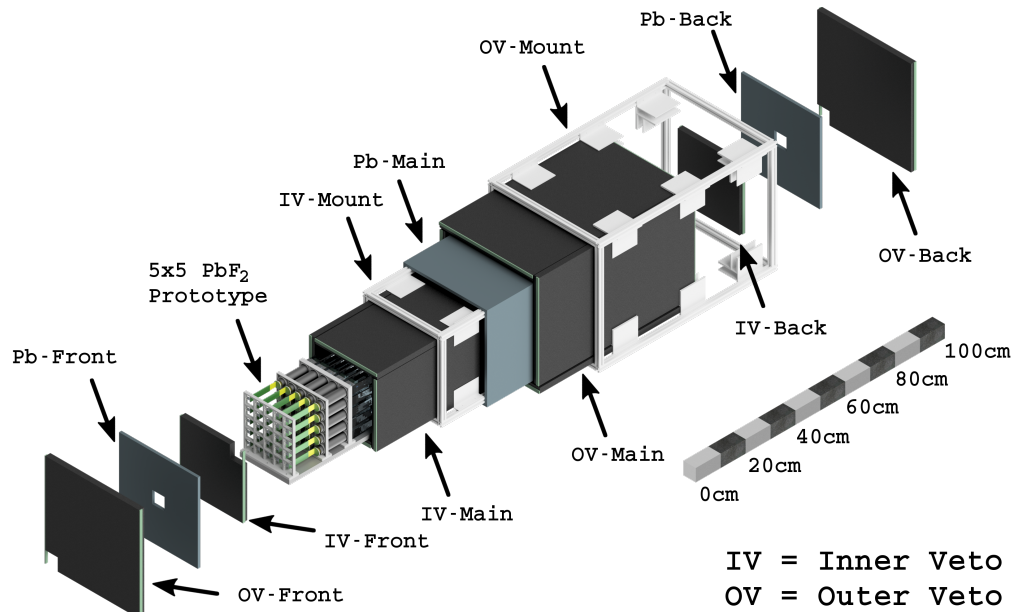


Figure 11.9: Exploded view of the prototype under construction at the Mainz Institute of Nuclear Physics. The detector system is composed by a matrix of 5×5 PbF_2 crystals and two hermetic layers (IV, OV) of scintillators separated by lead sheets for vetoing cosmic rays and surrounding radiation.

11.6 darkMESA Prototype

For assessing the capabilities of the darkMESA detector concept and further develop the simulation, a prototype is being constructed at the Mainz Institute for Nuclear Physics. The prototype detector is based on a matrix of 5×5 PbF_2 crystals coupled to PMTs. The crystal assembly is surrounded by a veto detector comprised of two layers of plastic scintillators³ separated by a 0.5 cm lead sheet (see Fig. 11.9).

The plastic scintillators have grooves where wavelength-shifting fibers⁴ are hosted. The light from the fibers is detected by silicon photomultipliers⁵ installed on read-out electronic cards installed on the edges of the scintillators (see Fig. 11.10).

³Type EJ-200, 20 mm thick

⁴St.-Gobain BCF92, multi-clad wavelength-shifting fibers with 1 mm diameter.

⁵SensL J-series

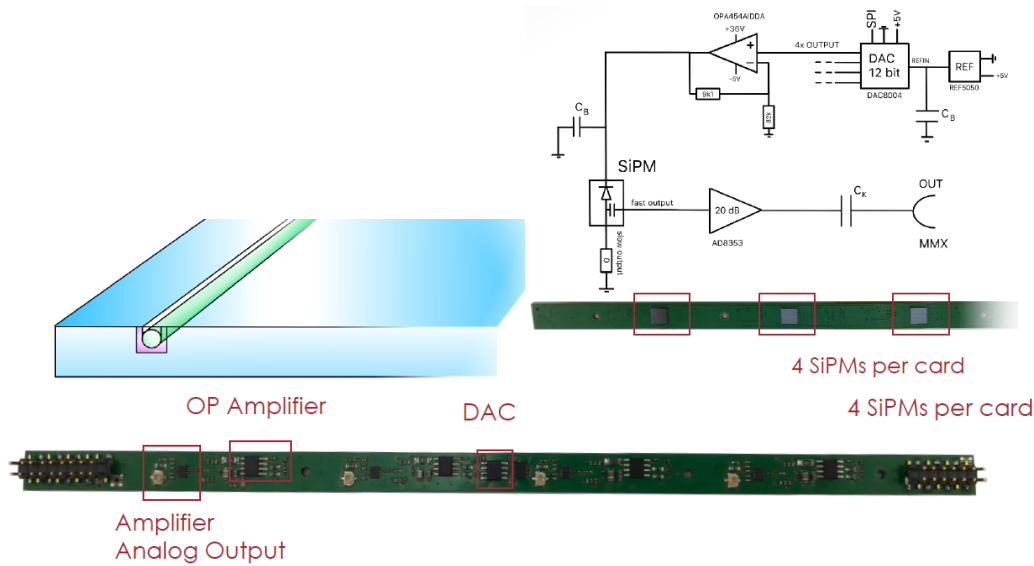


Figure 11.10: **Top-left:** Drawing of the grooved scintillator with the wavelength-shifting fiber. **Top-right:** Read-out electronics of the silicon photomultipliers. **Bottom:** Detail of the read-out card which contains 4 silicon photomultipliers. A card is installed on both the short sides of the scintillators, reading out both ends of the fibers.

11.7 Conclusion and Outlook

The new MESA accelerator will host three new experiments and two of them will be involved in dark matter searches. In particular, we described darkMESA, a new beam-dump experiment which will operate parasitically to the P2 experiment looking for DM particle interactions in a dense calorimeter placed in a shielded area and taking advantage of the very high luminosity of the new accelerator.

In order to assess the capabilities of such an experiment, a full simulation study and a detector test were performed. The results obtained show that already in its first phase, darkMESA has the potential to reach competitive sensitivities with respect to the existing experiments. The detector built in a first phase (with PbF₂ crystals) will be complemented by a larger one (based on Pb-Glasses) for fully exploiting the potential of the MESA beam. While the Phase 1 detector will cover novel regions of the param-

eter space, a larger detector will have the potential to reach the thermal target lines (see Fig. 11.7). This is a particularly exciting opportunity for testing the thermal character of DM in dark sector models. If DM is a thermal relic from the early Universe, all the phase space above the thermal lines is an extremely interesting region to investigate.

A second experiment, called MAGIX, is comprised by two high-resolution ($\delta p/p \sim 10^{-4}$) spectrometer setup coupled with a gas-jet target taking advantage of the high-current ($\sim 1\text{mA}$) recirculation and energy recovery mode of MESA. Part of the MAGIX program is dedicated to dark sector physics with planned measurements for both visible ($\gamma' \rightarrow e^+e^-$) and invisible ($\gamma' \rightarrow \chi\chi$) decays of the dark photon [289, 290, 286].

Dark matter is one of the most important mysteries in fundamental physics. Decades of intense research efforts did not result yet in an explanation of these puzzling phenomena. It is thus important to leave no stone unturned and pursue different search strategies in parallel. Dark sector theories provide a compelling explanation for dark matter and potentially can uncover a completely new set of particles which might be key to the understanding of phenomena at the cosmological scale.

Dark sector physics has exciting times ahead with a variety of existing and planned experiments for investigating a wide range of possible realizations of these theories. MESA will contribute to this endeavor with two completely new experiments, complementing the diverse research program the new accelerator will allow.

Appendices

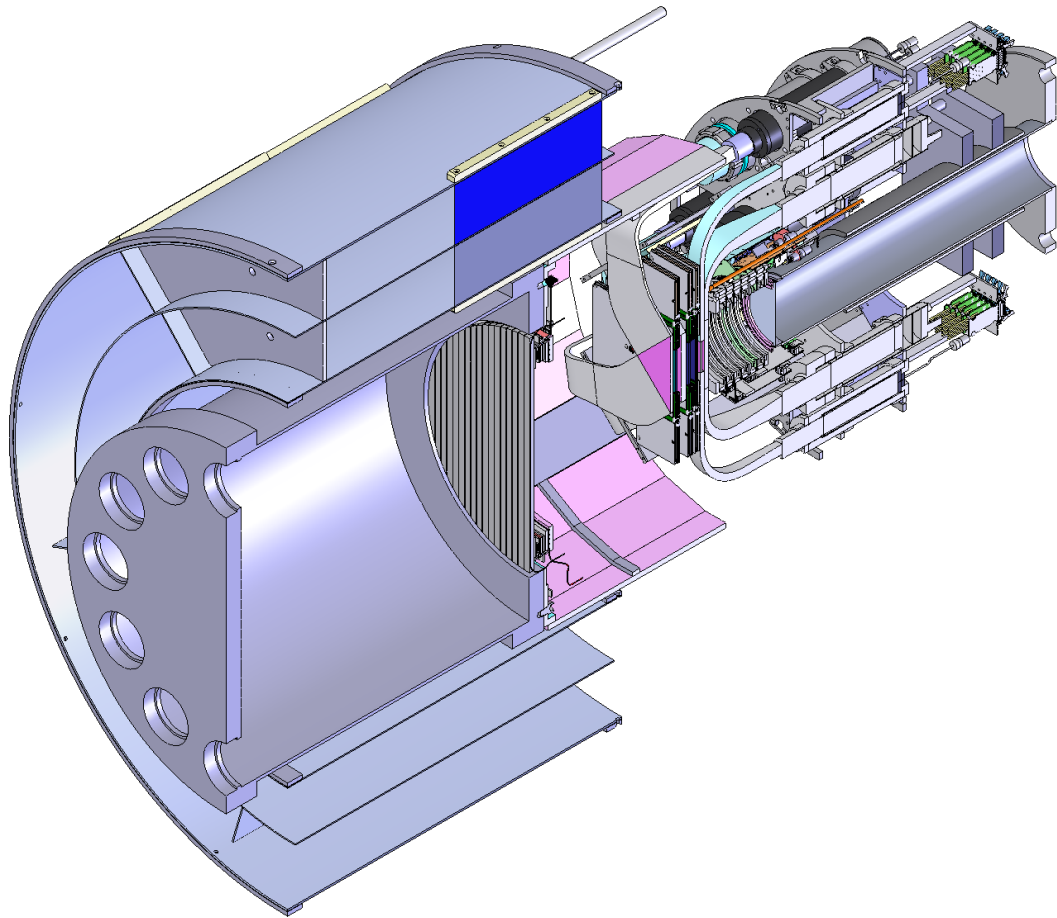


Figure A.1: Cross section of the PIENU Detector.

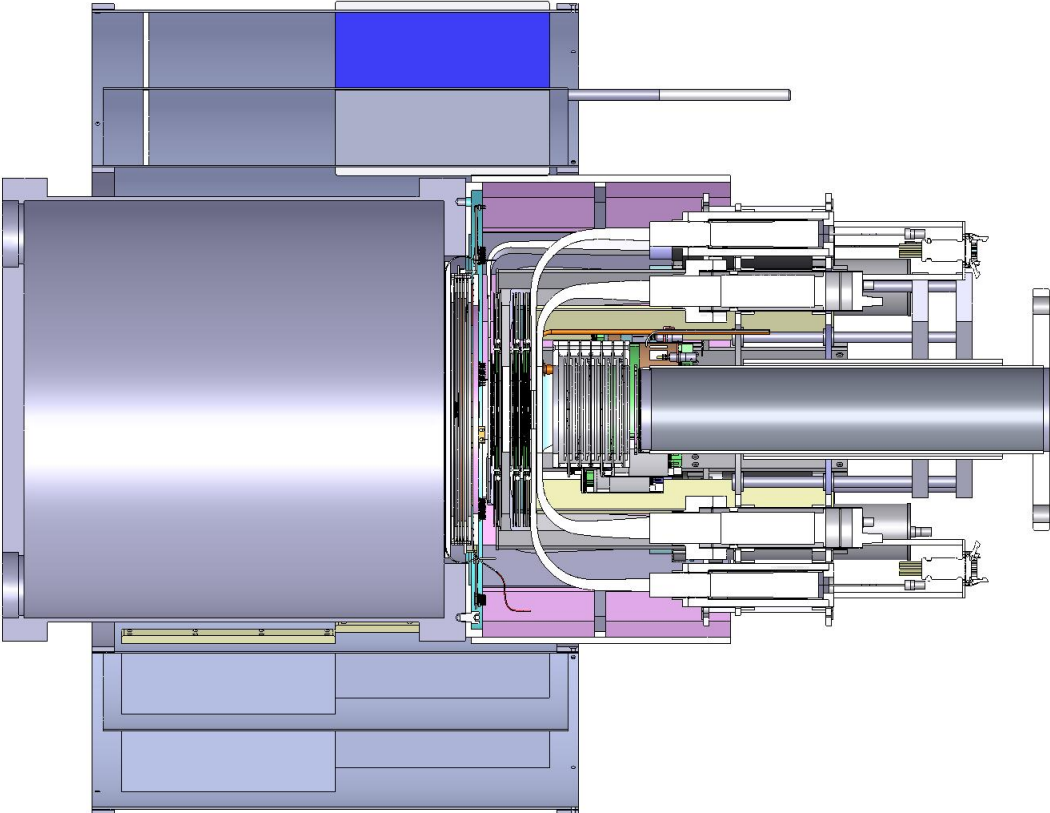


Figure A.2: Side view of the PIENU Detector. The pion beam comes from the right side.

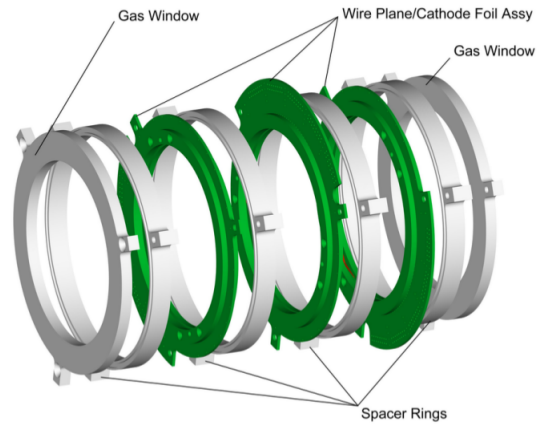


Figure A.3: Exploded view of a beam wire chamber (WC1/2).

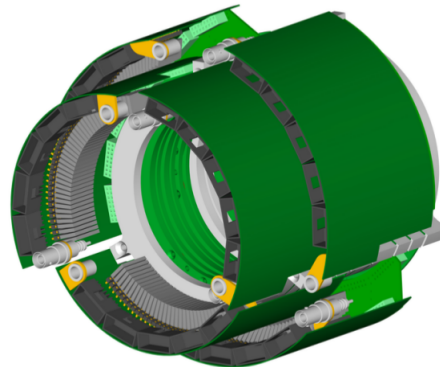


Figure A.4: The two beam wire chambers (WC1/2) assembled together. The beam direction is from left to right.

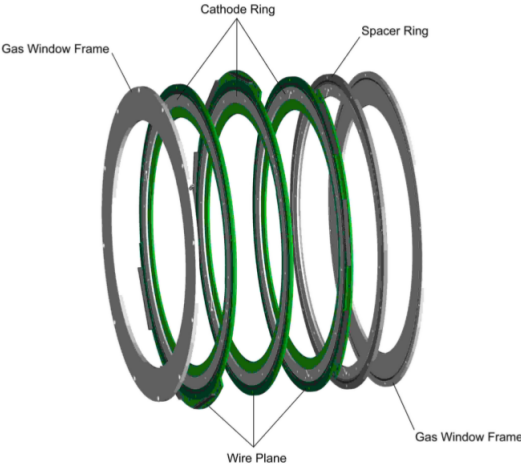


Figure A.5: Exploded view of the WC3 wire chamber.

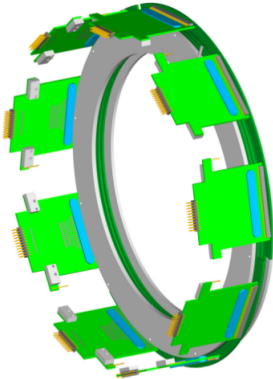


Figure A.6: Full WC3 assembly with read-out cards.

C Time spectrum for $\pi \rightarrow \mu \rightarrow e$

The $\pi^+ \rightarrow \mu^+ \nu_\mu \rightarrow e^+ \nu_e \bar{\nu}_\mu$ process is a decay chain composed by two decays characterized by the decay times $\tau_\pi = 1/\lambda_\pi$ and $\tau_\mu = 1/\lambda_\mu$. The pion decays with a rate dN_π/dt given by

$$\frac{dN_\pi}{dt} = -\lambda_\pi N_\pi \quad , \quad (\text{C.1})$$

where N_π is the number of pions at time t . Assuming that all the pions decay into muons, the formation rate of the muons equals the decay rate of the pions

$$\frac{dN_\mu}{dt} = +\lambda_\pi N_\pi \quad . \quad (\text{C.2})$$

At the same time, the muons decay according to

$$\frac{dN_\mu}{dt} = -\lambda_\mu N_\mu \quad . \quad (\text{C.3})$$

The overall change in the muon population is therefore given by

$$\frac{dN_\mu}{dt} = \lambda_\pi N_\pi - \lambda_\mu N_\mu \quad . \quad (\text{C.4})$$

Assuming a known initial amount of pions N_π^0 and muons N_μ^0 , the solution of Eq. C.4 is

$$N_\mu = \frac{\lambda_\pi}{\lambda_\mu - \lambda_\pi} N_\pi^0 \left(e^{-\lambda_\pi t} - e^{-\lambda_\mu t} \right) + N_\mu^0 e^{-\lambda_\mu t} \quad . \quad (\text{C.5})$$

From the last result, assuming no initial muons present, the normalized $\pi^+ \rightarrow \mu^+ \nu_\mu \rightarrow e^+ \nu_e \bar{\nu}_\mu$ time spectrum has a shape described by

$$f(t) = \frac{1}{\tau_\mu - \tau_\pi} \left(e^{-t/\tau_\mu} - e^{-t/\tau_\pi} \right) \quad . \quad (\text{C.6})$$

D Z-vertex determination with Tracking

Given the reconstructed pion and positron tracks, it is possible to determine the location of the decay vertex, which is defined as the point of closest approach of the two tracks. Using the track parameterization defined in Sec. 3.3.7, the track can be written in vectorial form as

$$\vec{x} = \vec{x}_0 + \vec{v} \cdot z \quad . \quad (\text{D.1})$$

The distance between the two tracks \vec{x}_1 and \vec{x}_2 is

$$d(z) = |\vec{\omega}(z)| = |\vec{x}_1 - \vec{x}_2| = |(\vec{x}_{0,1} - \vec{x}_{0,2}) + (\vec{v}_1 - \vec{v}_2) \cdot z| \quad . \quad (\text{D.2})$$

Redefining $(\vec{x}_{0,1} - \vec{x}_{0,2}) = \Delta X$ and $(\vec{v}_1 - \vec{v}_2) = \Delta V$, the squared distance is $\vec{\omega}(z) \cdot \vec{\omega}(z)$ and its extremum is:

$$\frac{\partial}{\partial z}(\vec{\omega}(z) \cdot \vec{\omega}(z)) = \frac{\partial}{\partial z}(\Delta X + \Delta V \cdot z)^2 = 0 \quad . \quad (\text{D.3})$$

Solving the equation for z , the extremal value z_{extr} is obtained

$$z_{extr} = -\frac{\Delta X \Delta V}{(\Delta V)^2} \quad . \quad (\text{D.4})$$

The condition for z_{extr} being the minimum for the distance function is

$$\frac{\partial^2}{\partial z^2}(\vec{\omega}(z) \cdot \vec{\omega}(z)) = (\Delta V)^2 > 0 \quad . \quad (\text{D.5})$$

The second derivative is always positive, so $z_{extr} = z_{min}$.

\vec{x}_0 and \vec{v} are a direct result of the fitting algorithm and knowing them allows to directly calculate z_{min} .

Substituting z_{min} into the track's equation, also the other two coordinates can be found. The explicit expression for the location in z (called Z_V within the PIENU experiment) of the point of minimum approach of the two tracks is

$$z_{min} = -\frac{(x_{0,1} - x_{0,2}) \cdot (v_{x,1} - v_{x,2}) + (y_{0,1} - y_{0,2}) \cdot (v_{y,1} - v_{y,2})}{(v_{x,1} - v_{x,2})^2 + (v_{y,1} - v_{y,2})^2} \quad . \quad (\text{D.6})$$

E Detector Scattering Kinematics

In the detector, the DM particles can interact with electrons, nucleons or nuclei and the exact form of the scattering cross-section depends from the nature of the DM particle χ .

E.1 $e\chi$ Scattering

In the simulations for the darkMESA experiment, χ was a Dirac particle. In the following, we report the treatment of the more general case where DM is a pseudo-Dirac particle without structure and the scattering is $\chi_1(p_1)X(p_2) \rightarrow \chi_2(k_1)X(k_2)$, where X is a SM particle with spin 1/2 like an electron or a nucleon, and the quantities in parentheses are the 4-momenta.

χ_1 and χ_2 are two DM states with mass splitting $\Delta = m_1 - m_2$. The amplitude for this process is

$$\mathcal{A} = \frac{eeg_D}{(t - m_{\gamma'}^2)} [\bar{u}(k_2)\gamma_\mu u(p_2)] [\bar{u}(k_1)\gamma^\mu u(p_1)] \quad . \quad (\text{E.1})$$

Squaring the last equation and averaging over the spins ($\alpha_D = g_D^2/4\pi$),

$$\begin{aligned} \langle |\mathcal{A}|^2 \rangle &= \frac{128\pi^2 e^2 \alpha_D}{(t - m_{\gamma'}^2)^2} \times \\ &[(k_1 \cdot k_2)(p_1 \cdot p_2) + (k_2 \cdot p_1)(p_2 \cdot k_1) \\ &- m_1 m_2 (k_2 \cdot p_2) - m_X^2 (p_1 \cdot k_1) + 2m_1 m_2 m_X^2] \quad , \end{aligned} \quad (\text{E.2})$$

where m_X is the mass of X. In the center-of-mass frame¹ the initial and final 3-momenta satisfy

$$|p^*|^2 = \frac{(s - m_X^2 - m_1^2)^2 - 4m_X^2 m_1^2}{4s} \quad , \quad (\text{E.3})$$

$$|k^*|^2 = \frac{(s - m_X^2 - m_2^2)^2 - 4m_X^2 m_2^2}{4s} \quad , \quad (\text{E.4})$$

with s the Mandelstam variable in the case of a stationary target

$$s = (p_1 + p_2)^2 = m_1^2 + m_X^2 + 2m_X E_{p_1} \quad . \quad (\text{E.5})$$

¹In this frame the corresponding coordinates are indicated with an "*".

Another useful relation is

$$k_1 \cdot p_1 = E_{p_1}^* E_{k_1}^* - |p^*| |k^*| \cos \theta^* \quad . \quad (\text{E.6})$$

The **elastic scattering case** of the darkMESA simulation is recovered with $|p^*|^2 = |k^*|^2$.

The scattering cross section is

$$\frac{d\sigma}{d\Omega^*} = \frac{1}{2\pi} \frac{d\sigma}{d \cos \theta^*} = \frac{\langle |\mathcal{A}|^2 \rangle |k^*|}{64\pi^2 s |p^*|} \quad . \quad (\text{E.7})$$

and changing variables

$$d \cos \theta^* = \frac{m_X}{|k^*| |p^*|} dE_X \quad , \quad (\text{E.8})$$

where $E_X = E_{k_2}$ is the electron/nucleon recoil energy, the recoil spectrum is finally given by

$$\frac{d\sigma}{dE_X} = \frac{m_X \langle |\mathcal{A}|^2 \rangle}{32\pi s |p^*|^2} \quad . \quad (\text{E.9})$$

E.2 $p\chi$ and $N\chi$ Scattering

If the target is a composite object like a nucleon or a nucleus, the amplitude can be generalized as

$$\mathcal{A} = \frac{\epsilon e g_D}{t - m_{\gamma'}^2} \left(g_{\mu\nu} - \frac{q_\mu q_\nu}{m_{\gamma'}^2} \right) [\bar{u}(k_1) \gamma^\mu u(p_1)] [\bar{u}(k_2) \Gamma^\nu u(p_2)] \quad , \quad (\text{E.10})$$

assuming monopole and dipole coupling to the electromagnetic current and $t = q^2$ with $q = p_1 - k_1$. The γ' -target vertex is parametrized by the Lorentz-invariant term

$$\Gamma^\mu = F_1(q^2) \gamma^\mu + F_2(q^2) \frac{i q_\nu \sigma^{\mu\nu}}{2M} \quad . \quad (\text{E.11})$$

M is the mass of the target, F_1 and F_2 are the electric monopole and dipole form factors which depend from the exact nature of the target and $\sigma^{\mu\nu} = (i/2)[\gamma^\mu, \gamma^\nu]$.

In the simulation, for the nucleon target case, the approximate dipole form factors were used

$$F_1 = \begin{cases} \frac{1}{(1 - q^2/m_p^2)^2} & \text{proton} \\ 0 & \text{neutron} \end{cases} , \quad (\text{E.12})$$

$$F_2 = \begin{cases} \frac{k_p}{(1 - q^2/m_p^2)^2} & \text{proton} \\ \frac{k_n}{(1 - q^2/m_n^2)^2} & \text{neutron} \end{cases} , \quad (\text{E.13})$$

with $k_p \sim 1.79$ and $k_n \sim -1.9$. In the case of a nucleus, a good approximation at low energies is $F_1 = Z$ and $F_2 = 0$, where Z is the atomic number.

The spin-averaged cross section is

$$\begin{aligned} \langle |\mathcal{A}|^2 \rangle &= \frac{16\pi^2 \epsilon^2 \alpha \alpha_D}{(t - m_\gamma^2)^2} \times \\ &\left\{ (F_1 + F_2)^2 [t(p_1 + k_1)^2 + 3t(t - \Delta^2) - (m_2^2 - m_1^2)^2] \right. \\ &\left. + (F_1^2 + F_2^2) [(p_1 + k_1) \cdot (p_2 + k_2)]^2 + (k_2 + p_2)^2 (t - \Delta^2) \right\} . \end{aligned} \quad (\text{E.14})$$

For a target at rest in the laboratory frame, the cross section is

$$\frac{d\sigma}{d\Omega^*} = \frac{1}{2E_\chi} \frac{1}{2M} \frac{1}{|v_\chi|} \frac{\beta(s, m_j^2, M^2)}{32\pi^2} \langle |\mathcal{A}(\chi_i X \rightarrow \chi_j X)|^2 \rangle , \quad (\text{E.15})$$

where

$$\beta(s, m_j^2, M^2) = \sqrt{1 - \frac{2(m_{\chi_j} + M)}{s} + \frac{(m_{\chi_j} - M)^2}{s^2}} . \quad (\text{E.16})$$

F Crystal Tests for darkMESA



Figure F.1: SF5 Pb-Glass crystal (from Schott AG).



Figure F.2: SF6 Pb-Glass crystal (from Schott AG).



Figure F.3: SF57HTultra Pb-Glass crystal (from Schott AG).

APPENDIX F. CRYSTAL TESTS FOR DARKMESA



Figure F.4: PbF_2 crystal (previously A4 collaboration).

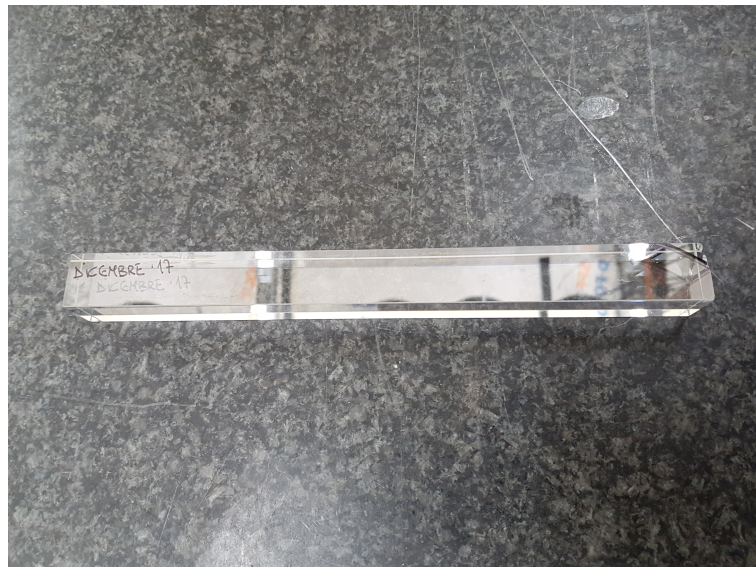


Figure F.5: BGO crystal (on loan from INFN Frascati).

Bibliography

- [1] G. Arnison et al. Experimental Observation of Isolated Large Transverse Energy Electrons with Associated Missing Energy at $\sqrt{s} = 540\text{-GeV}$. *Phys. Lett.*, B122:103–116, 1983. [611(1983)]. doi:10.1016/0370-2693(83)91177-2.
- [2] G. Arnison et al. Experimental Observation of Lepton Pairs of Invariant Mass Around $95\text{-GeV}/c^2$ at the CERN SPS Collider. *Phys. Lett.*, B126:398–410, 1983. [7.55(1983)]. doi:10.1016/0370-2693(83)90188-0.
- [3] F. Abe et al. Observation of Top Quark Production in $\bar{p}p$ Collisions with the Collider Detector at Fermilab. *Phys. Rev. Lett.*, 74:2626–2631, Apr 1995. Available from: <https://link.aps.org/doi/10.1103/PhysRevLett.74.2626>, doi:10.1103/PhysRevLett.74.2626.
- [4] S. Abachi et al. Search for high mass top quark production in $p\bar{p}$ collisions at $\sqrt{s} = 1.8\text{ tev}$. *Phys. Rev. Lett.*, 74:2422–2426, Mar 1995. Available from: <https://link.aps.org/doi/10.1103/PhysRevLett.74.2422>, doi:10.1103/PhysRevLett.74.2422.
- [5] S. Chatrchyan et al. Observation of a new boson at a mass of 125 GeV with the CMS experiment at the LHC. *Physics Letters B*, 716:30–61, 2012. doi:10.1016/j.physletb.2012.08.021.
- [6] G. Aad et al. Observation of a new particle in the search for the Standard Model Higgs boson with the ATLAS detector at the LHC. *Physics Letters B*, 716:1–29, 2012. doi:10.1016/j.physletb.2012.08.020.
- [7] G. Hinshaw, D. Larson, E. Komatsu, D. N. Spergel, C. L. Bennett, J. Dunkley, M. R. Nolte, M. Halpern, R. S. Hill, N. Ode-

- gard, L. Page, K. M. Smith, J. L. Weiland, B. Gold, N. Jarosik, A. Kogut, M. Limon, S. S. Meyer, G. S. Tucker, E. Wollack, and E. L. Wright. Nine-year wilkinson microwave anisotropy probe (wmap) observations: Cosmological parameter results. *The Astrophysical Journal Supplement Series*, 208(2):19, 2013. Available from: <http://stacks.iop.org/0067-0049/208/i=2/a=19>.
- [8] P. A. R. Ade et al. Planck 2015 results. XIII. Cosmological parameters. *Astron. Astrophys.*, 594:A13, 2016. arXiv:1502.01589, doi:10.1051/0004-6361/201525830.
- [9] Fred Jegerlehner. The hierarchy problem of the electroweak Standard Model revisited. 2013. arXiv:1305.6652.
- [10] J. P. Ostriker and Paul J. Steinhardt. Cosmic concordance. 1995. arXiv:astro-ph/9505066.
- [11] R.M. Wald. *General Relativity*. University of Chicago Press, 1984. Available from: <https://books.google.de/books?id=ibSdQgAACAAJ>.
- [12] M. Tanabashi et al. Review of particle physics. *Phys. Rev. D*, 98:030001, Aug 2018. Available from: <https://link.aps.org/doi/10.1103/PhysRevD.98.030001>, doi:10.1103/PhysRevD.98.030001.
- [13] Vincenzo Cirigliano and Ignasi Rosell. $\pi/K \rightarrow ev$ branching ratios to $O(e^2 p^4)$ in Chiral Perturbation Theory. *JHEP*, 10:005, 2007. arXiv:0707.4464, doi:10.1088/1126-6708/2007/10/005.
- [14] C. Patrignani et al. Particle data group. *Chin. Phys. C*, 40, 2016 and 2017 update.
- [15] C. M. G. Lattes, H. Muirhead, G. P. S. Occhialini, C. F. Powell. Processes involving charged mesons. *Nature*, 159:694–697, 1933.
- [16] H Yukawa. On the interaction of elementary particles. *Proc. Phys. Math. Soc. Jap.*, 17:48–57, 1935.
- [17] Official Website of the Nobel Prize. Available from: http://www.nobelprize.org/nobel_prizes/physics/laureates/1950/powell-bio.html.

BIBLIOGRAPHY

- [18] C.D. Neddermeyer, Anderson. Note on the nature of cosmic-ray particles. *Phys. Rev.*, 51:884–886, 1937.
- [19] H.L. Anderson and C. Lattes. Search for the electronic decay of the positive pion. *Il Nuovo Cimento (1955-1965)*, 6:1356–1381, 1957.
- [20] S. Lokanathan and J. Steinberger. *Suppl. Nuovo cimento*, 2:151, 1955.
- [21] E. C. G. Sudarshan and R. E. Marshak. Chirality Invariance and the Universal Fermi Interaction. *Phys. Rev.*, 109(5):1860–1862, Mar 1958. doi:10.1103/PhysRev.109.1860.2.
- [22] R. P. Feynman and M. Gell-Mann. Theory of the Fermi Interaction. *Phys. Rev.*, 109(1):193–198, Jan 1958. doi:10.1103/PhysRev.109.193.
- [23] C. S. Wu, E. Ambler, R. W. Hayward, D. D. Hoppes and R. P. Hudson. Experimental test of parity conservation in beta decay. *Phys. Rev.*, 105(4):1413–1415, Feb 1957. doi:10.1103/PhysRev.105.1413.
- [24] T. Fazzini *et al.* Electron Decay of the Pion. *Phys. Rev. Lett.*, 1:247–249, 1958.
- [25] G. Impeduglia, R. Plano, A. Prodell, N. Samios, M. Schwartz, and J. Steinberger. β decay of the pion. *Phys. Rev. Lett.*, 1:249–251, Oct 1958. Available from: <http://link.aps.org/doi/10.1103/PhysRevLett.1.249>, doi:10.1103/PhysRevLett.1.249.
- [26] J. Ashkin, T. Fazzini, G. Fidecaro, A. W. Merrison, H. Paul, and A. V. Tollestrup. The electron decay mode of the pion. *Il Nuovo Cimento (1955-1965)*, 13(6):1240–1262, Sep 1959. Available from: <https://doi.org/10.1007/BF02725130>, doi:10.1007/BF02725130.
- [27] Giuseppe Fidecaro. The Discoveries of Rare Pion Decays at the CERN Synchrocyclotron. *Adv. Ser. Direct. High Energy Phys.*, 23:397–414, 2015. doi:10.1142/9789814644150_0016.
- [28] H.L. Anderson *et al.* Branching Ratio of the Electronic Mode of Positive Pion Decay. *Phys. Rev.*, 119:2050–2067, 1960.

-
- [29] E. Di Capua, R. Garland, L. Pondrom, and A. Strelzoff. Study of the decay $\pi \rightarrow e + \nu$. *Phys. Rev.*, 133(5B):B1333–B1340, Mar 1964. doi:10.1103/PhysRev.133.B1333.
- [30] Douglas Bryman and Charles Picciotto. Revised value for the $\pi \rightarrow e\nu$ branching ratio. *Phys. Rev.*, D11:1337, 1975. doi:10.1103/PhysRevD.11.1337.
- [31] D. A. Bryman, R. Dubois, J. A. MacDonald, T. Numao, B. Olaniyi, A. Olin, J.-M. Poutissou, and M. S. Dixit. Measurement of the $\pi \rightarrow e\nu$ branching ratio. *Phys. Rev. D*, 33(5):1211–1221, Mar 1986. doi:10.1103/PhysRevD.33.1211.
- [32] G. Czapek, A. Federspiel, A. Flükiger, D. Frei, B. Hahn, C. Hug, E. Hugentobler, W. Krebs, U. Moser, D. Muster, E. Ramseyer, H. Scheidiger, P. Schlatter, G. Stucki, R. Abela, D. Renker, and E. Steiner. Branching ratio for the rare pion decay into positron and neutrino. *Phys. Rev. Lett.*, 70(1):17–20, Jan 1993. doi:10.1103/PhysRevLett.70.17.
- [33] D. I. Britton, S. Ahmad, D. A. Bryman, R. A. Burnham, E. T. H. Clifford, P. Kitching, Y. Kuno, J. A. Macdonald, T. Numao, A. Olin, J.-M. Poutissou, and M. S. Dixit. Measurement of the $\pi^+ \rightarrow e^+\nu$ branching ratio. *Phys. Rev. D*, 49(1):28–39, Jan 1994. doi:10.1103/PhysRevD.49.28.
- [34] W. J. Marciano. Proceedings of the Workshop on Future Directions in Nuclear and Particle Physics at Multi-GeV Hadron Beam Facilities, 1993.
- [35] D. I. Britton, S. Ahmad, D. A. Bryman, R. A. Burnham, E. T. H. Clifford, P. Kitching, Y. Kuno, J. A. Macdonald, T. Numao, A. Olin, J.-M. Poutissou, and M. S. Dixit. Measurement of the $\pi^+ \rightarrow e^+\nu$ branching ratio. *Phys. Rev. Lett.*, 68:3000–3003, May 1992. Available from: <http://link.aps.org/doi/10.1103/PhysRevLett.68.3000>, doi:10.1103/PhysRevLett.68.3000.
- [36] L. Michel. Interaction between Four Half-Spin Particles and the Decay of the μ -Meson. *Proceedings of the Physical Society. Section A*, 63(5):514, 1950. Available from: <http://stacks.iop.org/0370-1298/63/i=5/a=311>.

BIBLIOGRAPHY

- [37] A. Aguilar-Arevalo et al. Study of a large NaI(Tl) crystal. *Nucl. Instrum. Methods Phys. Res., Sect. A*, 621:188–191, September 2010.
- [38] D.J. Gross and F. Wilczek. Ultraviolet behavior of non-abelian gauge theories. *Phys. Rev. Lett.*, 30:1343–1346, 1973.
- [39] H.D. Politzer. Reliable perturbative results for strong interactions. *Phys. Rev. Lett.*, 30:1346–1349, 1973.
- [40] Steven Weinberg. Pion scattering lengths. *Phys. Rev. Lett.*, 17:616–621, Sep 1966. Available from: <https://link.aps.org/doi/10.1103/PhysRevLett.17.616>, doi:10.1103/PhysRevLett.17.616.
- [41] Steven Weinberg. Phenomenological lagrangians. *Physica A: Statistical Mechanics and its Applications*, 96(1):327 – 340, 1979. Available from: <http://www.sciencedirect.com/science/article/pii/0378437179902231>, doi:[https://doi.org/10.1016/0378-4371\(79\)90223-1](https://doi.org/10.1016/0378-4371(79)90223-1).
- [42] Nicola Cabibbo. Unitary symmetry and leptonic decays. *Phys. Rev. Lett.*, 10(12):531–533, Jun 1963. doi:10.1103/PhysRevLett.10.531.
- [43] Makoto Kobayashi and Toshihide Maskawa. CP-Violation in the Renormalizable Theory of Weak Interaction. *Progress of Theoretical Physics*, 49(2):652–657, 1973. Available from: <http://ptp.ipap.jp/link?PTP/49/652/>, doi:10.1143/PTP.49.652.
- [44] F. Englert and R. Brout. Broken symmetry and the mass of gauge vector mesons. *Phys. Rev. Lett.*, 13:321–323, Aug 1964. Available from: <https://link.aps.org/doi/10.1103/PhysRevLett.13.321>, doi:10.1103/PhysRevLett.13.321.
- [45] Peter W. Higgs. Broken symmetries and the masses of gauge bosons. *Phys. Rev. Lett.*, 13:508–509, Oct 1964. Available from: <https://link.aps.org/doi/10.1103/PhysRevLett.13.508>, doi:10.1103/PhysRevLett.13.508.
- [46] G. S. Guralnik, C. R. Hagen, and T. W. B. Kibble. Global conservation laws and massless particles. *Phys. Rev. Lett.*, 13:585–587, Nov 1964. Available from: <https://link.aps.org/doi/10.1103/PhysRevLett.13.585>, doi:10.1103/PhysRevLett.13.585.

- [47] S. Scherer and M.R. Schindler. A Chiral Perturbation Theory Primer. *Lectures given at the ECT* Doctoral Training Programme (arXiv:hep-ph/0505265)*, 2005. arXiv:hep-ph:0505265.
- [48] Kenneth G. Wilson. Confinement of quarks. *Phys. Rev. D*, 10:2445–2459, Oct 1974. Available from: <https://link.aps.org/doi/10.1103/PhysRevD.10.2445>, doi:10.1103/PhysRevD.10.2445.
- [49] C. T. H. Davies, E. Follana, A. Gray, G. P. Lepage, Q. Mason, M. Nobes, J. Shigemitsu, H. D. Trottier, M. Wingate, C. Aubin, C. Bernard, T. Burch, C. DeTar, Steven Gottlieb, E. B. Gregory, U. M. Heller, J. E. Hetrick, J. Osborn, R. Sugar, D. Toussaint, M. Di Pierro, A. El-Khadra, A. S. Kronfeld, P. B. Mackenzie, D. Menscher, and J. Simone. High-precision lattice qcd confronts experiment. *Phys. Rev. Lett.*, 92:022001, Jan 2004. Available from: <https://link.aps.org/doi/10.1103/PhysRevLett.92.022001>, doi:10.1103/PhysRevLett.92.022001.
- [50] T. Kajita and A.B. McDonald. 2015 Nobel Prize in Physics. Available from: http://www.nobelprize.org/nobel_prizes/physics/laureates/2015/.
- [51] Raymond Davis, Don S. Harmer, and Kenneth C. Hoffman. Search for neutrinos from the sun. *Phys. Rev. Lett.*, 20:1205–1209, May 1968. Available from: <https://link.aps.org/doi/10.1103/PhysRevLett.20.1205>, doi:10.1103/PhysRevLett.20.1205.
- [52] Q. R. Ahmad et al. Measurement of the rate of $\nu_e + d \rightarrow p + p + e^-$ interactions produced by ${}^8\text{B}$ solar neutrinos at the sudbury neutrino observatory. *Phys. Rev. Lett.*, 87:071301, Jul 2001. Available from: <https://link.aps.org/doi/10.1103/PhysRevLett.87.071301>, doi:10.1103/PhysRevLett.87.071301.
- [53] B. Pontecorvo. Inverse beta processes and nonconservation of lepton charge. *Zhurnal Éksperimental'noi i Teoreticheskoi Fiziki*, 34, 1957.
- [54] Ziro Maki, Masami Nakagawa, and Shoichi Sakata. Remarks on the unified model of elementary particles. *Progress of Theoretical Physics*, 28(5):870–880, 1962.

BIBLIOGRAPHY

- [55] Murray Gell-Mann, Pierre Ramond, and Richard Slansky. Complex Spinors and Unified Theories. *Conf. Proc.*, C790927:315–321, 1979. arXiv:1306.4669.
- [56] S.L. Adler. Axial-Vector Vertex in Spinor Electrodynamics. *Phys. Rev.*, 177: 2426-38(Jan. 25, 1969)., Jan 1969. doi:10.1103/PhysRev.177.2426.
- [57] J. S. Bell and R. Jackiw. A PCAC puzzle: $\pi^0 \rightarrow \gamma\gamma$ in the sigma model. *Nuovo Cim.*, A60:47–61, 1969. doi:10.1007/BF02823296.
- [58] M. Gell-Mann and Y. Ne’eman. *The Eightfold Way*. Benjamin, New York, 1964.
- [59] Yoichiro Nambu. Quasi-particles and gauge invariance in the theory of superconductivity. *Phys. Rev.*, 117:648–663, Feb 1960. Available from: <https://link.aps.org/doi/10.1103/PhysRev.117.648>, doi:10.1103/PhysRev.117.648.
- [60] J. Goldstone. Field theories with Superconductor solutions. *Il Nuovo Cimento*, 19:154–164, January 1961. doi:10.1007/BF02812722.
- [61] C. Vafa and E. Witten. Restrictions on symmetry breaking in vector-like gauge theories. *Nuclear Physics B*, 234(1):173 – 188, 1984. Available from: <http://www.sciencedirect.com/science/article/pii/055032138490230X>, doi:[https://doi.org/10.1016/0550-3213\(84\)90230-X](https://doi.org/10.1016/0550-3213(84)90230-X).
- [62] S. Coleman. The invariance of the vacuum is the invariance of the world. *J. Math. Phys.*, 7:787, 1966.
- [63] S. Coleman, J. Wess, and Bruno Zumino. Structure of Phenomenological Lagrangians. I. *Phys. Rev.*, 177:2239–2247, Jan 1969. Available from: <https://link.aps.org/doi/10.1103/PhysRev.177.2239>, doi:10.1103/PhysRev.177.2239.
- [64] Murray Gell-Mann, R. J. Oakes, and B. Renner. Behavior of Current Divergences under $SU_3 \times SU_3$. *Phys. Rev.*, 175:2195–2199, Nov 1968. Available from: <https://link.aps.org/doi/10.1103/PhysRev.175.2195>, doi:10.1103/PhysRev.175.2195.

-
- [65] S. M. Berman. Radiative corrections to pion beta decay. *Phys. Rev. Lett.*, 1(12):468–469, Dec 1958. doi:10.1103/PhysRevLett.1.468.
- [66] Toichiro Kinoshita. Radiative corrections to $\pi - e$ decay. *Phys. Rev. Lett.*, 2(11):477–480, Jun 1959. doi:10.1103/PhysRevLett.2.477.
- [67] Terrence J. Goldman and Warren J. Wilson. Radiative corrections to muon-electron universality in a gauge theory of charged-pion decay. *Phys. Rev. D*, 14(9):2428–2430, Nov 1976. doi:10.1103/PhysRevD.14.2428.
- [68] W. J. Marciano and A. Sirlin. Theorem on π_{l2} decays and electron-muon universality. *Phys. Rev. Lett.*, 36(24):1425–1428, Jun 1976. doi:10.1103/PhysRevLett.36.1425.
- [69] William J. Marciano and A. Sirlin. Radiative corrections to π_{l2} decays. *Phys. Rev. Lett.*, 71(22):3629–3632, Nov 1993. doi:10.1103/PhysRevLett.71.3629.
- [70] Vincenzo Cirigliano and Ignasi Rosell. Two-Loop Effective Theory Analysis of $\pi(K) \rightarrow e\nu_e[\gamma]$ Branching Ratios. *Phys. Rev. Lett.*, 99(23):231801, Dec 2007. doi:10.1103/PhysRevLett.99.231801.
- [71] D. A. Bryman, W. J. Marciano, R. Tschirhart and T. Yamanaka. Rare kaon and pion decays: Incisive probes for new physics beyond the standard model. *Annual Review of Nuclear and Particle Science*, 61:331–354, 2011. doi:10.1146/annurev-nucl-102010-130431.
- [72] M. V. Terent'ev. Branching ratio $\gamma(\pi \rightarrow e\nu)/\gamma(\pi \rightarrow \mu\nu)$ with account of electromagnetic corrections and contribution from strong interactions. *Yad. Fiz.*, 18(870), 1973.
- [73] Vincenzo Cirigliano and Ignasi Rosell. Two-Loop Effective Theory Analysis of $\pi(K) \rightarrow e\nu_e[\gamma]$ Branching Ratios. *Phys. Rev. Lett.*, 99(23):231801, Dec 2007. doi:10.1103/PhysRevLett.99.231801.
- [74] Martin Gonzalez-Alonso, Jorge Martin Camalich, and Kin Mimiouni. Renormalization-group evolution of new physics contributions to (semi)leptonic meson decays. *Physics Letters B*, 772:777 – 785, 2017. Available from: <http://www.sciencedirect.com/>

BIBLIOGRAPHY

science/article/pii/S0370269317305506, doi:<https://doi.org/10.1016/j.physletb.2017.07.003>.

- [75] O. Shanker. π_{l2} , K_{l2} and $K^0 - \bar{K}^0$ constraints on lept-quarks and supersymmetric particles. *Nuclear Physics B*, 204(3):375 – 386, 1982. Available from: <http://www.sciencedirect.com/science/article/B6TVC-471YVGM-1BM/2/ee44f89753090b75fc6b1a52f55fb98b>, doi:DOI:10.1016/0550-3213(82)90196-1.
- [76] Bruce A. Campbell and David W. Maybury. Constraints on scalar couplings from $\pi^+ \rightarrow l^+ + \nu_l$. *Nucl. Phys.*, B709:419–439, 2005. doi:10.1016/j.nuclphysb.2004.12.015.
- [77] A. Masiero, P. Paradisi, and R. Petronzio. Probing new physics through mu e universality in $K \rightarrow l\nu$. *Phys. Rev.*, D74:011701, 2006. arXiv:hep-ph/0511289, doi:10.1103/PhysRevD.74.011701.
- [78] Michael J. Ramsey-Musolf, Shufang Su, and Sean Tulin. Pion Leptonic Decays and Supersymmetry. *Phys. Rev.*, D76:095017, 2007. arXiv:0705.0028, doi:10.1103/PhysRevD.76.095017.
- [79] R. Carlini, J.M. Finn, S.Kowalski, and S. Page, spokespersons. JLab Experiment E-02-020.
- [80] D. A. Bryman, W. J. Marciano, R. Tschirhart and T. Yamanaka. Rare kaon and pion decays: Incisive probes for new physics beyond the standard model. *Annual Review of Nuclear and Particle Science*, 2011. To be published.
- [81] S. Rolli and M. Tanabashi. Leptoquarks. *Reviews of Particle Data Group: Hypothetical particles and Concepts*, 2016. Available from: <http://pdg.lbl.gov/2016/reviews/rpp2016-rev-leptoquark-quantum-numbers.pdf>.
- [82] Jogesh C. Pati and Abdus Salam. Lepton number as the fourth "color". *Phys. Rev. D*, 10:275–289, Jul 1974. Available from: <https://link.aps.org/doi/10.1103/PhysRevD.10.275>, doi:10.1103/PhysRevD.10.275.

- [83] Howard Georgi and S. L. Glashow. Unity of All Elementary-Particle Forces. *Phys. Rev. Lett.*, 32:438–441, Feb 1974. Available from: <https://link.aps.org/doi/10.1103/PhysRevLett.32.438>, doi:10.1103/PhysRevLett.32.438.
- [84] Howard Georgi. The State of the Art – Gauge Theories. *AIP Conference Proceedings*, 23(1):575–582, 1975. Available from: <http://aip.scitation.org/doi/abs/10.1063/1.2947450>, arXiv:<http://aip.scitation.org/doi/pdf/10.1063/1.2947450>, doi:10.1063/1.2947450.
- [85] Harald Fritzsch and Peter Minkowski. Unified interactions of leptons and hadrons. *Annals of Physics*, 93(1):193 – 266, 1975. Available from: <http://www.sciencedirect.com/science/article/pii/0003491675902110>, doi:[https://doi.org/10.1016/0003-4916\(75\)90211-0](https://doi.org/10.1016/0003-4916(75)90211-0).
- [86] M. Hirsch, H. V. Klapdor-Kleingrothaus, and S. G. Kovalenko. New low-energy leptoquark interactions. *Physics Letters B*, 378(1-4):17 – 22, 1996. Available from: <http://www.sciencedirect.com/science/article/B6TVN-3VSR0KP-H/2/56684102f9f82c683e1245f2ce2ea9bf>, doi:DOI:10.1016/0370-2693(96)00419-4.
- [87] Miriam Leurer. Comprehensive study of leptoquark bounds. *Phys. Rev. D*, 49(1):333–342, Jan 1994. doi:10.1103/PhysRevD.49.333.
- [88] David B. Kaplan and Howard Georgi. $SU(2) \times U(1)$ breaking by vacuum misalignment. *Physics Letters B*, 136(3):183 – 186, 1984. Available from: <http://www.sciencedirect.com/science/article/pii/0370269384911778>, doi:[https://doi.org/10.1016/0370-2693\(84\)91177-8](https://doi.org/10.1016/0370-2693(84)91177-8).
- [89] Francesco Sannino, Peter Stangl, David M. Straub, and Anders Eller Thomsen. Flavor physics and flavor anomalies in minimal fundamental partial compositeness. *Phys. Rev. D*, 97:115046, Jun 2018. Available from: <https://link.aps.org/doi/10.1103/PhysRevD.97.115046>, doi:10.1103/PhysRevD.97.115046.

BIBLIOGRAPHY

- [90] A. A. Aguilar-Arevalo et al. Event Excess in the MiniBooNE Search for $\bar{\nu}_\mu \rightarrow \bar{\nu}_e$ Oscillations. *Phys. Rev. Lett.*, 105(18):181801, Oct 2010. doi:10.1103/PhysRevLett.105.181801.
- [91] Takehiko Asaka and Mikhail Shaposhnikov. The ν MSM, dark matter and baryon asymmetry of the universe. *Physics Letters B*, 620(1):17 – 26, 2005. Available from: <http://www.sciencedirect.com/science/article/pii/S0370269305008087>, doi:<https://doi.org/10.1016/j.physletb.2005.06.020>.
- [92] Alexey Boyarsky, Oleg Ruchayskiy, and Mikhail Shaposhnikov. The role of sterile neutrinos in cosmology and astrophysics. *Annual Review of Nuclear and Particle Science*, 59(1):191–214, 2009. Available from: <https://doi.org/10.1146/annurev.nucl.010909.083654>, arXiv:<https://doi.org/10.1146/annurev.nucl.010909.083654>, doi:10.1146/annurev.nucl.010909.083654.
- [93] Graciela Gelmini, Efunwande Osoba, Sergio Palomares-Ruiz, and Silvia Pascoli. MeV sterile neutrinos in low reheating temperature cosmological scenarios. *JCAP*, 0810:029, 2008. arXiv:0803.2735, doi:10.1088/1475-7516/2008/10/029.
- [94] Takehiko Asaka, Shintaro Eijima, and Hiroyuki Ishida. Mixing of active and sterile neutrinos. *Journal of High Energy Physics*, 2011(4):11, Apr 2011. Available from: [https://doi.org/10.1007/JHEP04\(2011\)011](https://doi.org/10.1007/JHEP04(2011)011), doi:10.1007/JHEP04(2011)011.
- [95] Bridget Bertoni, Seyda Ipek, David McKeen, and Ann E. Nelson. Constraints and consequences of reducing small scale structure via large dark matter-neutrino interactions. *Journal of High Energy Physics*, 2015(4):170, Apr 2015. Available from: [https://doi.org/10.1007/JHEP04\(2015\)170](https://doi.org/10.1007/JHEP04(2015)170), doi:10.1007/JHEP04(2015)170.
- [96] Brian Batell, Tao Han, David McKeen, and Barmak Shams Es Haghi. Thermal Dark Matter Through the Dirac Neutrino Portal. *Phys. Rev.*, D97(7):075016, 2018. arXiv:1709.07001, doi:10.1103/PhysRevD.97.075016.
- [97] C. E. Picciotto, S. Ahmad, D. I. Britton, D. A. Bryman, E. T. H. Clifford, P. Kitching, Y. Kuno, J. A. Macdonald, T. Numao, A. Olin, J.-M.

- Poutissou, J. Summhammer, and M. S. Dixit. Searches for majoron production and other processes associated with $\pi \rightarrow e\nu$ decay. *Phys. Rev. D*, 37:1131–1133, Mar 1988. Available from: <https://link.aps.org/doi/10.1103/PhysRevD.37.1131>, doi:10.1103/PhysRevD.37.1131.
- [98] Y. Chikashige, R.N. Mohapatra, and R.D. Peccei. Are there real goldstone bosons associated with broken lepton number? *Physics Letters B*, 98(4):265 – 268, 1981. Available from: <http://www.sciencedirect.com/science/article/pii/0370269381900113>, doi:[https://doi.org/10.1016/0370-2693\(81\)90011-3](https://doi.org/10.1016/0370-2693(81)90011-3).
- [99] G.B. Gelmini and M. Roncadelli. Left-handed neutrino mass scale and spontaneously broken lepton number. *Physics Letters B*, 99(5):411 – 415, 1981. Available from: <http://www.sciencedirect.com/science/article/pii/0370269381905591>, doi:[https://doi.org/10.1016/0370-2693\(81\)90559-1](https://doi.org/10.1016/0370-2693(81)90559-1).
- [100] A. Aguilar-Arevalo et al. (PIENU Collaboration). Improved measurement of the $\pi \rightarrow e\nu$ branching ratio. *Phys. Rev. Lett.*, 115:071801, 2015. doi:10.1103/PhysRevLett.115.071801.
- [101] Lusiani, Alberto. Lepton universality and lepton flavour violation tests at the b-factories. *EPJ Web of Conferences*, 118:01018, 2016. doi:10.1051/epjconf/201611801018.
- [102] C. Lazzeroni et al. Test of lepton flavour universality in $K^+ \rightarrow l^+\nu$ decays. *Physics Letters B*, 698(2):105 – 114, 2011. doi:10.1016/j.physletb.2011.02.064.
- [103] A. Pich. Tau Physics: Theory Overview. *Nucl. Phys. Proc. Suppl.*, 181-182:300–305, 2008. arXiv:{0806.2793}.
- [104] J. Charles, A. Höcker, H. Lacker, S. Laplace, F. R. Le Diberder, J. Malclés, J. Ocariz, M. Pivk, and L. Roos. Cp violation and the ckm matrix: assessing the impact of the asymmetric b factories. *The European Physical Journal C - Particles and Fields*, 41(1):1–131, May 2005. Available from: <https://doi.org/10.1140/epjc/s2005-02169-1>. See also <http://ckmfitter.in2p3.fr>, doi:10.1140/epjc/s2005-02169-1.

BIBLIOGRAPHY

- [105] Heechang Na, Chris M. Bouchard, G. Peter Lepage, Chris Monahan, and Junko Shigemitsu. $B \rightarrow Dlv$. *Phys. Rev. D*, 92:054510, Sep 2015. Available from: <https://link.aps.org/doi/10.1103/PhysRevD.92.054510>, doi:10.1103/PhysRevD.92.054510.
- [106] Svjetlana Fajfer, Jernej F. Kamenik, and Ivan Nišandžić. $B \rightarrow D^* \tau \bar{\nu}_\tau$. *Phys. Rev. D*, 85:094025, May 2012. Available from: <https://link.aps.org/doi/10.1103/PhysRevD.85.094025>, doi:10.1103/PhysRevD.85.094025.
- [107] Jon A. Bailey, A. Bazavov, C. Bernard, C. M. Bouchard, C. DeTar, Daping Du, A. X. El-Khadra, J. Foley, E. D. Freeland, E. Gámiz, Steven Gottlieb, U. M. Heller, J. Komijani, A. S. Kronfeld, J. Laiho, L. Levkova, P. B. Mackenzie, E. T. Neil, Si-Wei Qiu, J. Simone, R. Sugar, D. Toussaint, R. S. Van de Water, and Ran Zhou. $b \rightarrow dlv$. *Phys. Rev. D*, 92:034506, Aug 2015. Available from: <https://link.aps.org/doi/10.1103/PhysRevD.92.034506>, doi:10.1103/PhysRevD.92.034506.
- [108] Gregory Ciezarek, Manuel Franco Sevilla, Brian Hamilton, Robert Kowalewski, Thomas Kuhr, Vera LĀijth, and Yutaro Sato. A challenge to lepton universality in B -meson decays. *Nature*, 546:227–233, Jun 2016. Available from: <http://dx.doi.org/10.1038/nature22346>.
- [109] J. Lees *et al.* Measurement of an excess of $\bar{B} \rightarrow D^{(*)} \tau^- \bar{\nu}_\tau$ decays and implications for charged higgs bosons. *Phys. Rev. D*, 88:072012, Oct 2013. Available from: <https://link.aps.org/doi/10.1103/PhysRevD.88.072012>, doi:10.1103/PhysRevD.88.072012.
- [110] Huschle *et al.* Measurement of the branching ratio of $\bar{B} \rightarrow D^{(*)} \tau^- \bar{\nu}_\tau$ relative to $\bar{B} \rightarrow D^{(*)} \ell^- \bar{\nu}_\ell$ decays with hadronic tagging at belle. *Phys. Rev. D*, 92:072014, Oct 2015. Available from: <https://link.aps.org/doi/10.1103/PhysRevD.92.072014>, doi:10.1103/PhysRevD.92.072014.
- [111] Y. Sato *et al.* Measurement of the branching ratio of $\bar{B}^0 \rightarrow D^{*+} \tau^- \bar{\nu}_\tau$ relative to $\bar{B}^0 \rightarrow D^{*+} \ell^- \bar{\nu}_\ell$ decays with a semileptonic tagging method. *Phys. Rev. D*, 94:072007, Oct 2016. Available from: <https://link.aps.org/doi/10.1103/PhysRevD.94.072007>, doi:10.1103/PhysRevD.94.072007.

-
- [//link.aps.org/doi/10.1103/PhysRevD.94.072007](https://link.aps.org/doi/10.1103/PhysRevD.94.072007), doi:10.1103/PhysRevD.94.072007.
- [112] Aaij *et al.* Measurement of the Ratio of Branching Fractions $\mathcal{B}(\bar{B}^0 \rightarrow D^{*+} \tau^- \bar{\nu}_\tau) / \mathcal{B}(\bar{B}^0 \rightarrow D^{*+} \mu^- \bar{\nu}_\mu)$. *Phys. Rev. Lett.*, 115:111803, Sep 2015. Available from: <https://link.aps.org/doi/10.1103/PhysRevLett.115.111803>, doi:10.1103/PhysRevLett.115.111803.
- [113] Heavy Flavor Averaging Group. Compilation of B^+ and B^0 leptonic branching fractions. Oct 2016. Available from: http://www.slac.stanford.edu/xorg/hfag/rare/ICHEP2016/rad11/OUTPUT/HTML/rad11_table4.html.
- [114] Heavy Flavor Averaging Group. Average of \mathcal{R}_D and \mathcal{R}_{D^*} for winter 2016. March 2016. Available from: http://www.slac.stanford.edu/xorg/hfag/semi/winter16/winter16_dtaunu.html.
- [115] J. Charles, Andreas Hocker, H. Lacker, S. Laplace, F. R. Le Diberder, J. Malcles, J. Ocariz, M. Pivk, and L. Roos. CP violation and the CKM matrix: Assessing the impact of the asymmetric B factories. *Eur. Phys. J.*, C41(1):1–131, 2005. arXiv:hep-ph/0406184, doi:10.1140/epjc/s2005-02169-1.
- [116] Heechang Na, Chris M. Bouchard, G. Peter Lepage, Chris Monahan, and Junko Shigemitsu. $B \rightarrow D\ell\nu$ form factors at nonzero recoil and extraction of $|V_{cb}|$. *Phys. Rev. D, erratum Phys. Rev.D93,119906(2016)*, 92:054510, Sep 2015. Available from: <https://link.aps.org/doi/10.1103/PhysRevD.92.054510>, doi:10.1103/PhysRevD.92.054510.
- [117] Heavy Flavour Averaging Group. Compilation of B^+ and B^0 leptonic branching fractions., Oct 2016. Available from: http://www.slac.stanford.edu/xorg/hfag/rare/ICHEP2016/rad11/OUTPUT/HTML/rad11_table4.html.
- [118] Heavy Flavour Averaging Group. Average of R_D and R_{D^*} for winter 2016, Mar 2016. Available from: http://www.slac.stanford.edu/xorg/hfag/semi/winter16/witer16_dtaunu.html.

BIBLIOGRAPHY

- [119] M. K. Craddock. Cyclotrons and fixed-field alternating-gradient accelerators. *Review of Accelerator Science and Technology*, 1:65–97, 2008.
- [120] J. Doornbos. M13: a new low energy pion channel at TRIUMF, Internal Design Report, 1978.
- [121] T Numao. PIENU Technote 07: Effects of Positrons in the Beam. Technical report, TRIUMF, 2008.
- [122] C.J. Oram, J.B. Warren, G.M. Marshall, and J. Doornbos. Commissioning of a new low energy π - μ at TRIUMF. *Nuclear Instruments and Methods*, 179(1):95 – 103, 1981. Available from: <http://www.sciencedirect.com/science/article/B73DN-473D9CG-CJ/2/c3623ef6898578bdd0590abf2c0f5777>, doi: DOI:10.1016/0029-554X(81)91166-6.
- [123] C. Kost and P. Reeve. TR-DN-82-28, 1982.
- [124] J. Doornbos. Technote TN01 : Reduction of electron contamination in M13 with degrader-. Technical report, PIENU collaboration, TRIUMF, January 2006.
- [125] A. Aguilar-Arevalo et al. High Purity Pion Beam at TRIUMF. *Nucl. Instrum. Methods Phys. Res., Sect. A*, 609:102–105, October 2009.
- [126] T. Numao, J. A. Macdonald, G. M. Marshall, A. Olin, and M. C. Fujiwara. New β^+ lifetime measurement. *Phys. Rev. D*, 52:4855–4859, Nov 1995. Available from: <https://link.aps.org/doi/10.1103/PhysRevD.52.4855>, doi:10.1103/PhysRevD.52.4855.
- [127] T. Numao, Yu. I. Davydov, J-M. Poutissou, T. C. Awes, V. Cianciolo, S. Berridge, W. Bugg, Yu. Efremenko, R. Gearhart, and S. Ovchinnikov. Search for free decay of negative pions in water and light materials. *Phys. Rev. D*, 73:092004, May 2006. Available from: <https://link.aps.org/doi/10.1103/PhysRevD.73.092004>, doi:10.1103/PhysRevD.73.092004.
- [128] A. Aguilar-Arevalo et al. Detector for measuring the $\pi^+ \rightarrow e^+ \nu_e$ branching fraction. *Nucl. Instrum. Methods Phys. Res., Sect. A*, 791:38–46, August 2015.

- [129] Saint Gobain Crystals. <http://www.crystals.saintgobain.com/>.
- [130] R.S. Henderson, Yu.I. Davydov, W. Faszer, D.D. Koetke, L.V. Mi-
asoedov, R. Openshaw, M.A. Quraan, J. Schaapman, V. Selivanov,
G. Sheffer, T.D.S. Stanislaus, and V. Torokhov. Precision planar drift
chambers and cradle for the twist muon decay spectrometer. *Nu-
clear Instruments and Methods in Physics Research Section A: Accel-
erators, Spectrometers, Detectors and Associated Equipment*, 548(3):306
– 335, 2005. Available from: [http://www.sciencedirect.com/
science/article/pii/S0168900205008247](http://www.sciencedirect.com/science/article/pii/S0168900205008247), doi:[https://doi.org/
10.1016/j.nima.2005.02.043](https://doi.org/10.1016/j.nima.2005.02.043).
- [131] TWIST experiment at TRIUMF. Available from: [http://twist.
triumf.ca/~e614/experiment.html](http://twist.triumf.ca/~e614/experiment.html).
- [132] C. Ohlmann, TRIUMF, Vancouver, Canada. VT48 Rev.A, 48-
Channel Time-to-Digital Module. User’s Manual, 2007.
- [133] Y. Unno. ATLAS silicon microstrip detector system (SCT).
*Nuclear Instruments and Methods in Physics Research Sec-
tion A: Accelerators, Spectrometers, Detectors and Associated
Equipment*, 511(1-2):58 – 63, 2003. Proceedings of the 11th
International Workshop on Vertex Detectors. Available
from: [http://www.sciencedirect.com/science/article/
B6TJM-48TM37W-4/2/684bf29d73d0103d7718120ccc799e3d](http://www.sciencedirect.com/science/article/B6TJM-48TM37W-4/2/684bf29d73d0103d7718120ccc799e3d),
doi:DOI:10.1016/S0168-9002(03)01751-0.
- [134] J.-P. Martin and P.-A. Amaudruz. A 48 channel pulse shape digitizer
with dsp. *IEEE Transactions on Nuclear Science*, 53(3):715 – 719, 2006.
doi:10.1109/TNS.2006.875049.
- [135] G. Blanpied, M. Blecher, A. Caracappa, C. Djalali, G. Giordano,
K. Hicks, S. Hoblit, M. Khandaker, O. C. Kistner, A. Kuczewski,
M. Lowry, M. Lucas, G. Matone, L. Miceli, B. Preedom, D. Re-
breyend, A. M. Sandorfi, C. Schaerf, R. M. Sealock, H. Ströher, C. E.
Thorn, S. T. Thornton, J. Tonnison, C. S. Whisnant, H. Zhang, and
X. Zhao. $N \rightarrow \Delta$ Transition from Simultaneous Measurements of
 $p(\vec{\gamma}, \pi)$ and $p(\vec{\gamma}, \gamma)$. *Phys. Rev. Lett.*, 79(22):4337–4340, Dec 1997.
doi:10.1103/PhysRevLett.79.4337.

BIBLIOGRAPHY

- [136] V. Bellini, M. Capogni, A. Caracappa, L. Casano, A. D'Angelo, F. Ghio, B. Girolami, S. Hoblit, L. Hu, M. Khandaker, O. C. Kistner, L. Miceli, D. Moricciani, A. M. Sandorfi, C. Schaerf, and C. E. Thorn. Polarized Compton scattering from ${}^4\text{He}$ in the Δ region. *Phys. Rev. C*, 68(5):054607, Nov 2003. doi:10.1103/PhysRevC.68.054607.
- [137] Cayouette F., Moisan C., Zhang Nan, Thompson C. J. DETECT2000: An Improved Monte-Carlo Simulator for the Computer Aided Design of Photon Sensing Devices. *IEEE Transactions on Nuclear Science*, 49:624–628, 2002.
- [138] Chloe Malbrunot. Presentation: Bina optical simulation, April 2008. Available from: <https://pienu.triumf.ca/InternalDocuments/Meetings/TRIUMF/Regular%20Meetings/apr-15-2008/simulation-Bina.pdf/view?searchterm=Detect2000>.
- [139] Alexis A. Aguilar-Arevalo, Ahmed Hussein and Chloé Malbrunot. Technote TN08 : Testing and Setting Up BINA Using Gamma Ray Calibration Sources. Technical report, PIENU collaboration, TRIUMF, May 2008.
- [140] I-H. Chiang *et al.* CsI endcap Photon detector for a $K^+ \rightarrow \pi^+ \nu \bar{\nu}$ Experiment at BNL. *IEEE Transactions on Nuclear Science*, 42, Aug 1995.
- [141] S. Adler *et al.* Measurement of the $K^+ \rightarrow \pi^+ \nu \bar{\nu}$ branching ratio. *Phys. Rev. D*, 77:052003, Mar 2008. Available from: <https://link.aps.org/doi/10.1103/PhysRevD.77.052003>, doi:10.1103/PhysRevD.77.052003.
- [142] Luca Doria. Technote TN11 : Installation of the CsI Calorimeter for the PIENU experiment. Technical report, PIENU collaboration, TRIUMF, February 2009.
- [143] T. K. Komatsubara, T. Morimoto, K. Omata, S. Sugimoto, K. Tauchi, T. Inagaki, S. Kabe, M. Kobayashi, Y. Kuno, T. Sato, T. Shinkawa, Y. Yoshimura, I. H. Chiang, S. Kettell, K. K. Li, L. S. Littenberg, A. Yamashita, H. Suzuki, and S. Suzuki. Performance of fine-mesh photomultiplier tubes designed for an undoped-csi endcap photon detector. *Nuclear Instruments and*

- Methods in Physics Research Section A: Accelerators, Spectrometers, Detectors and Associated Equipment*, 404(2-3):315 – 326, 1998. Available from: <http://www.sciencedirect.com/science/article/B6TJM-41FDHDB-G/2/991752e1295863553a80417ac3f8f893>, doi:DOI:10.1016/S0168-9002(97)01107-8.
- [144] Masaaki Kobayashi, Takao Shinkawa, Takahiro Sato, Shojiro Sugimoto, Michail V. Korzhik, Andrey A. Fyodorov, and Vasilij A. Kachanov. YAlO³: Ce-Am light pulsers as a gain monitor for undoped CsI detectors in a magnetic field. *Nuclear Instruments and Methods in Physics Research Section A: Accelerators, Spectrometers, Detectors and Associated Equipment*, 337(2-3):355–361, 1 1994. Available from: <http://www.sciencedirect.com/science/article/B6TJM-473FRB0-2N4/2/21b282cb90c7601d8eb982dd9abcb54c>.
- [145] Alexis A. Aguilar-Arevalo. Technote TN10 : Stand-Alone Setup and Testing of the Xe-Flash Tube Monitoring System. Technical report, PIENU collaboration, TRIUMF, October 2008.
- [146] Chloé Malbrunot. *Study of $\pi^+ \rightarrow e^+ \nu_e$ decay*. PhD thesis, The University of British Columbia, 2012.
- [147] Shintaro Ito. *Measurement of the $\pi^+ \rightarrow e^+ \nu_e$ Branching Ratio*. PhD thesis, Osaka University, 2016.
- [148] Y. Igarashi, H. Fujii, T. Higuchi, M. Ikeno, E. Inoue, T. Murakami, Y. Nagasaka, M. Nakao, K. Nakayoshi, M. Saitoh, S. Shimazaki, S.Y. Suzuki, M. Tanaka, K. Tauchi, T. Uchida, and Y. Yasu. A common data acquisition system for high-intensity beam experiments. *IEEE Transactions on Nuclear Science*, 52(6):2866 –2871, 2005.
- [149] K. Yamada. *Search for Massive Neutrinos in $\pi^+ \rightarrow e^+ \nu$ Decay*. PhD thesis, Osaka University, February 2010.
- [150] J.-P. Martin and P.-A. Amaudruz. A 48 channel pulse shape digitizer with dsp. *IEEE Transactions on Nuclear Science*, 53(3):715 – 719, 2006. doi:10.1109/TNS.2006.875049.
- [151] J.-P. Martin, C. Mercier, N. Starinski, C.J. Pearson, and P.-A. Amaudruz. The TIGRESS DAQ/Trigger System. *IEEE Transactions on Nuclear Science*, 55(1):84 –90, 2008. doi:10.1109/TNS.2007.910853.

BIBLIOGRAPHY

- [152] C. Ohlmann, TRIUMF, Vancouver, Canada. VT48 Rev.A, 48-Channel Time-to-Digital Module. User's Manual, 2007.
- [153] I-H. I-H. Chiang *et al.* Ags experiment proposal 926, 1996.
- [154] Y. Arai. AMT-3 -ATLAS Muon TDC version 3 & AMT-2- User's Manual, February 2005.
- [155] S. Ritt and P. A. Amaudruz. The MIDAS Data Acquisition System. Last retrieved September 26/16. Available from: `midas.triumf.ca`.
- [156] R. Brun and F. Rademakers. ROOT - An Object Oriented Data Analysis Framework. *Nucl. Inst. & Meth. in Phys. Res. A*, 389:81–86, 1997.
- [157] Tristan S. Sullivan. *A High-Precision Measurement of the $\pi^+ \rightarrow e^+\nu_e$ Branching Ratio*. PhD thesis, The University of British Columbia, 2017.
- [158] B. P. Abbott *et al.* Observation of gravitational waves from a binary black hole merger. *Phys. Rev. Lett.*, 116:061102, Feb 2016. Available from: <https://link.aps.org/doi/10.1103/PhysRevLett.116.061102>, doi:10.1103/PhysRevLett.116.061102.
- [159] D. S. Akerib *et al.* Results from a Search for Dark Matter in the Complete LUX Exposure. *Phys. Rev. Lett.*, 118:021303, Jan 2017. Available from: <https://link.aps.org/doi/10.1103/PhysRevLett.118.021303>, doi:10.1103/PhysRevLett.118.021303.
- [160] J. B. Birks. *The Theory and Practice of Scintillation Counting*. Pergamon, 1964.
- [161] NADS. CRY simulation package for cosmics, May 2010. Available from: <http://nuclear.llnl.gov/simulation/>.
- [162] T. S. Sullivan. PIENU Technote 54: Lineshape Analysis. Technical report, TRIUMF, 2017.
- [163] K B Beard, P Degtiarenko, and T J Roberts. G4 beamline program for radiation simulations. (JLAB-ACC-08-829):3 p, 2008.

-
- [164] William H. Press, Saul A. Teukolsky, William T. Vetterling, and Brian P. Flannery. *Numerical Recipes in C (2Nd Ed.): The Art of Scientific Computing*. Cambridge University Press, New York, NY, USA, 1992.
- [165] F. James. MINUIT – Function Minimization and Error Analysis, CERN Program Library Entry D 506.
- [166] M. Aoki, M. Blecher, D. A. Bryman, S. Chen, M. Ding, L. Doria, P. Gumplinger, C. Hurst, A. Hussein, Y. Igarashi, N. Ito, S. H. Kettell, L. Kurchaninov, L. Littenberg, C. Malbrunot, T. Numao, R. Poutissou, A. Sher, T. Sullivan, D. Vavilov, K. Yamada, and M. Yoshida. Search for massive neutrinos in the decay $\pi \rightarrow e\nu$. *Phys. Rev. D*, 84:052002, Sep 2011. Available from: <https://link.aps.org/doi/10.1103/PhysRevD.84.052002>, doi:10.1103/PhysRevD.84.052002.
- [167] Robert E. Shrock. General theory of weak processes involving neutrinos. ii. pure leptonic decays. *Phys. Rev. D*, 24:1275–1309, Sep 1981. doi:10.1103/PhysRevD.24.1275.
- [168] D.A. Bryman and R. Shrock. Improved constraints on sterile neutrinos in the mev to gev mass range. *Physical Review D*, 100(5), Sep 2019. Available from: <http://dx.doi.org/10.1103/PhysRevD.100.053006>, doi:10.1103/physrevd.100.053006.
- [169] Andre de Gouvea and Andrew Kobach. Global constraints on a heavy neutrino. *Physical Review D*, 93(3), Feb 2016. Available from: <http://dx.doi.org/10.1103/PhysRevD.93.033005>, doi:10.1103/physrevd.93.033005.
- [170] A. Aguilar-Arevalo, M. Aoki, M. Blecher, D. I. Britton, D. vom Bruch, D. A. Bryman, S. Chen, J. Comfort, S. Cuen-Rochin, L. Doria, P. Gumplinger, A. Hussein, Y. Igarashi, S. Ito, S. Kettell, L. Kurchaninov, L. S. Littenberg, C. Malbrunot, R. E. Mischke, T. Numao, D. Protopopescu, A. Sher, T. Sullivan, and D. Vavilov. Improved search for heavy neutrinos in the decay $\pi \rightarrow e\nu$. *Phys. Rev. D*, 97:072012, Apr 2018. Available from: <https://link.aps.org/doi/10.1103/PhysRevD.97.072012>, doi:10.1103/PhysRevD.97.072012.

BIBLIOGRAPHY

- [171] Cristina Lazzeroni et al. Search for heavy neutrinos in $K^+ \rightarrow \mu^+ \nu_\mu$ decays. *Phys. Lett.*, B772:712–718, 2017. arXiv:1705.07510, doi:10.1016/j.physletb.2017.07.055.
- [172] Eduardo Cortina Gil et al. Search for heavy neutral lepton production in K^+ decays. *Phys. Lett.*, B778:137–145, 2018. arXiv:1712.00297, doi:10.1016/j.physletb.2018.01.031.
- [173] J. Deutsch, M. Lebrun, and R. Prieels. Searches for admixture of massive neutrinos into the electron flavor. *Nucl. Phys.*, A518:149–155, 1990. doi:10.1016/0375-9474(90)90541-S.
- [174] D. A. Bryman and T. Numao. Search for massive neutrinos in $\pi^+ \rightarrow \mu^+ \nu$ decay. *Phys. Rev. D*, 53:558–559, Jan 1996. Available from: <https://link.aps.org/doi/10.1103/PhysRevD.53.558>, doi:10.1103/PhysRevD.53.558.
- [175] R. Abela, M. Daum, G.H. Eaton, R. Frosch, B. Jost, P.-R. Kettle, and E. Steiner. Search for an admixture of heavy neutrino states in pion decay. *Physics Letters B*, 105(4):263 – 266, 1981. Available from: <http://www.sciencedirect.com/science/article/pii/0370269381908844>, doi:[https://doi.org/10.1016/0370-2693\(81\)90884-4](https://doi.org/10.1016/0370-2693(81)90884-4).
- [176] M. Daum, B. Jost, R. M. Marshall, R. C. Minehart, W. A. Stephens, and K. O. H. Ziock. Search for Admixtures of Massive Neutrinos in the Decay $\pi^+ \rightarrow \mu^+ \text{Neutrino}$. *Phys. Rev.*, D36:2624, 1987. doi:10.1103/PhysRevD.36.2624.
- [177] A. Aguilar-Arevalo, M. Aoki, M. Blecher, D.I. Britton, D. vom Bruch, D.A. Bryman, S. Chen, J. Comfort, L. Doria, S. Cuen-Rochin, P. Gumplinger, A. Hussein, Y. Igarashi, S. Ito, S.H. Kettell, L. Kurchaninov, L.S. Littenberg, C. Malbrunot, R.E. Mischke, T. Numao, D. Protopopescu, A. Sher, T. Sullivan, and D. Vavilov. Search for heavy neutrinos in $\pi^+ \rightarrow \mu^+ \nu_\mu$ decay. *Physics Letters B*, 798:134980, 2019. Available from: <http://www.sciencedirect.com/science/article/pii/S0370269319307026>, doi:<https://doi.org/10.1016/j.physletb.2019.134980>.

- [178] Gary J. Feldman and Robert D. Cousins. A Unified approach to the classical statistical analysis of small signals. *Phys. Rev.*, D57:3873–3889, 1998. arXiv:physics/9711021, doi:10.1103/PhysRevD.57.3873.
- [179] M. Aoki, M. Blecher, D.A. Bryman, S. Chen, M. Ding, L. Doria, P. Gumplinger, C. Hurst, A. Hussein, Y. Igarashi, N. Ito, S.H. Kettell, L. Kurchaninov, L. Littenberg, C. Malbrunot, T. Numao, R. Poutissou, A. Sher, T. Sullivan, K. Yamada, M. Yoshida, D. Vavilov. Search for Massive Neutrinos in the Decay $\pi^+ \rightarrow e^+ \nu$. 2011. arXiv:1106.4055.
- [180] J.H. Oort. The force exerted by the stellar system in the direction perpendicular to the galactic plane and some related problems. *Bulletin of the Astronomical Institutes of the Netherlands*, 6:249, 1932.
- [181] V.C. Rubin *et al.* Extended rotation curves of high-luminosity spiral galaxies. *Astrophys. Journal*, 225:107, 1978.
- [182] F. Zwicky. Die Rotverschiebung von extragalaktischen Nebeln. *Helv. Physica Acta.*, 6:110, 1933.
- [183] Alexandre Refregier. Weak gravitational lensing by large scale structure. *Ann. Rev. Astron. Astrophys.*, 41:645–668, 2003. arXiv:astro-ph/0307212, doi:10.1146/annurev.astro.41.111302.102207.
- [184] Adam G. Riess *et al.* Observational evidence from supernovae for an accelerating universe and a cosmological constant. *Astron. J.*, 116:1009–1038, 1998. arXiv:astro-ph/9805201, doi:10.1086/300499.
- [185] S. Perlmutter *et al.* Measurements of Omega and Lambda from 42 high redshift supernovae. *Astrophys. J.*, 517:565–586, 1999. arXiv:astro-ph/9812133, doi:10.1086/307221.
- [186] M. Viel, J. S. Bolton, and M. G. Haehnelt. Cosmological and astrophysical constraints from the Lyman α forest flux probability distribution function. *Monthly Notices of the Royal Astronomical Society*.

BIBLIOGRAPHY

- [187] Kim Griest and Marc Kamionkowski. Unitarity limits on the mass and radius of dark-matter particles. *Phys. Rev. Lett.*, 64:615–618, Feb 1990. Available from: <https://link.aps.org/doi/10.1103/PhysRevLett.64.615>, doi:10.1103/PhysRevLett.64.615.
- [188] R. D. Peccei and Helen R. Quinn. CP. *Phys. Rev. Lett.*, 38:1440–1443, Jun 1977. Available from: <https://link.aps.org/doi/10.1103/PhysRevLett.38.1440>, doi:10.1103/PhysRevLett.38.1440.
- [189] R. D. Peccei. The Strong CP problem and axions. *Lect. Notes Phys.*, 741:3–17, 2008. [3(2006)]. arXiv:hep-ph/0607268, doi:10.1007/978-3-540-73518-2_1.
- [190] D. S. Akerib et al. Results from a search for dark matter in the complete LUX exposure. *Phys. Rev. Lett.*, 118(2):021303, 2017. arXiv:1608.07648, doi:10.1103/PhysRevLett.118.021303.
- [191] Andi Tan et al. Dark Matter Results from First 98.7 Days of Data from the PandaX-II Experiment. *Phys. Rev. Lett.*, 117(12):121303, 2016. arXiv:1607.07400, doi:10.1103/PhysRevLett.117.121303.
- [192] E. Aprile et al. First Dark Matter Search Results from the XENON1T Experiment. *Phys. Rev. Lett.*, 119(18):181301, 2017. arXiv:1705.06655, doi:10.1103/PhysRevLett.119.181301.
- [193] R. Agnese et al. New Results from the Search for Low-Mass Weakly Interacting Massive Particles with the CDMS Low Ionization Threshold Experiment. *Phys. Rev. Lett.*, 116(7):071301, 2016. arXiv:1509.02448, doi:10.1103/PhysRevLett.116.071301.
- [194] Leszek Roszkowski, Enrico Maria Sessolo, and Sebastian Trojanowski. WIMP dark matter candidates and searches - current issues and future prospects. 2017. arXiv:1707.06277.
- [195] D. S. Akerib et al. Limits on Spin-Dependent WIMP-Nucleon Cross Section Obtained from the Complete LUX Exposure. *Phys. Rev. Lett.*, 118:251302, Jun 2017. Available from: <https://link.aps.org/doi/10.1103/PhysRevLett.118.251302>, doi:10.1103/PhysRevLett.118.251302.

- [196] S. Profumo. *An Introduction of Particle Dark Matter*. World Scientific, 2017.
- [197] Jonathan L. Feng and Jason Kumar. The WIMPless Miracle: Dark-Matter Particles without Weak-Scale Masses or Weak Interactions. *Phys. Rev. Lett.*, 101:231301, 2008. arXiv:0803.4196, doi:10.1103/PhysRevLett.101.231301.
- [198] Clifford Cheung, Lawrence J. Hall, David Pinner, and Joshua T. Ruderman. Prospects and Blind Spots for Neutralino Dark Matter. *JHEP*, 05:100, 2013. arXiv:1211.4873, doi:10.1007/JHEP05(2013)100.
- [199] Hsin-Chia Cheng, Jonathan L. Feng, and Konstantin T. Matchev. Kaluza-klein dark matter. *Phys. Rev. Lett.*, 89:211301, Oct 2002. Available from: <https://link.aps.org/doi/10.1103/PhysRevLett.89.211301>, doi:10.1103/PhysRevLett.89.211301.
- [200] Geraldine Servant and Timothy M. P. Tait. Is the lightest Kaluza-Klein particle a viable dark matter candidate? *Nucl. Phys.*, B650:391–419, 2003. arXiv:hep-ph/0206071, doi:10.1016/S0550-3213(02)01012-X.
- [201] Frank Daniel Steffen. Gravitino dark matter and cosmological constraints. *JCAP*, 0609:001, 2006. arXiv:hep-ph/0605306, doi:10.1088/1475-7516/2006/09/001.
- [202] Mordehai Milgrom. MOND laws of galactic dynamics. *Mon. Not. Roy. Astron. Soc.*, 437(3):2531–2541, 2014. arXiv:1212.2568, doi:10.1093/mnras/stt2066.
- [203] Jacob D. Bekenstein. Relativistic gravitation theory for the MOND paradigm. *Phys. Rev.*, D70:083509, 2004. [Erratum: *Phys. Rev.*D71,069901(2005)]. arXiv:astro-ph/0403694, doi:10.1103/PhysRevD.70.083509, 10.1103/PhysRevD.71.069901.
- [204] Erik P. Verlinde. On the Origin of Gravity and the Laws of Newton. *JHEP*, 04:029, 2011. arXiv:1001.0785, doi:10.1007/JHEP04(2011)029.

BIBLIOGRAPHY

- [205] Lasha Berezhiani, Benoit Famaey, and Justin Khoury. Phenomenological consequences of superfluid dark matter with baryon-phonon coupling. 2017. arXiv:1711.05748.
- [206] Benjamin W. Lee and Steven Weinberg. Cosmological lower bound on heavy-neutrino masses. *Phys. Rev. Lett.*, 39:165–168, Jul 1977.
- [207] J.L. Feng. Dark Matter Candidates from Particle Physics and Methods of Detection. *Ann. Rev. Astron. Astrophys.*, 48:495, 2010.
- [208] Scott Dodelson and Lawrence M. Widrow. Sterile-neutrinos as dark matter. *Phys. Rev. Lett.*, 72:17–20, 1994. arXiv:hep-ph/9303287, doi:10.1103/PhysRevLett.72.17.
- [209] Douglas P. Finkbeiner, Silvia Galli, Tongyan Lin, and Tracy R. Slatyer. Searching for dark matter in the cmb: A compact parametrization of energy injection from new physics. *Phys. Rev. D*, 85:043522, Feb 2012. Available from: <https://link.aps.org/doi/10.1103/PhysRevD.85.043522>, doi:10.1103/PhysRevD.85.043522.
- [210] Kalliopi Petraki and Raymond R. Volkas. Review of asymmetric dark matter. *Int. J. Mod. Phys.*, A28:1330028, 2013. arXiv:1305.4939, doi:10.1142/S0217751X13300287.
- [211] David Tucker-Smith and Neal Weiner. Inelastic dark matter. *Phys. Rev.*, D64:043502, 2001. arXiv:hep-ph/0101138, doi:10.1103/PhysRevD.64.043502.
- [212] Stacy S. McGaugh. *Astronomical Journal*, 143:40, Jan 2012.
- [213] Stacy McGaugh Benoit Famaey. *Living Reviews in Relativity*, 15:10, 2012. Available from: arXiv:1112.3960v2, doi:10.12942/lrr-2012-10.
- [214] Jacob D. Bekenstein and Robert H. Sanders. A primer to relativistic MOND theory. 2005. [EAS Publ. Ser.20,225(2006)]. arXiv:astro-ph/0509519, doi:10.1051/eas:2006075.
- [215] Daniel J. H. Chung, Edward W. Kolb, and Antonio Riotto. Super-heavy dark matter. *Phys. Rev.*, D59:023501, 1999. arXiv:hep-ph/9802238, doi:10.1103/PhysRevD.59.023501.

-
- [216] Teresa Marrodan Undagoitia and Ludwig Rauch. Dark matter direct-detection experiments. *J. Phys.*, G43(1):013001, 2016. arXiv:1509.08767, doi:10.1088/0954-3899/43/1/013001.
- [217] A. Liam Fitzpatrick, Wick Haxton, Emanuel Katz, Nicholas Lubbers, and Yiming Xu. The Effective Field Theory of Dark Matter Direct Detection. *JCAP*, 1302:004, 2013. arXiv:1203.3542, doi:10.1088/1475-7516/2013/02/004.
- [218] E. Aprile et al. Dark Matter Search Results from a One Ton-Year Exposure of XENON1T. *Phys. Rev. Lett.*, 121:111302, Sep 2018. Available from: <https://link.aps.org/doi/10.1103/PhysRevLett.121.111302>, doi:10.1103/PhysRevLett.121.111302.
- [219] R. Agnese et al. Projected sensitivity of the SuperCDMS SNO-LAB experiment. *Phys. Rev. D*, 95:082002, Apr 2017. Available from: <https://link.aps.org/doi/10.1103/PhysRevD.95.082002>, doi:10.1103/PhysRevD.95.082002.
- [220] R. Agnese et al. Low-Mass Dark Matter Search with CDMSlite. *Phys. Rev. D*, 97:022002, 2018.
- [221] Rouven Essig, Tomer Volansky, and Tien-Tien Yu. New constraints and prospects for sub-gev dark matter scattering off electrons in xenon. *Phys. Rev. D*, 96:043017, Aug 2017. Available from: <https://link.aps.org/doi/10.1103/PhysRevD.96.043017>, doi:10.1103/PhysRevD.96.043017.
- [222] Felix Kahlhoefer. Review of LHC Dark Matter Searches. *Int. J. Mod. Phys.*, A32(13):1730006, 2017. arXiv:1702.02430, doi:10.1142/S0217751X1730006X.
- [223] S. Fukuda et al. The Super-Kamiokande detector. *Nuclear Instruments and Methods in Physics Research Section A: Accelerators, Spectrometers, Detectors and Associated Equipment*, 501(2):418 – 462, 2003. Available from: <http://www.sciencedirect.com/science/article/pii/S016890020300425X>, doi:[https://doi.org/10.1016/S0168-9002\(03\)00425-X](https://doi.org/10.1016/S0168-9002(03)00425-X).
- [224] R. Abbasi et al. Calibration and Characterization of the IceCube Photomultiplier Tube. *Nucl.Instrum.Meth. A*, 618:139–152, 2010.

BIBLIOGRAPHY

- [225] R. Abbasi et al. The IceCube Data Acquisition System: Signal Capture, Digitization, and Timestamping. *Nucl. Instrum. Meth.*, A601:294–316, 2009. arXiv:0810.4930, doi:10.1016/j.nima.2009.01.001.
- [226] R. Acciarri et al. Long-Baseline Neutrino Facility (LBNF) and Deep Underground Neutrino Experiment (DUNE). 2015. arXiv:1512.06148.
- [227] K. Abe et al. Physics potential of a long-baseline neutrino oscillation experiment using a J-PARC neutrino beam and Hyper-Kamiokande. *PTEP*, 2015:053C02, 2015. arXiv:1502.05199, doi:10.1093/ptep/ptv061.
- [228] C. Kachulis et al. Search for Boosted Dark Matter Interacting With Electrons in Super-Kamiokande. *Phys. Rev. Lett.*, 120(22):221301, 2018. arXiv:1711.05278, doi:10.1103/PhysRevLett.120.221301.
- [229] K. Choi et al. Search for neutrinos from annihilation of captured low-mass dark matter particles in the Sun by Super-Kamiokande. *Phys. Rev. Lett.*, 114(14):141301, 2015. arXiv:1503.04858, doi:10.1103/PhysRevLett.114.141301.
- [230] T. Tanaka et al. An Indirect Search for WIMPs in the Sun using 3109.6 days of upward-going muons in Super-Kamiokande. *Astrophys. J.*, 742:78, 2011. arXiv:1108.3384, doi:10.1088/0004-637X/742/2/78.
- [231] M. G. Aartsen et al. Search for Neutrinos from Dark Matter Self-Annihilations in the center of the Milky Way with 3 years of IceCube/DeepCore. *Eur. Phys. J.*, C77(9):627, 2017. arXiv:1705.08103, doi:10.1140/epjc/s10052-017-5213-y.
- [232] G. Angloher et al. Results on light dark matter particles with a low-threshold CRESST-II detector. *Eur. Phys. J.*, C76(1):25, 2016. arXiv:1509.01515, doi:10.1140/epjc/s10052-016-3877-3.
- [233] R. Agnese, , et al. Improved WIMP-search reach of the CDMS II germanium data. *Phys. Rev. D*, 92:072003, Oct 2015. Available from: <https://link.aps.org/doi/10.1103/PhysRevD.92.072003>, doi:10.1103/PhysRevD.92.072003.

- [234] N.J.T. Smith. The development of deep underground science facilities. *Nuclear Physics B - Proceedings Supplements*, 229-232:333 – 341, 2012. Neutrino 2010. Available from: <http://www.sciencedirect.com/science/article/pii/S0920563212002691>, doi:<https://doi.org/10.1016/j.nuclphysbps.2012.09.052>.
- [235] Chris Jillings. The snolab science program. *J. Phys.: Conf. Ser.*, 718:062028, 2016.
- [236] R. Agnese, , et al. Projected sensitivity of the SuperCDMS SNO-LAB experiment. *Phys. Rev. D*, 95:082002, Apr 2017. Available from: <https://link.aps.org/doi/10.1103/PhysRevD.95.082002>, doi:10.1103/PhysRevD.95.082002.
- [237] A. Aguilar-Arevalo et al. Search for low-mass WIMPs in a 0.6 kg day exposure of the DAMIC experiment at SNOLAB. *Phys. Rev.*, D94(8):082006, 2016. arXiv:1607.07410, doi:10.1103/PhysRevD.94.082006.
- [238] Javier Tiffenberg, Miguel Sofo-Haro, Alex Drlica-Wagner, Rouven Essig, Yann Guardincerri, Steve Holland, Tomer Volansky, and Tien-Tien Yu. Single-electron and single-photon sensitivity with a silicon Skipper CCD. *Phys. Rev. Lett.*, 119(13):131802, 2017. arXiv:1706.00028, doi:10.1103/PhysRevLett.119.131802.
- [239] S. Abrahamyan *et al.* Search for a new gauge boson in electron-nucleus fixed-target scattering by the apex experiment. *Phys. Rev. Lett.*, 107:191804, Nov 2011. Available from: <https://link.aps.org/doi/10.1103/PhysRevLett.107.191804>, doi:10.1103/PhysRevLett.107.191804.
- [240] Andrea Celentano and the HPS Collaboration. The Heavy Photon Search experiment at Jefferson Laboratory. *Journal of Physics: Conference Series*, 556(1):012064, 2014. Available from: <http://stacks.iop.org/1742-6596/556/i=1/a=012064>.
- [241] J. Balewski et al. The DarkLight Experiment: A Precision Search for New Physics at Low Energies. 2014. Available from: <https://inspirehep.net/record/1334361/files/arXiv:1412.4717.pdf>, arXiv:1412.4717.

BIBLIOGRAPHY

- [242] E. M. Riordan, M. W. Krasny, K. Lang, P. de Barbaro, A. Bodek, S. Dasu, N. Varelas, X. Wang, R. Arnold, D. Benton, P. Bosted, L. Clogher, A. Lung, S. Rock, Z. Szalata, B. W. Filippone, R. C. Walker, J. D. Bjorken, M. Crisler, A. Para, J. Lambert, J. Button-Shafer, B. Debebe, M. Frodyma, R. S. Hicks, G. A. Peterson, and R. Gearhart. Search for short-lived axions in an electron-beam-dump experiment. *Phys. Rev. Lett.*, 59:755–758, Aug 1987. Available from: <https://link.aps.org/doi/10.1103/PhysRevLett.59.755>, doi:10.1103/PhysRevLett.59.755.
- [243] J. D. Bjorken, S. Ecklund, W. R. Nelson, A. Abashian, C. Church, B. Lu, L. W. Mo, T. A. Nunamaker, and P. Rassmann. Search for neutral metastable penetrating particles produced in the SLAC beam dump. *Phys. Rev. D*, 38:3375–3386, Dec 1988. Available from: <https://link.aps.org/doi/10.1103/PhysRevD.38.3375>, doi:10.1103/PhysRevD.38.3375.
- [244] A. Bross, M. Crisler, S. Pordes, J. Volk, S. Errede, and J. Wrbanek. Search for short-lived particles produced in an electron beam dump. *Phys. Rev. Lett.*, 67:2942–2945, Nov 1991. Available from: <https://link.aps.org/doi/10.1103/PhysRevLett.67.2942>, doi:10.1103/PhysRevLett.67.2942.
- [245] Patrick deNiverville, Maxim Pospelov, and Adam Ritz. Observing a light dark matter beam with neutrino experiments. *Phys. Rev.*, D84:075020, 2011. arXiv:1107.4580, doi:10.1103/PhysRevD.84.075020.
- [246] Brian Batell, Rouven Essig, and Ze’ev Surujon. Strong Constraints on Sub-GeV Dark Sectors from SLAC Beam Dump E137. *Phys. Rev. Lett.*, 113(17):171802, 2014. arXiv:1406.2698, doi:10.1103/PhysRevLett.113.171802.
- [247] A. A. Aguilar-Arevalo et al. Dark Matter Search in a Proton Beam Dump with MiniBooNE. *Phys. Rev. Lett.*, 118:221803, May 2017. Available from: <https://link.aps.org/doi/10.1103/PhysRevLett.118.221803>, doi:10.1103/PhysRevLett.118.221803.
- [248] L. Marsicano, M. Battaglieri, A. Celentano, R. De Vita, and Yi-Ming Zhong. Probing Leptophilic Dark Sectors at Electron Beam-Dump

-
- Facilities. *Phys. Rev.*, D98(11):115022, 2018. arXiv:1812.03829, doi:10.1103/PhysRevD.98.115022.
- [249] James D. Bjorken, Rouven Essig, Philip Schuster, and Natalia Toro. New Fixed-Target Experiments to Search for Dark Gauge Forces. *Phys. Rev.*, D80:075018, 2009. arXiv:0906.0580, doi:10.1103/PhysRevD.80.075018.
- [250] C. F. v. Weizsäcker. Ausstrahlung bei stößen sehr schneller elektronen. *Zeitschrift für Physik*, 88(9):612–625, Sep 1934. Available from: <https://doi.org/10.1007/BF01333110>, doi:10.1007/BF01333110.
- [251] E. J. Williams. Nature of the high energy particles of penetrating radiation and status of ionization and radiation formulae. *Phys. Rev.*, 45:729–730, May 1934. Available from: <https://link.aps.org/doi/10.1103/PhysRev.45.729>, doi:10.1103/PhysRev.45.729.
- [252] Kwang Je Kim and Yung-Su Tsai. Improved Weizsäcker-Williams Method and Its Application to Lepton and W -Boson Pair Production. *Phys. Rev. D*, 8:3109–3125, Nov 1973. Available from: <https://link.aps.org/doi/10.1103/PhysRevD.8.3109>, doi:10.1103/PhysRevD.8.3109.
- [253] Yung-Su Tsai. Pair production and bremsstrahlung of charged leptons. *Rev. Mod. Phys.*, 46:815–851, Oct 1974. Available from: <https://link.aps.org/doi/10.1103/RevModPhys.46.815>, doi:10.1103/RevModPhys.46.815.
- [254] Yung Su Tsai. Axion bremsstrahlung by an electron beam. *Phys. Rev. D*, 34:1326–1331, Sep 1986. Available from: <https://link.aps.org/doi/10.1103/PhysRevD.34.1326>, doi:10.1103/PhysRevD.34.1326.
- [255] Yu-Sheng Liu and Gerald A. Miller. Validity of the Weizsäcker-Williams approximation and the analysis of beam dump experiments: Production of an axion, a dark photon, or a new axial-vector boson. *Phys. Rev.*, D96(1):016004, 2017. arXiv:1705.01633, doi:10.1103/PhysRevD.96.016004.
- [256] Luca Doria, Patrick Achenbach, Mirco Christmann, Achim Denig, Pepe Guelker, and Harald Merkel. Search for light dark matter

BIBLIOGRAPHY

- with the MESA accelerator. *Proceedings of the 13th Conference on the Intersections of Particle and Nuclear Physics, Palm Springs (CA, USA)*, 2018. arXiv:1809.07168.
- [257] Dominik Becker et al. The P2 Experiment - A future high-precision measurement of the electroweak mixing angle at low momentum transfer. 2018. arXiv:1802.04759.
- [258] T. Stengler et al. Modified ELBE type cryomodules for the Mainz energy-recovery superconducting accelerator MESA. *Proceedings of SRF2015, Whistler, BC, Canada*, 2015.
- [259] Sebastian Baunack. Parity violating electron scattering at MAMI. *J. Phys. Conf. Ser.*, 349:012010, 2012. doi:10.1088/1742-6596/349/1/012010.
- [260] J. Sulkimo et al. GEANT4 a simulation toolkit. *Nucl. Inst. & Meth. in Phys. Res. A*, 506:250–303, 2003.
- [261] J. Alwall et al. MadGraph/MadEvent v4: The New Web Generation. *JHEP*, 0709:028, 2007.
- [262] Eder Izaguirre, Gordan Krnjaic, Philip Schuster, and Natalia Toro. New Electron Beam-Dump Experiments to Search for MeV to few-GeV Dark Matter. *Phys. Rev.*, D88:114015, 2013. arXiv:1307.6554, doi:10.1103/PhysRevD.88.114015.
- [263] J Brose, G Dahlinger, and K.R Schubert. Properties of CsI(Tl) crystals and their optimization for calorimetry of high energy photons¹¹Work supported by BMBF under contract No. 06 DD 558 I. *Nuclear Instruments and Methods in Physics Research Section A: Accelerators, Spectrometers, Detectors and Associated Equipment*, 417(2):311 – 324, 1998. Available from: <http://www.sciencedirect.com/science/article/pii/S0168900298007657>, doi:[https://doi.org/10.1016/S0168-9002\(98\)00765-7](https://doi.org/10.1016/S0168-9002(98)00765-7).
- [264] B. Aubert et al. The BABAR detector. *Nuclear Instruments and Methods in Physics Research Section A: Accelerators, Spectrometers, Detectors and Associated Equipment*, 479(1):1 – 116, 2002. Detectors for Asymmetric B-factories. Available from: <http://www.sciencedirect.com>.

com/science/article/pii/S0168900201020125, doi:[https://doi.org/10.1016/S0168-9002\(01\)02012-5](https://doi.org/10.1016/S0168-9002(01)02012-5).

- [265] D.F. Anderson, M. Kobayashi, C.L. Woody, and Y. Yoshimura. Lead fluoride: An ultra-compact Cherenkov radiator for em calorimetry. *Nuclear Instruments and Methods in Physics Research Section A: Accelerators, Spectrometers, Detectors and Associated Equipment*, 290(2):385 – 389, 1990. Available from: <http://www.sciencedirect.com/science/article/pii/016890029090553I>, doi:[https://doi.org/10.1016/0168-9002\(90\)90553-I](https://doi.org/10.1016/0168-9002(90)90553-I).
- [266] S. Baunack, D. Balaguer Rios, L. Capozza, J. Diefenbach, R. Frascaria, B. Gläser, D.v. Harrach, Y. Imai, R. Kothe, R. Kunne, J.H. Lee, F.E. Maas, M.C. Mora Espi, M. Morlet, S. Ong, E. Schilling, J. van de Wiele, and C. Weinrich. Real-time calibration of the A4 electromagnetic lead fluoride (PbF₂) calorimeter. *Nuclear Instruments and Methods in Physics Research Section A: Accelerators, Spectrometers, Detectors and Associated Equipment*, 640(1):58 – 68, 2011. Available from: <http://www.sciencedirect.com/science/article/pii/S0168900211005006>, doi:<https://doi.org/10.1016/j.nima.2011.02.099>.
- [267] Richard Sumner. The L3 BGO electromagnetic calorimeter. *Nuclear Instruments and Methods in Physics Research Section A: Accelerators, Spectrometers, Detectors and Associated Equipment*, 265(1):252 – 257, 1988. Available from: <http://www.sciencedirect.com/science/article/pii/0168900288910789>, doi:[https://doi.org/10.1016/0168-9002\(88\)91078-9](https://doi.org/10.1016/0168-9002(88)91078-9).
- [268] Fernando Ferroni. The L3 BGO electromagnetic calorimeter at LEP. *Nuclear Physics B - Proceedings Supplements*, 23(1):100 – 106, 1991. Available from: <http://www.sciencedirect.com/science/article/pii/092056329190036E>, doi:[https://doi.org/10.1016/0920-5632\(91\)90036-E](https://doi.org/10.1016/0920-5632(91)90036-E).
- [269] U. Buchner, J.P. Donker, B. Spaan, J. Spengler, G. Schweda, D. Wegener, and W. Schmidt-Parzefall. Performance of a scintillating glass calorimeter for electromagnetic showers. *Nuclear Instruments and Methods in Physics Research Section A: Accelerators,*

BIBLIOGRAPHY

- Spectrometers, Detectors and Associated Equipment*, 272(3):695 – 706, 1988. Available from: <http://www.sciencedirect.com/science/article/pii/0168900288907504>, doi:[https://doi.org/10.1016/0168-9002\(88\)90750-4](https://doi.org/10.1016/0168-9002(88)90750-4).
- [270] B. Adeva et al. The construction of the l3 experiment. *Nuclear Instruments and Methods in Physics Research Section A: Accelerators, Spectrometers, Detectors and Associated Equipment*, 289(1):35 – 102, 1990. Available from: <http://www.sciencedirect.com/science/article/pii/016890029090250A>, doi:[https://doi.org/10.1016/0168-9002\(90\)90250-A](https://doi.org/10.1016/0168-9002(90)90250-A).
- [271] Hooman Davoudiasl and William J. Marciano. Running of the U(1) coupling in the dark sector. *Phys. Rev. D*, 92:035008, Aug 2015. Available from: <https://link.aps.org/doi/10.1103/PhysRevD.92.035008>, doi:10.1103/PhysRevD.92.035008.
- [272] D. Banerjee et al. Search for Invisible Decays of Sub-GeV Dark Photons in Missing-Energy Events at the CERN SPS. *Phys. Rev. Lett.*, 118:011802, Jan 2017. Available from: <https://link.aps.org/doi/10.1103/PhysRevLett.118.011802>, doi:10.1103/PhysRevLett.118.011802.
- [273] D. Banerjee et al. Search for vector mediator of dark matter production in invisible decay mode. *Phys. Rev. D*, 97:072002, Apr 2018. Available from: <https://link.aps.org/doi/10.1103/PhysRevD.97.072002>, doi:10.1103/PhysRevD.97.072002.
- [274] J. P. Lees et al. Search for invisible decays of a dark photon produced in e^+e^- collisions at babar. *Phys. Rev. Lett.*, 119:131804, Sep 2017. Available from: <https://link.aps.org/doi/10.1103/PhysRevLett.119.131804>, doi:10.1103/PhysRevLett.119.131804.
- [275] A. A. Aguilar-Arevalo et al. Dark Matter Search in a Proton Beam Dump with MiniBooNE. *Phys. Rev. Lett.*, 118:221803, May 2017. Available from: <https://link.aps.org/doi/10.1103/PhysRevLett.118.221803>, doi:10.1103/PhysRevLett.118.221803.
- [276] G. Angloher et al. Dark-photon search using data from CRESST-II Phase 2. *The European Physical Journal C*, 77(5):299, May 2017. Avail-

- able from: <https://doi.org/10.1140/epjc/s10052-017-4878-6>,
doi:10.1140/epjc/s10052-017-4878-6.
- [277] Patrick deNiverville, Chien-Yi Chen, Maxim Pospelov, and Adam Ritz. Light dark matter in neutrino beams: production modelling and scattering signatures at MiniBooNE, T2K and SHiP. *Phys. Rev.*, D95(3):035006, 2017. arXiv:1609.01770, doi:10.1103/PhysRevD.95.035006.
- [278] Sarah Andreas, Carsten Niebuhr, and Andreas Ringwald. New limits on hidden photons from past electron beam dumps. *Phys. Rev. D*, 86:095019, Nov 2012. Available from: <https://link.aps.org/doi/10.1103/PhysRevD.86.095019>, doi:10.1103/PhysRevD.86.095019.
- [279] A. Bross, M. Crisler, S. Pordes, J. Volk, S. Errede, and J. Wrbanek. Search for short-lived particles produced in an electron beam dump. *Phys. Rev. Lett.*, 67:2942–2945, Nov 1991. Available from: <https://link.aps.org/doi/10.1103/PhysRevLett.67.2942>, doi:10.1103/PhysRevLett.67.2942.
- [280] S. Abrahamyan et al. Search for a new gauge boson in electron-nucleus fixed-target scattering by the apex experiment. *Phys. Rev. Lett.*, 107:191804, Nov 2011. Available from: <https://link.aps.org/doi/10.1103/PhysRevLett.107.191804>, doi:10.1103/PhysRevLett.107.191804.
- [281] P. Adlarson et al. Search for a dark photon in the $\pi^0 \rightarrow e^+e^-\gamma$ decay. *Physics Letters B*, 726(1):187 – 193, 2013. Available from: <http://www.sciencedirect.com/science/article/pii/S0370269313006941>, doi:<https://doi.org/10.1016/j.physletb.2013.08.055>.
- [282] D. Babusci et al. Limit on the production of a light vector gauge boson in ϕ meson decays with the KLOE detector. *Physics Letters B*, 720(1):111 – 115, 2013. Available from: <http://www.sciencedirect.com/science/article/pii/S037026931300124X>, doi:<https://doi.org/10.1016/j.physletb.2013.01.067>.
- [283] G. Agakishiev et al. Searching a dark photon with HADES. *Physics Letters B*, 731:265 – 271, 2014. Available from: <http://www>.

BIBLIOGRAPHY

- sciencedirect.com/science/article/pii/S0370269314001336,
doi:<https://doi.org/10.1016/j.physletb.2014.02.035>.
- [284] B. Aubert et al. Search for dimuon decays of a light scalar boson in radiative transitions $Y \rightarrow \gamma A^0$. *Phys. Rev. Lett.*, 103:081803, Aug 2009. Available from: <https://link.aps.org/doi/10.1103/PhysRevLett.103.081803>, doi:10.1103/PhysRevLett.103.081803.
- [285] Bertrand Echenard. Search for light new physics at b factories. *Advances in High Energy Physics*, 2012:13 pages, 2012. doi:<https://doi.org/10.1155/2012/514014>.
- [286] H. Merkel et al. Search at the mainz microtron for light massive gauge bosons relevant for the muon $g - 2$ anomaly. *Phys. Rev. Lett.*, 112:221802, Jun 2014. Available from: <https://link.aps.org/doi/10.1103/PhysRevLett.112.221802>, doi:10.1103/PhysRevLett.112.221802.
- [287] A. Adare et al. Search for dark photons from neutral meson decays in $p + p$ and $d + \text{Au}$ collisions at $\sqrt{s_{NN}} = 200$ GeV. *Phys. Rev.*, C91(3):031901, 2015. arXiv:1409.0851, doi:10.1103/PhysRevC.91.031901.
- [288] Babette Doebrich. Axion-like Particles from Primakov production in beam-dumps. 2017. arXiv:1708.05776.
- [289] Harald Merkel. Experimente zur Suche nach dunklen Photonen am Mainzer Microtron - Experiments for the search of dark photons at MAMI (Habilitation Thesis). 2014. Available from: <http://wwwa1.kph.uni-mainz.de/A1/publications/habil/>.
- [290] H. Merkel et al. Search for light gauge bosons of the dark sector at the mainz microtron. *Phys. Rev. Lett.*, 106:251802, Jun 2011. Available from: <https://link.aps.org/doi/10.1103/PhysRevLett.106.251802>, doi:10.1103/PhysRevLett.106.251802.

List of Figures

1	(Left) The particle content of the Standard Model of Particle Physics (figure from the ATLAS collaboration at CERN). (Right) Matter content of the Universe according to the latest measurements supporting the Λ CDM model [7, 8]. . . .	vi
1.1	History of the $\pi^+ \rightarrow e^+ \nu_e$ branching ratio measurements. The blue band is the average reported in [14] and the red star represents the most recent Standard Model calculation [13].	6
1.2	Time (left) and energy (right) distributions for the $\pi^+ \rightarrow e^+ \nu_e$ (blue line) and $\pi^+ \rightarrow \mu^+ \nu_\mu \rightarrow e^+ \nu_e \bar{\nu}_\mu$ (red dashed line) decays normalized to the same number of events. . . .	7
1.3	Left: Experimental setup of the E248 experiment at TRIUMF. Right: Positron energy spectrum obtained suppressing $\pi^+ \rightarrow \mu^+ \nu_\mu \rightarrow e^+ \nu_e \bar{\nu}_\mu$ events. Events in the low energy side if the $\pi^+ \rightarrow e^+ \nu_e$ peak come mainly from pions decaying in flight.	9
1.4	Working principle of the stopped pion technique. Pions loose energy through different detectors and stop in an active target. The muon remains confined in the target and only positrons from both decays $\pi^+ \rightarrow e^+ \nu_e$ and $\pi^+ \rightarrow \mu^+ \nu_\mu \rightarrow e^+ \nu_e \bar{\nu}_\mu$ emerge from it.	10
2.1	Left: neutrino mixing matrix elements, Right: quark mixing matrix elements. The surface of the squares represents the absolute value of the relative magnitudes of the matrix elements. In the quark CKM matrix a hierarchical pattern can be seen, in contrast to the present knowledge of the neutrino PMNS matrix.	17

2.2	Lowest order diagram describing the pion decay. From a chiral effective field theory point of view, the pion is a structure-less Goldstone boson which couples with the external electroweak field W through the lagrangian $\mathcal{L}_{W\phi}$. The W decays into lepton-neutrino pairs with coupling described by \mathcal{L}_{Wl}	24
2.3	Helicity suppression mechanism in the pion decay. p_{e^+} and p_{ν_e} represent the particles' momenta. The horizontal arrows over the decay particles describe their spin state: black arrows are the spins according to angular momentum conservation, red arrows show the helicity state (in the case of massless particles) forced by the chiral V-A structure of the weak interactions.	25
2.4	Feynman diagrams for the radiative corrections to pion decay, from real (a) and virtual (b) photons. \bar{l}^+ denotes an anti-lepton.	28
2.5	Leading Feynman diagrams contributing to the QED corrections of the branching ratio. A_{SD-ER} is the amplitude of the structure-dependent virtual correction. A_{I-IB} is the interference amplitude between structure-dependent and structure-independent IB corrections.	29
2.6	The curves enclose the allowed region for the RPV parameters given the available experimental data. The blue curve shows the constraint using the PDG (2007) value for the branching ratio, and the dashed red curve shows the projected constraint from a 0.1% precision measurement of the branching ratio, with the same central value as the blue curve. The green curve shows the expected limits from the Qweak experiment measuring the weak charge of the proton at Jefferson Lab [79].	33
2.7	Majoron emission in a meson decay (figure from [97]). . . .	38
2.8	Experimental results for \mathcal{R}^{D^*} from BaBar, Belle and LHCb. The 1σ contours include statistical and systematic errors together with their correlations (figure from [108]).	40

LIST OF FIGURES

2.9 Single experimental results from BaBar [109], Belle [110, 111] and LHCb [112]. ST and HT refer to measurements with semileptonic and hadronic tags respectively (figure from [108]). The vertical red lines and bands are the average values with combined errors calculated by the Heavy Flavor Averaging group [113, 114]. The blue bands are SM calculations [115, 116, 106]. 41

3.1 **(Left)** Shape of the TRIUMF cyclotron main magnet, which was designed for coping with the defocusing effects arising from the relativistic motion of particles on the spiral orbits [119]. **(Right)** Picture of the fully assembled cyclotron taken in March 1972. 44

3.2 A schematic of the M13 beamline with the extension and the collimator constructed for the PIENU experiment in 2008. 45

3.3 **Left:** Position distribution of π^+ , μ^+ and e^+ at F3 measured with wire chambers. Particle identification was achieved with a plastic scintillator giving energy loss and TOF measurements. Solid lines are Gaussian fits. **Right:** π^+ and e^+ rates at F4 as a function of the selected momentum. 46

3.4 **Left:** fraction of beam positrons as a function of the selected momentum. **Right:** fit of the delayed component of the positrons' time-of-flight showing consistency with the pion decay time. 47

3.5 The end of the M13 beamline, before **(left)** and after **(right)** the extension. Part of the detector was in place to measure the particle content of the beam. 48

3.6 Schematic illustration of the PIENU detector. The target region is magnified in the insert. 49

3.7 **(Left)** B1, B2, B3 and T1 plastic scintillators were read out with 4 PMTs (gray cylinders). Light was collected by four acrylic lightguides (light green). **(Right)** Readout scheme with wavelength-shifting fibers of the T2 plastic scintillator. 54

3.8 **(Left)** WC1/2 wire chamber plane and its preamplifier board. Each chamber consisted of three planes. **(Right)** W1/2 after installation on the beam pipe. 55

3.9	(Left) Picture of the wire chamber WC3 placed in front of the NaI(Tl) calorimeter. (Right) S1 and S2 assembly on their support structure.	56
3.10	Schematic drawing of the silicon readout scheme. Four silicon strips were bonded together and these groups were further connected to a capacitor network. Every fourth group, the signal was fed to amplifiers. This readout scheme allowed the reduction of the number of channels to 48 per plane with a final resolution of about 300 μm	57
3.11	(Left) Back side of the NaI(Tl) crystal on the test bench. (Right) The NaI(Tl) crystal and the 97 pure CsI crystals while the calorimeter assembly was under construction in a low-humidity clean room at TRIUMF.	58
3.12	Schematic view of the xenon lamp monitoring system for the CsI calorimeter (from [145]).	60
3.13	Simplified scheme of the PIENU trigger system. The complete diagram is showed in App. B (from C. Malbrunot [146]).	65
3.14	Picture of a COPPER board with in the four FINESSE front-end cards [147].	68
3.15	COPPER data samples fitted by a waveform template. . . .	69
3.16	Web interface of MIDAS. The green boxes show the different front-end programs and the name of the device on which they were running. The corresponding collected events and rates are showed on the right. MIDAS integrated also an E-log and a history system.	71
3.17	(Left) PIENU-1 and (Right) PIENU-2 detector assemblies. PIENU-1 was comprised of the beam wire chambers WC1/2, the B1, B2, B3, T1 scintillators, and the silicon microstrip detectors S1 and S2. The PIENU-2 assembly contained the NaI(Tl) and CsI calorimeters, the T2 scintillator, and the WC3 wire chamber.	72
3.18	The PIENU detector and beamline after the last bending magnet, showing the steel wall used for radiation shielding.	73
4.1	Blind analysis technique. On a random basis, events are removed from one of the two regions of the target energy spectrum corresponding to either $\pi^+ \rightarrow e^+\nu_e$ or $\pi^+ \rightarrow \mu^+\nu_\mu \rightarrow e^+\nu_e\bar{\nu}_\mu$ events.	78

4.2 Calibration of the scintillators and NaI(Tl) crystal via the Monte Carlo simulation. **a)** Spectrum of the energy sum in the scintillators B1, B2, B3 and silicon detectors S1 and S2. The red histogram represents the MC generated $\pi^+ \rightarrow e^+ \nu_e$ events. The blue histogram shows events happening 200 ns after the pion stop (almost only $\pi^+ \rightarrow \mu^+ \nu_\mu \rightarrow e^+ \nu_e \bar{\nu}_\mu$ events). The black histogram is enriched with $\pi^+ \rightarrow e^+ \nu_e$ events selecting an early time window (< 20 ns) after the pion stop. After calibration, the $\pi^+ \rightarrow e^+ \nu_e$ peak in the data results aligned with the one in the simulation. **b)** The histograms have the same cuts as in a), but refer to the energy deposit in the whole calorimeter system (NaI(Tl)+CsI). **c)** Same as b), but with a cut around the $\pi^+ \rightarrow e^+ \nu_e$ peak in the target. This cut strongly suppresses the $\pi^+ \rightarrow \mu^+ \nu_\mu \rightarrow e^+ \nu_e \bar{\nu}_\mu$ background. In the red and black histograms, the $\pi^+ \rightarrow e^+ \nu_e$ peaks were normalized to the same number of events for direct comparison. 80

4.3 Comparison between data taken with the cosmic ray trigger (black) and a MC simulation (red) based on the CRY [161] simulation package. The spectra are relative to the 21 crystals in the inner-upstream CsI ring. 83

4.4 **(Left)** Energy deposit in B1 versus time of flight. **(Right)** Beam profile in the transverse direction as measured by WC1 and the corresponding selection cut (red box). 84

4.5 Energy deposit in S1, T1 and T2 as a function of the energy deposited in the NaI(Tl) crystal. The proton band is clearly visible. The red line is the cut applied to the data. 85

4.6 Time regions of the waveform digitized by COPPER for the charge integration (figure from S.Ito [147]). The signal region was defined by the trigger signal arrival time, corresponding to $-1.35\mu\text{s}$ in the COPPER timing window. The times before $-1.35\mu\text{s}$ constituted the "pre-region" and contained for example old muon decays. An event was discarded if hits in the pre-region were present (pre-pileup cut). Pile-up hits were searched for $t > -1.35\mu\text{s}$ and an event was rejected if all the four PMTs reading the same scintillator saw more than one hit. 86

4.7	Wide-gate integrated charge in the target B3 as a function of the time difference between the target and B1. False triggers (due to positrons from pions decaying before the Target) are visible in the blue box (corresponding to the values of the cut) in the lower-right part of the 2d-histogram.	87
4.8	Ratio of the integrated charge and the fitted amplitude as a function of the amplitude. The real pileup events are above the red line which represent the value of the applied cut. . . .	88
4.9	Radius at the center of WC3 reconstructed with the tracking. The vertical blue line shows the cut adopted in [100]. The black spectrum represents the distribution of all events, while the red spectrum is the result after the cuts. The wiggles in the spectra correspond to the wire positions in WC3.	89
4.10	Positron energy spectrum after all the analysis cuts (with the prescale factor of the $\pi^+ \rightarrow \mu^+ \nu_\mu \rightarrow e^+ \nu_e \bar{\nu}_\mu$ events taken into account). The spectrum is divided in low-energy and high-energy regions by a cut-off energy E_c (vertical red dashed line).	90
4.11	Time difference between consecutive hits in T1 for each PMT. The edge of the distributions were fitted with an error function. The peaks around 30 ns are due to fake hits at a characteristic time after the real hit.	94
4.12	The T1res shape arising from the finite time resolution of T1.	95
4.13	The oldmu_both shape used in the fit for pileup events where only one positron hits T1.	96
4.14	The simulated distribution of the radiative decays $\pi^+ \rightarrow \mu^+ \nu_\mu \gamma$. The contribution from the NaI(Tl) calorimeter corresponds to the red histogram, while the black histogram is relative to the CsI. The blue histogram is the total time spectrum for the radiative decay.	97
5.1	(Left) Positron spectrum for the 0° case after the RF positron and WC1/2 selection cuts. The peak due to beam muons is visible at ~ 18 MeV. (Right) Muon events selected with the RF cut. The muon peak is visible, together with the high-energy tail due to the integration of the decay positron energy.	102

LIST OF FIGURES

5.2 (Black) Lineshape for the 0° case after subtraction of the muon contribution. The step at 35 MeV is due to the two-dimensional muon cut, which was well reproduced by the simulation (red). The additional peaks at lower energies were due to neutron escapes from from the crystal. Neutrons were emitted by iodine nuclei after capture of a photon from the positron-initiated shower. 103

5.3 NaI(Tl) energy spectrum for events with late timing hits in the CsI with respect to the trigger. The photonuclear peaks are clearly isolated in the data (black) and well reproduced by the rescaled Geant4 simulation (red). The higher peak in the data histogram is due to beam background in the CsI crystals. 104

5.4 G4beamline simulation of the extended M13 beamline. The color lines are particle tracks, mainly coming from the initial part of the beamline. 105

5.5 (Top four histograms) Correlations among independently sampled beam variables. (Bottom four histograms) Correlations among sampled beam variables after applying the Choleski transformation. 109

5.6 Acceptance correction A_{corr} as a function of the WC3 radius for the 2012 dataset (the errors are statistical only). 110

5.7 Simulated energy distributions of positrons coming from the $\pi^+ \rightarrow e^+ \nu_e$ decay chain. The black histogram corresponds to positrons from stopped muons, while the red histogram corresponds to events where the muon decayed in flight in the target. 111

5.8 Fitted value of t_0 as a function of the positron energy. 112

6.1 **2010 Dataset results.** (Top) Fit of the LE (a) and HE (b) time spectra. HE fit residuals for the time before (center left) and after the prompt time (center right). LE fit residuals for the time before (bottom left) and after the prompt time (bottom right). 116

6.2	2011 Dataset results. (Top) Fit of the LE (a) and HE (b) time spectra. HE fit residuals for the time before (center left) and after the prompt time (center right). LE fit residuals for the time before (bottom left) and after the prompt time (bottom right).	117
6.3	2012 Dataset results. (Top) Fit of the LE (a) and HE (b) time spectra. HE fit residuals for the time before (center left) and after the prompt time (center right). LE fit residuals for the time before (bottom left) and after the prompt time (bottom right).	118
6.4	(Top) Dependence of the BR from the choice of the acceptance radius set with WC3 before (black) and after (red) the LET correction and the (blue) μ DIF correction. (Bottom) Dependence of the BR from the choice of the cut-off energy E_c before (black) and after (red) corrections (figure from S. Ito, 2011 dataset).	120
6.5	a) Sum of the energies in B1, B2, S1, S2, and B3. (b) Z vertex for events with positron energy $E_{e^+} < 52$ MeV (shaded histogram) and $E_{e^+} > 52$ MeV (blue full line). The two distributions are normalized to the same number of events, and cuts applied are indicated by the red vertical dashed lines.	127
6.6	Suppressed positron energy spectrum (black histogram). Fitted components: muon decays in flight (blue line, from MC), $\pi^+ \rightarrow e^+ \nu_e$ (green, dot-dashed line, fit to MC), and $\pi^+ \rightarrow \mu^+ \nu_\mu \rightarrow e^+ \nu_e \bar{\nu}_\mu$ (red dashed line, from late-time data events). The top insert shows the residuals (Data-Fit) with statistical error bars and the signal shape in the example case of $E_{e^+} = 40$ MeV and $ U_{ei} ^2 = 10^{-8}$	128
6.7	Acceptance correction $Acc(E_{e^+})$ determined via MC simulation with statistical error bars.	128
6.8	90% C.L. upper limits on the square of the mixing matrix elements $ U_{ei} ^2$ of heavy neutrinos coupled to electrons (thick red line). The black dashed line shows the results from [166].	129

6.9	Global analysis of sterile neutrino limits from [168] (see also [169]) where for simplicity only one additional sterile neutrino was assumed ($i=4$). The black line marked with Pie2 is the latest peak-search PIENU result [170], while the one marked with Ke2 is the peak-search from the NA62 experiment [171, 172]. Other limits are from pion beta decay (PIBETA experiment [173]), previous limits from beta decay (BD1, and the re-analysis of [168] BD2), PIENU and PIENU-H using the $\pi^+ \rightarrow e^+\nu_e$ branching ratio (see Sec. 7.5), KENU and KENU-H using the $K^+ \rightarrow e^+\nu_e$ branching ratio. The Dse2 and Be2 lines come from the $D_s^+ \rightarrow e^+\nu_e$ and $B_s^+ \rightarrow e^+\nu_e$ decays, respectively.	131
6.10	Summary of the 90% C.L. upper limits to $ U_{\mu i} ^2$. The blue and red lines are the results of [174] and [175], respectively. The gray shaded region is the result of [176]. The black full circles are the PIENU results for $0 < E_\mu < 1.2$ MeV, while the black open circles refer to $1.1 < E_\mu < 3.3$ MeV [177]. . .	132
6.11	Simulated positron spectra for the $\pi^+ \rightarrow e^+\nu_e J$ decay for different m_J cases.	133
7.1	95% upper limits for the mixing matrix element $ U_{ei} ^2$ derived from the $\pi^+ \rightarrow e^+\nu_e$ branching ratio.	139
8.1	Rotational curves for different galaxies as measured by Rubin <i>et al.</i> in [181].	146
8.2	Power spectrum from the Planck satellite mission [8]. This is the so-called <i>TT spectrum</i> , which is the power spectrum of the angular temperature fluctuations $(T - T_0)/T_0$ as a function of the spherical harmonics number ℓ . The position and relative amplitude of the peaks can be directly related to cosmological models and the matter content of the Universe. For example, the position of the first peak is approximately $\ell_1 \sim \Omega_m/\sqrt{220}$ and thus gives information about the total matter content.	148

9.1 Summary of DM direct searches for spin-independent DM-nucleus scattering. Solid lines are experimental results, while dashed lines are projected sensitivities of future experiments. The shaded area below the orange line is the "neutrino floor". The current best limits are provided by LUX [190], Panda-X II [191], XENON1T [192] and CDMSlite-II [193]. (Figure from [194]). 154

9.2 Summary of DM direct searches for spin-dependent DM-nucleus scattering [195]. **Left:** DM-neutron limits. **Right:** DM-proton limits. LHC limits are reported only in the DM-neutron limits since they are derived from processes involving Z^0 decays. The DAMA signal is present only in the DM-proton case, since in the DM-neutron case the cross section is smaller and out from range. Comparisons with selected SUSY models are also reported. 155

9.3 Graphical representation of the freeze-out process. The DM number density (normalized to the entropy density: $Y = n/s$) is showed as a function of the temperature (or time) of the Universe. Initially the DM is in equilibrium and the expansion of the Universe dilutes it causing the exponential drop of the annihilation rate. When $n_\chi \Gamma \sim H$, the DM freezes out (blue curves). The plot represents solutions of the Boltzmann equation for the expanding universe $\dot{Y} = \langle \sigma v \rangle s (Y_{eq}^2 - Y^2)$ (see e.g. [196]). 156

9.4 Graphical representation of the two sides of Eq. 9.6. The dashed blue line corresponds to $1/(m \cdot M_p \cdot \sigma) = 10^{-14}$ calculated with the weak scale "miracle" values $m_\chi = 100$ GeV and $\sigma = G_F^2 m_\chi^2$. Other two horizontal lines at 10^{-8} and 10^{-20} are added for reference. 157

9.5 Acceleration parameter for various astrophysical systems as a function of the baryonic mass M_b . The data show a common characteristic acceleration scale which is natural in MOND models but requires large fine-tuning in Λ CDM models. Figure from [213]. 165

LIST OF FIGURES

10.1 Beam-Dump experimental concept. A beam is impinging into a thick target (beam-dump) where dark photons are produced with a bremsstrahlung-like process. A detector shielded from the SM background can detect DM particles from dark photon decay. The detection proceeds through a dark photon-mediated interaction with nuclei or electrons in the detector. 170

10.2 The SLAC beam-dump experiment E137 [243]. The plastic scintillator and wire chambers detector was located after 200 m of earth shielding provided by a hill after the beam-dump (Figures from [243] and [248]). 171

11.1 The MESA (Mainz Energy-Recovery Superconducting Accelerator) complex with the three foreseen experiments. . . 176

11.2 Picture of the existing aluminum beam-dump, previously used by the A4 experiment. 177

11.3 Experimental test stand for the investigation of the crystals response to the MAMI electron beam (photo and figure from M. Christmann). 182

11.4 Calibrated data in photoelectrons (p.e.) versus the simulated number of photoelectrons. Points indicate the (Gaussian distribution) fitted averages and the error bars indicate the fitted widths of the energy spectra. 184

11.5 QDC spectra obtained at MAMI for the different crystal types (figure from M. Christmann). 185

11.6 Proton and electron energy spectra after recoiling against a DM particle. 186

11.7 Simulated exclusion limits for the three foreseen construction phases of the darkMESA experiment compared to the existing limits from NA64 [272, 273], E137 [243], BaBar [274], MiniBooNE [275], and CRESST (direct detection) [276]. 188

11.8 Projected exclusion limits for the MAGIX experiment in the case of $\gamma' \rightarrow e^+e^-$ visible decays. The reported existing limits are from the re-analysis [278] of the E774 [279] data, APEX [280], WASA [281], KLOE-2 [282], HADES [283], BABAR [284, 285], A1 [286], PHENIX [287], E141 [242, 288] (Figure from H. Merkel). 189

11.9	Exploded view of the prototype under construction at the Mainz Institute of Nuclear Physics. The detector system is composed by a matrix of 5×5 PbF_2 crystals and two hermetic layers (IV, OV) of scintillators separated by lead sheets for vetoing cosmic rays and surrounding radiation.	190
11.10	Top-left: Drawing of the grooved scintillator with the wavelength-shifting fiber. Top-right: Read-out electronics of the silicon photomultipliers. Bottom: Detail of the read-out card which contains 4 silicon photomultipliers. A card is installed on both the short sides of the scintillators, reading out both ends of the fibers.	191
A.1	Cross section of the PIENU Detector.	196
A.2	Side view of the PIENU Detector. The pion beam comes from the right side.	197
A.3	Exploded view of a beam wire chamber (WC1/2).	198
A.4	The two beam wire chambers (WC1/2) assembled together. The beam direction is from left to right.	198
A.5	Exploded view of the WC3 wire chamber.	199
A.6	Full WC3 assembly with read-out cards.	199
B.1	Complete trigger diagram of the PIENU Experiment.	201
F.1	SF5 Pb-Glass crystal (from Schott AG).	211
F.2	SF6 Pb-Glass crystal (from Schott AG).	211
F.3	SF57HTultra Pb-Glass crystal (from Schott AG).	211
F.4	PbF_2 crystal (previously A4 collaboration).	212
F.5	BGO crystal (on loan from INFN Frascati).	212

List of Tables

2.1	Pion decay modes and corresponding branching fractions. .	26
2.2	Corrections to the leading-order value for R_{π}^{SM} from [13, 70].	29
2.3	Experimental results on lepton universality from π , K, τ , and W decays. \mathcal{B} represents the branching ratio of a specific decay mode.	39
3.1	Characteristics of the PIENU detector. The z position is given with respect to the centre of the detector which was defined as the centre of the B3 scintillator. A more detailed data table can be found in [128].	51
3.2	Typical rates of each trigger in normal datataking conditions.	67
3.3	Datataking periods with the special runs taken for calibration and detector studies.	74
5.1	Estimated low energy tails for different values of the angle and cut-off energy E_c	107
6.1	Results from the timing spectra for the three datataking periods. The exact fit values are truncated for a more compact presentation. The errors are statistical only as obtained by the MINUIT [165] fit and the parameters marked as <i>fixed</i> (or <i>fxd</i>) were kept fixed during the fit. The statistical errors on the BR reflect the magnitude of the data samples collected in the three periods. The complete value of the branching ratio is not reported, since the datasets are still blinded. The first unblinded result referring to the 2010 dataset was published in [100].	119
6.2	Preliminary systematic tests for the time spectrum fits. . . .	122

6.3	Preliminary (blinded) results for the branching ratio. All the numbers are in units of 10^{-4}	125
11.1	Comparison among candidate materials for the construction of the darkMESA calorimeter.	181
11.2	Crystals tested with the MAMI 14 MeV electron beam. The two PbF_2 crystals are truncated pyramids with bases 30×30 mm and 26×26 mm.	182

Glossary

ADC

Analog-to-digital converter.

B1 B1 and B2 are plastic scintillators in the PIENU detector.

Bhabha scattering

Electron-positron scattering. In PIENU it is relevant since decay positrons can be affected by this process.

BINA

The cylindrical monolithic NaI(Tl) crystal used as positron calorimeter in the PIENU detector.

BinaHigh

A trigger used in the PIENU experiment to record events with large energy deposit in the NaI(Tl) and CsI.

Blinding

A procedure whereby the result of an analysis is changed by an unknown random factor, to avoid analysis bias.

Branching ratio

The ratio of the rate of a specific decay mode to the full decay rate.

Bremsstrahlung

A process by which charged particles emit photons when accelerating.

ChPT

Chiral perturbation theory, sometimes written χ PT: it is a low-energy effective field theory description of QCD.

COPPER

A 500 MHz ADC used to digitize the waveforms from some elements of the PIENU detector. In particular COPPER digitizes the plastic scintillators and the fit to its waveforms is the primary time measurement used for building the time spectra.

CsI Cesium iodide, a type of crystal scintillator that forms the outer part of the PIENU calorimeter. It is used to detect the shower leakage from the main NaI(Tl) calorimeter.

Cyclotron

A circular particle accelerator with constant magnetic field and variable orbital radius. This is the main accelerator system present at TRIUMF.

darkMESA

Name for the Beam-Dump eXperiment at the MESA accelerator facility.

ΔT The time interval below which multiple hits cannot be resolved in T1. It is a parameter in the fitting function for the high energy time spectrum.

DM Dark Matter.

Early Trigger

A trigger used in the PIENU experiment to record events shortly after t_0 , the pion arrival time. It is used to enrich the sample with $\pi \rightarrow e\nu$ events.

E_c Threshold used to separate low energy and high energy events. Typically set at 52 MeV.

ERL Energy-recovery LINAC.

Flavour

Particle species. In the Standard Model, there are three flavours of quarks and three flavours of leptons.

FLRW

Friedmann-Lemaître-Robertson-Walker metric used in General Relativity for describing homogeneous and isotropic space-times.

FPGA

Field-programmable gate array. A programmable chip that performs logic operations.

GEANT4

A C++ software package for simulating particles and their interactions with matter.

Generation

In the Standard Model, there are three generations of fermions, each consisting of two quarks, a charged lepton, and a neutrino. The particles within generations differ from their counterparts only by mass. For the quarks and charged leptons, each generation is heavier than the one before, while the mass ordering of neutrinos is unknown.

Kink

Angle between the track reconstructed using WC1 and WC2 and the track reconstructed using S1 and S2. Used to identify π DIF events.

Lepton universality

The assumption in the Standard Model that the electroweak couplings of the three lepton generations are the same.

MAGIX

MESA Gas Internal target eXperiment. It is one of the foreseen experiments at the new accelerator facility MESA. MAGIX is based on a two-spectrometer setup and a gas-jet target mounted on one of the recirculation arcs of MESA.

MESA

Mainz Energy-recovery Superconducting Accelerator. It is an accelerator being constructed at the Institute for Nuclear Physics at the Johannes-Gutenberg university in Mainz, Germany.

M13

A secondary beamline at TRIUMF, used to deliver particles to the PIENU experiment.

Michel decay

The 3-body decay of a muon to an electron and two neutrinos.

Michel edge

The endpoint of the energy spectrum of electrons produced via muon decay.

MIDAS

A web-based DAQ interface developed at TRIUMF and PSI.

Muon correction

A correction applied to the positron beam data to correct for the presence of muons.

 μ DAR

Muon decay-at-rest.

 μ DIF

Muon decay-in-flight.

 μ DIF correction

A multiplicative factor that must be applied to the branching ratio obtained from the time spectrum fit to take into account muon decay-in-flight events in the target. These events have the same time dependence as $\pi \rightarrow e\nu$ events and can have measured energy above E_c .

NaI(Tl)

Thallium-doped sodium iodide, a type of inorganic crystal scintillator.

oldmu_both

A component in the fitting function for the high energy time spectrum. It describes events where two Michel positrons enter the crystal array but only passes through T1.

Old muon

A muon present in B3 prior to the arrival of the primary pion.

PbGlass

Lead glass: it is a type of glass where lead replaces other common chemical elements like calcium. The lead percentage lies between 15 and 40%. As a particle detector, it produces Čerenkov light.

PbF₂

Lead-fluoride. Material used in particle detectors based on Čerenkov light emission.

 π DAR

Pion decay-at-rest.

π DIF

Pion decay-in-flight.

Positron beam data

Data taken with a positron beam, instead of the usual pion beam. Used to obtain the response function of the crystal array to 70 MeV positrons.

Prescale

One of the triggers used in the PIENU experiment. In the PIENU experiment, the prescale factor is sixteen, meaning one event out of sixteen is stored.

proof

Software written for the PIENU experiment to convert raw data into ROOT trees.

PSI Paul Scherrer Institute. A research facility in Villigen, Switzerland, with a cyclotron similar to the TRIUMF cyclotron, but based on superconducting technology.

QCD

Quantum chromodynamics. The theory that describes the strong interaction.

r A parameter in the fitting functions for the time spectra. Describes the proportion of low energy events promoted to the high energy time spectrum via mechanisms whose timing is independent of t_0 .

R The distance between the centre of WC3 and the reconstructed positron track.

R_π The pion branching ratio.

Reduced χ^2

The χ^2 of a fit divided by the number of degrees of freedom of the fit.

RF Radio-frequency. In this context, refers to the accelerating electric field used in the TRIUMF cyclotron.

ROOT

Object-oriented C++ based data analysis software commonly used in high-energy physics.

Scintillator

A material that emits photons of a characteristic wavelength when charged particles pass through it. Common types include crystal, organic, and liquid noble gas scintillators. The PIENU detector includes crystal and plastic scintillators.

Silicon strip detector

A position-sensitive particle detector, consisting of segmented pieces of silicon with a bias voltage applied.

S1 S1, S2, and S3 are the three silicon strip detectors used in the PIENU experiment.

Standard Model

A theoretical model of the fundamental particles and their interactions.

t₀ The pion stop time.

t₀ correction

A multiplicative factor that must be applied to the branching ratio obtained from the time spectrum fit to take into account the dependence of the measured value of the time on the decay positron energy.

T1 T1 and T2 are plastic scintillators in the PIENU detector.

T1res

A component in the fitting function for the high energy time spectrum. It describes events where two Michel positrons pass through T1 into the crystal array sufficiently close together in time that only a single hit in T1 is recorded.

Tail correction

A multiplicative factor that must be applied to the branching ratio obtained from the time spectrum fit to take into account $\pi \rightarrow e\nu$ events whose measured energy was less than E_c .

TDC

Time-to-digital converter.

B3 A plastic scintillator in the PIENU detector that functions as the pion stopping (active) target.

TIGC

A VME module used in the BinaHigh trigger from 2010 onwards for summing the pulse height of BINA and CsI, and issuing a trigger if it exceeds a defined threshold.

TOF

Time of flight.

Trigger

A digital logic circuit that takes detector signals as inputs, and sends a signal to the data acquisition system if the event should be stored.

Trk Trk1, Trk2, Trk3 are the three defined tracker systems in the PIENU experiment.

TRIUMF

Canada's national laboratory for particle and nuclear physics. TRIUMF was founded in 1968 by Simon Fraser University (SFU), the University of British Columbia (UBC), and the University of Victoria (UVic). The original meaning of the acronym is "Three-universities meson facility", but nowadays it is a consortium of 20 universities across Canada. It is situated on the south campus of UBC.

VF48

A 60 MHz ADC used to record waveforms from some elements of the PIENU detector.

VT48

A 1.6 GHz TDC used to record signals from some elements of the PIENU detector and trigger modules.

Wire chamber

A position-sensitive particle detector, consisting of wires in a gas-filled chamber with high voltage applied across it.

WC1

WC1, WC2, and WC3 are the three wire chambers used in the PIENU detector.

Zv Reconstructed Z-position of the pion decay vertex in the target B3.

Related Publications

1. *Detector response of Cherenkov radiators for calorimetry in the energy range below 14 MeV*
M. Christmann *et al.*: submitted to Nucl. Instr. Meth. A (2019).
2. *Instrumentation and optimization studies for a beam dump experiment (BDX) at MESA - DarkMESA*
M. Christmann *et al.*: Nucl. Instr. Meth. A, 162398 (2019).
3. *Dark Matter at the Intensity Frontier: the new MESA electron accelerator facility*
L. Doria *et al.*: Proceedings of the ALPS 2019 Conference (2019), arXiv:1908.07921.
4. *Search for Massive Neutrinos in the $\pi \rightarrow \mu\nu$ Decay*
A. Aguilar-Arevalo *et al.*: Phys. Lett. B, **798**, 134980 (2019).
5. *Search for light dark matter with the MESA accelerator*
L. Doria *et al.*: to be published in Proceedings of CIPANP18, arXiv:1809.07168 (2018).
6. *Improved Search for Heavy Neutrinos in the Decay $\pi \rightarrow e\nu$*
A. Aguilar-Arevalo *et al.*: Phys. Rev. D **97** (7), 072012 (2018).
PRD Editor's suggestion.
7. *Looking for new Physics with Pion Decays*
L. Doria : Proceedings of Science, BORMIO2017 (2017)
8. *Improved Measurement of the $\pi \rightarrow e\nu / \pi \rightarrow \mu\nu$ Branching Ratio*
A. Aguilar-Arevalo *et al.*: Phys. Rev. Lett. **115**, 071801 (2015).
9. *Detector for Measuring the $\pi \rightarrow e\nu$ Branching Fraction.*
A. Aguilar-Arevalo *et al.*: Nucl. Instr. Meth. A, **791**, 38-46 (2015).
10. *Search for new Physics with the $\pi \rightarrow e\nu$ Decay.*
L. Doria, Eur. Phys. J. Web of Conferences, INPC 2013, Florence (Italy) **Vol 66**, 05004 (2014).
11. *Search for Massive Neutrinos in the Decay $\pi \rightarrow e\nu$*
M. Aoki *et al.*: Phys. Rev. D **84**, 052002 (2011).

12. *Study of a large NaI(Tl) Crystal*
A. Aguilar-Arevalo *et al.*: Nucl. Inst. and Meth. **A 621**, 188-191 (2010).
13. *The PIENU experiment: a precision measurement of the $\pi \rightarrow e\nu / \pi \rightarrow \mu\nu$ branching ratio*
L. Doria, Proceedings of the Lake Louise Winter Institute, Lake Louise, Alberta (Canada), 2010.
14. *High Purity Pion Beam at TRIUMF*
A. Aguilar-Arevalo *et al.*, Nucl. Inst. Meth. **A 609**, 102 (2009).

Acknowledgments

At the end of this work, I would like to thank all the people whom helped me in reaching this important milestone. Since the present work spans an entire decade, the list will be rather long.

First of all, I would like to thank Prof. Douglas A. Bryman and Dr. Toshio Numao for giving me the opportunity to join the PIENU Collaboration from its beginning. Most of what I know about experimental physics and how a complex experiment should be thought and built, I have learned from them.

I am very much indebted with Prof. Concettina Sfienti and Prof. Achim Denig for enthusiastically welcoming me in Mainz and for starting a fruitful collaboration.

I would like to thank my office mates over the years for always bringing good mood in the Trailer Ff: Dr. Aleksey Sher, Dr. Alexis A. Aguilar-Arevalo, Dr. Belina von Krosigk, Dr. Matek Lewczuk, Dr. Alice Miceli, Dr. Astrid Münnich, Dr. Dmitry Vavilov, and Dr. Bob Velghe.

In constructing the experiment and in analyzing its huge amount of data, I enjoyed the collaboration with many students and co-op students to whom I'm very thankful: Dr. Dorothea vom Bruch, Dr. Saul Cuen-Rochin, Dr. Shintaro Ito, Dr. Chloe Malbrunot, Mingming Ding, Dr. Kaoru Yamada, Naosuke Ito, Katharina Gill, Kevin Hildebrand, Cameron Hurst, Haotian Pang, Dr. Tristan S. Sullivan, Eric Thewalt, Ben Walker, and Kevin Yin. I am particularly grateful to Dorothea, Saul, Shintaro (Ito-san), and Tristan for all their work in the final phases of the analysis.

Over the years, I was lucky to collaborate with outstanding scientists: Prof. Masaharu Aoki, Prof. Marvin Blecher, Prof. Ahmed Hussein, Dr. Laurence Littenberg, Dr. Steve Kettell, and Dr. Richard "Dick" E. Mischke. Dick in particular represents for me a rare example of passion and dedication to physics.

Without great scientists and technicians, no experiment could be built. I am grateful to the TRIUMF DAQ experts Pierre Amaudruz, Dr. Konstantin Olchanski, Dr. Chris Pearson, and Dr. Renee Potissou, the electrical/electronics experts Ray Bula, Miles Constable, Dr. Leonid Kurchaninov, Alex Sorokin, the mechanical technicians Steve Chan, Marielle Goyette, Chapman Lim, Philip Lu, Robert Openshaw, Jaroslaw Zielinski, and the detector engineer Grant F. Sheffer. I am particularly indebted with Chapman, an expert in nearly everything and always ready to help.

The whole experimental infrastructure would not have been timely in place without the extremely careful engineering of Naimat Khan, the

beamline technicians Bruno Gasbarri, Bruce Keeley and John McKinnon.

A lot of what I know about simulations and Geant4 was learned from Dr. Peter Gumplinger: vielen Dank! Ich hoffe, dass du jetzt viel mehr Zeit haben wirst, um deine Berge zu geniessen.

Everything would be way more difficult without and excellent administration: many thanks to Kai-Mei Chu, Sharina Dupree, Josie Farrell, Niki Martin, and Jill Seeley.

Non posso dimenticare in questi ringraziamenti tutti i miei amici italiani e italo-canadesi che hanno rallegrato un bellissimo periodo a Vancouver: Simone Baroni, Angelo Calci, Anadi Canepa e Zoltan, Franco Mammarella e ARPICO, Marco Marchetto, Anna Grassellino, Marcello Pavan, Francesco Raimondi e Alice, Matteo Vorabbi. Nell'ultimo periodo il laboratorio e' diventato un posto molto piú divertente dopo l'arrivo di Giacomo Gallina.

In the last year, transitioning into new projects, I enjoyed the collaboration and mentoring of Dr. Fabrice Retiere, who enthusiastically welcomed me in his group: merci! Working in the eLINAC control room would not have been the same without the presence of Dr. Martin Alcorta Moreno: gracias y eskerrick asko! Ich möchte auch Dr. Beatrice Franke danken: ihre Freundschaft und Espresso-Maschine sind für mich sehr wichtig gewesen!

Als ich nach vielen Jahren wieder nach Mainz kam, war es schön wieder Freunde und Kollegen zu treffen: Prof. Patrick Achenbach, Dr. Sebastian Baunack, Dr. Luigi Capozza, Dr. Michael Otto Distler, Boris Gläser, Dr. Harald Merkel, Dr. Ulrich Müller, Martina Hahner, and Dr. Sören Schlimme. Ich danke auch meinen neuen Kollegen Dr. Stefano Caiazza, Dr. Matthias Höck, Dr. Björn Spruck und Dr. Michaela Thiel für ihre Freundschaft und viele Mittagspausen. Beim Start der neuen Dunkle Materie Experimente, genieße ich die Zusammenarbeit mit einem exzellenten Doktoranden: Mirco Christmann.

Gli ultimi ringraziamenti sono sempre i piú importanti: ringrazio quindi infine la mia famiglia - Sonia Leo e Manu - per essermi stata sempre vicina in tutti questi anni in giro per il mondo.

Graxie ~ Thank You ~ Danke